Continuous synthesis of sulfonate metal–organic frameworks for proton conducting membrane applications

Chao Sun

Submitted in accordance with the requirements the

degree of *Doctor of Philosophy*

The University of Leeds

School of Chemical and Process Engineering

December 2024

Intellectual Property and Publication Statements

The candidate confirms that the work submitted is his own, except where work which has formed part of jointly authored publications has been included. The contribution of the candidate and the other authors to this work has been explicitly indicated below. The candidate confirms that appropriate credit has been given within the thesis where reference has been made to the work of others.

Chapters 2, 3 and 4 are comprised of jointly authored material. The details for each of these works and the authors contributions are summarized below. An overall thesis summary is provided in Chapter 1.7.

Chapter 2: Droplet-based Millifluidic Synthesis of a Proton-conducting Sulfonate Metal–organic Framework

Authors: Chao Sun, Matthew Barton, Christopher M. Pask, Mohamed Edokali, Lina Yang, Andrew J. Britton, Stuart Micklethwaite, Francesco Iacoviello, Ali Hassanpour, Maximilian Besenhard, Rik Drummond-Brydson, Ke-Jun Wu, Sean M. Collins

Publication: Chemical Engineering Journal

Volume: 474

Page number (or article number): 145892

Date of acceptance: 4 September 2023.

I led the design of the experiments in consultation with my PhD supervisors, and I carried out the majority of the experimental work, analysed the data, drafted the manuscript, and revised it following co-author and peer reviewer comments. In terms of experimental work, I created the flow reactors and carried out the syntheses reported in the manuscript. M. Barton assisted in scaling up one synthesis as part of a MChem project which I oversaw as an in-lab (day-to-day) supervisor. I also carried out all membrane fabrication and proton conductivity tests. C. M. Pask solved the single crystal structure of Cu-SAT in this paper using a high-quality single crystal that I prepared. M. Edokali and A. Hassanpour provided tools and experimental space for the fabrication of membranes. L. Yang assisted in the construction of the flow reactor at the start of this work, but the final two-phase flow reactor reported in the paper I

constructed myself. A. J. Britton acquired X-ray photoelectron spectroscopy (XPS) data from samples I prepared. I then carried out the analysis of the XPS data. S. Micklethwaite conducted the cryogenic scanning electron microscopy (SEM) and X-ray energy dispersive spectroscopy (EDS) of the membranes that I prepared. In turn, I interpreted the results from the SEM and EDS data. F. Iacoviello collected X-ray computed tomography images of the membranes I prepared. K.J. Wu assisted in computational fluid dynamics (CFD) simulation of flow reactor based on experimental results I provided. S. M. Collins and I acquired scanning electron diffraction (SED) data together on samples I prepared. I then processed and analyzed the SED data. S. M. Collins, K.-J. Wu, M. Besenhard, and R. Drummond-Brydson provided supervision of the work.

Chapter 3: Modulating proton conductivity through crystal structure tuning in arenedisulfonate coordination polymers

Authors: Chao Sun, Christopher M. Pask, Sang The Pham, Emilio Rapaccioli, Andrew J. Britton, Stuart Micklethwaite, Andrew Bell, Maximilian O. Besenhard, Rik Drummond-Brydson, Ke-Jun Wu, Sean M. Collins

Publication: Journal of Materials Chemistry A

Volume: 12

Page number (or article number): 18440

Date of acceptance: 18 June 2024.

I led the design of the experiments in consultation with my PhD supervisors, and I performed the majority of the experimental work, analysed the data, drafted the manuscript, and revised it following co-author and peer reviewer comments. For the experimental work, I carried out the syntheses reported in the manuscript. E. Rapaccioli assisted in the synthesis of one of five total sulfonate MOFs reported as part of an MChem project which I oversaw as an in-lab (day-to-day) supervisor. I also carried out all pellet and membrane fabrication and proton conductivity tests. C. M. Pask assisted in solving the single crystal structures in this paper. I prepared high quality single crystals and carried out most of tests and data analysis of single crystal XRD. S. T. Pham performed SEM and EDS of the different sulfonate crystals that I synthesized, S. Micklethwaite conducted the cryogenic SEM and EDS of the

membranes that I prepared. In turn, I interpreted the results from all these SEM and EDS data. A. J. Britton acquired XPS data from samples I prepared. I then carried out the analysis of the XPS data. A. Bell provided tools and experimental space for the pellet making in this work. S. T. Pham acquired SED data on samples I prepared. I then processed and analyzed the SED data. S. M. Collins, R. Drummond-Brydson, M. Besenhard, and K.-J. Wu provided supervision of the work.

Chapter 4: Ultrasound-assisted continuous aqueous synthesis of sulfonate, imidazolate, and carboxylate MOFs with high space time yield

Authors: Chao Sun, Sang The Pham, Sarah L. Boyall, Ben Douglas, Andrew J. Britton, Stuart Micklethwaite, Thomas W. Chamberlain, Maximilian O. Besenhard, Rik Drummond-Brydson, Ke-Jun Wu, Sean M. Collins

Publication: submitted.

I led the design of the experiments in consultation with my PhD supervisors, and I performed the majority of the experimental work, analysed the data, drafted the manuscript, and revised it following co-author and peer reviewer comments. In terms of the experimental work, I created the ultrasound-assisted flow reaction platform and carried out the syntheses reported in the manuscript. I also carried out all pellet and membrane fabrication and proton conductivity tests. S. T. Pham performed SEM and EDS of the different MOFs that I synthesized. S. Micklethwaite conducted the cryogenic SEM and EDS of the membranes that I prepared. In turn, I interpreted the results from all these SEM and EDS data. S. L. Boyall and T. W. Chamberlain provided equipment in the form of a gas mass flow controller to build the two-phase flow reactor (one of two reactors used in this work). B. Douglas assisted with some gas sorption measurements of samples that I prepared at the start of this work. I then analysed the results of these gas sorption measurements. A. J. Britton acquired XPS data from samples I prepared. I then carried out the analysis of the XPS data. S. M. Collins, K.-J. Wu, M. Besenhard, and R. Drummond-Brydson provided supervision of the work.

Additional Publications:

Adam F Sapnik, **Chao Sun**, et al. Mapping nanocrystalline disorder within an amorphous metal–organic framework, Communications Chemistry, 6 (2023) 2106.

Sang T, Pham, Anh K. Tieu, **Chao Sun**, et al. Direct Visualization of Chemical Transport in Solid-State Chemical Reactions by Time-of-Flight Secondary Ion Mass Spectrometry, Nano Letters, 24 12 (2024) 3702–3709.

Mohamed Edokali, Mozhdeh Mehrabi, Oscar Cespedes, **Chao Sun**, et al. Antifouling and stability enhancement of electrochemically modified reduced graphene oxide membranes for water desalination by forward osmosis, Journal of Water Process Engineering, 59 (2024) 104809.

Acknowledgments

I would firstly like to thank my main supervisor Dr Sean Collins for his support, guidance, and encouragement to work on such an exciting and multidisciplinary project. I would also want to take this opportunity to express my great thanks to my co-supervisors, Prof. Rik Drummond-Brydson, Dr Ke-jun Wu and Dr Maximilian Besenhard, for their excellent guidance, huge help and technical assistance during my PhD studies.

I would like to thank a wide range of researchers/lecturers/technicians, without their help and assistance, much of my work would not have been possible. These include Dr Sang The Pham, Dr Christopher M. Pask, Dr Ben Douglas, Prof. Andrew Bell, Prof. Dr Andrew J. Britton, Stuart Micklethwaite, Prof. Thomas Chamberlain, Robert Simpson, Dr Mohammed Javed and Dr Adrian Cunliffe, they provided a lot of help for the analysis of samples. And, it has been a great pleasure to work in Lab G14 and 1.40b in the School of Chemical and Process Engineering and Lab G39 and 1.06 in the School of Chemistry with my dear colleagues, Lina Yang, Matthew Simmons, Tom Bailey, Matthew Barton, Mohamed Edokali, Evangelos Daskalakis, Emily Wynne, Martha Ilett, Jack Hallas, Conor Dougen, and Sarah Boyall, they have given me useful discussions and helps regarding my research.

Thanks for the support and encouragement to all of my families, their continual encouragement for me to pursue higher education from a young age still remains one of the biggest contributors to my motivation. Thanks to my friend Jianting Feng for his countless help during my studies in Leeds.

Finally, I would also appreciate the financial support from Leeds-CSC scholarship.

Abstract

Metal–organic frameworks (MOFs) have emerged as very promising materials for applications from gas uptake and separations to catalysis and proton exchange membranes (PEMs). The increasing commercialization of MOFs has, in turn, stimulated significant interest in developing scalable and green chemical synthesis. The under-developed class of sulfonate MOFs and non-porous coordination polymers (CPs) offers particularly well-suited functional group chemistry for proton conduction.

To advance these areas, first a batch synthesis of a Cu^{2+} based MOF incorporating both sulfonate and amine groups, termed Cu-SAT, was transferred to continuous synthesis in a millifluidic flow reactor. Next, the exploration of alternative sulfonate ligands, metal ions, and greener solvents were explored to identify targets for simpler, green chemical syntheses of proton conducting sulfonate CPs. Finally, aqueous-phase synthesis of a Ca^{2+} sulfonate CP, termed Ca-NDS (water), was transferred to an ultrasound-assisted flow reactor to increase production rate and space time yield up to 12.6 g h^{-1} and 3.4×10^4 kg m^{-3} day^{-1}, respectively. The generalization of this reactor design was also demonstrated by developing imidazolate ZIF-8, and carboxylate UiO-66-NH_2 MOFs syntheses in the same ultrasound-assisted flow reactor.

The prepared sulfonate MOFs and CPs exhibited proton conductivities spanning 10^{-4} to 10^{-3} S cm^{-1} in pellet and polymer composite forms. Structural analysis revealed a consistent structure-function relationship between the proton conductivity and the tortuosity of the hydrogen bonding network in these crystals. Guiding work in developing millifluidic reactors, design of experiments and response surface modelling were used to evaluate flow syntheses revealing trade-offs in particle size control and yield in Cu-SAT, but highlighting a single optimum for size-controlled particles in high space time yield through ultrasound-assisted continuous synthesis of Ca-NDS (water). The culmination of a general, aqueous flow-reactor platform for MOFs establishes an approach for scalable and green chemical synthesis of MOFs achieving top production rates greater than 10 g h^{-1} and space time yields greater than 10^4 kg m^{-3} day^{-1}. Probing the effects of ultrasound power on MOF synthesis identified enhanced nucleation as the key factor. Together, these results outline routes for reduced environment impact in the scalable, high-quality MOF synthesis.

Table of Contents

Figures

Tables

Abbreviations

MOFs	Metal-organic frameworks
PEMs	Proton exchange membranes
STY	Space time yield
DoE	Design of experiment
CPs	Coordination polymers
REACH	Registration, Evaluation, Authorization, and Restriction of Chemicals
DMF	N, N-dimethylformamide
PCPs	Porous coordination polymers
SBUs	Secondary building units
IRMOF	Isoreticular metal organic framework
ZIF	Zeolitic imidazolate framework
MIL	Materials of institute Lavoisier
PCN	Porous coordination network
UiO	University of Oslo
MMMs	Mixed matrix membranes
PDMS	Poly dimethylsiloxane
RH	Relative humidity
Him	Imidazole
PEM	Proton exchange membrane
PEMFCs	Proton exchange membrane fuel cells
FCs	Fuel cells
COFs	Covalent organic frameworks
PVP	Poly(vinylpyrrolidone)
PVDF	Poly(vinylidene fluoride)
SPEEK	Sulfonated poly(ether ether ketone)
SPAEK	Sulfonated poly(arylene ether ketone)
EIS	Electrochemical impedance spectroscopy
AC	Alternating current
E_a	Activation energy
SEM	Scanning electron microscope
FTIR	Fourier-transform infrared spectroscopy

XRD	X-ray diffraction
TGA	Thermogravimetric analysis
TEA	Triethylamine
DMAc	N,N-dimethylacetamide
NMP	N-methylpyrrolidone
DMSO	Dimethyl sulfoxide
SAV	Surface area to volume
PTFE	Polytetrafluoroethylene
PFA	Polyfluoroalkoxy
RTD	Residence time distribution
OVAT	one-variable-at-time
RSM	Response surface modelling
PCA	Principal component analysis
CFD	Computational fluid dynamic
NDS	Naphthalenedisulfonate
ADS	Anthraquinone-1,5-disulfonate
IQR	Interquartile range
EDS	Energy dispersive X-ray spectroscopy
XPS	X-ray photoelectron spectroscopy
STEM	Scanning transmission electron microscopy
CHNS	Carbon, hydrogen, nitrogen and sulphur
ATR	Attenuated Total Reflection
SED	Scanning electron diffraction
CV	Cyclic Voltammetry
SC-XRD	Single crystal XRD
SI	Supporting Information
RMSE	Root mean square error
EtOH	ethanol
Mw	Molecular Weight
DI	Deionized
RMSD	Root mean squared displacement
H_2ATA	2-aminoterephthalic acid
NaOH	Sodium hydroxide

CFIR	Coiled flow inverter reactor
GMFC	Gas mass flow controller
BBD	Box-Behnken design
BPR	Back-up pressure regulator

Chapter 1 Introduction

Chemical separations, gas adsorption/separation and energy storage devices need to use abundant porous materials and materials with controlled functional group chemistry [1]. MOFs have shown great potential for applications ranging from chemical separations [2], proton conduction [3] and catalysis [4, 5] to gas storage [6, 7] and presented improved efficiencies and reduced waste in these applications. The mass production of MOFs is required for their practical applications. However, the scalable synthesis of MOFs is very challenging because precise reaction conditions, e.g. specific solvents, temperature and controlled crystallization are required. Typical synthesis methods, such as hydrothermal or solvothermal synthesis, have several disadvantages: they are low-yielding, time-consuming, and difficult to maintain at industrial scales, resulting in high costs and variable quality. In addition, MOFs are sensitive to environmental factors, which complicates the synthesis of consistent products for practical application.

With the introduction of the Registration, Evaluation, Authorization, and Restriction of Chemicals (REACH), industry is increasingly moving towards safe production and use of chemicals [8]. For the scale-up production of MOFs, sustainability will need to be considered hand-in-hand, and green chemistry principles of using lower toxicity solvents and reducing solvent waste should be followed in MOF synthesis. Toxic reagents and solvents, such as N,N-dimethylformamide (DMF) [9], have been widely used in MOF synthesis. However, REACH has listed DMF as a “substance of very high concern”, promoting development of alternative MOF synthetic routes. In addition, some metal precursors and organic ligands can be toxic or environmentally harmful. Moreover, the toxicity of MOF crystals themselves is also a key issue, and a comprehensive toxicity assessment is required to ensure their safe use in practical applications [10]. Solving these toxicity issues is very significant for sustainable and safe production of MOFs, which will require the development of more environmentally friendly synthesis methods.

Different chemicals, solvents, and reaction conditions are involved in each MOF, resulting in different growth mechanisms, such as La Mer Theory [11] and Classical Nucleation Theory [12], and crystals with 2D layered or 3D porous structures. These variabilities impede the development of universal principles for MOF formation,

because the factors that have effects on nucleation rates, growth rates, and morphology can vary widely [13]. Due to the enormous diversity of MOF chemistry, it is currently unclear which aspects of MOF crystal growth are generalizable and which are unique to specific coordination-metal interactions. Understanding which growth processes are broadly applicable to MOFs and which is specific to certain chemistries is critical for optimizing synthesis and scalability. However, most of them remain poorly understood due to the complexity of the interactions involved in MOF synthesis.

Gas uptake and separation are the main applications of MOFs that have been used so far, due to their porosity and tuneable structures [14]. But, their potential for 'dense material properties' such as proton conductivity is not well understood and exploited. Proton conductivity needs continuous, stable pathways within the framework, which is a challenging for MOF structures. Design principles for optimizing dense performance are still emerging, and MOFs are usually short of structural robustness and conductive networks, which are required for achieving high performance proton conductivity. Therefore, the realization of using MOFs for applications in dense materials will require more focused study of how the framework structure affects these complex properties. And more and more researches for scalable and green synthesis with be required for commercialisation of MOF technologies.

1.1 MOFs

MOFs are a class of highly porous materials with ultrahigh porosity, also known as porous coordination polymers (PCPs). MOFs can be traced back to B. F. Hoskins and Richard Robson with the diamond-related $[N(CH_3)_4][CuZn(CN)_4]$ cubic framework structures in 1990 [15]. After that, MOFs have become an expansive class of crystalline materials with enormous internal surface areas [16, 17]. MOF materials are usually composed of metal ions or secondary building units (SBUs), coordinated to organic ligands such as carboxylate or imidazolate ligands [18, 19]. The representation of MOF structure is depicted in Figure 1.1a, showing metal ions or SBUs connected with ligands to build repeating structure of MOFs, which forms one-, two- or three-dimensional structures [20, 21].

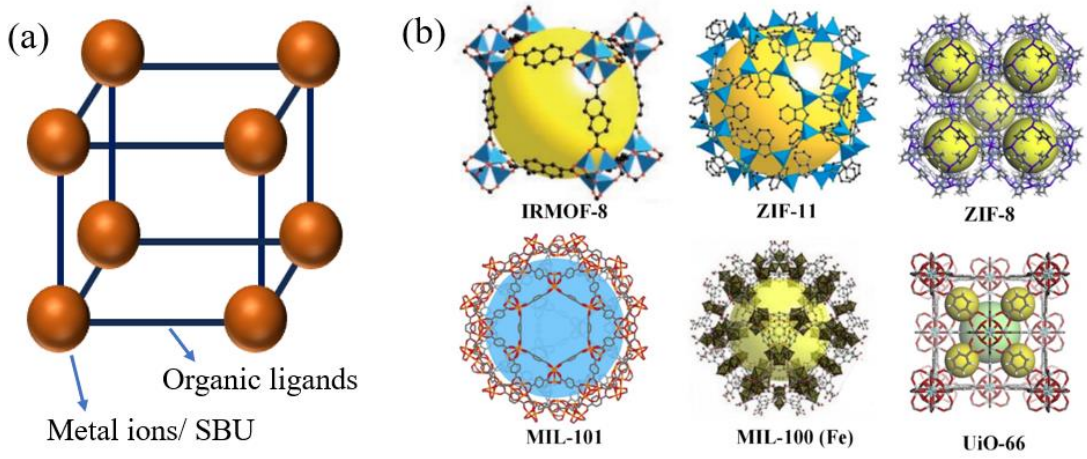

Figure 1.1 Components and structure representation of MOF and (b) structure of representative MOFs: IRMOF-8 [22], ZIF-11 [23], ZIF-8 [24], MIL-101 [25], MIL-100 (Fe) [26] and UiO-66 [27].

Isoreticular metal–organic frameworks (IRMOFs) [22], zeolitic imidazolate frameworks (ZIFs) [23], materials of institute Lavoisier (MIL) MOFs [28, 29], porous coordination network (PCN) [30], and Universitetet i Oslo (UiO) MOFs [31] are five major MOF classes, Figure 1.1b shows structures representative of these MOFs. IRMOFs are usually fabricated by the $[Zn_4O]^{+6}$ SBU and a series of carboxylic acid ligands, forming octahedral bridge connected microporous crystals [22]. ZIF MOFs are typically constructed from Zn^{2+} or Co^{2+} ions and imidazolate ligands [23]. MIL MOFs are composed by diverse transition metal ions and succinic acid, glutaric acid, carboxylic acid ligands synthesis. Among these, the structure of MIL-53 can be adjusted between large and narrow pores under external stimuli, a characteristic arising from its 'wine-rack' structure [29]. PCN MOF materials contain multiple cubic octahedral nanopores, producing materials with great potential in gas storage [32]. UiO MOF materials contain octahedra consisting of $[M_6O_4(OH)_4]$, commonly constructed with M = Zr, and terephthalate ligands, with a three-dimensional microporous structure [31]. The UiO MOFs have been particularly well known as stable MOFs in water and air [33].

1.1.1 Applications of MOFs

The highly porous structure, adjustable pore size and functionalizable surfaces make MOFs ideal candidates for practical applications from gas adsorption/separation, and catalysis to proton conduction [34-38]. Mitigation of greenhouse gases, the storage of clean energy gases, and the separation of industrially relevant gas mixtures are some of the main application areas that MOFs have been used in the last two decades [39].

Because of the high specific surface area and porosity, tuned pore size and functionalized crystal structures, such as UiO-66 [31] and HKUST-1 [40], MOFs are one of the most promising CO_2 absorption materials. MOFs have shown better CO_2 uptake compared to traditional adsorbents such as activated carbon because of their flexible design and higher porosity [39]. Many MOFs are highly efficient under moderate pressure and temperature conditions for practical applications, and some MOFs also exhibit reversible adsorption [41]. MOF-177 which prepared by Yaghi et al. has shown an excellent high surface area (4500 $m^2\ g^{-1}$) and remarkable CO_2 uptake of 33.5 mmol g^{-1} (at 35 bar and 25 ℃) [42]. Amine-functionalized MOFs, such as NH_2-MIL-101 and NH_2-UiO-66, have presented good CO_2 capture through chemical interactions between amine groups and CO_2 molecules [43]. MOFs have also been used in storing energy-related gases, such as H_2 and CH_4 [41], and toxic gases including CO and NH_3 [44]. Their high porosity and tuneable pore structures allow for high-density gas storage, making them suitable for clean energy applications and environmental protection [45].

In addition, the ability of MOFs to distinguish gas molecules through host-guest interactions and screening effects has made them very effective in gas separation [46]. Pure MOF membranes and MOF-based mixed matrix membranes (MMMs) have shown superior performance compared to conventional polymer membranes and zeolite membranes [47]. A thin ZIF-8 based membrane has been reported for H_2, CO_2 and N_2 separation, and the prepared membrane showed better performance than both glassy and rubbery polymer membranes [48]. Defect-free MOF-based MMMs were fabricated through dispersing UiO-66 particles evenly in polydimethylsiloxane (PDMS). The prepared MMMs were defect-free even with a high UiO-66 loading at 50 wt%, and this membrane presented an excellent CO_2/N_2 selectivity of 10 ± 1 [49].

MOFs have also achieved a lot attention as catalysts in diverse chemical reactions because of their porous and hybrid organic-inorganic framework structures. The metal ions or SBUs can be served as catalytic sites, and the organic linkers can be modified to tailor the chemical environment, leading to precise control over the reactivity, selectivity, and stability of the catalyst [50]. MOFs have been used in a range of catalytic reactions, such as CO_2 reduction, photocatalysis and organic transformations [51, 52]. A range of Ni-based MOFs such as $[Ni_3(OH)_2(1,4\text{-}BDC)_2\text{-}(H_2O)_4]\cdot 2H_2O$, BDC = 1,4-benzenedicarboxylate (Ni-BDC) with good photoreduction of diluted CO_2

have been reported, and these MOFs presented strong binding between CO_2 and open Ni sites [52]. Synthesized single-layer Ni-BDC MOF nanosheets have large sizes and are highly active in photocatalytic CO_2-to-CO conversion, with a high production rate of 104 mmol g^{-1} h^{-1} and a high Faraday selectivity of 96.8%.

MOF materials with acid groups, such as sulfonate groups and phosphonate groups, present good proton exchange performance, as the acid groups provide additional hopping sites for proton migration [53]. The modular structure of MOFs allows for fine-tuning of their properties, making them attractive candidates for efficient proton-conducting materials [54]. Using a -SO_3H modified ligand and carriers to tune the cavities in a group of proton conducting MOFs comprising MIL-101, S-MIL-101 and acids@MIL-101 have been found to be an efficient method to improve the interfacial compatibility of the hybrid membranes [53]. The highest conductivity value of the optimized sample was 9.4×10^{-2} S cm^{-1} at 100 ℃ and 100% relative humidity (RH) [53]. Imidazole (Him) units have been introduced into the channels of UiO-67, and the proton conductivity performance of prepared sample was quite stable in a broad working temperature range [55]. The Him@UiO-67 reached a maximum proton conductivity value of 1.52×10^{-3} S cm^{-1} at 130 ºC under anhydrous conditions. In general, proton conductivity in the range of 10^{-3} to 10^{-1} S cm^{-1} is considered as good performance for MOFs, while proton conductivities below 10^{-3} S cm^{-1} are typically considered poor performance [3]. Many MOFs can only reach conductivities around 10^{-6} to 10^{-4} S cm^{-1}, which limits their practical applications [56]. MOFs with conductivities approaching or higher than 10^{-2} S cm^{-1} are considered as promising candidates for proton conduction applications [3]. Nafion is a widely used material for PEMs, which achieves proton conductivities in the range of 10^{-2} to 10^{-1} S cm^{-1} under high relative humidity and temperatures [57].

Although, MOFs have presented great promise in these application fields, they do come with some limitations and shortcomings. Most MOFs, especially those porous MOFs, are not stable when exposed to moisture or acidic/basic environments after activation, because of their weak metal-ligand coordination bonds and the hydrolysis of the metal-ligand bonds [58]. Many MOFs have a narrow range of thermal resistance because of the decomposition of organic linkers, and the performance of some MOFs may degrade after repeated cycles of gas adsorption and desorption and catalytic reactions due to their structural collapse during cycles [59]. The synthesis of MOFs

usually requires expensive organic ligands and long reaction times under high temperature, leading to high costs. These shortcomings highlight the need for ongoing research to develop more robust and cost-effective MOFs and more promising synthesis methods for practical applications.

1.1.2 Sulfonate MOFs

Sulfonic acids comprise a class of water-soluble compounds, exhibiting strong Brønsted acidity [60]. This functional group is notable in the top-performing PEM material, Nafion, where the high density of sulfonic acid moieties and strongly ionic characteristics promote the transfer of protons in the material [61]. However, organic sulfonate groups, denoted RSO_3^- and comprising a sulphur atom terminated by three oxygens, have not seen wide use in MOF materials because of their relatively weak coordination with many transition metals [60]. MOF formation relies on metal-centre coordination for successful growth of a porous MOF crystal structure. Therefore, there are few reports on porous crystalline organic sulfonate-based MOFs.

Sulfonates can be used as coordinating groups on the organic linkers to form well-defined metal-sulfonate coordination motifs with soft metal centres (for instance, Cu^{2+}, Ag^{+}, Cd^{2+}, Ba^{2+}), because of the stronger coordination arising from soft-soft interactions with the sulfonate moiety [60]. The soft-soft interaction is described by the hard and soft acid and base theory. This theory proposes that soft acids react faster and form stronger bonds with soft bases, whereas hard acids react faster and form stronger bonds with hard bases [62, 63]. Hence, a coordinating sulfonate group is displaced by many solvents including water, which prefer hard-hard interactions due to their poorly polarisable orbitals [64]. Nevertheless, with appropriate combinations of metals and solvents, the multi-topic organic sulfonates are suitable linker candidates for MOFs [65]. Table 1.1 presents a variety of sulfonate linker molecules that have been reported to date.

Table 1.1 Structures of reported sulfonate ligands

Ligands	Ligand structures	Ref.
5-sulfoisophthalate	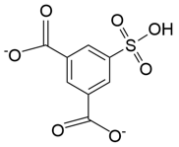	[66, 67]
2,6-naphthalenedisulfonate	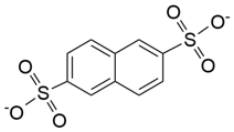	[68]
4,4'-disulfo-2,2'-bipyridine-N,N'-dioxide	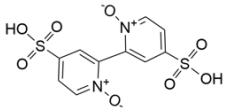	[69]
1,3,5-tris(sulfonmethyl)benzene	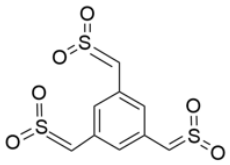	[70]
4,5-dihydroxybenzene-1,3-disulfonate	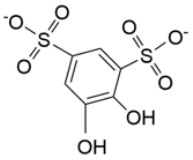	[71]
anthraquinone-2,6-disulfonate	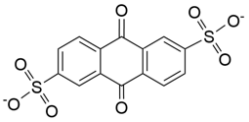	[72]
1,4-benzene-dimethanesulfonate	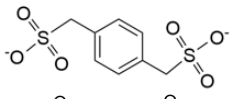	[73]
N,N'-disulfonatenaphthalenediimide	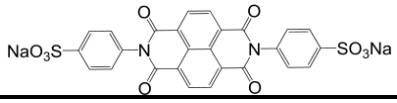	[74]

Researchers have also employed sulfonate groups in MOFs using different approaches to incorporate sulfonates within the MOF structure, such as post-synthetic sulfonation treatments [75] and synthesis with non-coordinating (to metal) sulfonate-containing ligands [76] as well as synthesis with sulfonate-metal coordination (sulfonate MOFs) [77]. Sulfonate MOFs can be divided into MOFs that have been modified with added groups [78] and those in which sulfonate groups are grafted into MOFs during the synthesis processes [79, 80]. As sulfonate MOF structures have the characteristics of strong designability and strong acidity of the sulfonate acid groups, they have been considered as promising materials for gas sorption [69, 70, 81] and proton conduction materials for membrane applications [82, 83]. Shimizu and co-workers synthesized a family of alkaline earth organic sulfonate coordination polymers

based on 4,5-dihydroxybenzene-1,3-disulfonate ligand [71]. Under catechol chelation, the softest Ba^{2+} forms a three-dimensional network of micropores in these samples, and the activated MOF can capture several polar gas guests (such as H_2S, H_2O). MOF materials functionalized with sulfonic-based acid groups have demonstrated outstanding proton conduction performance [53, 84]. Sulfonate MOF is promising for proton conductivity, but not well researched. In this research, a series of sulfonate MOFs have been fabricated by using different sulfonate ligands, metal ions and solvents, and how crystal structures affect proton conductivity has been explored as well.

1.2 Proton exchange membrane fuel cells (PEMFCs)

PEMFCs are a kind of fuel cell that transfers the chemical energy of hydrogen and oxygen into electrical energy through an electrochemical reaction. PEMFCs have merits of high efficiencies, low operating temperatures, environmental benefits and lightweight.

1.2.1 Overview of fuel cells

The global energy crisis has forced scientists to research clean energy sources to solve the dependence on non-renewable energy sources such as fossil fuels [37]. To solve this challenge, fuel cells (FCs) have emerged as promising candidates as a component in green energy systems [85]. FCs are a type of electromechanical equipment that convert low carbon fossil fuels or carbon-free fuels into electrical energy, and are of great importance, due to their broad scope for many fuels and industrial adaptability [86]. FCs usually consist of a pair of electrodes (anode and cathode) acting as the redox reaction sites, with an electrolyte and membrane between the two electrodes. Figure 1.2 is the structure representation of a hydrogen FC [87]. Different types of FCs have been developed, including alkaline FC, solid oxide FC, phosphoric acid FC and PEMFCs. PEMFCs in particular offer virtues of efficient energy conversion and almost zero emission [88]. In PEMFCs, the PEM offers channels for proton transport, with protons passing through the membrane from the anode to the cathode and the electron transfer occurring in an external circuit to provide current for electrical work. Higher proton conductivity of PEMs means reduced internal resistance and ohmic loss, which can help to achieve faster electrochemical reactions, allowing PEMFCs to obtain higher current density and power output. FCs

are typically operated at higher temperatures (> 100 °C) and humidity to maximize the conductivity of protons, for enhancing the balance between proton transport and water management to further improve the performance of PEMFCs [85, 89]. Hence, PEMs affect the overall performance of PEMFCs.

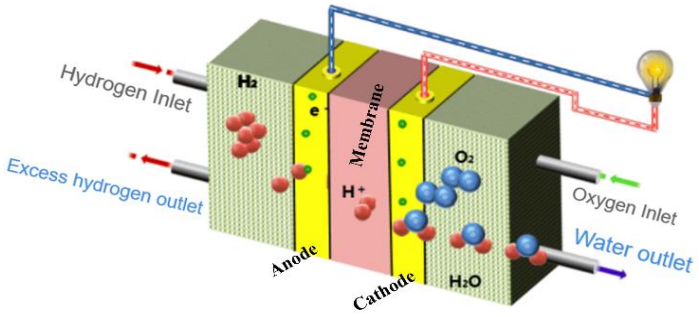

Figure 1.2 Hydrogen FC structure diagram [87].

1.2.2 Membranes for PEMFCs

Currently, the most commonly used PEMs consist of Nafion membranes because of their good proton conductivity and chemical stability [90]. However, Nafion membranes suffer from several disadvantages [91]: (1) tetrafluoroethylene and perfluoro-3,6-dioxa-4-methyl-7-octenesulfonyl fluoride are the main chemical precursors for Nafion synthesis, resulting in hazards and costly film fabrication; (2) requirements on temperature and H_2O content imposed by Nafion's stability window restrict the operating parameters of the FC overall; (3) the poor crystallinity structural characteristics of such membranes make it challenging to deeply analyze and study the proton conduction mechanism.

In Nafion membranes, when the temperature rises above 80 ℃, water in it will evaporate quickly [92]. The evaporation rate in turn will exceed its generation rate, resulting in the decrease of the water stored in this membrane [92]. In contrast, the optimal working conditions of catalyst components is above 100 ℃ [93]. Water plays an important role in proton transport across the membrane, so poor water management in PEMs will reduce the effective transmission efficiency of protons, thus affecting working performance [94]. Therefore, there is interest in developing either membranes with improved operation at higher temperatures, membranes with similar performance characteristics with more easily manufactured polymers, or a combination of improved performance at higher temperatures with simpler materials. In the past decade, a significant body of research aimed at developing MOFs [38, 90] and covalent organic

frameworks (COFs) [95, 96] as components for improved PEMs has arisen, leveraging the chemical tunability of these structures to substitute for or augment polymer-only membranes.

1.2.3 Sulfonate MOFs for PEMFCs

Sulfonate MOFs materials have presented good potential for the application in PEMFCs because they have tuneable structural properties, and sulfonate groups in the structure can offer additional hopping sites for proton transportation [53]. Furthermore, the acid groups can link the base groups in MOFs to generate acid–base pairs, which can increase proton migration [53]. Sulfonate BUT-8(Cr) MOFs made by a solvothermal reaction of $H_2NDC(SO_3H)_2$ and $Cr(NO_3)_3 \cdot 9H_2O$ have presented a high proton conductivity of 4.50×10^{-2} S cm^{-1} at 100% RH and 80 °C [97]. Moi et al. incorporated both amine and sulfonate groups in a Cu based MOF (Cu-SAT) as proton conductors [82]. The synthesized Cu-SAT presented a good proton conductivity of 0.53×10^{-3} S cm^{-1} at 80 °C and 98% RH. Because poly(vinylidene fluoride) (PVDF) presents good mechanical strength and good chemical stability [98, 99], meanwhile poly(vinylpyrrolidone) (PVP) provides hydrophilic properties to compensate for the native hydrophobicity of PVDF for PEM applications [100]. Cu-SAT particles were blended with PVDF and PVP as PEMFCs using different mass loading of Cu-SAT, and these PEMFCs displayed a proton conductivity as high as 0.80×10^{-3} S cm^{-1} at 80 °C and 98% RH. Although sulfonate MOFs have been shown as good candidates for proton conductivity, their proton conductivities are still much lower than Nafion (between 10^{-2} to 10^{-1} S cm^{-1}) [101]. And the thermal and humidity stability of sulfonate MOFs still need to be improved before their practical application.

1.2.4 Other MOFs for proton conduction

Besides sulfonate MOFs, other MOF materials with porous structures can achieve high proton conductivity [38]. UiO MOF [102] and MIL MOF [38] families are typical MOF materials explored for proton conductivity, because of their high porosity and strong designability features. UiO-66 with a 3D porous structure is composed of $[Zr_6O_4(OH)_4]$ clusters with 1,4-benzenedicarboxylic acid (p-H_2BDC) ligands, the strong Zr-O bond enhances the stability of the structure [103, 104]. A series of UiO-66-based MOFs, including UiO-66-SO_3H, UiO-66-$(COOH)_2$, UiO-66-NH_2, UiO-66-Br and UiO-66-NH_2, have been assessed for proton conductivity [102]. By modifying

the p-H_2BDC ligand in UiO-66 and comparing the proton conductivity of these different UiO-66 MOF materials, the value of proton conductivities of the -SO_3H and -COOH modified MOFs were found to be significantly greater than that of MOFs modified by -NH_2 and –Br, as well as original UiO-66 MOF. UiO-67 MOF a with similar crystal structure to UiO-66 has also been assessed for proton conductivity [55], using biphenyl-4,4-dicarboxylic acid (H_2bpdc) to replace p-H_2BDC in UiO-66 A hydrolytically stable titanium carboxylate-based MIP-177-SO_4H-LT MOF has been reported as achieving an outstanding proton conductivity of 26 mS cm^{-1} at 25 °C and 95% RH, and this performance can be maintained for over one week [84]. The proton conductivities of a variety of MOFs are listed in Table 1.2. However, how the crystal structure affects proton conductivity is not very clear. In this work, a series of sulfonate MOFs will be synthesized, and the effect of crystal structure on their proton conductivity will be explored.

Table 1.2 Proton conductivity of different MOFs

Compounds	Conductivity (S cm^{-1})	Analysis conditions (°C/RH%)	Ref.
BUT-8(Cr)	4.5×10^{-2}	80/90	[97]
MIP-177-SO_4H-LT	2.6×10^{-2}	25/95	[84]
H_2SO_4@MIL-101	6.09×10^{-1}	70/90	[105]
Cr-MIL-88B	4.5×10^{-2}	100/85	[78]
TEPA@ZIF-8-H_2CO_3	2.08×10^{-3}	20/99	[106]
MIL-101–SO_3H	9.4×10^{-2}	100/100	[53]
MIL-101(Cr)-$NH(CH_2)_3SO_3H$	4.8×10^{-3}	90/95	[38]
MIL-68-In-OH	1.72×10^{-3}	100/98	[107]
UiO-66-SO_3H	0.34×10^{-2}	30/97	[102]
Him@UiO-67	1.52×10^{-3}	130/50	[55]
JUK-13- SO_3H-SO_2	0.23×10^{-3}	75/60	[108]
$[Cd(H_2BBT)_2]_n$	0.18×10^{-3}	100/98	[109]
$[Ba(o\text{-}CPH_2IDC)]_n$	0.31×10^{-3}	100/98	[110]
Cu-SAT	0.53×10^{-3}	80/98	[82]
Tb-MOF	0.54×10^{-3}	100/98	[111]
$[Ni(p\text{-}IPhH_2IDC)_2]\cdot H_2O$	0.04×10^{-5}	100/98	[56]

1.2.5 Mechanism of proton conduction

The Grotthuss and vehicle mechanism have been reported as the primary mechanisms of proton conduction [112, 113]. The Grotthuss (also known as the hopping) mechanism usually transfers the charged proton from one location to another by the rotational motion of their respective bonds in hydrogen-bonded networks (usually with water), with the position of the site itself remaining unchanged [114]. Meanwhile for the vehicle mechanism, the free proton interacts to form a larger charged species, which itself migrates as a diffusing protonated group (e.g., H_3O^+) [115]. Grotthuss mechanism is usually characterized by a proton conductivity activation energy (E_a) less than 0.4 eV, whereas the vehicular mechanism has $E_a > 0.4$ eV [116]. Between two water molecules, a proton can migrate via the species $[H_2O\text{- - -H- - -}OH_2]^+$, but this can also occur between two different groups acting as an acid and a base, such as a sulfonate group and an amine: $[SO_2O\text{- - -H- - -}NH_2]$ [82]. There are several other suggested mechanisms for proton conduction, such as the packed-acid mechanism [117] and proton transfer and rotational motion mechanism [118]. The choice of proton conduction mechanism has consequences on the chemistry and structures of proton-conducting materials [119]. Materials relying on the Grotthuss mechanism usually present obvious structural rearrangements to boost proton transfer, this results in dynamic changes in the hydrogen bonding network, leading to the material's stability and performance [120]. The structure of materials has a significant effect on their proton conduction, for example, MOFs and COFs with aligned mesoporous channels can increase proton hopping and proton conductivity [121, 122].

1.2.6 Polymers used for MOF based PEMs

MOFs still face a number of challenges in terms of processing for future applications in FCs and other devices because of their brittleness and poor mechanical strength [123]. Embedding MOFs with polymer membranes represents an alternative method to overcome this challenge [17, 53, 82]. PVDF, sulfonated poly(ether ether ketone) (SPEEK), sulfonated poly(arylene ether ketone) (SPAEK) are broadly used in industrial membrane applications, because of their good mechanical strength and high thermal and chemical stabilities [98, 99]. A MOF based composite PEM can reach a proton conductivity of 1.84×10^{-3} S cm^{-1} (55 °C, 98% RH) in a PVP and PVDF composite by adding up to 60 wt% of MOF-801 [124]. PVP was used to compensate

for the native hydrophobicity of PVDF. This MOF mixed PEM conducted protons better than the pristine PVP/PVDF membrane which presented much lower proton conductivity (4.46×10^{-3} mS cm^{-1}) at 25 °C. Nafion has also been used to prepare MMMs, a composite PEM made by mixing a Zr-MOF with Nafion present much good proton conductivities for FCs [61]. The sulfonate sites in the MOF network retain an ample amount of water, which can enhance proton conduction at low humidity. These results indicate that the proton conductivity was increased by 23% for a Nafion/Zr-MOF composite PEM in comparison with a pure Nafion membrane. In addition, the hybrid membrane also presented better properties at 35% RH.

Table 1.3 Proton conductivity of MOF based PEMs

Compounds	Conductivity (S cm^{-1})	Analysis conditions (°C /RH %)	Ref.
PVA@PA@Zn-MOF-4	1.85×10^{-2}	80/90	[125]
UiO-66-NH-SO_3H@SPEEK	2.7×10^{-1}	80/100	[126]
sul-MIL-7.5@SPEEK	3.6×10^{-1}	75/100	[79]
UiO-66-NH_2 MOF@Nafion	7.7×10^{-2}	90/95	[127]
Zn-MOF-NH_3@Nafion	2.13×10^{-2}	58/80	[128]
MIL-101-Cr-NH_2@Nafion	2.45×10^{-1}	98/100	[129]
MOF808@PVDF-25	7.58×10^{-3}	42/99	[130]
ZIF-8@PBI	3.1×10^{-3}	200/75	[131]
ZIF-8@DNA	1.7×10^{-1}	75/97	[132]
MOF-801@PP-60	1.84×10^{-3}	52/98	[133]
Cu-MOF@PVP/PVDF	0.45×10^{-3}	80/98	[134]
Cu-SAT@PVDF/PVP	0.8×10^{-3}	80/98	[82]
Fe-MOF@PVDF/PVP	1.77×10^{-3}	80/98	[135]
Cu-BTC MOF@NENU	1.4×10^{-5}	24/97	[136]
Nafion (as benchmark)	10^{-2}-10^{-1}	Over 50/95	[101]

Information on the proton conductivity of a range of MOF based composite membranes is listed in Table 1.3, proton conductivity of Nafion was included as a benchmark. Usually, MOFs in polymers can enhance the proton conductivity of PEMs

because of the high intrinsic proton conductivity of the dispersed MOF materials. However, in some cases, MOFs only improve conductivity by modifying the structure of the polymer rather than actively participating in proton conduction. The PEMs made by mixing UiO-66 or the analogous sulfonated SO_3H-UiO-66 with Nafion showed greater proton conductivity than pristine Nafion, even with the addition of the fairly poorly-conducting UiO-66 at 2 wt% [137]. This was due to the reduction in the tortuosity of the proton pathways in the PEM.

There are many trial-and-error reports that show some effects of MOF based polymer membranes for proton conduction, but there are far fewer comparisons reported between different systems or evaluations of the particular features that make the systems work best. This project has advanced in this area by controlling the structure of the synthesized MOF crystals to disentangle structure effects in PEMs.

1.2.7 Conductivity testing of PEMs

Conductivity testing of PEMs is crucial to evaluate their performance, especially in FCs and electrochemical systems. These tests help to understand how the efficiency of proton transport through membranes affects the power and energy density of FCs. Conductivity tests are usually conducted under different temperatures and relative humidities to provide results on the efficiency and durability of PEMs, and these results can be used to optimise their performance. The proton conductivity is measured in Siemens per centimeter (σ, S cm^{-1}), which is usually calculated by the following equation:

$$\sigma = \frac{l}{AR}$$

where l presents the membrane thickness (cm), A presents membrane area (cm^{-2}), R refers to the resistance of membrane (Ω). R is usually detected by electrochemical impedance spectroscopy (EIS), and the intercept at the x axis corresponding to the real part of the complex impedance (Z') is taken as the resistance [89]. EIS is one of the most common methods used to study the electrochemical systems, and EIS can analysis the impedance of a system over a wide range of frequencies to provide insights into processes of charge transfer, diffusion and capacitance at interfaces in fields such as battery, fuel cells, and corrosion science [138]. EIS applies a small alternating current (AC) with different frequencies (typically from millihertz to megahertz) to the

electrochemical system and measures the ratio of the AC potential to the current signal [139]. EIS data are usually interpreted using equivalent circuit models, e.g. a Randles circuit [139]. The Randles circuit is typically composed of a solution resistance (Rs), a double-layer capacitance (Cdl), a charge transfer resistance (Rct), and a Warburg impedance (Zw). The Rs refers to the resistance of the electrolyte solution between the working and reference electrodes, the Cdl arises from the capacitor-like behaviour formed between the interface of electrode and the electrolyte. The Rct is the resistance of the electrode surface to electron transfer during the electrochemical reaction, and the Wz describes the diffusion of ions in the electrolyte. Nyquist plots are usually used to visualize EIS data, and this plot has a semi-circular arc in a lot of electrochemical systems. The intercept of the compressed arc on the real axis presents to the equivalent series Rs, while the diameter of the arc represents the Rct, and the straight line in the low frequency region is the Warburg impedance [140].

The activation energy (E_a) is the energy required for protons migrating through PEMs, and it is the key result for determining the mechanism of proton conduction. E_a for PEMS is usually calculated by the following Arrhenius equation [141]:

$$\mathrm{In}(\mathrm{T}\sigma) = \mathrm{In}(\sigma_0) - (\frac{E_a}{\mathrm{R}})(\frac{1000}{\mathrm{T}})$$

where T presents testing temperature (K), σ refers to the proton conductivity (S cm^{-1}), σ_0 equals to the pre-exponential factor (S (K cm) $^{-1}$), and R presents the ideal gas constant (8.314 J $(mol\ K)^{-1}$). E_a is calculated from the slope of this Arrhenius plot.

Water uptake is also considered during conductivity measurement on PEMs because proton conduction significantly relies on water content with higher hydration generally leading to better conductivity.

1.3 Synthesis of MOFs

MOFs can be synthesized through different methods, such as hydrothermal [9, 142, 143], solvothermal [144-146], ultrasound-assisted [147, 148], microwave-assisted [149-151], and mechanochemical synthesis [152, 153]. These methods have been used to produce MOFs with specific structures, properties, and applications.

1.3.1 Nucleation process in MOF synthesis

In the MOF synthesis processes, nucleation is the moment when metal ions and

organic ligands begin to arrange into a high-level cluster structure to form the initial crystal nucleus. The generated nuclei can be produced spontaneously or induced by external conditions, for instance, temperature, pressure, and reactant concentration [154]. The nucleation in MOF synthesis is also affected by supersaturation, solvent effects and modulators. The synthesis of MOFs involves complicated nucleation and growth processes, which can be roughly divided into homogeneous and heterogeneous nucleation [155]. The balance between these nucleation phases is critical for tunning the final size, morphology and defect density of MOF crystals.

Homogeneous nucleation happens uniformly throughout the solution without any preferential nucleation sites, and it usually has a higher energy barrier as it needs the system to overcome the surface energy associated with the creation of new crystal interfaces in solution [156]. Rapid homogeneous nucleation usually leads to produce smaller and uniformly sized particles, which is used for synthesizing nanoscale MOFs or highly uniform crystals [157]. Heterogeneous nucleation happens at specific locations e.g. pre-existing surfaces or interfaces of MOFs, because the surface provides nucleation sites that reduce the energy needed to form a new crystal [155]. By carefully choosing the surface or substrate, researchers can control the size, shape, and orientation of MOFs [158]. Heterogeneous nucleation can inhibit the quick precipitation of amorphous structures and promote the crystallization of highly crystalline frameworks [159]. Small molecule-assisted nucleation can be used to synthesize heterostructures, and a heterogeneous nucleation-growth strategy has been used for the fabrication of Au@UiO-66(NH_2) using PVP modified Au (PVP–Au) nanoparticles as molecular assistant [160]. Slow nucleation usually leads to fewer and larger crystals, whereas fast nucleation can result in the generation of many small crystals. In this research, we have explored how reaction methods and conditions affect the crystal size and morphology of sulfonate MOFs.

Models of crystallisation in MOFs are usually evaluated using a combination of qualitative and quantitative methods, often including direct observations and comparisons with theoretical predictions [155]. The crystallization process of MOFs can be qualitatively observed by light microscopy or scanning electron microscopy (SEM), which can provide information on crystal size and shape as well as growth habits. Spectroscopic methods, for instances Fourier-transform infrared spectroscopy (FTIR), can provide qualitative information about the MOF crystallization through

tracking the changes of ions and ligands in the coordination environment. Powder or single crystal X-ray diffraction (XRD) can assess the crystallinity and phase purity of MOF samples, confirming whether the crystallization process is proceeding as expected. Crystallization models can predict MOF nucleation and growth rates, which can be quantitatively assessed using in situ XRD. The quality, crystallinity and purity of the final MOF products can be quantified by gravimetric analysis or thermal methods i.e. thermogravimetric analysis (TGA). These metrics can be used to compare with model predictions to assess crystallization efficiency. Other quantitative data, such as gas adsorption studies can be compared with predictions from crystallization models. Some classical nucleation theory and growth models, such as Ostwald ripening [161], predict crystallization kinetics, particle size distributions, and crystal morphologies, which can be used to quantitatively compare with experimental results in MOF crystallization.

1.3.2 Standard methods for MOF synthesis

The hydrothermal and solvothermal methods are typical methods for producing MOF crystals [9, 145]. The principles of these two methods are similar, in both cases organic linkers and metal salts are dissolved in a solvent or solvent system and transferred into a reaction vessel which is then heated at a selected temperature (normal reaction temperatures are between 50-250 ℃) for a certain time to achieve high quality crystals [149]. The typical hydrothermal or solvothermal methods usually need several hours to days to complete MOF synthesis in lab-scale setups, and STYs are low, often in the range of 0.1-10 kg m^{-3} day^{-1} [31, 162]. Microwave-assisted synthesis, mechanochemistry, and rapid precipitation have been developed to shorten reaction times to minutes or hours (usually 10-60 minutes), with STYs improving to 10–1000 kg m^{-3} day^{-1} [163]. In recent years, techniques, such as continuous flow synthesis and ultrasonication, have brought MOF reaction times down to the range of seconds to minutes and pushed STYs above 1000 kg m^{-3} day^{-1} [164].

Difference between hydrothermal and solvothermal methods lies in the solvents employed. Aqueous solvents are used in the hydrothermal method, i.e. water [165]. While the solvents used in the solvothermal method are organic solvents, such as DMF and acetonitrile [9]. These solvents can be used alone or mixed and used in different volume ratios. The advantages of the hydrothermal/solvothermal route are that the

chemical reactions can be accelerated, in terms of their hydrolysis rate, by using higher temperature and pressure conditions, thereby achieving rapid reactions. However, these methods also have some disadvantages, for instance, the relatively long reaction times for achieving high quality crystals, the high energy consumption, and also the harsh reaction environment. ZIF MOFs were firstly created by Yaghi and coworkers by using hydrothermal methods (140 ℃ for 24 h) [23]. Twelve ZIFs were fabricated by combining either Zn^{2+} and Co^{2+} with imidazolate-type linkers. Two ZIFs presented good thermal stability (higher than 550 °C). A simple hydrothermal method to synthesise ZIF-8 MOFs has then been reported [9]. Different amounts of triethylamine (TEA), and Zinc nitrate, Hmim and water with molar ratio of 1: 4: 1240 were used as raw materials. The obtained single-phase ZIF-8 presented a surface area of 1340 m^{-2} g, and this material showed high capacity for I_2 uptake. The reported surface area of ZIF MOFs ranges from hundreds to a current record of 7800 m^{-2} g [166].

Compared with the first reported syntheses of ZIF [23], MIL-100 [28] and UiO type MOFs [142], researchers have obtained these MOFs in optimized hydrothermal methods with lower synthesis temperature and time. But hydrothermal/solvothermal methods still have the disadvantages of long reaction times and high reaction temperatures. Hence, ultrasound, microwave, vapor phase diffusion assistant hydrothermal/solvothermal syntheses have been developed with the target of addressing these problems. Control of MOF properties, such as particle size, particle size dispersity, and their dependence on synthesis conditions, remains underexplored in hydrothermal/solvothermal synthesis, presenting a gap in the literature that this project has sought to address.

1.3.3 Sono-chemical synthesis of MOFs

Using ultrasound waves to accelerate the reaction between metal salts and organic linkers has been proven to be superior of simplicity and increased energy efficiency compared to hydrothermal and solvothermal methods of MOF synthesis [167]. Sonochemistry has been applied in the production of MOFs, catalysts, and nanoparticles. Sono-chemical synthesis can improve reaction kinetics and chemical production yields through acoustic cavitation [168]. The cavitation phenomenon of the ultrasound generates microbubbles and disperses them throughout the liquid solution, the rapid formation and collapse of microbubbles in the solvent essentially creates tiny,

intense “hot spots” or “pressure points” in the liquid, boosting molecular activity in these zones, which in turn creates conditions favorable for faster nucleation [148]. Sono-chemical synthesis has been considered a more environmentally friendly method because of its low energy consumption and short reaction times [169].

During the preparation of MOFs, ultrasound disperses the energy evenly in the liquid reaction medium, increasing the crystallization rate and surface areas of MOFs compared to conventional solvothermal or microwave methods [170, 171]. MOFs synthesized by sonochemistry tend to have more defect sites and more uniform particles. For example, MOF-545 has been reported to has a significantly smaller (1.0 μm) particle size in the ultrasound-assisted synthesis than the conventionally prepared sample (4.8 μm) [172]. This method was successfully employed to fabricate various MOFs, demonstrating its broad applicability. The synthesis times and the properties of Ni-MOFs between solvothermal synthesis and ultrasound synthesis methods have been compared by Sargiazi et al. [173]. They used pyridine-2,5-dicarboxilic acid and Ni $(NO_3)_2{\cdot}6H_2O$ as precursors, and solvothermal synthesis needed 7 h at 80 °C, while the ultrasound synthesis reaction only needed 38 min at 45 °C. The Ni-MOF fabricated by the ultrasound method presented higher specific surface area and crystallinity as compared with Ni-MOFs synthesized by traditional methods [173-175]. Different methods have been employed to fabricate Cu–BTC nanoparticles for investigating their uptake and release properties with respect to rifampicin which is an antibiotic [147]. Sono-chemical synthesis needed 1 h to produce a MOF sample with an average particle size of 80 nm, while solvothermal synthesis needed 24 h at 80 °C achieving a particle size of 140 nm. The sono-chemically prepared MOF sample, with a smaller particle size, exhibited better uptake and release performance.

Ultrasound can also be used to affect the polymorphism of MOFs. Polymorphism in MOFs is the ability of a single chemical composition to generate in more than one distinct crystal structure. These different polymorphic forms differ in their properties e.g. porosity, stability and adsorption behavior [176]. As ultrasound promotes the faster nucleation, MOFs synthesized using ultrasound may adopt polymorphic forms that are not the most thermodynamically stable [167] or forms that do not occur under standard synthesis conditions.

Ultrasound promotes smaller, more uniform MOF crystals, which in turn can

cause polymorphism, as smaller crystals may have different packing arrangements and have different preferred crystal growth orientations than larger crystals caused by size-dependent effects and surface-dominated phenomena [177]. Ultrasound can also change the surface characteristics of MOF crystals, potentially stabilizing certain polymorphs by changing how metal ions and organic linkers assemble on the crystal surface. However, obtaining consistent results is challenging. Small changes in ultrasound intensity, frequency, or reaction settings can result in different results, making reproducibility extremely difficult [178].

1.3.4 Green chemical synthesis of MOFs

Conventional chemical processes pose a number of environmental and health hazards. In order to reduce these hazards and achieve more environmentally friendly results, the search for alternative chemical processes and solvents and chemicals has always been an area of interest [179]. Green chemistry strives to work at the molecular level in order to realize sustainable development [180]. Green chemistry is an important area of innovation to advance the future of the chemical industry.

MOFs have shown great potential in diverse applications, but traditional synthesis methods often rely on harmful solvents and high energy consumption [9, 145]. In response, more and more researchers have focused on clean chemical synthesis of MOFs by elimination or reduction of hazardous solvents, such as DMF and acid regulators [181, 182]. These solvents are used because of their high boiling points as well as beneficial acid-base chemistry. The industrial-scale synthesis of MOFs can produce a large amount of DMF waste, which exhibits regeneration toxicity [8, 183]. Future legislation under EU Registration, Evaluation and Authorization of Chemicals [8] may limit several traditional dipolar aprotic solvents, including DMF, and N-methylpyrrolidone (NMP), which are currently listed as ‘substances of very high concern’ [184].

Water-based solvents [185], dimethyl sulfoxide (DMSO) [186], as well as super-critical liquids and ionic liquids [187] have been reported as green solvents for MOF synthesis. Water-based solvents for MOF fabrication have attracted widespread attention, because they avoid or minimize the use of organic solvents. Compared with organic solvents, water has merits of being stable, cheap, and clean [185]. Recently, some attempts of using water as a solvent for ZIF MOFs fabrication have been reported.

The water synthesized ZIF-93 achieved a yield of 80%, and had the same properties as the one obtained using DMF [188]. Particle size and crystallinity of ZIF-8 MOFs have been researched using water as a solvent, and results indicated that $Zn(OAc)_2$ was the best precursor. The resultant ZIF-8 particles have presented rhombic dodecahedron morphology [189]. Ionic liquids are new organic solvents, which have the characteristics of negligible vapor pressure, low melting point and high solubility [187]. Because of their adjustable nature and large number of applications, ionic liquids can also be used as designer solvents [187]. Aprotic ionic liquids have been reported as solvents to produce Zr-based MOFs with increased nucleation process [190].

1.4 Microreactors and continuous synthesis

Microreactors and continuous synthesis are advanced methods in chemical processing and manufacturing with an emphasis on efficiency and precision of reactions. Microreactors are small reactors designed to carry out chemical reactions within micron-sized channels. Microreactors are usually operated in a continuous mode because of their ability to precisely control chemical solutions, this combination has advantages of highly efficiency, safety, and scalability of chemical production.

1.4.1 Introduction of microreactors

Microreactors are miniaturized devices used to carry out chemical reactions in the field of continuous synthesis with highly controlled environment [191]. It combines knowledge and techniques at the intersection of physics, chemistry and fluid mechanics [192]. Microreactors consist of channels or chambers on the microscale, usually ranging from a few micrometers to millimeters in size for continuous synthesis. Continuous synthesis including microfluidic and millifluidic technologies have attracted lots of attention due to their potential in diverse applications, e.g. drug delivery [193] and nanomaterials fabrication [194-196]. Microfluidic and millifluidic technologies are systems that process small volumes of fluids or have small structural sizes [194]. Compared with microreactor synthesis, the traditional batch methods have low mass and heat transfer efficiency [194]. Over the last decade, microfluidic and millifluidic technologies have been widely used in the extraction of rare metals [197, 198], MOF production [199, 200], biopharmaceutical engineering [16, 201], and the preparation of nanoparticles as well as in other fields [201, 202]. In academia, microfluidic and millifluidic synthesis is mainly employed to explore fundamental

questions, miniaturize experiments and develop new methods for chemistry, biology, materials science and engineering. In an industrial environment, microfluidic and millifluidic methods can serve as a basis for adapting larger reactors or for parallel scaling up of small reactors for large-scale production, and these methods have the merits of high production efficiency and reduced cost.

Numerous methods have been reported for the synthesis of MOFs in the last few years. However, standard synthesis methods, with their drawbacks of long reaction times [203] and high temperatures [9], still restrict practical application of MOFs on an industrial scale. Continuous synthesis of MOFs by using microfluidic methods has become popular in the research community, because it allows for the continuous production of MOFs in a short time and a lower temperature compared with traditional methods [200]. Microfluidic synthesis achieved the greatest reduction in reaction time to synthesize HKUST-1 and ZIF-8 MOFs in comparison with sono-chemical, hydrothermal, solvothermal, and microwave methods (Figure 1.3) [144, 149, 164, 167, 199, 204-207]. Compared with hydrothermal and solvothermal synthesis methods, microfluidic synthesis can reduce reaction times by more than 500 times, showing its promise for producing MOFs on a large scale. Although, microreactors are promising for the fabrication of MOFs, they also have some limitations. Continuous synthesis methods need precise control of flow, temperature, and concentration, making experimental operations more difficult than traditional batch synthesis. Furthermore, the small volumes in microreactors can lead to clogging, especially when synthesizing MOFs with high crystallization rates and/or large particle sizes.

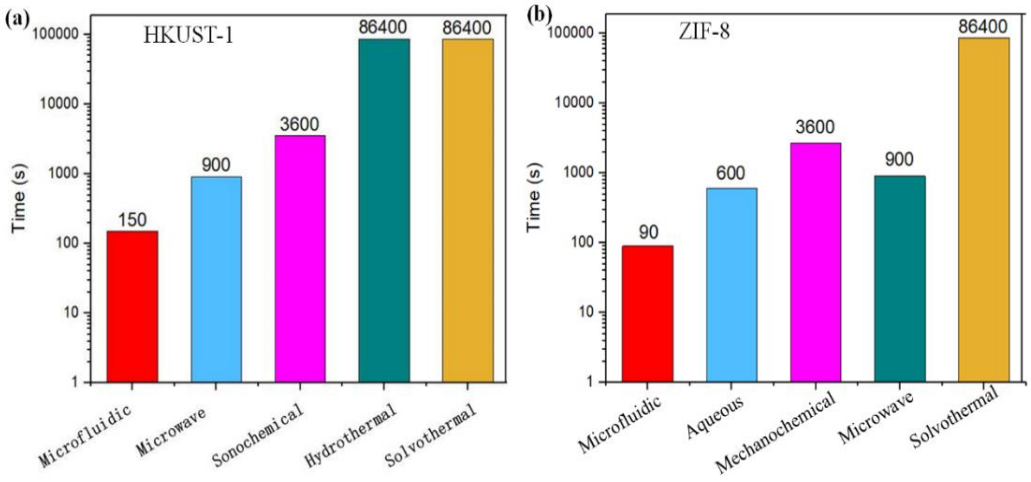

Figure 1.3 Comparison of synthesis times of different methods for preparing HKUST-1 MOFs [144, 149, 167, 199, 204] and ZIF-8 MOFs [164, 205-207].

1.4.2 Advantages of microreactors

Slow mass transfer remains one of the challenges faced by traditional synthesis reactions. Microreactors allow for faster reactions because rapid mixing and diffusion can be achieved in microreactors, due to the reduced characteristic length scale [208]. Micromixers can also be designed to further increase mixing chemicals [209]. For reactions with limited mass transfer in traditional systems, improved mass transfer can increase the reaction rate and process enhancement [210]. Microreactors benefit from high surface area to volume (SAV) ratios, the SAV of a microreactor is normally between 10,000 to 50,000 m^{-1}, much higher compared with traditional reactors (100-1000 m^{-1}) [208]. Higher SAV ratios can enhance the surface available for heat transfer to occur and contribute to higher heat transfer in microreactors. The higher mass and heat transfer in a flow reactor compared with a batch reactor allows for faster reactions so achieving better reaction yield and STY [211, 212].

Eliminating the heat transfer limitation in the reactor is also beneficial to the safe operation and isothermal operation of the highly exothermic reaction [213]. If enough heat is not discharged from the reaction system, temperature enhancement in the reactor may cause an uncontrolled reaction [214]. Microreactors also benefit from continuous operation, which can reduce the time required to conduct extra experiments. A continuous synthesis system does not need to be stopped and cleaned after each experiment, and continuous operation can change the parameters, monitor the system until it reaches a stable state, and collect samples in the shortest possible time [213]. Furthermore, there is less ambiguity in the process of scaling up to industrial scale, and continuous synthesis is compatible for scale-up using established principles [215].

1.4.3 Mechanisms of continuous synthesis

Microfluidic systems include single-phase flow, multiphase flow and integrated microfluidic systems. Single-phase flow systems can process both single or multiple miscible reagents in a laminar flow stream, making them simpler to analyse compared to multiphase flow systems [216]. The flow speeds are different at the channel wall relative to the flow speed of the fluid in the centre of the channel, which can cause channel wall fouling problem [217]. Multiphase flow microfluidic systems present a solution to the fouling problem. The design principle of this system is to avoid the direct contact between the reagents and tubing [216]. Multiphase flow microfluidic

systems include gas-liquid [197] and liquid-liquid systems [218]. In these approaches, liquid reagents are segmented by a regular stream of gas bubbles or a second liquid phase, for example, silicone oil [219] and heptane [220]. The properties of each phase, such as density, wettability and viscosity, significantly influence the flow pattern. In the droplet flow system, the ratio of the carrier phase to precursor solution is usually equal or higher than 1 to avoid an unstable droplet pattern [221, 222]. Flow rates can also affect multiphase flow synthesis. A stable droplet/slug pattern is more achievable at a slower flow rate rather than at a high flow rate [223]. Accurately controlling the gas bubbles in the gas-liquid system and difficulties in maintaining a controlled and consistent separation between synthesized samples and a second phase liquid are the main disadvantages of multiphase flow microfluidic systems [224].

1.4.4 Design principles of microreactors

Microreactors are usually made of polymer tubes, such as polytetrafluoroethylene (PTFE) or polyfluoroalkoxy alkane (PFA) [214]. Space time, volumetric flow rate, residence time, and residence time distribution (RTD) are key parameters in the continuous synthesis. Space time is a critical parameter used to describe the time required to process one reactor volume of fluid. This is the time it takes for the amount of liquid occupying the entire reactor volume to completely enter or completely leave the reactor. Residence time is an average time a particle or fluid element spends inside the reactor. In ideal reactors, the residence time often equals the space time. In most reactors, space time is not equivalent to residence time as non-ideal flow patterns such as dead zones and reverse mixing can cause flow elements to spend varying amounts of time in the reactor [225]. Deviations from ideal plug flow or perfect mixing can cause a distribution of residence times rather than a single uniform value [226]. The space time (τ) is the ratio of the reactor volume (V) to the flow rate (Q) [227], the formula is showing below:

$$\tau = \frac{\mathrm{V}}{Q}$$

Flow rate (Q) is the volume of fluid that passes through a given point in the reactor per unit of time, which is a key parameter in flow reactors and is usually measured in units such as milliliter per minute (mL/min). Volumetric flow rate is usually calculated by the production capacity based on the design of reactors, if the reactor operates under

continuous flow, the volumetric flow rate is determined by the following equation [228]:

$$Q = \left(\frac{1}{4}\right)\pi d^2 L \Big/ t$$

where t is the residence time, d and L represent the inner diameter and length of reactor tubing, respectively. The total volume of the reactor tubing is given by $(1/4)\pi d^2 L$. Dividing this value by the residence time gives the flow rate.

The RTD is defined as the distribution of times that different fluid elements spend in a flow reactor. Space time is an idealized single value, while the RTD shows a time range that reflects real flow behavior. The RTD presents how long different portions of the fluid actually stay in the reactor, revealing non-idealities in the flow pattern. Determining the RTD can reveal information about mixing and flow patterns within the reactor and provide insights into the flow characteristics and deviations from ideal behaviour, helping to understand how well the reactor approximates the ideal models of plug flow reactors (PFR) and continuous stirred-tank reactors (CSTR) [226]. The RTD is usually represented by the the Exit Age Distribution function (E(t)) [229], which gives the probability that fluid leaving the reactor has a residence time of exactly t. E(t) is the fraction of fluid that spends time t in the reactor.

$$\int_0^\infty E(t)dt = 1$$

The RTD can be used to determine flow problems, e.g. dead zones or short-circuiting, which lead to reduced reaction efficiency [230]. Understanding RTDs and analyzing flow behavior within a reactor are critical to optimizing performance, improving conversion rates, and diagnosing operational problems.

1.4.5 MOFs synthesized by microreactors

MOFs synthesis using microreactors has garnered significant attention because microreactors provide enhanced control over the reaction conditions, thereby improving the uniformity, scalability, and efficiency of MOF synthesis [231]. Most of MOFs synthesized in flow have followed a segmented droplet strategy, which is conducive to effective mixing and can be set up to reduce clogging of the reaction channel relative to single-phase flow. Figure 1.4 is a schematic illustration of

microfluidic setup for MIL-88B MOFs with using silicone oil as the continuous phase [232]. To avoid further crystallization, the synthesized crystals were stored in a cooled beaker. For final separation of the MOF product, the samples were centrifuged, washed and dried after the microfluidic synthesis.

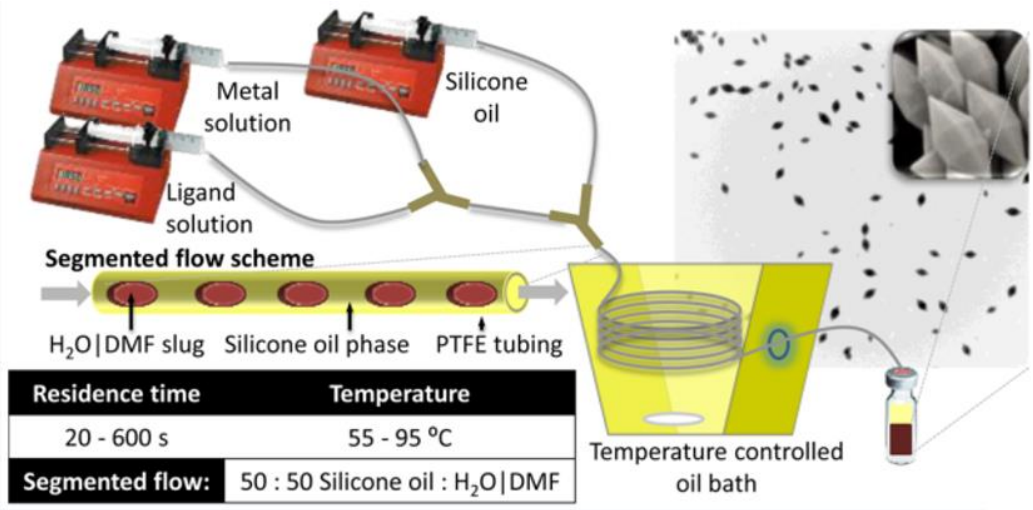

Figure 1.4 Schematic of MIL-88B type MOF synthesized by microfluidics [232].

Uniform HKUST-1 MOF particles with a hierarchical pore structure were synthesized using a droplet-based microfluidics and evaporative crystallization method [199]. The pore size distribution results showed that this synthetic approach could generate monodisperse single-crystalline microcubes, and the size and porosity of the achieved cubes could be tailored by varying the preparation conditions. The continuous synthesis of ZIF-8 in a single-phase flow has been reported. In this report, ZIF-8 were obtained a remarkable STY of 21 0,000 kg m^{-3} day^{-1} [164]. UiO-66-NH_2 using water as the solvent has been synthesized in a flow reactor achieving a high STY of 4346 kg m^{-3} day^{-1} [233].

Table 1.4 presents an overview information of MOF materials synthesized by using microfluidic techniques. Compared with traditional synthesis methods, MOFs can be made by microfluidic systems with a shorter synthesis time at similar temperatures. A comparison of reaction temperatures and times of synthesizing the same MOF by different methods are listed in Table 1.5. Microfluidic synthesis can fabricate MOFs in a short time with better control of reaction parameters. This project has advanced in this area by combining the flow synthesis of MOFs using green chemical principles with an ultrasound-assisted reactor for the scaled-up synthesis of three distinct MOF chemistries whilst achieving a high STY.

Table 1.4 Overview of MOFs synthesized in microfluidic systems

MOFs	Crystal size (μm)	Tube diameters (mm)	Residence time (s)	Temp (°C)	Ref.
HKUST-1	5-15	ID: 0.51	60-720	90	[234]
MOF-5	10−15	ID: 0.51	180	120	
IRMOF-3	10−15	ID: 0.51	180	120	
UiO-66	0.1-1	ID: 0.51	900	150	
HKUST-1	0.5-3	Not available	180	60	[199]
HKUST-1	0.02	ID: 2	180	90	[221]
UiO-66	0.21	Not available	<3	<120	[235]
UiO-66-NH_2	2-12	ID: 3	60-90	90	[236]
UiO-66-NH_2	Not available	ID: 4	1200	85	[233]
UiO-67	0.2-0.4	ID: 0.8	1800	140	[228]
UiO-67	0.065	ID: 0.8	30	140	[237]
UiO-67	0.4-0.9	ID: 0.8	Not available	70/120	[238]
ZIF-8	0.08	ID: 1.6	60	25	[164]
ZIF-8	0.3-1.1	OD: 2.5 ID: 1.5	24-160	80	[239]
ZIF-8	0.355	ID: 1.6	600	25	[240]
ZIF-8	0.1-0.2	ID: 1.5	10800	25-80	[241]
ZIF-8	0.6-0.8	ID: 0.6	3.6	25	[242]
ZIF-8	0.04-0.7	ID: 1.58	Not available	21	[243]
MOF-545	0.1-0.3	ID: 0.8	1.6-160	120	[244]
MOF-808	0.02-0.07	Not available	900-7200	110	[245]
HMNMs-Cu	350-500	OD: 0.85 ID: 0.5	300	70	[246]
Fe-MIL-88B	0.520	ID: 1.0	240	95	[232]
ZrBTB	Not available	OD: 3 ID: 2	480	130	[247]

Table 1.5 Time comparison of MOFs synthesized by traditional and microfluidic methods

MOFs	Methods	Synthesis time	Temperature (°C)	Ref.
HKUST-1	Solvothermal	12 h	110	[40]
HKUST-1	Microfluidic	180 s	60	[199]
ZIF-8	Solvothermal	24 h	140	[23]
ZIF-8	Microfluidic	90 s	140	[164]
MIL-100	Solvothermal	96 h	220	[28]
MIL-100	Microfluidic	50 min	100-110	[248]
UiO-66	Solvothermal	24 h	120	[142]
UiO-66	Microfluidic	22 min	100	[249]
UiO-67	Solvothermal	12 h	150	[250]
UiO-67	Microfluidic	0.5 h	140	[228]

Except microfluidic synthesis, continuous dry synthesis, such as twin-screw extruder (TSE) reactors, without using any solvent has also been reported as promising methods for MOF fabrication, relying on mechanical and thermal energy to drive the reaction [251]. TSE has been successfully applied to the synthesis of MOFs, enabling continuous production at multi-kilogram per hour scales [252]. The use of TSE in MOF synthesis demonstrated significant improvements in STY. For example, a study reported a 100-fold increase in STY when translating a reaction from a mixer mill to a TSE reactor (STY: 3395 kg m^{-3} day^{-1}) [253]. However, only certain MOFs with robust frameworks (e.g., ZIFs and UiO-66) can be synthesized by dry methods, porous MOFs, such as HKUST-1, require solvents for crystallization [254]. And continuous dry synthesis may result in lower surface area and reduced crystallinity of MOFs compared to liquid-phase synthesis, achieving uniform particle size and shape is challenging in the continuous dry synthesis [255]. Although continuous synthesis methods with using microfluidic/millifluidic reactors reported in this thesis have problems of solvent wastes and potential of fouling, continuous flow reactors are suitable for synthesizing different types of MOFs with better crystal quality and size control.

1.5 Design of Experiments (DoE)

DoE involves planning, conducting, and analysing controlled experiments in order to assess the factors that influence a particular outcome. DoE is a powerful tool, which can be employed in a variety of research situations with the benefits of improved quality, efficiency, and cost saving.

1.5.1 Background of DoE

DoE is a structured method of conducting and analysing controlled tests to assess factors that are influencing a response variable [256]. Before DoE, one-variable-at-time (OVAT) analysis is the traditional method for reaction optimisation. The OVAT method needs some scientific intuition, where only one variable is changed in each experiment [257]. As an optimization technique, the OVAT method is usually bad in accurate and efficient, and the method often misinterprets chemical processes. Interactions between variables in chemical reactions are the combined effects of two or more factors on the reaction outcome, where the influence of one factor depends on the level of another. These interactions are neglected because this linear experimental procedure applied to a chemical reaction output only gives a nonlinear response.

Multivariate statistical methods e.g. DoE, have been employed to overcome the main shortage of OVAT. DoE is good at maximizing the amount of information gained from a study while minimizing the amount of data to be collected with advantages of process efficiency, reduced costs, and enhanced product quality [258]. Using a predefined, space-filling experimental design eliminates the need for chemical intuition to guide optimization, and it has been proven time and time again to be a more efficient approach [259, 260]. As shown in Figure 1.5, compared to a traditional OVAT study, this space-filling DoE allows the construction of statistical models to describe the chemical process across the entire parameter space [261]. These statistical models are also often intuitive to chemists, and it may be easier to analyse results from these DoE models than physical models. However, physical models can provide interpretation directly. Whilst DoE has many advantages for chemical synthesis, it still has limitations. DoE relies on factors and levels which can be managed, while chemical reactions usually include many variables, such as temperature, solvent, pH, concentration of precursors, and each factor can have multiple levels. This high dimensionality makes DoE difficult to apply in practice. Many chemical reactions

display nonlinear reactions between factors, which can be difficult to accurately capture in DoE, especially if the model is too simple.

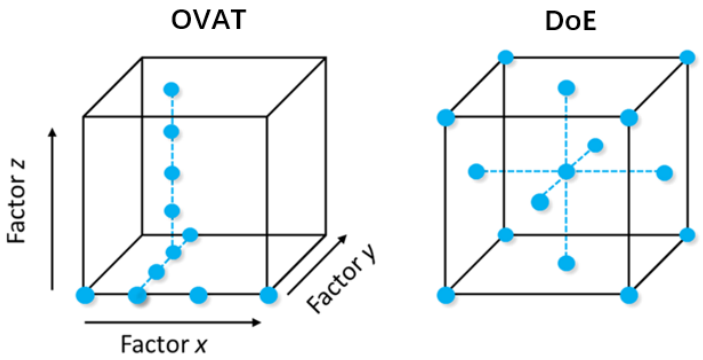

Figure 1.5 Parameter space exploration expected when comparing a typical OVAT optimization with a DoE design, where represents an experiment [261].

Running DoE activities concentrates on executing experiments from a structured experimental design, these designs could be templates for performing experiments based on factors and bounds of interest, efficiently exploring reaction parameter range, and providing data infrastructure formats to build powerful statistical models [262]. The DoE is usually implemented by software, for instance MODDE, Design-Expert, Minitab, or coding languages such as MATLAB [263].

1.5.2 Response surface modelling (RSM)

RSM is a predictive modelling technique, which employs regression equations to explore the relationship between factors and the response variable [256]. Factors are parameters that can be changed on their own. Response or dependent variable is measurement of the experiment being performed. RSM is especially useful when several input variables influence a desired output, and the goal of RSM is to understand how these variables interact to optimize the output or response [264]. Combining DoE with RSM offers insight into the entire high-dimensional parameter space and develops predictive models by using a minimum number of experiments [265].

In RSM, fitting is constructed by creating a polynomial model to approximate the relationship between factors and responses. Regression analysis is usually used to estimate the parameters (coefficients) of the polynomial model [266]. The quality of the fit is evaluated through several statistical metrics. R^2 measures the proportion of variance in the response explained by the model, higher R^2 values indicate a better fit [267]. The p-value for coefficients measures the significance of each term in the model.

A significant p-value (typically < 0.05) presents that a term is meaningful to the model. Analysis of variance (ANOVA) checks whether the overall regression model is statistically significant. Residuals are usually used to analyse patterns or anomalies. In an ideal situation, the residuals should be randomly distributed around zero, indicating that model captures data well and has no systematic bias.

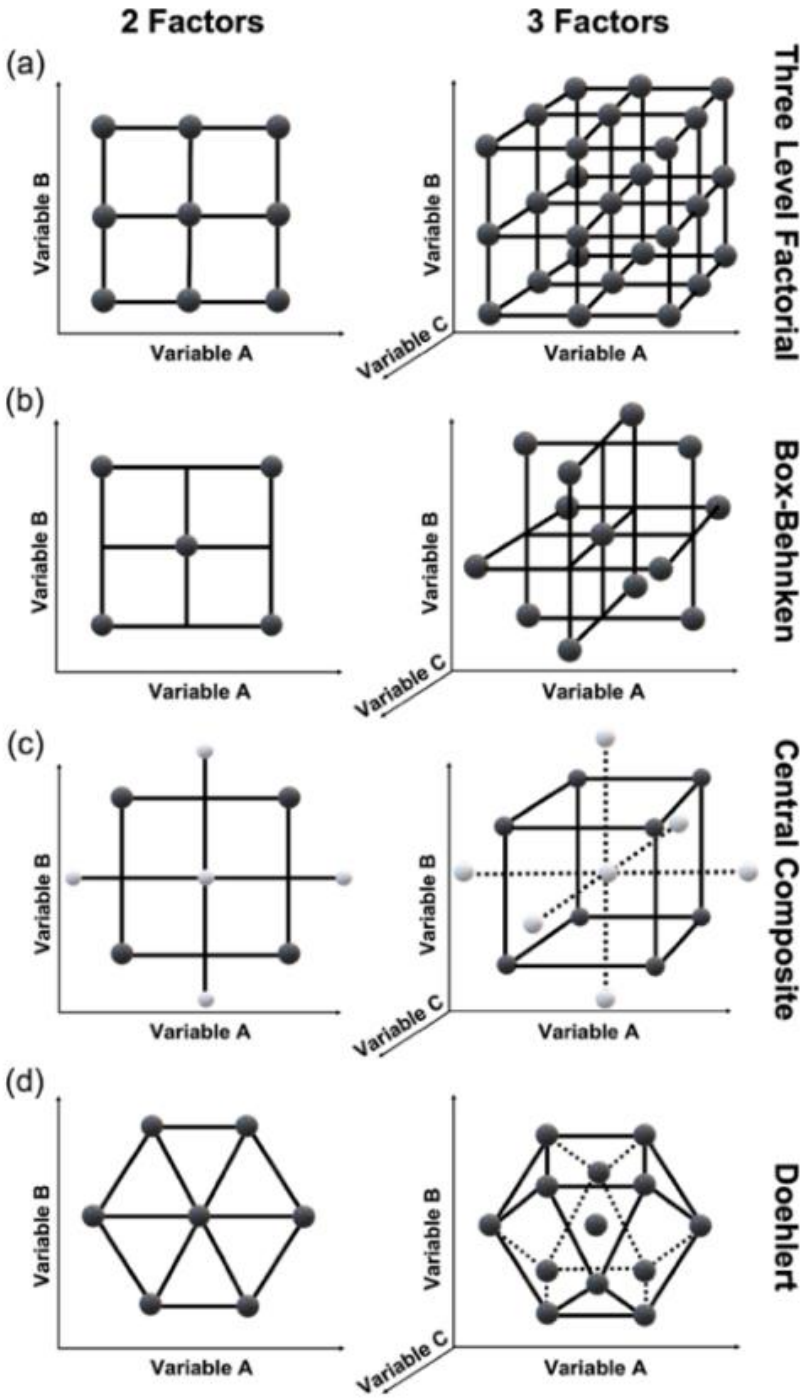

Figure 1.6 Visualization of the 2- and 3-factor optimization designs in parameter space (a) 3-level factorial, (b) Box−Behnken, (c) central composite, and (d) Doehlert designs [256].

RSM can be used to design experiments where experimenters systematically change input variables and observe the resulting output. Popular experimental designs for RSM are included in Figure 1.6 [256]. Full 3-level design is a simple design that includes all combinations of the 3 levels of each factor (Figure 1.6a); Box−Behnken 3-level design contains a subset of runs in the full 3-level factorial (Figure 1.6b); central composite design (CCD) consists of a central 2-level factorial and additional points (Figure 1.6c); Doehlert designs have an dodecahedral shape within the design space that permits for a deeper study of certain factors (Figure 1.6d).

A response surface presents the relationship between the input variables and the response by a surface. By analysing the response surface, RSM helps determine a set of conditions that maximize or minimize the response. This is usually done by locating the peaks (maxima) or valleys (minima) of the surface that correspond to the optimal conditions. A RSM with 3-levels and 2-factors (milling time and speed) design has been employed to investigate and optimise CO conversion in a medium temperature shift reaction for the synthesis of nanostructured Ce-Cu mixed oxide [268]. According to contour plots from the RSM, the interaction between parameters of time and speed was very crucial for CO conversion.

1.5.3 DoE in continuous synthesis

DoE in continuous synthesis is a systematic way to optimize chemical processes by determining relationships between factors and responses. Continuous-flow systems combined with DoE can significantly speed up the development and optimization of synthetic methods, making processes more efficient, safer, and reproducible [269]. DoE helps to study the effects of multiple factors efficiently, for instance the effects of the concentration of precursors, reaction times and temperatures, and flow rates on critical responses e.g. yield, STY, purity, and particle size of samples. By using statistical methods, DoE permits the development of predictive models that can optimize processes with fewer experimental runs compared to traditional trial-and-error methods. This is important in continuous synthesis, because precise control of conditions can lead to more consistent and scalable production.

Popular DoE methods, such as RSM and principal component analysis (PCA), can reduce experimental costs and the number of required experiments, while optimizing reaction conditions and improving product yield [270]. A 2-level with 3

factors full factorial DoE approach has been reported for the precipitation of calcium phosphate nanoparticles (CaP NPs) using a sonication-assisted continuous synthesis [271]. Reactant flow rate, sonication amplitude, and maturation time were used as three factors for the evaluation of chemical properties of the CaP NPs, results indicated that the dimension of particles was influenced by reactor flow rate. This research provided a good understanding of how reaction factors influence CaP NP properties through using a DoE method. Computational fluid dynamic (CFD) simulations with experimental DoE can also identify significant factors affecting production results, and provide strong correlations between predicted and experimental results [272]. A screening DoE with the CFD simulations has been employed in the flow synthesis of the pharmaceutical ingredient (dolutegravir); CFD simulations and experimental results identified the reaction temperature and residence time as the most important factors impacting product yield [272].

As continuous flow chemistry continues to grow, the integration of DoE will be a critical factor in driving further advancements in chemical manufacturing. In this work, I have combined DoE with continuous synthesis to optimise reaction parameters for the fabrication of sulfonate MOFs in flow reactors.

1.6 Aims

Continuous synthesis has been presented as promising method for scalable chemical synthesis with better control of reaction results. However, there are still a limited number of reports for the scalable and green chemical synthesis of sulfonate MOFs in flow reactors, how reaction parameters affect the continuous synthesis of MOFs remains unclear, and how the crystal structures of sulfonate MOFs affects their proton conductivities has not been well explored.

Throughout this thesis, I have been guided by the aims to further study the continuous synthesis of sulfonate MOFs for scalable production using green solvents, seeking to address questions of how the reaction parameters in flow affect the yield and particle properties compared to in batch reactions. Within this work, I have also explored the relationship between the crystal structure and proton conductivities of a set of structurally similar sulfonate MOFs. As ultrasound energy can increase the nucleation rate of MOFs, an ultrasound-assisted flow reaction platform was constructed, aiming for the scaled-up production across sulfonates, imidazolates, and

carboxylate MOFs using green solvents. In the scalable synthesis, fabrication of MOFs with improved functional properties, such as proton conductivity and gas uptake, has also been the chief aim as the ultrasound-assisted synthesis can achieve high quality MOF crystals with smaller and more uniform particle size.

1.7 Thesis summary

The thesis will include an introduction and literature review chapter, the three full-article manuscripts, and a final chapter on conclusions, discussion of the results in concert, and future work. The introduction will outline the thesis aims, scientific background, and current state-of-the-art, providing a conceptual overview and linking the themes across the manuscripts. Each results chapter will feature one manuscript and corresponding supporting information along with experimental details for reproducibility. The final chapter will draw together the results from all chapter and discuss them together as well as compare them with existing literature and highlight the connections across studies to unify the thesis. This final chapter will also discuss the overall scope and limitations of the thesis, leading to proposed directions for future research.

A batch synthesis of a Cu^{2+} based MOF incorporating both sulfonate and amine groups, termed Cu-SAT, has been firstly reported by Moi *et al*, showing promising proton conductivity [82]. However, how reaction parameters affect reaction results are not clear, and it is worth trying to scalable synthesis this MOFs for practical application. In Chapter 2, the batch synthesis of Cu-SAT was firstly transferred to a continuous synthesis in a millifluidic flow reactor. This study showed the reaction yields in the flow reactor were typically 10-20% higher than those obtained in a batch reactor under matched reaction times, temperatures and reagent concentrations. The improved yield was attributed to greater mass and heat transfer in the flow reactor. DoE and response surface modelling revealed the key correlations between the process parameters and yields and particle size distributions. The proton conductivity of Cu-SAT based PEMs was also investigated in this work. Finally, all these results were descripted in the first article, titled ‘Droplet-based Millifluidic Synthesis of a Proton-conducting Sulfonate Metal–organic Framework’, which has been published in *Chemical Engineering Journal* in 2023.

The promising proton conductivity properties of Cu-SAT (~10^{-3} S cm^{-1} compared

to 10^{-1}-10^{-2} S cm^{-1} for the benchmark Nafion proton-conducting polymer [57]), prompted further investigation of how the crystal structure of 2D sulfonate MOFs affects the proton conductivity, and green chemical synthesis was also considered. In Chapter 3, a series of Cu^{2+} and Ca^{2+} CPs have been synthesized by using naphthalenedisulfonic acid (NDS) and anthraquinone-1,5-disulfonic acid (ADS) ligands and different greener solvents. Starting from the Cu^{2+}-based Cu-SAT and the aqueous synthesis of the known Ca^{2+}-NDS structure incorporating water ligands, a further five sulfonate CP structures have been reported in this work. Proton conductivities of these sulfonate CPs are from 10^{-4} to 10^{-3} S cm^{-1} at 80 °C and 95% RH. Through analyzing the proton conductivities and comparing the structure similarities and differences of these crystals, an experimental structure-function relationship linking the tortuosity of the hydrogen bonding pathway with proton conductivities across the synthesized sulfonate CPs was established. These results were detailed in the second research paper, named 'Modulating proton conductivity through crystal structure tuning in arenedisulfonate coordination polymers', which has been published in the *Journal of materials chemistry A* in June 2024.

Building on the work in Chapter 3, I have found that Ca-NDS (water) has promising proton conductivity (~10^{-3} S cm^{-1}) while also offering a simplified and fast synthesis relative to Cu-SAT. The Ca-NDS CP incorporates a single NDS ligand and uses water as reaction solvent, presenting a greener synthesis route than for Cu-SAT or other analogous sulfonate CPs. High reaction yield and production rate of Ca-NDS (water) synthesis as well as eliminating the grinding of this crystal, make its application in proton conductivity worthy of further investigation for its practical application. In Chapter 4, an ultrasound-assisted two-phase flow reaction platform was created for the scale-up synthesis of the sulfonate Ca-NDS (water), as well as the imidazolate ZIF-8 and the carboxylate UiO-66-NH_2 MOFs in aqueous solvent. With using this reaction platform, STYs for Ca-NDS (water), ZIF-8, and UiO-66-NH_2 can reach up to $3.4\times10^4 \pm 1\times10^3$, $4.0\times10^3 \pm 2\times10^2$ and $2.0\times10^3 \pm 1\times10^2$ kg m^{-3} day^{-1}, respectively. The Ca-NDS (water) and ZIF-8 synthesized in this reaction platform presented a good proton conductivity (0.94 ± 0.03 mS cm^{-1} in MMM form at 80 °C in 95 % RH) and high specific surface area (1886 m^2 g^{-1}), respectively. In addition, the fouling-free reactor platform can be operated with continuous synthesis of Ca-NDS (water) for more than 2 hours with no reduction in production rate and crystal product

quality. All these results were descripted in the third paper, titled ‘Ultrasound-assisted continuous aqueous synthesis of sulfonate, imidazolate, and carboxylate MOFs with high space time yield’ and submitted.

Except my research works presented Chapter 2, 3 and 4 with publishing three first author papers, I have also collaborated with other researchers in the University of Leeds and University of Cambridge and published 3 co-author papers. And I have joined three international conferences with poster presentations and joined several school organized conferences and seminars with oral presentations for knowledge sharing and building connections.

1.8 References

[1] D.S. Sholl, R.P. Lively, Seven chemical separations to change the world, Nature 532 (2016) 435-437.

[2] D. Lv, P. Zhou, J. Xu, S. Tu, F. Xu, J. Yan, H. Xi, W. Yuan, Q. Fu, X. Chen, Q. Xia, Recent advances in adsorptive separation of ethane and ethylene by C_2H_6-selective MOFs and other adsorbents, Chem. Eng. J. 431 (2022) 133208-133230.

[3] S.C. Pal, M.C. Das, Superprotonic conductivity of MOFs and other crystalline platforms beyond 10^{-1} S cm^{-1}, Adv. Funct. Mater. 31 (2021) 2101584.

[4] L. Mitchell, B. Gonzalezsantiago, J.P.S. Mowat, M.E. Gunn, P. Williamson, N. Acerbi, M.L. Clarke, P.A. Wright, CCYG, Remarkable Lewis acid catalytic performance of the scandium trimesate metal organic framework MIL-100(Sc) for C–C and C-N bond-forming reactions, Catal. Sci. Technol. 3 (2012) 606-617.

[5] D. Yang, B.C. Gates, Catalysis by Metal Organic Frameworks: Perspective and Suggestions for Future Research, ACS Catal. 9 (2019) 1779-1798.

[6] X.L. Hu, K. Wang, X. Li, Q.Q. Pan, Z.M. Su, Two Anthracene Chromophores based Metal-Organic Frameworks for Gas Absorption and Promising Nitro Aromatic Sensing, New J. Chem. 44 (2020) 1249-1252.

[7] H. Li, K. Wang, Y. Sun, C.T. Lollar, J. Li, H.C. Zhou, Recent advances in gas storage and separation using metal–organic frameworks, Mater. Today 21 (2018) 108-121.

[8] J. Zhang, G.B. White, M.D. Ryan, A.J. Hunt, M.J. Katz, Dihydrolevoglucosenone (Cyrene) As a Green Alternative to N,N-Dimethylformamide (DMF) in MOF Synthesis, ACS Sustain. Chem. Eng. 4 (2016) 7186-7192.

[9] V.V. Butova, A.P. Budnyk, E.A. Bulanova, C. Lamberti, A.V. Soldatov, Hydrothermal synthesis of high surface area ZIF-8 with minimal use of TEA, Solid State Sci. 69 (2017) 13-21.

[10] R. Ettlinger, U. Lächelt, R. Gref, P. Horcajada, T. Lammers, C. Serre, P. Couvreur, R.E. Morris, S. Wuttke, Toxicity of metal–organic framework nanoparticles: from essential analyses to potential applications, Chem. Soc. Rev. 51 (2022) 464-484.

[11] C.B. Whitehead, S. Özkar, R.G. Finke, LaMer's 1950 model for particle formation of instantaneous nucleation and diffusion-controlled growth: a historical look at the model's origins, assumptions, equations, and underlying sulfur sol formation kinetics data, Chem. Mater. 31 (2019) 7116-7132.

[12] V.I. Kalikmanov, Classical nucleation theory, Nucleation theory, Springer2012, pp. 17-41.

[13] P.Z. Moghadam, A. Li, S.B. Wiggin, A. Tao, A.G. Maloney, P.A. Wood, S.C. Ward, D. Fairen-Jimenez, Development of a Cambridge Structural Database subset: a collection of metal–organic frameworks for past, present, and future, Chem. Mater. 29 (2017) 2618-2625.

[14] W. Fan, X. Zhang, Z. Kang, X. Liu, D. Sun, Isoreticular chemistry within metal–organic frameworks for gas storage and separation, Coord. Chem.Rev. 443 (2021) 213968.

[15] B.F.H.a.R. Robson, Design and construction of a new class of scaffolding-like materials comprising infinite polymeric frameworks of 3D-linked molecular rods. A reappraisal of the zinc cyanide and cadmium cyanide structures and the synthesis and structure of the diamond-related frameworks $[N(CH_3)_4][CuIZnII(CN)_4]$ and CuI[4,4',4",4"'-tetracyanotetraphenylmethane]BF4.x$C_6H_5NO_2$, J. Am. Chem. Soc. 112 (1990) 1546-1554.

[16] J. Boken, S.K. Soni, D. Kumar, Microfluidic Synthesis of Nanoparticles and their Biosensing Applications, Crit. Rev. Anal. Chem. (2016) 538-561.
[17] G. Xu, K. Otsubo, T. Yamada, S. Sakaida, H. Kitagawa, Superprotonic conductivity in a highly oriented crystalline metal-organic framework nanofilm, J. Am. Chem. Soc. 135 (2013) 7438.
[18] P. Falcaro, R. Ricco, A. Yazdi, I. Imaz, S. Furukawa, D. Maspoch, R. Ameloot, J.D. Evans, C.J. Doonan, Application of Metal and Metal Oxide Nanoparticles @ MOFs, Coord. Chem. Rev. 307 (2016) 237-254.
[19] G. Férey, Hybrid porous solids: past, present, future, Chem. Soc. Rev. 37 (2008) 191-214.
[20] H.-Y. Bai, J.-F. Ma, J. Yang, L.-P. Zhang, J.-C. Ma, Y.-Y. Liu, Eight two-dimensional and three-dimensional metal− organic frameworks based on a flexible tetrakis (imidazole) ligand: synthesis, topological structures, and photoluminescent properties, Cryst. Growth Des. 10 (2010) 1946-1959.
[21] W. Yin, G. Zhang, X. Wang, H. Pang, One–dimensional metal–organic frameworks for electrochemical applications, Adv. Colloid Interface Sci. 298 (2021) 102562.
[22] M. Eddaoudi, Systematic design of pore size and functionality in isoreticular MOFs and their application in methane storage, Science 295 (2002) 469-472.
[23] Z.N. Kyo Sung Park, Adrien P. Coˆte´, Omar M. Yaghi., Exceptional chemical and thermal stability of zeolitic imidazolate frameworks, Proc. Natl. Acad. Sci. 103 (July 5, 2006) 10186–10191.
[24] X.C. Huang, Y.Y. Lin, J.P. Zhang, X.M. Chen, Ligand-directed strategy for zeolite-type metal-organic frameworks: zinc(II) imidazolates with unusual zeolitic topologies, Angew. Chem. Int. Ed. 45 (2010) 1557-1559.
[25] G. Ferey, C. Mellot-Draznieks, C. Serre, F. Millange, J. Dutour, S. Surble, I. Margiolaki, A Chromium Terephthalate-Based Solid with Unusually Large Pore Volumes and Surface Area, Science 309 (2005) p.2040-2042.
[26] J. Panda, S.N. Sahu, R. Pati, P.K. Panda, B.C. Tripathy, S.K. Pattanayak, R. Sahu, Role of Pore Volume and Surface Area of Cu-BTC and MIL-100 (Fe) Metal-Organic Frameworks on the Loading of Rifampicin: Collective Experimental and Docking Study, ChemistrySelect 5 (2020) 12398-12406.
[27] J.H. Cavka, S. Jakobsen, U. Olsbye, N. Guillou, K.P. Lillerud, A New Zirconium Inorganic Building Brick Forming Metal Organic Frameworks with Exceptional Stability, J. Am. Chem. Soc. 130 (2008) 13850-13851.
[28] G. Ferey, C. Serre, C. Mellot-Draznieks, F. Millange, S. Surble, J. Dutour, I. Margiolaki, A hybrid solid with giant pores prepared by a combination of targeted chemistry, simulation, and powder diffraction, Angew Chem. Int. Ed. Engl. 43 (2004) 6296-6301.
[29] F. Salles, D.I. Kolokolov, H. Jobic, G. Maurin, S.G. Ferey, Adsorption and Diffusion of H-2 in the MOF Type Systems MIL-47(V) and MIL-53(Cr), A Combination of Microcalorimetry and QENS Experiments with Molecular Simulations, J. Phys. Chem. C 113 (2009) 7802.
[30] J.A. Mason, M. Veenstra, J.R. Long, ChemInform Abstract: Evaluating Metal—Organic Frameworks for Natural Gas Storage, Cheminform 45 (2014) 31-39.
[31] Z. Hu, Y. Peng, Z. Kang, Y. Qian, D. Zhao, A Modulated Hydrothermal (MHT) Approach for the Facile Synthesis of UiO-66-Type MOFs, Inorg. Chem. 54 (2015) 4862-4868.
[32] J. Mason, M. Veenstra, J. Long, Evaluating metal–organic frameworks for natural gas storage, Chem. Sci. 5 (2013) 32-51.

[33] N.C. Burtch, H. Jasuja, K.S. Walton, Water stability and adsorption in metal–organic frameworks, Chem. Rev. 114 (2014) 10575-10612.
[34] Y. Om., M. O'Keeffe, O. Nw., C. Hk., M. Eddaoudi, J. Kim, Reticular synthesis and the design of new materials [Review], Nature 423 (2003) 705-714.
[35] P. Falcaro, A.J. Hill, K.M. Nairn, J. Jasieniak, J.I. Mardel, T.J. Bastow, S.C. Mayo, M. Gimona, D. Gomez, H.J. Whitfield, A new method to position and functionalize metal-organic framework crystals, Nat. Commun. 2 (2011) 237.
[36] J.Y. Lee, O.K. Farha, J. Roberts, K.A. Scheidt, S. Nguyen, J.T. Hupp, Metal–organic framework materials as catalysts, Chem. Soc. Rev. 38 (2009) 1450-1459.
[37] Dresselhaus, M.S. Amp, I.L. Thomas, overview Alternative energy technologies, Nature 6861 (2001) 332-337.
[38] S. Devautour-Vinot, E.S. Sanil, A. Geneste, V. Ortiz, P.G. Yot, J.S. Chang, G. Maurin, Guest-Assisted Proton Conduction in the Sulfonic Mesoporous MIL-101 MOF, Chem. Asian J. 14 (2019) 3561-3565.
[39] H. Roohollahi, H. Zeinalzadeh, H. Kazemian, Recent advances in adsorption and separation of methane and carbon dioxide greenhouse gases using metal–organic framework-based composites, Ind. Eng. Chem. Res. 61 (2022) 10555-10586.
[40] B. Liu, Y. Li, S.C. Oh, Y. Fang, H. Xi, Fabrication of a hierarchically structured HKUST-1 by a mixed-ligand approach, RSC Adv. 6 (2016) 61006-61012.
[41] H. Li, K. Wang, Y. Sun, C.T. Lollar, J. Li, H.C. Zhou, Recent advances in gas storage and separation using metal–organic frameworks, Mater.Today 21 (2017) 108-120.
[42] A.R. Millward, O.M. Yaghi, Metal-organic frameworks with exceptionally high capacity for storage of carbon dioxide at room temperature, J. Am. Chem. Soc. 127 (2005) 17998-18009.
[43] S. Mahajan, M. Lahtinen, Recent progress in metal-organic frameworks (MOFs) for CO_2 capture at different pressures, J. Environ. Chem. Eng. 10 (2022) 108930.
[44] E. Martinez-Ahumada, M.L. Diaz-Ramirez, M.J. Velasquez-Hernandez, V. Jancik, I.A. Ibarra, Capture of toxic gases in MOFs: SO(2), H(2)S, NH(3) and NO(x), Chem. Sci. 12 (2021) 6772-6799.
[45] H. Li, L. Li, R.B. Lin, W. Zhou, Z. Zhang, Porous Metal-Organic Frameworks for Gas Storage and Separation: Status and Challenges, EnergyChem 1 (100006) 100006.
[46] R.B. Lin, S. Xiang, W. Zhou, B. Chen, Microporous Metal-Organic Framework Materials for Gas Separation, Chemistry 6 (2020) 337-363.
[47] Q. Qian, P.A. Asinger, M.J. Lee, H. Gang, Z.P. Smith, MOF-Based Membranes for Gas Separations, Chem. Rev. 120 (2020) 8161−8266.
[48] X. Mei, S. Yang, P. Lu, Y. Zhang, J. Zhang, Improving the selectivity of ZIF-8/polysulfone-mixed matrix membranes by polydopamine modification for H_2/CO_2 separation, Front. Chem. 8 (2020) 528.
[49] Y. Katayama, K.C. Bentz, S.M. Cohen, Defect-Free MOF-Based Mixed-Matrix Membranes Obtained by Corona Cross-Linking, ACS Appl. Mater. Interfaces 11 (2019) 13029-13037.
[50] M.S. Alhumaimess, Metal–organic frameworks and their catalytic applications, J. Saudi Chem. Soc. 24 (2020) 461-473.
[51] L. Cao, C. Wang, Metal–Organic Layers for Electrocatalysis and Photocatalysis, ACS Cent. Sci. 23 (2020) 2149-2158.
[52] H. Chang, Y. Zhou, S. Zhang, X. Zheng, Q. Xu, CO_2-Induced 2D Ni-BDC Metal–Organic Frameworks with Enhanced Photocatalytic CO_2 Reduction Activity, Adv. Mater. Interfaces 8 (2021) 2100205.

[53] X.Y. Dong, J.J. Li, Z. Han, P.G. Duan, L.K. Li, S.Q. Zang, Tuning the functional substituent group and guest of metal–organic frameworks in hybrid membranes for improved interface compatibility and proton conduction, J. Mater. Chem. A 5 (2017) 3464-3474.
[54] P. Jhariat, P. Kumari, T. Panda, Structural features of proton-conducting metal organic and covalent organic frameworks, CrystEngComm 22 (2020) 6425-6443.
[55] S. Liu, Z. Yue, Y. Liu, Incorporation of imidazole within the metal-organic framework UiO-67 for enhanced anhydrous proton conductivity, Dalton Trans. 44 (2015) 12976-12980.
[56] H. Zhao, Z.-H. Du, C.-Y. Mu, G. Li, Proton conductive properties of a substituted imidazole dicarboxylate-based hydrogen-bonded organic framework and a related nickel-organic framework, J. Solid State Chem. 315 (2022) 123550.
[57] M. Casciola, G. Alberti, M. Sganappa, R. Narducci, On the decay of Nafion proton conductivity at high temperature and relative humidity, J. Power Sources 162 (2006) 141-145.
[58] H. Jasuja, K.S. Walton, Effect of catenation and basicity of pillared ligands on the water stability of MOFs, Dalton Trans. 42 (2013) 15421-15426.
[59] L. Feng, K.-Y. Wang, G.S. Day, M.R. Ryder, H.-C. Zhou, Destruction of metal–organic frameworks: positive and negative aspects of stability and lability, Chem. Rev. 120 (2020) 13087-13133.
[60] G. Zhang, H. Fei, Synthesis and Applications of Porous Organosulfonate-Based Metal-Organic Frameworks, Top Curr. Chem. 377 (2019) 32.
[61] H.A. Patel, N. Mansor, S. Gadipelli, D.J. Brett, Z. Guo, Superacidity in Nafion/MOF Hybrid Membranes Retains Water at Low Humidity to Enhance Proton Conduction for Fuel Cells, ACS Appl. Mater. Inter. 8 (2016) 30687-30691.
[62] B. Pinter, N. Nagels, W.A. Herrebout, F.D. Proft, Halogen Bonding from a Hard and Soft Acids and Bases Perspective: Investigation by Using Density Functional Theory Reactivity Indices, Chem. Eur. J. 19 (2012) 519-530.
[63] J.L. Reed, Hard and Soft Acids and Bases: Small Molecules, Inorg. Chem. 48 (2009) 7151-7158.
[64] G.K. Shimizu, R. Vaidhyanathan, J.M. Taylor, Phosphonate and sulfonate metal organic frameworks, Chem. Soc. Rev. 38 (2009) 1430-1449.
[65] S.A. Dalrymple, G. Shimizu, An open channel coordination framework sustained by cooperative primary and secondary sphere interactions, Chem. Comm. (2002) 2224-2225.
[66] D.K. Maity, K. Otake, S. Ghosh, H. Kitagawa, D. Ghoshal, Sulfonic Group Functionalized Mixed Ligand Coordination Polymers: Synthesis, Characterization, Water Sorption, and Proton Conduction Studies, Inorg. Chem. 56 (2017) 1581-1590.
[67] B. Joarder, J.B. Lin, Z. Romero, G. Shimizu, Single Crystal Proton Conduction Study of a Metal Organic Framework of Modest Water Stability, J. Am. Chem. Soc. 139 (2017) 7176-7179.
[68] J. Perles, N. Snejko, M. Iglesias, M.á. Monge, 3D scandium and yttrium arenedisulfonate MOF materials as highly thermally stable bifunctional heterogeneous catalysts, J. Mater. Chem. 19 (2009) 6504-6511.
[69] Brett, D., Chandler, Joanne, O., Yu, David, T., Cramb, George, Series of Lanthanide-Alkali Metal-Organic Frameworks Exhibiting Luminescence and Permanent Microporosity, Chem. Mater. 19 (2007) 4467–4473.
[70] S.A. Dalrymple, G.K.H. Shimizu, Anion Exchange in the Channels of a Robust Alkaline Earth Sulfonate Coordination Network, Chemistry 8 (2002) 3010-3015.

[71] A. Côté, G. Shimizu, Coordination Solids via Assembly of Adaptable Components: Systematic Structural Variation in Alkaline Earth Organosulfonate Networks, Chemistry 9 (2010) 5361-5370.
[72] A.E. Platero-Prats, M. Iglesias, N. Snejko, A. Monge, E. GutieRrez-Puebla, From Coordinatively Weak Ability of Constituents to Very Stable Alkaline-Earth Sulfonate MetalOrganic Frameworks, Cryst. Growth Des. 11 (2011) 1750-1758.
[73] G. Zhang, H. Fei, Missing metal-linker connectivities in a 3-D robust sulfonate-based metal–organic framework for enhanced proton conductivity, Chem. Comm. 53 (2017) 4156-4159.
[74] D.K. Panda, K. Maity, A. Palukoshka, F. Ibrahim, S. Saha, Li⁺ Ion-Conducting Sulfonate-Based Neutral Metal–Organic Framework, ACS Sustain. Chem. Eng. 7 (2019) 4619-4624.
[75] A. Romieu, D. Tavernier-Lohr, S. Pellet-Rostaing, M. Lemaire, P.-Y. Renard, Water solubilization of xanthene dyes by post-synthetic sulfonation in organic media, Tetrahedron Lett. 51 (2010) 3304-3308.
[76] P. Thuéry, Molecular and Polymeric Uranyl and Thorium Complexes with Sulfonate-Containing Ligands, Eur. J. Inorg. Chem. 2014 (2013) 58-68.
[77] R. Moi, A. Ghorai, S. Banerjee, K. Biradha, Amino and Sulfonate Functionalized Metal-Organic Framework for Fabrication of Proton Exchange Membranes with Improved Proton Conductivity, Crystal Growth & Design 20 (2020) 5557-5563.
[78] S.S. Liu, Z. Han, J.S. Yang, S.Z. Huang, X.Y. Dong, S.Q. Zang, Sulfonic Groups Lined along Channels of Metal-Organic Frameworks (MOFs) for Super-Proton Conductor, Inorg. Chem. 59 (2020) 396-402.
[79] Z. Li, G. He, Y. Zhao, Y. Cao, H. Wu, Y. Li, Z. Jiang, Enhanced proton conductivity of proton exchange membranes by incorporating sulfonated metal-organic frameworks, J. Power Sources 262 (2014) 372-379.
[80] Y. Peng, G. Xu, Z. Hu, Y. Cheng, C. Chi, D. Yuan, H. Cheng, D. Zhao, Mechanoassisted Synthesis of Sulfonated Covalent Organic Frameworks with High Intrinsic Proton Conductivity, Acs Appl. Mater. Interfaces (2016) 18505-18512.
[81] Fang, Guo, Hong-lin, Li, Lei, Li, Hong-cui, Yu, Na, Lu, Structure and inclusion property of supramolecular host framework [H₂ L1][XCl₄], L1 = N,N,N′,N′-tetra-p-methoxybenzyl-ethylenediamine; X = Fe, Co, Pd, Struct. Chem. 24 (2013) 1111-1119.
[82] R. Moi, A. Ghorai, S. Banerjee, K. Biradha, Amino- and Sulfonate-Functionalized Metal–Organic Framework for Fabrication of Proton Exchange Membranes with Improved Proton Conductivity, Cryst. Growth Des. 20 (2020) 5557-5563.
[83] X. Meng, S.Y. Song, X.Z. Song, M. Zhu, S.N. Zhao, L.L. Wu, H.J. Zhang, A tetranuclear copper cluster-based MOF with sulfonate-carboxylate ligands exhibiting high proton conduction properties, Chem Commun (Camb) 51 (2015) 8150-8152.
[84] M. Wahiduzzaman, S. Wang, J. Schnee, A. Vimont, V. Ortiz, P.G. Yot, R. Retoux, M. Daturi, J.S. Lee, J.S. Chang, A High Proton Conductive Hydrogen-Sulfate Decorated Titanium Carboxylate MOF, ACS Sustain. Chem. Eng. 7 (2019) 5776-5783.
[85] A.B. Stambouli, E. Traversa, Fuel cells, an alternative to standard sources of energy, Renew. Sustain. Energy Rev. 6 (2002) 295-304.
[86] M. Dhimish, R.G. Vieira, G. Badran, Investigating the stability and degradation of hydrogen PEM fuel cell, Int. J. Hydrogen Energy. 46 (2021) 37017-37028.

[87] N.A. Mohd Nazrul Aman, A. Muchtar, M.R. Somalu, M.I. Rosli, N.A. Baharuddin, N.S. Kalib, A short review on the modeling of solid-oxide fuel cells by using computational fluid dynamics: assumptions and boundary conditions, Int. J. Integr. Eng. 10 (2018) 87-92.
[88] M. Shabani, H. Younesi, M. Pontié, A. Rahimpour, A.A. Zinatizadeh, A critical review on recent proton exchange membranes applied in microbial fuel cells for renewable energy recovery, J. Clean. Prod. 264 (2020) 121446.
[89] S.M. Rezaei Niya, M. Hoorfar, Study of proton exchange membrane fuel cells using electrochemical impedance spectroscopy technique – A review, J. Power Sources 240 (2013) 281-293.
[90] X. Chen, G. Li, Proton conductive Zr-based MOFs, Inorg. Chem. Front. 7 (2020) 3765-3784.
[91] N.A. Nazir, N. Kim, W.G. Iglesias, A. Jakli, T. Kyu, Conductive behaviour in relation to Domain Morphology and Phase Diagram of Nafion/Poly(vinylidene co triflouoroethylene) Blends, Polymer 53 (2011) 196-204.
[92] N.A. Nazir, N. Kim, W.G. Iglesias, A. Jakli, T. Kyu, Conductive behavior in relation to domain morphology and phase diagram of Nafion/poly(vinylidene-co-trifluoroethylene) blends, Polymer 53 (2012) 196-204.
[93] R. Tian, J. Sun, J. Wang, Study on behavior of plasma nitrided 316L in PEMFC working conditions, Int. J. Hydrogen Energy 33 (2008) 7507-7512.
[94] C. Laberty-Robert, K. Valle, F. Pereira, C. Sanchez, Design and properties of functional hybrid organic-inorganic membranes for fuel cells, Chem. Soc. Rev. 40 (2011) 961-1005.
[95] Z.C. Guo, Z.Q. Shi, X.Y. Wang, Z.F. Li, G. Li, Proton conductive covalent organic frameworks, Coord. Chem. Rev. 422 (2020) 213465.
[96] B. Zhou, J.B. Le, Z. Cheng, X. Zhao, H. Chen, A Simple Transformation of Covalent Organic Frameworks to Highly Proton Conductive Electrolytes, ACS Appl. Mater. Interfaces 12 (2020) 8198-8205.
[97] F. Yang, G. Xu, Y. Dou, B. Wang, H. Zhang, H. Wu, W. Zhou, J.-R. Li, B. Chen, A flexible metal–organic framework with a high density of sulfonic acid sites for proton conduction, Nat. Energy 2 (2017) 877-883.
[98] L. Fu, N.A. Hashim, Y. Liu, M. Abed, K. Li, Progress in the production and modification of PVDF membranes, J. Membrane. Sci. 375 (2011) 1-27.
[99] Y. Zhang, J. Li, L. Ma, W. Cai, H. Cheng, Recent Developments on Alternative Proton Exchange Membranes: Strategies for Systematic Performance Improvement, Energy Technol. 3 (2015) 675-691.
[100] C. Wu, S. Lu, H. Wang, X. Xu, S. Peng, Q. Tan, Y. Xiang, A novel polysulfone–polyvinylpyrrolidone membrane with superior proton-to-vanadium ion selectivity for vanadium redox flow batteries, J. Mater. Chem. A 4 (2016) 1174-1179.
[101] L.-Y. Zhu, Y.-C. Li, J. Liu, J. He, L.-Y. Wang, J.-D. Lei, Recent developments in high-performance Nafion membranes for hydrogen fuel cells applications, Pet. Sci. 19 (2022) 1371-1381.
[102] F. Yang, H. Huang, X. Wang, F. Li, J.R. Li, Proton Conductivities in Functionalized UiO-66: Tuned Properties, Thermogravimetry Mass, and Molecular Simulation Analyses, Cryst. Growth Des. 15 (2015) 5827-5833.
[103] J.H. Cavka, S. Jakobsen, U. Olsbye, N. Guillou, K.P. Lillerud, A New Zirconium Inorganic Building Brick Forming Metal Organic Frameworks with Exceptional Stability, J. Am. Chem. Soc. 130 (2008) 13850-13851.

[104] F. Yang, H. Huang, X. Wang, F. Li, J.R. Li, Proton Conductivities in Functionalized UiO-66: Tuned Properties, Thermogravimetry Mass, and Molecular Simulation Analyses, Crystal Growth & Design 15 (2015) 5827-5833.
[105] X.-M. Li, L.-Z. Dong, S.-L. Li, G. Xu, J. Liu, F.-M. Zhang, L.-S. Lu, Y.-Q. Lan, Synergistic Conductivity Effect in a Proton Sources-Coupled Metal–Organic Framework, ACS Energy Lett. 2 (2017) 2313-2318.
[106] Q. Ren, J.-W. Yu, H.-B. Luo, J. Zhang, L. Wang, X.-M. Ren, Design and Preparation of a Superior Proton Conductor by Confining Tetraethylenepentamine in the Pores of ZIF-8 To Induce Further Adsorption of Water and Carbon Dioxide, Inorg. Chem. 58 (2019) 14693-14700.
[107] Y.J. Song, Y.L. Sang, K.Y. Xu, H.L. Hu, Q.Q. Zhu, G. Li, Ligand-Functionalized MIL-68-type Indium(III) Metal-Organic Frameworks with Prominent Intrinsic Proton Conductivity, Inorg. Chem. 63 (2024) 4233-4248.
[108] M. Szufla, A. Krawczuk, G. Jajko, P. Kozyra, D. Matoga, Flattening of a Bent Sulfonated MOF Linker: Impact on Structures, Flexibility, Gas Adsorption, CO(2)/N(2) Selectivity, and Proton Conduction, Inorg. Chem. 63 (2024) 151-162.
[109] L.X. Xie, Z.J. Ye, X.D. Zhang, G. Li, Two stable phenyl acyl thiourea carboxylate-based MOFs: Syntheses, crystal structures and proton conductive properties, J. Solid State Chem. 311 (2022) 123154.
[110] Z. Guo, Y. Zhang, J. Liu, B. Han, G. Li, Two imidazole multicarboxylate-based MOFs: syntheses, structures and proton conductive properties, New J. Chem. 45 (2021) 16971-16977.
[111] Y.L. Hong, S.W. Zuo, H.Y. Du, Z.Q. Shi, H. Hu, G. Li, Four Lanthanide(III) Metal-Organic Frameworks Fabricated by Bithiophene Dicarboxylate for High Inherent Proton Conduction, ACS Appl. Mater. Interfaces 16 (2024) 13745-13755.
[112] E.J. Mapes, M.F. Schumaker, Framework Models of Ion Permeation Through Membrane Channels and the Generalized King–Altman Method, Bull. Math. Biol. 68 (2006) 1429-1460.
[113] K. Kreuer, A. Rabenau, W. Weppner, Vehicle Mechanism, A New Model for the Interpretation of the Conductivity of Fast Proton Conductors, Angew Chem. Int. Ed. Engl. 21 (1982) 208-209.
[114] E.J. Mapes, M.F. Schumaker, Framework Models of Ion Permeation Through Membrane Channels and the Generalized King–Altman Method, Bulletin of Mathematical Biology 68 (2006) 1429-1460.
[115] D.I. Kolokolov, D.W. Lim, H. Kitagawa, Characterization of Proton Dynamics for the Understanding of Conduction Mechanism in Proton Conductive Metal-Organic Frameworks, Chem. Rec. 20 (2020) 1297-1313.
[116] J. Escorihuela, R. Narducci, V. Compa, F. Costantino, Proton Conductivity of Composite Polyelectrolyte Membranes with Metal-Organic Frameworks for Fuel Cell Applications, Adv. Mater. Interfaces 6 (2019) 1801146.
[117] Y. Oshiba, J. Tomatsu, T. Yamaguchi, Thin pore-filling membrane with highly packed-acid structure for high temperature and low humidity operating polymer electrolyte fuel cells, J. Power Sources 394 (2018) 67-73.
[118] I. Popov, Z. Zhu, A.R. Young-Gonzales, R.L. Sacci, E. Mamontov, C. Gainaru, S.J. Paddison, A.P. Sokolov, Search for a Grotthuss mechanism through the observation of proton transfer, Commun. Chem. 6 (2023) 77.
[119] S. Paddison, Proton conduction mechanisms at low degrees of hydration in sulfonic acid–based polymer electrolyte membranes, Annu. Rev. Mater. Res. 33 (2003) 289-319.

[120] K. Kreuer, On the complexity of proton conduction phenomena, Solid State Ion. 136 (2000) 149-160.
[121] H. Xu, S. Tao, D. Jiang, Proton conduction in crystalline and porous covalent organic frameworks, Nat. Mater. 15 (2016) 722-726.
[122] D.-W. Lim, H. Kitagawa, Proton transport in metal–organic frameworks, Chem. Rev. 120 (2020) 8416-8467.
[123] V. Chernikova, O. Shekhah, M. Eddaoudi, Advanced Fabrication Method for the Preparation of MOF Thin Films: Liquid-Phase Epitaxy Approach Meets Spin Coating Method, ACS Appl. Mater. Inter. 8 (2016) 20459-20464.
[124] B.H.J. Zhang J, Ren Q, Luo H-B, Ren X M, Tian Z F, , Extra Water- and Acid-Stable MOF-801 with High Proton Conductivity and Its Composite Membrane for Proton-Exchange Membrane, ACS Appl. Mater. Inter. 10 (2018) 28656–28663.
[125] Y. Zhou, S. Liu, X. Hu, Y. Ge, C. Shi, H. Wu, T. Zhou, Z. Li, J. Qiao, Facilitating the proton conductivity of polyvinyl alcohol based proton exchange membrane by phytic acid encapsulated Zn-azolate MOF, Process Saf. Environ. Prot. 172 (2023) 48-56.
[126] P. Li, Y. Chen, F. Xiao, M. Cao, J. Pan, J. Zheng, H. Li, K. Zhao, X. Zhang, Y. Zhang, Efficient proton exchange membranes based on bifunctional metal–organic frameworks, J. Mater. Sci. 58 (2023) 14154-14176.
[127] Z. Rao, B. Tang, P. Wu, Proton Conductivity of Proton Exchange Membrane Synergistically Promoted by Different Functionalized Metal-Organic Frameworks, ACS Appl. Mater. Inter. 9 (2017) 22597-22603.
[128] H. Wang, Y. Zhao, Z. Shao, W. Xu, Q. Wu, X. Ding, H. Hou, Proton Conduction of Nafion Hybrid Membranes Promoted by NH(3)-Modified Zn-MOF with Host-Guest Collaborative Hydrogen Bonds for H(2)/O(2) Fuel Cell Applications, ACS Appl. Mater. Inter. 13 (2021) 7485-7497.
[129] X. Li, D. Zhang, S. Chen, Y. Geng, Y. Liu, L. Qian, X. Chen, J. Li, P. Fang, C. He, Outstanding proton conductivity over wide temperature and humidity ranges and enhanced mechanical, thermal stabilities for surface-modified MIL-101-Cr-NH_2/Nafion composite membranes, Green Energy Environ. 9 (2024) 1734-1746.
[130] H.B. Luo, M. Wang, S.X. Liu, C. Xue, Z.F. Tian, Y. Zou, X.M. Ren, Proton Conductance of a Superior Water-Stable Metal–Organic Framework and Its Composite Membrane with Poly(vinylidene fluoride), Inorg. Chem. 56 (2017) 4169-4175.
[131] Jorge, Escorihuela, óscar, Sahuquillo, Abel, García-Bernabé, Enrique, Giménez, Vicente, Compa, Phosphoric Acid Doped Polybenzimidazole (PBI)/Zeolitic Imidazolate Framework Composite Membranes with Significantly Enhanced Proton Conductivity under Low Humidity Conditions, Nanomater. 8 (2018) 775.
[132] Y. Guo, Z. Jiang, W. Ying, L. Chen, Y. Liu, X. Wang, Z.J. Jiang, B. Chen, X. Peng, A DNA-threaded ZIF-8 membrane with high proton conductivity and low methanol permeability, Adv. Mater. 30 (2018) 1705155.
[133] Jin, Zhang, Huijuan, Bai, Qiu, Ren, Hong-Bin, Luo, Xiaoming, Zheng-Fang, Extra water- and acid-stable MOF-801 with high proton conductivity and its composite membrane for proton exchange membrane, ACS Appl. Mater. Inter. 10 (2018) 28656-28663.
[134] Y.-L. Bao, J.-Y. Zheng, H.-P. Zheng, G.-D. Qi, J.-R. An, Y.-P. Wu, Y.-L. Liu, W.-W. Dong, J. Zhao, D.-S. Li, Cu-MOF@ PVP/PVDF hybrid composites as tunable proton-conducting materials, J. Solid State Chem. 310 (2022) 123070.
[135] T. Wen, Z. Shao, H. Wang, Y. Zhao, Y. Cui, H. Hou, Enhancement of Proton Conductivity in Fe-Metal–Organic Frameworks by Postsynthetic Oxidation and

High-Performance Hybrid Membranes with Low Acidity, Inorg. Chem. 60 (2021) 18889-18898.
[136] F. Zhang, T. Zhang, X. Zou, X. Liang, G. Zhu, F. Qu, Electrochemical synthesis of metal organic framework films with proton conductive property, Solid State Ionics 301 (2017) 125-132.
[137] A. Donnadio, R. Narducci, M. Casciola, F. Marmottini, R. D'Amato, M. Jazestani, H. Chiniforoshan, F. Costantino, Mixed Membrane Matrices Based on Nafion/UiO-66/SO_3H-UiO-66 Nano-MOFs: Revealing the Effect of Crystal Size, Sulfonation, and Filler Loading on the Mechanical and Conductivity Properties, ACS Appl. Mater. Inter. 9 (2017) 42239-42246.
[138] F. Ciucci, Modeling electrochemical impedance spectroscopy, Curr. Opin. Electroche. 13 (2019) 132-139.
[139] A.C. Lazanas, M.I. Prodromidis, Electrochemical Impedance Spectroscopy-A Tutorial, ACS Meas. Sci. Au 3 (2023) 162-193.
[140] C. Sun, X. Li, Z. Cai, F. Ge, Carbonized cotton fabric in-situ electrodeposition polypyrrole as high-performance flexible electrode for wearable supercapacitor, Electrochim. Acta 296 (2019) 617-626.
[141] M. Mamlouk, P. Ocon, K. Scott, Preparation and characterization of polybenzimidzaole/diethylamine hydrogen sulphate for medium temperature proton exchange membrane fuel cells, J. Power Sources 245 (2014) 915-926.
[142] S.N. Tambat, P.K. Sane, S. Suresh, N. Varadan O, A.B. Pandit, S.M. Sontakke, Hydrothermal synthesis of NH_2-UiO-66 and its application for adsorptive removal of dye, Adv. Powder Technol. 29 (2018) 2626-2632.
[143] C.G. Lin, W. Zhou, X.T. Xiong, W. Xuan, P.J. Kitson, D.L. Long, W. Chen, Y.F. Song, L. Cronin, Digital Control of Multistep Hydrothermal Synthesis by Using 3D Printed Reactionware for the Synthesis of Metal-Organic Frameworks, Angew. Chem. Int. Ed. 57 (2018) 16716-16720.
[144] B. Zhang, Y. Luo, K. Kanyuck, N. Saenz, K. Reed, P. Zavalij, J. Mowery, G. Bauchan, Facile and template-free solvothermal synthesis of mesoporous/macroporous metal–organic framework nanosheets, RSC Adv. 8 (2018) 33059-33064.
[145] L.A. Lozano, C.M. Iglesias, B.M.C. Faroldi, M.A. Ulla, J.M. Zamaro, Efficient solvothermal synthesis of highly porous UiO-66 nanocrystals in dimethylformamide-free media, J. Mater. Sci. 53 (2017) 1862-1873.
[146] K. Kamal, M.A. Bustam, M. Ismail, D. Grekov, A. Mohd Shariff, P. Pre, Optimization of Washing Processes in Solvothermal Synthesis of Nickel-Based MOF-74, Materials 13 (2020) 2741.
[147] A.R. Abbasi, M. Rizvandi, Influence of the ultrasound-assisted synthesis of Cu-BTC metal-organic frameworks nanoparticles on uptake and release properties of rifampicin, Ultrason. Sonochem. 40 (2018) 465-471.
[148] A. Bakhshi, H. Saravani, G. Sargazi, M. Shahbakhsh, Ultrasound-assisted efficient synthesis of a novel Nd–MOF polymer as a new candidate for electrocatalytic activity in hydrogen storage, J. Appl. Electrochem. 51 (2020) 399-410.
[149] C. Forsyth, T. Taras, A. Johnson, J. Zagari, C. Collado, M.M. Hoffmann, C.R. Reed, Microwave Assisted Surfactant-Thermal Synthesis of Metal-Organic Framework Materials, Appl. Sci. 10 (2020) 4563.
[150] A. Laybourn, J. Katrib, R.S. Ferrari-John, C.G. Morris, S. Yang, O. Udoudo, T.L. Easun, C. Dodds, N.R. Champness, S.W. Kingman, Metal–organic

frameworks in seconds via selective microwave heating, J. Mater. Chem. A 5 (2017) 7333-7338.
[151] I. Thomas Hillman, L.A. Stevens, M. Lange, J. Mllmer, W. Lewis, C. Dodds, S.W. Kingman, A. Laybourn, Developing a sustainable route to environmentally relevant metal–organic frameworks: ultra-rapid synthesis of MFM-300(Al) using microwave heating, Green Chem. 21 (2019) 5039-5045.
[152] D. Rambabu, S. Bhattacharyya, T. Singh, L.C. M, T.K. Maji, Stabilization of $MAPbBr_3$ Perovskite Quantum Dots on Perovskite MOFs by a One-Step Mechanochemical Synthesis, Inorg. Chem. 59 (2020) 1436-1443.
[153] J. Yang, X. Feng, G. Lu, Y. Li, C. Mao, Z. Wen, W. Yuan, NaCl as a solid solvent to assist the mechanochemical synthesis and post-synthesis of hierarchical porous MOFs with high I_2 vapour uptake, Dalton T. 47 (2018) 5065-5071.
[154] X. Lv, P. Sullivan, D. Feng, MOFs the movie: Molecule to nuclei evolution during metal-organic framework formation, Matter 5 (2022) 11-13.
[155] M.J. Van Vleet, T. Weng, X. Li, J. Schmidt, In situ, time-resolved, and mechanistic studies of metal–organic framework nucleation and growth, Chem. rev. 118 (2018) 3681-3721.
[156] R. Wu, Y. Li, A. Huang, Synthesis of high-performance Co-based ZIF-67 membrane for H2 separation by using cobalt ions chelated PIM-1 as interface layer, J. Membr. Sci. 620 (2020) 118841.
[157] B. Seoane, S. Castellanos, A. Dikhtiarenko, F. Kapteijn, J. Gascon, Multi-scale crystal engineering of metal organic frameworks, Coord. Chem. Rev. 307 (2016) 147-187.
[158] I.E. Khalil, J. Fonseca, M.R. Reithofer, T. Eder, J.M. Chin, Tackling orientation of metal-organic frameworks (MOFs): The quest to enhance MOF performance, Coord. Chem. Rev. 481 (2023) 215043.
[159] Y. Yuan, B. Sun, A.M. Cao, D. Wang, L.J. Wan, Heterogeneous nucleation and growth of highly crystalline imine-linked covalent organic frameworks, Chem. Comm. 47 (2018) 5976-5979.
[160] Z. Gu, L. Chen, B. Duan, Q. Luo, C. Duan, Synthesis of Au@UiO-66(NH_2) structures by small molecule-assisted nucleation for plasmon-enhanced photocatalytic activity, Chemi. Comm. 52 (2015) 116.
[161] J.A. Thompson, K.W. Chapman, W.J. Koros, C.W. Jones, S. Nair, Sonication-induced Ostwald ripening of ZIF-8 nanoparticles and formation of ZIF-8/polymer composite membranes, Micropor. Mesopor. Mat. 158 (2012) 292-299.
[162] Jian, Meipeng, Wang, Huanting, Liu, Bao, Jiuhui, Zhang, Xiwang, Ruiping, Water-based synthesis of zeolitic imidazolate framework-8 with high morphology level at room temperature, RSC Adv. 5 (2015) 48433.
[163] R.M. Guerrero, I.D. Lemir, S. Carrasco, C. Fernandez-Ruiz, S. Kavak, P. Pizarro, D.P. Serrano, S. Bals, P. Horcajada, Y. Perez, Scaling-Up Microwave-Assisted Synthesis of Highly Defective Pd@UiO-66-NH_2 Catalysts for Selective Olefin Hydrogenation under Ambient Conditions, ACS Appl. Mater. Interfaces 16 (2024) 24108-24121.
[164] A. Polyzoidis, T. Altenburg, M. Schwarzer, S. Loebbecke, S. Kaskel, Continuous microreactor synthesis of ZIF-8 with high space–time-yield and tunable particle size, Chem. Eng. J. 283 (2016) 971-977.
[165] I. Pakamor, J. Rousseau, C. Rousseau, E. Monflier, P.g. Szilágyi, An ambient-temperature aqueous synthesis of zirconium-based metal–organic frameworks, Green Chem. 20 (2018) 5292.

[166] R.-B. Lin, S. Xiang, W. Zhou, B. Chen, Microporous Metal-Organic Framework Materials for Gas Separation, Chem 6 (2020) 337-363.
[167] C. Vaitsis, G. Sourkouni, C. Argirusis, Metal Organic Frameworks (MOFs) and ultrasound: A review, Ultrason. Sonochem. 52 (2019) 106-119.
[168] D.S. Karousos, K.I. Desdenakis, P.M. Sakkas, G. Sourkouni, B.G. Pollet, C. Argirusis, Sonoelectrochemical one-pot synthesis of Pt - Carbon black nanocomposite PEMFC electrocatalyst, Ultra. Sonochem. 35 (2017) 591-597.
[169] V. Safarifard, A. Morsali, Applications of ultrasound to the synthesis of nanoscale metal–organic coordination polymers, Coord. Chem. Rev. 292 (2015) 1-14.
[170] A. Dastbaz, J. Karimi-Sabet, M.A. Moosavian, Sonochemical synthesis of novel decorated graphene nanosheets with amine functional Cu-terephthalate MOF for hydrogen adsorption: Effect of ultrasound and graphene content, International Journal of Hydrogen Energy 44 (2019) 26444-26458.
[171] B. Pollet, The Use of Power Ultrasound for the Production of PEMFC and PEMWE Catalysts and Low-Pt Loading and High-Performing Electrodes, Catalysts 9 (2019) 246.
[172] K.Y. A, Y.R.L. B, J.Y.S. B, K.Y.B. B, Y.M.C. C, W.S.A. A, Sonochemical synthesis of Zr-based porphyrinic MOF-525 and MOF-545: Enhancement in catalytic and adsorption properties, Micropor. Mesopor. Mat. 316 (2021) 110985.
[173] G. Sargazi, D. Afzali, N. Daldosso, H. Kazemian, N.P.S. Chauhan, Z. Sadeghian, T. Tajerian, A. Ghafarinazari, M. Mozafari, A systematic study on the use of ultrasound energy for the synthesis of nickel-metal organic framework compounds, Ultrason. Sonochem. 27 (2015) 395-402.
[174] D. Peralta, G. Chaplais, A. Simon-Masseron, K. Barthelet, G.D. Pirngruber, Metal–Organic Framework Materials for Desulfurization by Adsorption, Energy Fuel. 26 (2012) 4953–4960.
[175] A. Abbasi, T. Moradpour, K. Van Hecke, A new 3D cobalt (II) metal–organic framework nanostructure for heavy metal adsorption, Inorganica Chimica Acta 430 (2015) 261-267.
[176] D. Aulakh, J.R. Varghese, M. Wriedt, The importance of polymorphism in metal–organic framework studies, Inorgan. Chem. 54 (2015) 8679-8684.
[177] K.M. Steed, J.W. Steed, Packing problems: high Z′ crystal structures and their relationship to cocrystals, inclusion compounds, and polymorphism, Chem. Rev. 115 (2015) 2895-2933.
[178] G. Cravotto, P. Cintas, Power ultrasound in organic synthesis: moving cavitational chemistry from academia to innovative and large-scale applications, Chem. Soc. Rev. 35 (2006) 180-196.
[179] W. Abdussalam-Mohammed, A.Q. Ali, A. Errayes, Green chemistry: principles, applications, and disadvantages, Chem. Methodol. 4 (2020) 408-423.
[180] C. Blum, D. Bunke, M. Hungsberg, E. Roelofs, A. Joas, R. Joas, M. Blepp, H.-C. Stolzenberg, The concept of sustainable chemistry: Key drivers for the transition towards sustainable development, Sustain. Chem. Pharm. 5 (2017) 94-104.
[181] S. Yuan, W. Lu, Y.P. Chen, Q. Zhang, T.F. Liu, D. Feng, W. Xuan, J. Qin, H.C. Zhou, Sequential Linker Installation: Precise Placement of Functional Groups in Multivariate Metal–Organic Frameworks, J. Am. Chem. Soc. 137 (2015) 3177-3180.
[182] P. Horcajada, S. Surble, C. Serre, D.Y. Hong, Y.K. Seo, J.S. Chang, J.M. Greneche, I. Margiolaki, G. Ferey, Synthesis and catalytic properties of MIL-

100(Fe), an iron(III) carboxylate with large pores, Chem. Comm. 27 (2007) 2820-2822.
[183] D.W. Lynch, M.E. Placke, R.L. Persing, M.J. Ryan, Thirteen-Week Inhalation Toxicity of N,N-Dimethylformamide in F344/N Rats and B6C3F1 Mice, Toxicol. Sci. 72 (2003) 347-358.
[184] C. James, F. Thomas, H. Andrew, S. James, Opportunities for Bio-Based Solvents Created as Petrochemical and Fuel Products Transition towards Renewable Resources, Int. J. Mol. Sci. 16 (2015) 17101-17159.
[185] S.L. James, C.J. Adams, C. Bolm, D. Braga, P. Collier, T. Fri??I?, F. Grepioni, K. Harris, G. Hyett, W. Jones, Mechanochemistry: opportunities for new and cleaner synthesis, Chem. Soc. Rev. 41 (2011) 413-447.
[186] J. Hungerford, K.S. Walton, Room-Temperature Synthesis of Metal-Organic Framework Isomers in the Tetragonal and Kagome Crystal Structure, Inorg. Chem. 58 (2019) 7690-7697.
[187] H. Song, X. Li, B. Jiang, M. Gong, T. Hao, Preparation of Novel and Highly Stable Py/MOF and Its Adsorptive Desulfurization Performance, Ind. Eng. Chem. Res. 58 (2019) 19586-19598.
[188] Ramos-Fernandez, V. E., Grau-Atienza, A., Farrusseng, D., Aguado, S., A water-based room temperature synthesis of ZIF-93 for CO_2 adsorption, J. Mater. Chem. A 6 (2018) 5598-5602.
[189] L.B. Jian M, Liu R, Qu J, Wang H, Zhang X, Water-based synthesis of zeolitic imidazolate framework-8 with high morphology level at room temperature, RSC Adv. 5 (2015) 48433-48441.
[190] X. Sang, J. Zhang, J. Xiang, J. Cui, L. Zheng, J. Zhang, Z. Wu, Z. Li, G. Mo, Y. Xu, Ionic liquid accelerates the crystallization of Zr-based metal–organic frameworks, Nat. Commun. 8 (2017) 175.
[191] A. Manz, J. Fettinger, E. Verpoorte, H. Lüdi, D.J. Harrison, Micromachining of monocrystalline silicon and glass for chemical analysis systems A look into next century's technology or just a fashionable craze?, Trac-Trend. Anal. Chem. 10 (2015) 144-149.
[192] D.R. Reyes, D. Iossifidis, P.A. Auroux, A. Manz, Micro total analysis systems. 1. Introduction, theory, and technology, Anal. Chem. 74 (2002) 2623-2636.
[193] C.T. Kung, H.Y. Gao, C.Y. Lee, Y.N. Wang, W.J. Dong, C.H. Ko, G. Wang, L.M. Fu, Microfluidic synthesis control technology and its application in drug delivery, bioimaging, biosensing, environmental analysis and cell analysis, Chem. Eng. J. 399 (2020) 125748.
[194] J. Wang, Y. Song, Microfluidic Synthesis of Nanohybrids, Small 13 (2017) 1604084.
[195] I. Rossetti, M. Compagnoni, Chemical reaction engineering, process design and scale-up issues at the frontier of synthesis: Flow chemistry, Chem. Eng. J. 296 (2016) 56-70.
[196] O. Długosz, M. Banach, Inorganic nanoparticle synthesis in flow reactors – applications and future directions, React. Chem. Eng. 5 (2020) 1619-1641.
[197] S.A. Khan, S. Duraiswamy, Controlling bubbles using bubbles--microfluidic synthesis of ultra-small gold nanocrystals with gas-evolving reducing agents, Lab Chip 12 (2012) 1807-1812.
[198] L.L. Lazarus, C.T. Riche, B.C. Marin, M. Gupta, N. Malmstadt, R.L. Brutchey, Two-phase microfluidic droplet flows of ionic liquids for the synthesis of gold and silver nanoparticles, ACS Appl. Mater. Interfaces 4 (2012) 3077-3083.

[199] J. Cui, N. Gao, X. Yin, W. Zhang, Y. Liang, L. Tian, K. Zhou, S. Wang, G. Li, Microfluidic synthesis of uniform single-crystalline MOF microcubes with a hierarchical porous structure, Nanoscale 10 (2018) 9192-9198.
[200] C. Echaide-Górriz, C. Clément, F. Cacho-Bailo, C. Téllez, J. Coronas, New strategies based on microfluidics for the synthesis of metal–organic frameworks and their membranes, J. Mater. Chem. A 6 (2018) 5485-5506.
[201] N. Hao, Y. Nie, J.X.J. Zhang, Microfluidic synthesis of functional inorganic micro-/nanoparticles and applications in biomedical engineering, Int. Mater. Rev. 63 (2018) 461-487.
[202] X. Wang, J. Liu, P. Wang, A. deMello, L. Feng, X. Zhu, W. Wen, R. Kodzius, X. Gong, Synthesis of Biomaterials Utilizing Microfluidic Technology, Genes (Basel) 9 (2018) 283.
[203] O.M. Yaghi, H. Li, Hydrothermal Synthesis of a Metal-Organic Framework Containing Large Rectangular Channels, J. Am. Chem. Soc. 117 (1995) 10401-10402.
[204] A. Ghosh, G. Das, Green synthesis of Sn(II)-BDC MOF: Preferential and efficient adsorption of anionic dyes, Micropor. Mesopor. Mat. 297 (2020) 110039.
[205] Y.-R. Lee, M.-S. Jang, H.-Y. Cho, H.-J. Kwon, S. Kim, W.-S. Ahn, ZIF-8: A comparison of synthesis methods, Chem. Eng. J. 271 (2015) 276-280.
[206] V.V. Butova, A.P. Budnik, E.A. Bulanova, A.V. Soldatov, New microwave-assisted synthesis of ZIF-8, Mendeleev Commun. 1 (2016) 43-44.
[207] L. Hu, L. Chen, Y. Fang, A. Wang, C. Chen, Z. Yan, Facile synthesis of zeolitic imidazolate framework-8 (ZIF-8) by forming imidazole-based deep eutectic solvent, Micropor. Mesopor. Mat. 268 (2018) 207-215.
[208] R. Munirathinam, J. Huskens, W. Verboom, Supported Catalysis in Continuous-Flow Microreactors, Adv. Synth. Catal. 357 (2015) 1093-1123.
[209] Y.J. Wu, G. Thierry, K. Strijkers, D. Hermans, R.D. Kentalis, G. Thierry, Micromixers - a review, J. Micromech. Microeng. 15 (2005) 1-16.
[210] S.Y. Yang, F.Y. Cheng, C.S. Yeh, G.B. Lee, Size-controlled synthesis of gold nanoparticles using a micro-mixing system, Microfluid. Nanofluidics 8 (2010) 303-311.
[211] C. Sun, M. Barton, C.M. Pask, M. Edokali, L. Yang, A.J. Britton, S. Micklethwaite, F. Iacoviello, A. Hassanpour, M. Besenhard, R. Drummond-Brydson, K.-J. Wu, S.M. Collins, Droplet-based millifluidic synthesis of a proton-conducting sulfonate metal–organic framework, Chem. Eng. J. 474 (2023) 145892.
[212] M.O. Besenhard, S. Pal, G. Gkogkos, Non-fouling flow reactors for nanomaterial synthesis, React. Chem. Eng. 8 (2023) 955-977.
[213] X. Yao, Y. Zhang, L. Du, J. Liu, J. Yao, Review of the applications of microreactors, Renew. Sustain. Energy Rev. 47 (2015) 519-539.
[214] N.D. Mas, A. Gu?Nther, M.A. Schmidt, K.F. Jensen, Increasing Productivity of Microreactors for Fast GasLiquid Reactions: The Case of Direct Fluorination of Toluene, Ind. Eng. Chem. Res. 48 (2009) 1428-1434.
[215] R.L. Hartman, K.F. Jensen, Microchemical systems for continuous-flow synthesis, Lab Chip. 9 (2009) 2495-2507.
[216] J. Ma, S.M.-Y. Lee, C. Yi, C.-W. Li, Controllable synthesis of functional nanoparticles by microfluidic platforms for biomedical applications–a review, Lab Chip 17 (2017) 209-226.
[217] G. Niu, A. Ruditskiy, M. Vara, Y. Xia, Toward continuous and scalable production of colloidal nanocrystals by switching from batch to droplet reactors, Chem. Soc. Rev. 44 (2015) 5806-5820.

[218] S. Duraiswamy, S.A. Khan, Droplet-based microfluidic synthesis of anisotropic metal nanocrystals, Small 5 (2009) 2828-2834.
[219] P. Karandikar, M. Gupta, Synthesis of functional particles by condensation and polymerization of monomer droplets in silicone oils, Langmuir 33 (2017) 7701-7707.
[220] A. Pohar, I. Plazl, P. Žnidaršič–Plazl, Lipase-catalyzed synthesis of isoamyl acetate in an ionic liquid/n–heptane two-phase system at the microreactor scale, Lab Chip 9 (2009) 3385-3390.
[221] Y. Wang, L. Li, H. Liang, Y. Xing, L. Yan, P. Dai, X. Gu, G. Zhao, X. Zhao, Superstructure of a metal–organic framework derived from microdroplet flow reaction: an intermediate state of crystallization by particle attachment, Acs Nano 13 (2019) 2901-2912.
[222] Y. Wang, L. Li, L. Yan, L. Cao, P. Dai, X. Gu, X. Zhao, Continuous synthesis for zirconium metal-organic frameworks with high quality and productivity via microdroplet flow reaction, Chinese Chem. Lett. 29 (2018) 849-853.
[223] Z. Wu, Z. Cao, B. Sunden, Flow patterns and slug scaling of liquid-liquid flow in square microchannels, Int. J. Multiph. Flow 112 (2019) 27-39.
[224] C.-X. Zhao, A.P. Middelberg, Two-phase microfluidic flows, Chem. Eng. Sci. 66 (2011) 1394-1411.
[225] M.T. Nechita, G.D. Suditu, A.C. Puițel, E.N. Drăgoi, Residence Time Distribution: Literature Survey, Functions, Mathematical Modeling, and Case Study—Diagnosis for a Photochemical Reactor, Processes 11 (2023) 3420.
[226] F. Liotta, P. Chatellier, G. Esposito, M. Fabbricino, E.D. Van Hullebusch, P.N. Lens, Hydrodynamic mathematical modelling of aerobic plug flow and nonideal flow reactors: a critical and historical review, Crit. Rev. Env. Sci. Tec. 44 (2014) 2642-2673.
[227] A. Towne, A. Lozano-Durán, X. Yang, Resolvent-based estimation of space–time flow statistics, J. Fluid Mech. 883 (2020) 17.
[228] T. Bailey, M. Pinto, N. Hondow, K.J. Wu, Continuous microfluidic synthesis of zirconium-based UiO-67 using a coiled flow invertor reactor, MethodsX 8 (2021) 101246.
[229] J.J. Carberry, Chemical reaction and reactor engineering, CRC Press2020.
[230] J.F. Holland, J.F. Martin, T. Granata, V. Bouchard, M. Quigley, L. Brown, Effects of wetland depth and flow rate on residence time distribution characteristics, Ecol. Eng. 23 (2004) 189-203.
[231] D.S. Raja, D.-H. Tsai, Recent Advances in Continuous Flow Synthesis of Metal-Organic Frameworks and Their Composites, Chem. Commun. 60 (2024) 8497-8515.
[232] L. Paseta, B. Seoane, D. Julve, V. Sebastian, C. Tellez, J. Coronas, Accelerating the controlled synthesis of metal-organic frameworks by a microfluidic approach: a nanoliter continuous reactor, ACS Appl. Mater. Inter. 5 (2013) 9405-9410.
[233] H. Reinsch, S. Waitschat, S.M. Chavan, K.P. Lillerud, N. Stock, A Facile "Green" Route for Scalable Batch Production and Continuous Synthesis of Zirconium MOFs, Eur. J. Inorg. Chem. 2016 (2016) 4490-4498.
[234] M. Faustini, J. Kim, G.Y. Jeong, J.Y. Kim, H.R. Moon, W.S. Ahn, D.P. Kim, Microfluidic approach toward continuous and ultrafast synthesis of metal-organic framework crystals and hetero structures in confined microdroplets, J. Am. Chem. Soc. 135 (2013) 14619-14626.

[235] E.G. Rasmussen, J. Kramlich, I.V. Novosselov, Scalable continuous flow metal–organic framework (MOF) synthesis using supercritical CO_2, ACS Sustainable Chem. Eng. 8 (2020) 9680-9689.
[236] C. Avci-Camur, J. Troyano, J. Pérez-Carvajal, A. Legrand, D. Farrusseng, I. Imaz, D. Maspoch, Aqueous production of spherical Zr-MOF beads via continuous-flow spray-drying, Green Chem. 20 (2018) 873-878.
[237] T. Bailey, L. Yang, E. Humphreys, F. Esat, B. Douglas, N. Hondow, The controlled microfluidic formation of stable mixed phase HCP/FCC-UiO-67 (Zr)-benzoic acid through modification of water concentration, J. Porous Mat. 31 (2024) 267-279.
[238] S. Kevat, V. Lad, Microfluidics-facilitated spontaneous synthesis of ZIF-67 metal–organic framework, Chem. Pap. 77 (2023) 6351-6363.
[239] H. Wu, C. Wu, W. Liao, B.M. Matsagar, K. Chang, J. Huang, K.C.W. Wu, Continuous and ultrafast MOF synthesis using droplet microfluidic nanoarchitectonics, J. Mater. Chem. A 11 (2023) 9427-9435.
[240] O. Kolmykov, J.M. Commenge, H. Alem, E. Girot, K. Mozet, G. Medjahdi, R. Schneider, Microfluidic reactors for the size-controlled synthesis of ZIF-8 crystals in aqueous phase, Mater. Des. 122 (2017) 31-41.
[241] Y.-H. Sung, C.-L. Wu, J.-H. Huang, D.-H. Tsai, Real-Time Quantifying Microdroplet Synthesis of Metal–Organic Framework Colloids Using Gas-Phase Electrophoresis, Anal. Chem. 95 (2023) 4513-4520.
[242] S. Chen, X. Zhou, G. Li, F. Yang, Controlled synthesis of metal-organic frameworks via AC electrokinetic mixing-assisted microfluidics: A case study of ZIF-8, Chem. Eng. J. 480 (2024) 148208.
[243] X. Yu, J. Andreo, M. Walden, J.F. Del Campo, L. Basabe-Desmonts, F. Benito-Lopez, T.P. Burg, S. Wuttke, The Importance of Dean Flow in Microfluidic Nanoparticle Synthesis: A ZIF-8 Case Study, Small Methods 8 (2024) 2300603.
[244] A. Zuliani, M. Carmen Castillejos, N. Khiar, Continuous flow synthesis of PCN-222 (MOF-545) with controlled size and morphology: a sustainable approach for efficient production, Green Chem. 25 (2023) 10596-10610.
[245] X. Ge, Z. Liu, N. Wei, X. Lin, C. Hu, Microfluidic Synthesis of Defective and Hierarchical Pore Zr Metal–Organic Framework Materials and CO_2 Adsorption Performance Study, Cryst. Growth Des. (2024).
[246] S. Wu, Z. Xin, S. Zhao, S. Sun, High-throughput droplet microfluidic synthesis of hierarchical metal-organic framework nanosheet microcapsules, Nano Res. 12 (2019) 2736-2742.
[247] Y. Wang, L. Li, L. Yan, X. Gu, P. Dai, D. Liu, J.G. Bell, G. Zhao, X. Zhao, K.M. Thomas, Bottom-up fabrication of ultrathin 2D Zr metal–organic framework nanosheets through a facile continuous microdroplet flow reaction, Chem. Mat. 30 (2018) 3048-3059.
[248] V.N. Le, H.T. Kwon, T.K. Vo, J.-H. Kim, W.-S. Kim, J. Kim, Microwave-assisted continuous flow synthesis of mesoporous metal-organic framework MIL-100 (Fe) and its application to Cu(I)-loaded adsorbent for CO/CO2 separation, Mater. Chem. Phys. 253 (2020) 123278.
[249] A. Polyzoidis, M. Schwarzer, S. Loebbecke, C.G. Piscopo, Continuous synthesis of UiO-66 in microreactor: Pursuing the optimum between intensified production and structural properties, Mater. Lett. 197 (2017) 213-216.
[250] N. Ko, J. Hong, S. Sung, K.E. Cordova, H.J. Park, J.K. Yang, J. Kim, A significant enhancement of water vapour uptake at low pressure by amine-functionalization of UiO-67, Dalton Trans. 44 (2015) 2047-2051.

[251] D.E. Crawford, S.L. James, T. McNally, Use of Batch Mixing To Investigate the Continuous Solvent-Free Mechanical Synthesis of OLED Materials by Twin-Screw Extrusion (TSE), ACS Sustainable Chem. Eng. 6 (2017) 193-201.
[252] D.E. Crawford, C.K. Miskimmin, A.B. Albadarin, G. Walker, S.L. James, Organic synthesis by Twin Screw Extrusion (TSE): continuous, scalable and solvent-free, Green Chem. 19 (2017) 1507-1518.
[253] Q. Cao, J.L. Howard, D.E. Crawford, S.L. James, D.L. Browne, Translating solid state organic synthesis from a mixer mill to a continuous twin screw extruder, Green Chem. 20 (2018) 4443-4447.
[254] D. Chen, J. Zhao, P. Zhang, S. Dai, Mechanochemical synthesis of metal–organic frameworks, Polyhedron 162 (2019) 59-64.
[255] S. Głowniak, B. Szczęśniak, J. Choma, M. Jaroniec, Mechanochemistry: Toward green synthesis of metal–organic frameworks, Materials Today 46 (2021) 109-124.
[256] E.M. Williamson, Z. Sun, L. Mora-Tamez, R.L. Brutchey, Design of Experiments for Nanocrystal Syntheses: A How-To Guide for Proper Implementation, Chem. Mater. 34 (2022) 9823-9835.
[257] D.D. Frey, F. Engelhardt, E.M. Greitzer, A role for "one-factor-at-a-time" experimentation in parameter design, Res. Eng. Des. 14 (2003) 65-74.
[258] F. Paulo, L. Santos, Design of experiments for microencapsulation applications: A review, Mater. Sci. Eng. C Mater. Biol. Appl. 77 (2017) 1327-1340.
[259] P. Elliott, S. Billingham, J. Bi, H. Zhang, Quality by design for biopharmaceuticals: a historical review and guide for implementation, Pharm. Bioprocess. 1 (2013) 105-122.
[260] M.R. Owen, C. Luscombe, Lai, S. Godbert, D.L. Crookes, D. Emiabata-Smith, Efficiency by Design: Optimisation in Process Research, Org. Process Res. Dev. 5 (2001) 308-323.
[261] D.W. Lendrem, B.C. Lendrem, D. Woods, R. Rowland-Jones, M. Burke, M. Chatfield, J.D. Isaacs, M.R. Owen, Lost in space: design of experiments and scientific exploration in a Hogarth Universe, Drug Discovery Today. 20 (2015) 1365-1371.
[262] Varinder, K., Aggarwal, Anne, C., Staubitz, Martin, Owen, Optimization of the Mizoroki−Heck Reaction Using Design of Experiment (DoE), Org.Process Res. Dev. 10 (2006) 64-69.
[263] C.J. Taylor, A. Pomberger, K.C. Felton, R. Grainger, M. Barecka, T.W. Chamberlain, R.A. Bourne, C.N. Johnson, A.A. Lapkin, A Brief Introduction to Chemical Reaction Optimization, Chem. Rev. 123 (2023) 3089-3126.
[264] N.R. Draper, Response surface methodology: Process and product optimization using designed experiments, J. Stat. Plan. Inference 59 (1997) 185–186.
[265] M.A. Bezerra, R.E. Santelli, E.P. Oliveira, L.S. Villar, L.A. Escaleira, Response surface methodology (RSM) as a tool for optimization in analytical chemistry, Talanta 76 (2008) 965-977.
[266] W. Sauerbrei, C. Meier-Hirmer, A. Benner, P. Royston, Multivariable regression model building by using fractional polynomials: description of SAS, STATA and R programs, Comput. Stat. Data Anal. 50 (2006) 3464-3485.
[267] C.M. Anderson-Cook, C.M. Borror, D.C. Montgomery, Response surface design evaluation and comparison, J. Stat. Plan. Inference 139 (2009) 629-641.
[268] Y. Davoodbeygi, A. Irankhah, Nanostructured Ce Cu mixed oxide synthesized by solid state reaction for medium temperature shift reaction: Optimization using response surface method, Int. J. Hydrogen Energy. 43 (2018) 22281-22290.

[269] A. Gioiello, V. Mancino, P. Filipponi, S. Mostarda, B. Cerra, Concepts and optimization strategies of experimental design in continuous-flow processing, J. Flow Chem. 6 (2016) 167-180.
[270] S. Saxena, S. Bawa, D. Katare, Statistical and Continuous Manufacturing approach by Design of Experiment (DoE) for a Robust Synthetic Process of a Sorafenib Analogue, Res. J. Pharm. Technol. 13 (2020) 1-8.
[271] L. Degli Esposti, A. Dotti, A. Adamiano, C. Fabbi, E. Quarta, P. Colombo, D. Catalucci, C. De Luca, M. Iafisco, Calcium Phosphate Nanoparticle Precipitation by a Continuous Flow Process: A Design of Experiment Approach, Crystals 10 (2020) 953.
[272] C.T. Armstrong, C.Q. Pritchard, D.W. Cook, M. Ibrahim, B.K. Desai, P.J. Whitham, B.J. Marquardt, Y. Chen, J.T. Zoueu, M.J. Bortner, Continuous flow synthesis of a pharmaceutical intermediate: a computational fluid dynamics approach, React. Chem. Eng. 4 (2019) 634-642.

Chapter 2 Droplet-based Millifluidic Synthesis of a Proton-conducting Sulfonate Metal–organic Framework

2.1 Introduction

Metal–organic frameworks (MOFs), a class of coordination polymers, are composed of metal ions or clusters interconnected by organic linker molecules in extended three-dimensional networks [1, 2]. The wide variety of both the organic and inorganic components in these structures demonstrated to date, and particularly the range of functional groups that can be incorporated to coordinate metal sites or modify interior pore structures, endow MOF materials with versatile functions from gas storage [3, 4], chemical separations [5], and catalysis [6, 7] to proton conduction [8-11]. Proton exchange and ion transport membranes for fuel cells and energy conversion and storage applications benefit from the well-defined crystal structures and diverse functional group chemistry controlled by linker selection in MOFs [12].

Sulfonate MOFs are considered to be promising materials for proton conduction, as sulfonic acid groups can provide proton hopping sites which promote proton transfer within the material [13]. Sulfonates are typically weakly coordinating moieties, favoring the formation of well-defined metal-sulfonate coordination motifs with soft metal ions (e.g. Cu^{2+}, Ag^{+}, Cd^{2+}, Ba^{2+}) [14]. Cu-based sulfonate MOFs incorporating N-donor ligands to form 3D frameworks have been reported [15], where N-donor ligands appear to serve a structure-directing role to promote 3D network formation in sulfonate MOFs [14, 16]. Sulfonate MOFs with triazolate ligands present elevated proton conductivity, attributed to the complementary acid−base and hydrogen bonding interactions of the sulfonate and amine groups [17, 18]. However, compared with other MOF families (e.g. carboxylate and imidazolate MOFs), much remains unknown about the crystallization processes of sulfonate MOFs and their dependence on synthesis parameters.

The breadth of MOF research has inspired the development of different synthetic methodologies. Hydrothermal synthesis [19-21] and solvothermal synthesis [22-24] are two common methods for MOF production. Both methods, however, often require reaction times of hours or days and suffer from batch-to-batch variability due to nonuniform reagent concentrations and low heat transfer in batch reactors. Recently,

synthetic procedures for MOFs utilizing ultrasound [25, 26], microwave radiation [27-29], mechanochemistry [30, 31] and electrochemistry [32, 33] have also been reported. Compared with these emerging alternatives to batch syntheses, continuous reactors preserve the crystal growth process as in batch reactions with improved mass and heat transfer, offering scalability through reduced reaction time and parallelizable, continuously operable flow reactors with improved uniformity of the target product.

Continuous synthesis methods such as microfluidic and millifluidic technologies, in which a chemical reaction occurs in a flowing stream rather than in a fixed batch vessel [34], can offer tight control over synthetic conditions and are favored in applications ranging from nanomaterials fabrication [35-37] to drug delivery [38, 39]. Continuous synthesis allows for faster reactions because high surface area to volume ratios can enhance higher heat transfer in microreactors, and reagents undergo rapid mixing when flowing through reactor tubing [40, 41]. Applied to MOFs, microfluidic synthesis has been shown to enable the continuous production of MOFs in several minutes at lower temperatures than those used in traditional solvothermal syntheses, with simultaneous control of the reaction parameters to synthesize MOFs with targeted properties [42].

Reaction yields and MOF particle sizes are particularly irreproducible in scaled-up batch reactions, as the depletion of metal ions and linkers in batch processes affects the kinetics of the oligomerization reaction and the nucleation and growth rates [43, 44]. Two-phase droplet flow systems, including slug flow, offer a promising route to fabricate MOF particles whilst simultaneously inhibiting channel clogging and enhancing particle size control [45]. Because each droplet is essentially a miniature batch reactor, this ensures a narrow residence time distribution, which is difficult to achieve in a single phase microreactor. In addition, vortices within the droplets further enhance the mixing and the heat and mass transfer [46]. This results in droplets which are highly uniform in terms of chemical composition and reaction temperature, providing a highly controlled environment for chemical reactions to take place. The droplets are isolated from the reaction channel walls by using a second phase as an inert ‘carrier’, which can eliminate reactor fouling due to the precipitation of reactants or products, providing a stable reaction environment during continuous synthesis [47]. The development of continuous syntheses for a number of carboxylate and imidazolate MOFs [48-53] now prompts the exploration of such techniques for the distinct

coordination chemistry of sulfonate MOFs.

Despite promising proton conductivity characteristics, the brittleness and poor mechanical strength of MOFs [54, 55] often precludes their direct use in membranes for PEM fuel cell applications. Nafion polymer membranes are the most commonly used membranes in fuel cells because of their good proton conductivity [56]. However, Nafion manufacturing depends on toxic precursors and highly reactive intermediates, presenting hazards as well as contributing to high production costs [57, 58]. As an alternative to Nafion, mixed-matrix membranes (MMMs) are fabricated by mixing inorganic/inorganic-organic materials and a polymer matrix and are also promising for PEM applications [59]. A key strategy for MMMs is to improve the properties of polymers with intrinsically poor proton conductivity. One such polymer system is the polyvinylpyrrolidone (PVP)/Polyvinylidene fluoride (PVDF) polymer blend. PVDF exhibits excellent mechanical strength and good stability [60, 61], whilst PVP imparts hydrophilic properties to compensate for the native hydrophobicity of PVDF for PEM applications [62]. However, the PVP/PVDF blends do not exhibit substantial proton conductivity.

Here we evaluate a sulfonate MOF prepared by millifluidic synthesis incorporated into a PVP/PVDF MMM as a candidate composite membrane for fuel cell applications. We focus on Cu-SAT, a MOF consisting of Cu^{2+} centers coordinated with sulfonate and triazolate groups, a known candidate material for proton conducting MMMs [15]. In order to fabricate this MOF with consistent properties, a self-designed droplet-based microreactor delivering a stable slug flow pattern was employed to continuously synthesize Cu-SAT with controlled reaction yields and sample particle size. We have carried out single crystal and powder X-ray diffraction as well as electron diffraction and spectroscopic analyses to confirm the structure and composition of Cu-SAT. Using a factorial design of experiments (DoE) approach, we reveal the trade-offs between continuous synthesis process parameters (residence time, temperature and reagent concentrations) and the reaction yield, MOF particle size, and the particle size distribution. Finally, we report the proton conductivities of Cu-SAT MOF-based membranes fabricated by incorporating the synthesized material within PVP and PVDF polymers to highlight the PEM performance properties.

2.2 Experimental

2.2.1 Materials

1,5-Naphthalenedisulfonic acid tetrahydrate (H_2NDS, Molecular Weight: 360.36 g mol^{-1}), 1,2,4-triazol-4-amine (T4A, Molecular Weight: 84.08 g mol^{-1}), copper nitrate hemi(pentahydrate) (Molecular Weight:232.59 g mol^{-1}), N, N-dimethylformamide (DMF, ≥ 99.9%), 2-propanol (IPA, ≥ 99.9%), silicone oil (viscosity: 150 CST, density: 1.075 g mL^{-1}, employed as the continuous phase in continuous synthesis), polyvinylpyrrolidone (PVP) [M_W 360,000], and polyvinylidene fluoride (PVDF) [M_W 534,000] were purchased from Sigma Aldrich and used as received.

2.2.2 Batch synthesis of the Cu-SAT MOF

The batch reaction was adapted from the procedure reported by Moi *et al.* [15]. First, 8.4 mg (0.1 mmol) T4A was dissolved in deionized water in a 20 mL glass vial, then 23.2 mg (0.1 mmol) of copper nitrate and 36 mg (0.1 mmol) of H_2NDS were dissolved in this solution successively. Next, DMF was added to the initial aqueous solution of the precursors. The volume ratio of the DMF-water solvent was 10:3, and the total volume of solvent for the reaction was fixed between 2.6 and 3.9 mL. The prepared chemical solutions were heated by immersing reaction vials in an oil bath at temperatures ranging from 80 to 110 °C for reaction times between 60 and 300 min. At the end of the set reaction time, blue solids were recovered by vacuum filtration and washed with 5 mL DMF three times. Samples were then dried in an oven at 80 °C for 10 h. For the scaled-up batch reaction, the reagents and solvents were scaled up by a factor of 3.3. Reaction procedures were otherwise the same as for the small-scale batch reactions. To examine the effect of stirring on batch reactions, a stir bar with a length of 10 mm was placed in the reaction vial with a stirring speed of 500 revolutions/min during the reaction, and identical reaction procedures were followed as for the unstirred batch reaction. Based on the identified crystal structure (single crystal XRD, this work), the molecular weight of Cu-SAT is 688.64 g mol^{-1}. The synthetic yields were calculated using recovered sample weight (the weight of the dried sample on the filter paper minus the weight of the filter paper) divided by the weight expected for complete conversion of the precursors to Cu-SAT.

2.2.3 Continuous synthesis of Cu-SAT MOF

As T4A and H_2NDS ligands undergo a side reaction with copper nitrate at room temperature, in order to achieve better mixing of precursors and form stable droplets for continuous synthesis of Cu-SAT MOF, the two ligands (combined) and the Cu^{2+} nitrate precursor were introduced via two different syringes. In the droplet-based millifluidic setup, glass syringes (25 mL, SGE) were used to carry chemical precursors and silicone oil, a cross connector (P-723, IDEX) was used to mix all precursors simultaneously and form stable slugs within the continuous silicone oil phase, with each slug containing the same volume and concentration of reagents. For stable slug flow, we found a 1:1 ratio to be optimal, with variations producing shorter and longer slugs that were, however, unstable. Before carrying out a reaction, the silicone oil and the reagent solutions were degassed in a sonicator at 60 °C for 1 h. All reagents used for continuous synthesis were prepared with a ratio of DMF to water equal to 10:3. A preheating step was used to ensure all solutions reached a well-defined temperature prior to mixing and droplet segmentation. The preheating system consisted of three PFA inlet tubings (1/32 inch ID, Adtech) with a 50 cm length immersed in the oil bath ahead of the cross connector. The reactor tubing (PFA, 1/16 inch ID, 10 m, Adtech) was coiled around a circular metal mesh cylinder (diameter ~10 cm) and the reaction started after the oil bath reached the set temperature.

The flow rates of the reagent solutions and the silicone oil were set to be equal. The residence time was taken as the volume of the reactor divided by total flow rate, a suitable estimate for segmented flow. Flow rates and oil bath temperatures were controlled to give residence times and reaction temperatures from 60 to 120 min and from 80 to 90 °C, respectively. After the reaction, synthesized particles together with unreacted reagents and silicone oil were collected in a vial and separated via centrifugation at 6800 rpm for 10 min. The solvent was then decanted to recover reusable silicone oil, and the product (a blue powder) was washed with 10 mL IPA three times and recovered by vacuum filtration. The recovered solid powder was then dried in an oven at 80 °C for 10 h.

2.2.4 Computational fluid dynamics (CFD) simulation methods

Simulations were performed using ANSYS Fluent software (ANSYS 2022R2). In this work, incompressible two–phase (silicone oil–DMF/water mixture) flow is

considered, where the silicone oil and the DMF/water mixed solvent are the continuous and dispersed phases, respectively. The interface is tracked by the volume of fluid method, which solves a single set of conservation equations for both phases. This set of equations comprises an equation of continuity:

$$\nabla \cdot (\rho \mathbf{u}) = 0 \tag{1}$$

and an equation of motion:

$$\frac{\partial(\rho \mathbf{u})}{\partial t} + \nabla \cdot (\rho \mathbf{u}\mathbf{u}) = -\nabla \mathrm{P} + \nabla \cdot [\mu(\nabla \mathbf{u} + \nabla \mathbf{u}^{\mathrm{T}})] + \rho \mathrm{g} + \mathrm{F_S} \tag{2}$$

where ρ is the volume-averaged density, $\mathbf{u}$ is the velocity vector, t is time, P is the pressure, μ is the dynamic viscosity, g is the gravitational acceleration, and $\mathrm{F_s}$ is the continuum surface tension.

The volume-averaged properties are defined as:

$$\rho = \alpha_o \rho_o + (1 - \alpha_w)\rho_w \tag{3}$$

where α_o and ρ_o represent the volume fraction and density of the silicone oil, α_w and ρ_w are the volume fraction and density of the DMF/water mixture. The dynamic viscosity is further defined as:

$$\mu = \alpha_o \mu_o + (1 - \alpha_w)\mu_w \tag{4}$$

where subscripts likewise refer to the silicone oil (o) and DMF/water mixture (w), respectively. The volume fraction of each liquid phase is calculated by solving the equation:

$$\frac{\partial \alpha_i}{\partial t} + \mathbf{u} \cdot \nabla \alpha_i = 0 \tag{5}$$

The geometric model used in the simulation is shown in Figure 2.1. The system has one inlet (the horizontal one) for the continuous phase and two inlets (the vertical ones) for the dispersed phases. The velocity-flow inlet boundary condition was used at all three inlets. The outlet was defined as a pressure outlet, and the no-slip boundary condition was used at the walls. The values of the density and viscosity of the two phases and the interfacial tension are listed in Table 2.1. The analysis to evaluate the sensitivity of mesh size on the droplet length was conducted as shown in Table 2.2. After the grid independence test, a mesh consisting of 87,172 cells was adopted to

ensure a reasonable trade-off between simulation accuracy and computational cost. The numerical simulation was verified by comparing the simulated droplet length ($V_{inlet\text{-}1}$=0.002 m s^{-1}, $V_{inlet\text{-}2}$=$V_{inlet\text{-}3}$=0.001 m s^{-1}) with photographs of the experimental system (Figure 2.2). The relative difference in the length of the droplets observed in the experimental system and the simulations was less than 5%.

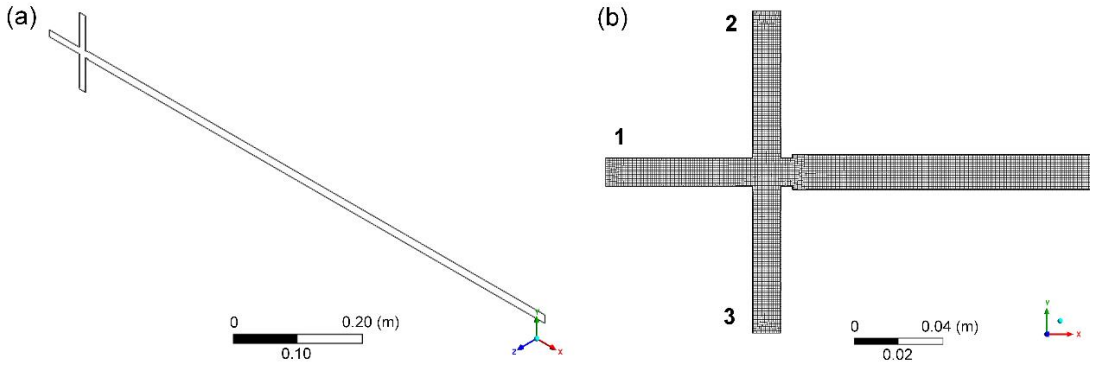

Figure 2.1 (a) Schematic of the double T-junction device and (b) the mesh structure used in the double T-junction device.

Table 2.1 Physical properties of the fluids

Fluid	Density (kg m^{-3})	Viscosity (kg m s)	Interfacial tension (N m^{-1})
Continuous phase	1070	0.150	0.035
Dispersed phase	995.2	0.001	

Table 2.2 Mesh independence analysis[a]

Cell number	Droplet size (L W^{-1})
24,850	2.82
36,829	2.88
87,172	3.05
227,619	3.06

[a]$V_{inlet\text{-}1}$: 0.002 m s^{-1}, $V_{inlet\text{-}2}$= $V_{inlet\text{-}3}$: 0.001 m s^{-1}

2.2.5 Linear response surface modelling of continuous synthesis

A minimal factorial DoE approach was carried out using the millifluidic reactor for three reaction parameters: temperature, time, and reagent concentration. The response variables were selected as yield, particle size, and particle size interquartile range (IQR). In total, a two-level, three factor design was set up to give 11 experiments (two levels for each reaction parameter with three repeats at the center of the resulting

parameter cube, see also Figure 2.2). Linear response modelling was performed using Minitab (version 21.2). An analysis of variance was carried out to identify statistically significant terms for linear response model fitting. Terms associated with low probability values (p-values) were excluded from model fitting. The p-values together with an inspection of the distribution of contributions of all terms were used to select retained terms, targeting the minimum number of terms to describe the response. For yield and mean particle size, a clear separation between significant terms and terms with low p-values (<0.05) was observed. For particle size IQR, all terms showed effects and were retained in the model fitting.

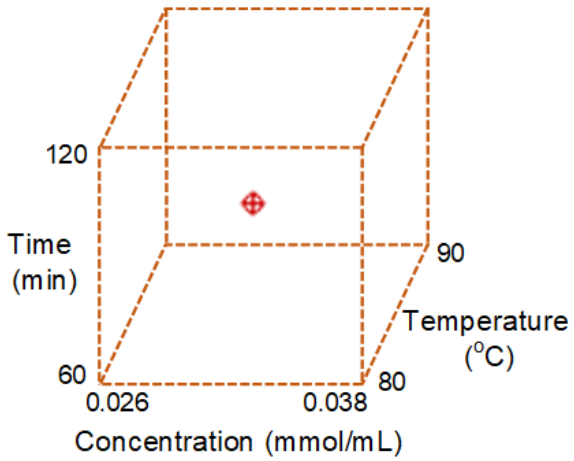

Figure 2.2 Reaction parameters in a box from the DoE.

Linear response surface modelling was carried out for yield, particle size, and particle size IQR. Equations were used to fit the results across the parameter space: 80 °C ≤ Temperature (T) ≤ 90 °C, 60 min ≤ Residence time (t) ≤ 120 min, and 0.026 mmol/mL ≤ Reagent Concentrations (C) ≤ 0.038 mmol/mL. The retained terms for each are given below (coefficients differ between equations as a result of independent fitting for each measured response), with coefficients in lower case *a, b, c,…* etc. and reaction parameters denoted as temperature *T*, residence time *t*, and concentration of reagents *C*. Coefficient values in these equations are listed in Table 2.3.

$$yield = a + bT + ct$$

$$particle\ size = a - bT - ct + e(Tt)$$

$$particle\ size\ IQR = a - bT + ct - dC - e(Tt) - f(TC) - g(tC) + h(TtC)$$

Table 2.3 Coefficient values in above equations

Equations	Coefficient values								R^2	R^2 (pred)
	a	b	c	d	e	f	g	h		
Yield	277.3	3.200	0.5917						0.8914	0.8197
Particle size	404	5.25	14.48	0.19					0.9474	0.8492
Particle size IQR	205.0	2.142	1.131	417	0.0118	4.2	240.3	2.986	0.9998	0.9826

Note: no transformations of the data were used during the modelling.

2.2.6 Membrane fabrication

The MMMs were fabricated using 60% by weight (wt%) of Cu-SAT incorporated into PVP and PVDF (denoted as MMM-60 wt%). Typically, 180 mg of continuously synthesized Cu-SAT were ground in a mortar and pestle and dispersed in 1.8 mL DMF by sonication for 20 min. Then, 30 mg PVDF and 90 mg PVP were added successively and dissolved in the Cu-SAT suspension in DMF while stirring at room temperature for 300 min to obtain a homogeneous gel. This gel was poured onto a high-temperature resistant glass and cast using a BGO 209/2 adjustable applicator (Biuged Laboratory Instruments Co., Ltd). The thickness of membrane was adjusted by changing the gap between the glass and the casting blade; in this study the gap value in the adjustable applicator was set to 100 μm. The membrane was then dried at 70 °C for 1 h in a vacuum oven to remove excess DMF. The solidified membrane was finally washed with deionized water three times and then dried at room temperature.

2.2.7 Material Characterization

Powder X-ray diffraction patterns were recorded using a Bruker D2 diffractometer (Cu Kα λ = 1.541 Å, 2θ scan range = 5-50°). Single crystal X-ray diffraction measurements were carried out at 100 K on a Rigaku SuperNova diffractometer equipped with an Atlas CCD detector and connected to an Oxford Cryostream low temperature device using mirror monochromated Cu Kα radiation (λ= 1.54184 Å) from a microfocus X-ray source. The structure was solved by intrinsic phasing using SHELXT [63] and refined by a full matrix least squares technique based on F^2 using SHELXL2014 [64]. Vesta software (version 3.5.7) was employed to produce calculated XRD patterns of Cu-SAT from the single crystal structure.

The morphologies of the MOF samples were characterized by light microscopy (LM, Olympus, BX51) and scanning electron microscopy (SEM, Hitachi/TM-

3030Plus, equipped with a backscattered electron detector and operated at 15 kV accelerating voltage). Particle sizes were measured from light micrographs using ImageJ, determined as the average of (a) the length taken as the longest dimension of the particle and (b) the width perpendicular to the length. More than 100 particles were measured for each sample. Cryo-SEM was carried out using an FEI Helios G4 CX cryo-FIBSEM, operated at 10 kV and equipped with a Quorum Technologies PP3010 cryo-stage and an Oxford instruments 150 X-Max energy dispersive X-ray spectroscopy (EDS) detector, to check the thickness, surface morphology, and elemental composition of the hydrated membrane.

FTIR spectra of the MOF samples and membranes were obtained using a Bruker Vertex 80V Fourier Transform Infrared (FTIR) spectrometer with a diamond prism Attenuated Total Reflection (ATR) crystal. Using a 6 mm aperture, data were collected for wavenumbers between 500 and 4000 cm^{-1} and averaged over 16 scans. Cu-SAT crystals were ground to a fine powder before FTIR measurements. Thermogravimetric analyses (TGA) were carried out using a Netzsch STA 449F3 instrument with a heating rate of 10 °C min^{-1} in a nitrogen atmosphere (40 mL min^{-1}). N_2 adsorption-desorption measurements were attempted but showed generally low adsorption and did not offer physically interpretable isotherms. We infer Cu-SAT has very low if any accessible porosity for N_2.

A Thermo Scientific Flash EA2000 elemental analyser was used to detect carbon, hydrogen, nitrogen and sulphur (CHNS) in Cu-SAT samples. Briefly, this analysis entailed dropping samples into a furnace at 900 °C in a continual flow of helium. Pure oxygen was added for a few seconds to facilitate combustion. The combustion products pass through an oxidation/reduction reactor to convert them to CO_2, H_2O, N_2 and SO_2 which are then separated by gas chromatography and detected using thermal conductivity. X-ray photoelectron spectroscopy (XPS) was used to characterize the surface chemistry of the materials. The sample powder was pressed lightly onto carbon tape and adhered to a standard omicron plate. Excess powder was knocked off to obtain a uniform flat sample. The experiment was carried out in UHV ($<1\times10^{-9}$ mbar) on a Specs FlexMod system. The illuminating X-ray source was a monochromatic Al Kα ($h\nu$ = 1486.7 eV) anode at a power of 100 W and 15 kV. A Specs Phoibos 150 hemispherical analyser with 1D delay line detectors was used to detect the photoelectrons. The powder is insulating so to reduce any differential charging at the

surface which could distort the spectra, an electron flood gun (energy 1 keV and current 75 μA) was used to charge neutralize the sample. Survey spectra were obtained with a pass energy of 50 eV, a step width of 1 eV and a dwell time of 0.1 seconds. High resolution spectra were collected with a pass energy of 30 eV, a step width of 0.1 eV and a dwell time of 0.1 seconds. After collecting the spectra, the data was analysed using CasaXPS software. Binding energies were calibrated using the C-C C1s peak at 285 eV and the intensity was calibrated using a previously calculated transmission function for the specific instrument settings. All spectra were fitted with a Shirley background and the peak areas were determined. We quantified the relative atomic percentages using these peak areas and the respective relative sensitivity functions for each peak.

Analytical scanning transmission electron microscopy (STEM) was employed to analyse individual microscopic crystals using scanning electron diffraction (SED). Data was acquired using a JEOL ARM300CF transmission electron microscope at the Diamond Light Source, fitted with a high-resolution pole piece, cold field emitter, and JEOL spherical aberration correctors in both the probe forming and image forming optics. The instrument was operated at 300 kV with a gun lens setting calibrated to give a probe current of 1.9 pA. The diffraction-limited probe diameter was taken as $1.22\lambda/\alpha$ where λ is the electron wavelength at 300 kV (1.97 Å) and the convergence angle α is 0.8 milliradians, defined by a 10 μm condenser aperture. A Merlin-medipix direct electron detector was used to record the electron diffraction pattern at each probe position (step size ca. 5.2 nm) with an exposure time of 1 ms per probe position. Assuming a circular probe with a diffraction-limited diameter (3 nm), the total fluence was approximately 17 electrons $Å^{-2}$. SED data was acquired over a raster scan comprising 256 × 256 probe positions and each diffraction pattern comprised 512 × 512 pixels. Following SED acquisition, EDS maps were acquired from the same regions using a larger probe current (obtained with a 100 μm condenser aperture) to generate sufficient X-ray counts. SED data were processed using pyXem, an open source Python library [65]. Images and diffraction patterns were calibrated using a standard gold cross-grating with a period of 500 nm. Relative rotation of the diffraction pattern and the raster image was calibrated using a MoO_3 standard.

The three-dimensional microstructure of a representative Cu-SAT and PVP/PVDF membrane was investigated using X-ray micro-computed tomography

(Zeiss Xradia 620 Versa operated at 50 kV and 90 mA). 1,101 radiographs were acquired over a 360° sample rotation range with an exposure time of 10 s per radiograph. The sample was mounted on a steel pin and placed between the X-ray source and a 2k × 2k detector providing a voxel resolution of 364 nm using a 40× objective magnification. Raw transmission images were reconstructed using a commercial image reconstruction software package (Zeiss XMReconstructor, Carl Zeiss X-ray Microscopy Inc., Pleasanton, CA), which employs a filtered back-projection algorithm. The 3D reconstructed volume of the sample was analyzed with the Zeiss proprietary software, TXM3DViewer.

2.2.8 Proton Conductivity

An important parameter to evaluate PEM performance is the proton conductivity (σ, S cm^{-1}) defined as:

$$\sigma = \frac{L}{AR} \tag{6}$$

where L is the length between the two electrodes (cm), A is the membrane area (cm^{-2}, equal to the width × thickness of the hydrated membrane, as measured by Cryo-SEM), and R is the resistance of membrane (Ω). R is often measured by electrochemical impedance spectroscopy (EIS) and the intercept at the axis corresponding to the real part of the complex impedance (Z') is taken as the resistance [56] or by Cyclic Voltammetry (CV) using the slope of the voltage versus current response. A BT-110 conductivity clamp (L = 0.425 cm) was used to measure the in-plane resistance and hence ionic conductivity of fabricated membrane samples using a Gamry 1010E electrochemical workstation. A four electrode setup was used for the CV test with a scan rate of 10 mV/s between -0.1 V and 0.1 V. EIS was measured between frequencies of 1 Hz and 1 MHz using a two electrode setup in order to minimize artifacts, such as additional inductive and capacitive features arising from the testing coaxial cables [66].

All EIS and CV measurements were performed 30 min after the testing temperature reached the set value. Before resistance testing, the membrane was placed in a 95% relative humidity (RH) chamber (Memmert HCP150) at room temperature for 12 h to fully hydrate the membrane, matching commonly applied RH equilibration conditions prior to testing [67, 68]. Figure 2.25a and b present the EIS and CV results of MMM-60 wt% measured at different times when the temperature reached 70 °C in

95% RH, indicating the highest proton conductivity was reproducibly achieved 30 min after the testing temperature reached the set value. The subsequent reduction in the observed proton conductivity was attributed to the finite stability of Cu-SAT at elevated temperatures (see also Results and Discussion) or gradual dehydration of the polymer matrix at elevated temperatures; signs of dehydration were visible on removal of membranes from the testing chamber. We therefore report the membrane conductivity at this reproducible 30 min point in order to determine the achievable conductivity, RH, and temperature response, without further optimization of the polymer composition or Cu-SAT stability.

The activation energy (E_a) for membrane proton conduction was determined via the Arrhenius relationship [69]:

$$\mathrm{In}(\mathrm{T}\sigma) = \mathrm{In}(\sigma_0) - (\frac{E_a}{\mathrm{R}})(\frac{1000}{\mathrm{T}}) \quad (7)$$

where T is testing temperature (K), σ is the proton conductivity (S cm^{-1}), σ_0 is the pre-exponential factor (S (K cm)$^{-1}$) and R is the ideal gas constant (8.314 J (mol K)$^{-1}$). E_a was determined from the slope of this Arrhenius plot.

2.3 Results and Discussion

2.3.1 Batch Synthesis of Cu-SAT MOF

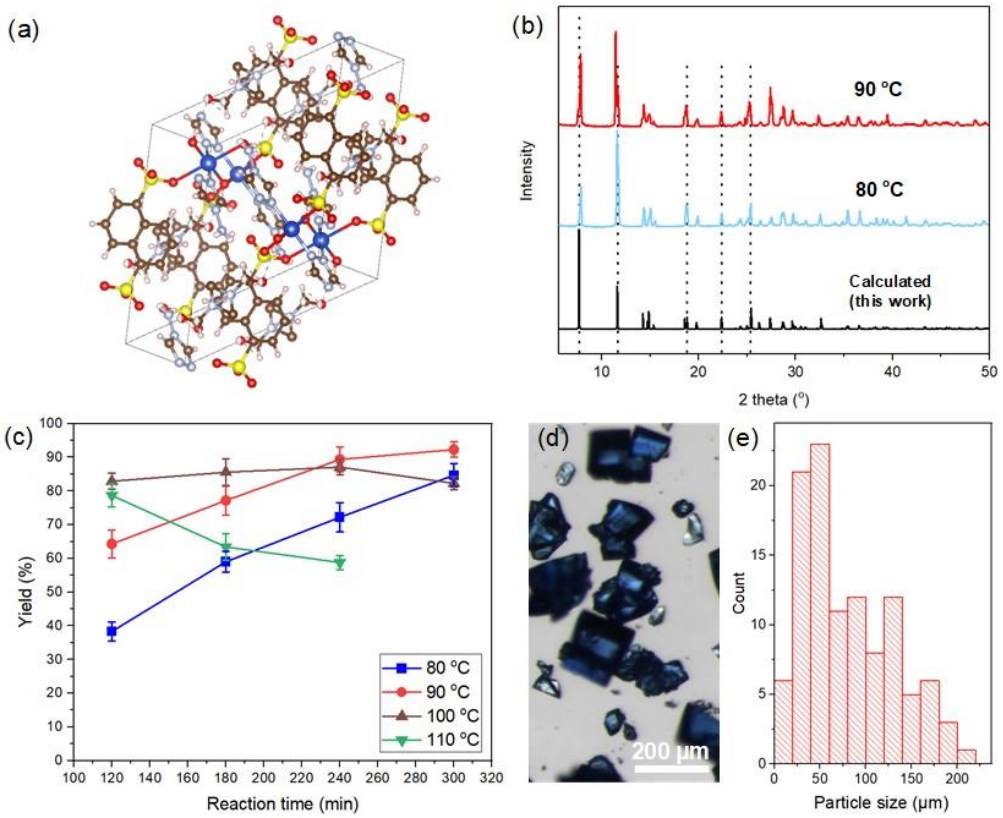

Figure 2.3 Single-crystal structure of Cu-SAT and results of batch synthesis under different reaction parameters: (a) Depiction of the crystal structure of Cu-SAT MOF (S, yellow; Cu, blue; O, red; N, lavender; H, pink; C, gray), (b) XRD patterns of batch samples synthesized under different temperatures with 120 min reaction time compared with single crystal simulated pattern, (c) percentage yield of Cu-SAT achieved from different synthesis times and temperatures, (d) light micrograph of Cu-SAT synthesized at 80 °C for 120 min and (e) associated histogram of the particle size distribution.

Cu-SAT synthesis has been previously reported by Moi *et al.* using a 180-min batch synthesis at 80 °C [15]. In order to resolve a discrepancy between the experimental powder XRD and the reported Cu-SAT crystal structure [15], we carried out a single crystal XRD (SC-XRD) structure determination for our own replicate batch synthesis at 80 °C (Figure 2.3a). We found that Cu-SAT can be described by a monoclinic unit cell (*C 2/m*) with lattice parameters a = 15.2535(7) Å, b = 6.7877(2) Å, c = 14.1582(6) Å and β = 125.469(7)° (denoted 'this work', deposited at the CCDC, reference number 2247539). The crystallographic parameters of Cu-SAT are listed in Table 2.4. This structure is similar to the previously reported structure for Cu-SAT

(CCDC reference number 1995454) in terms of the coordination and molecular packing with Cu^{2+} octahedrally coordinated by *trans*-coordinated pairs of hydroxyl, T4A, and NDS ligands. The Cu^{2+} centers form quasi-1D chains which are linked along the chain by two of the sulfonate oxygens and two of the T4A N-donor sites at the base of the triazolate ring. The NDS ligands bridge between the Cu^{2+} chains, positioned with aromatic ring faces aligned and interleaved by residual DMF molecules. The third un-coordinated oxygen on each of the sulfonate SO_3^- groups and the R-NH_2 groups of T4A align parallel with the Cu^{2+} chains (*b*-axis). As shown in Figure 2.3b, XRD patterns of Cu-SAT made in batch at different temperatures match all peak positions observed in the single crystal simulated result, and samples prepared at 80 °C with different reaction times also presented consistent XRD patterns (Figure 2.4).

Table 2.4 Crystallographic parameters for Cu-SAT MOF

Empirical formula	$C_{17}H_{23}N_9O_9S_2Cu_2$
Formula weight	688.64
Temperature/K	100.00(10)
Crystal system	monoclinic
Space group	*C*2/*m*
a/Å	15.2535(7)
b/Å	6.7877(2)
c/Å	14.1582(6)
α/°	90
β/°	125.469(7)
γ/°	90
Volume/Å^3	1193.86(12)
Z	4
ρ_{calc}/gcm^{-3}	1.916
μ/mm^{-1}	4.476
F(000)	700.0
Crystal size/mm^3	0.48 × 0.31 × 0.14
Radiation	Cu Kα (λ = 1.54184 Å)

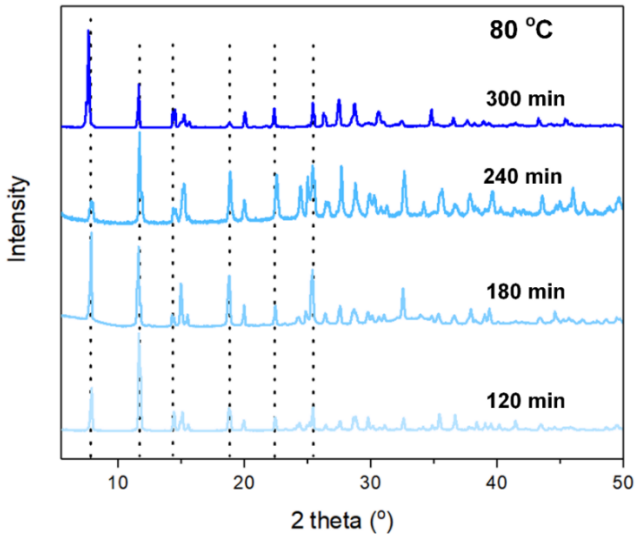

Figure 2.4 XRD patterns of Cu-SAT synthesized in batch at 80 °C for different reaction times.

Table 2.5 Yield (%) of Cu-SAT MOFs made in 300 min at 80 °C for different reagent concentrations.

Volume (mL) of solvents used for the reaction	2.6	3.25	3.9
Concentration of each reagent (mmol mL^{-1})	0.038	0.031	0.026
Yield (%)	85	82	67

We have further varied reaction time, reaction temperature, and concentration of reagents to map their effects on the reaction yield and particle size and to establish suitable parameters for continuous synthesis. Figure 2.3c presents yields for Cu-SAT solvothermal batch syntheses at reaction temperatures ranging between 80-110 °C and for reaction times ranging between 120-300 min. Gravimetric yields were justified to track reaction yield, given the apparent phase-purity of the XRD patterns and the recovery of consistent faceted blue particles as observed by light microscopy (Figure 2.3b and d). For 80 °C, the yield continued to increase up to 300 min, with a plateau in the yield observed after 240 min at 90 °C, indicating faster reaction kinetics with increased temperature. Maximum yields of approximately 90% were recorded at 90 °C. Above 90 °C, however, yields decreased. At 110 °C, a change in the solvent colour from transparent blue to opaque black indicated decomposition of reagents over the course of reactions at elevated temperatures. The effect of solution concentration on yield was also studied by adjusting the total volume of the reaction mixture (2.6, 3.25

and 3.9 mL of solvents, fixed precursor quantities, Table 2.5), and exhibited a consistent decrease in yield for reduced reagent concentrations.

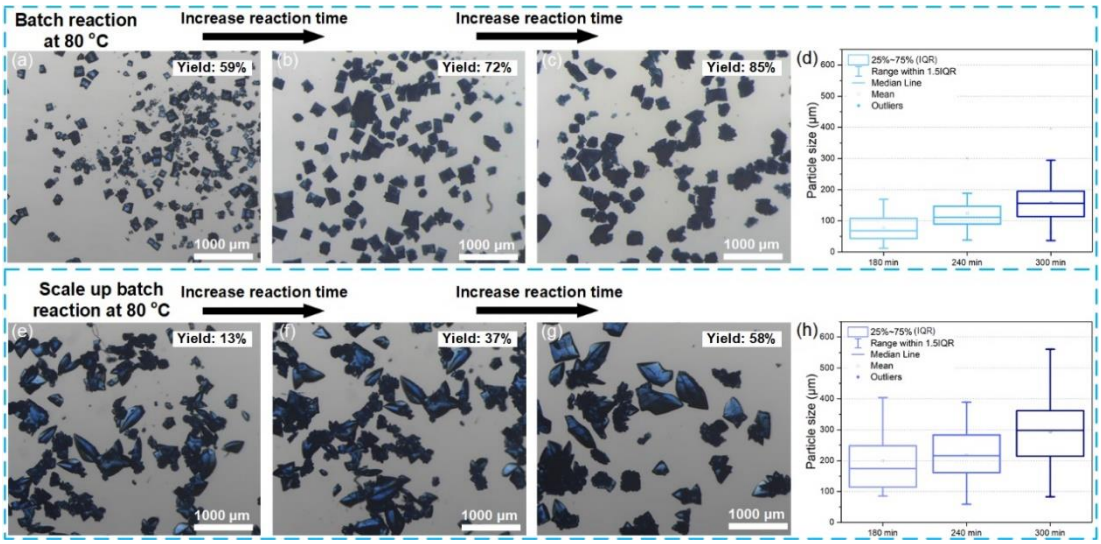

Figure 2.5 Light micrographs of batch synthesized Cu-SAT at 80 °C for reaction times of: (a) 180 min, (b) 240 min, (c) 300 min, and (d) box plot of the particle size in the three samples. Light micrographs of scaled-up batch synthesized Cu-SAT at 80 °C with reaction times of: (e) 180 min, (f) 240 min, (g) 300 min, and (h) box plot of the particle size in the three samples.

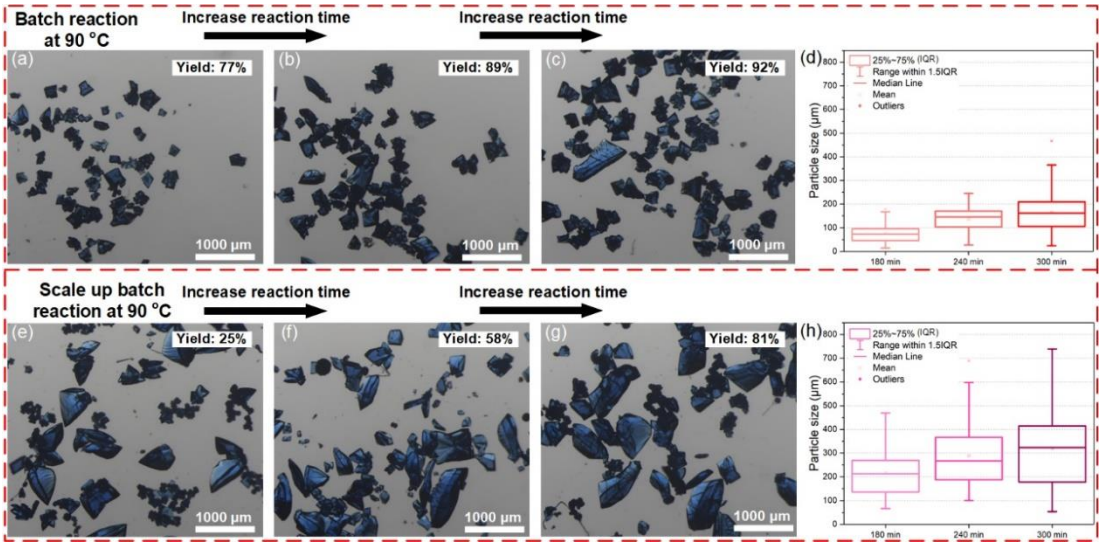

Figure 2.6 Light micrographs of batch synthesized Cu-SAT at 90 °C with reaction times of: (a) 180 min, (b) 240 min, (c) 300 min and (d) box plot of the particle size in the three samples. Light micrographs of scaled-up batch synthesized Cu-SAT at 90 °C with reaction times of: (e) 180 min, (f) 240 min, (g) 300 min and (h) box plot of the particle size in the three samples.

Figure 2.3d and e presents a light micrograph and an associated histogram of the particle size distribution of Cu-SAT prepared at 80 °C and for a 120 min reaction time.

The particles exhibit a characteristic blue colour and possess a blocky morphology with a wide and skewed size distribution up to ~200 μm. Figures 2.5 and 2.6 present additional light micrographs and box plots of particle size from different batch samples. For small-scale batch syntheses at 80 °C, an increase in reaction time from 180 min to 300 min resulted in an increase in the median particle size from 74 μm to 156 μm as well as an increase in the particle size interquartile range (IQR, a direct measure of the width of skew and non-skew distributions) from 62 μm to 83 μm. At 90 °C, both the median particle size and particle size dispersity (as recorded in the IQR) increased with longer reaction times as well. These results indicate batch synthesis is consistent with a crystal growth process comprising heterogeneous nucleation and growth as well as additional homogeneous nucleation events occurring over the course of the batch reaction. In batch reactions scaled up by a factor of 3.3 (8.6 mL of reagents rather than 2.6 mL), the yield decreased and the sample particle size and particle size IQR increased relative to small-scale reactions, which we attribute to the poor heat and mass transfer in these batch reactions.

2.3.2 Continuous Synthesis of Cu-SAT MOFs

In order to establish a reproducible method for Cu-SAT synthesis with higher space-time yield and particle size control, we developed a continuous synthesis for Cu-SAT using a millifluidic flow reactor. A schematic diagram of the two-phase continuous synthesis setup with a preheating system is shown in Figure 2.7a. Slug flow was achieved in one step by mixing the preheated reagents (dispersed phase) with silicone oil (continuous phase) using a cross connector. This setup allowed for the simultaneous mixing and segmentation of the reagents and the formation of stable slugs (Figure 2.7b). Figure 2.7c shows reagent slugs all with a consistent size and with slug diameters approximately equal to the diameter of the reaction tubing, and the slug length is approximately twice the diameter of the reaction tubing; these features reflect the stable slug pattern achieved in this reactor.

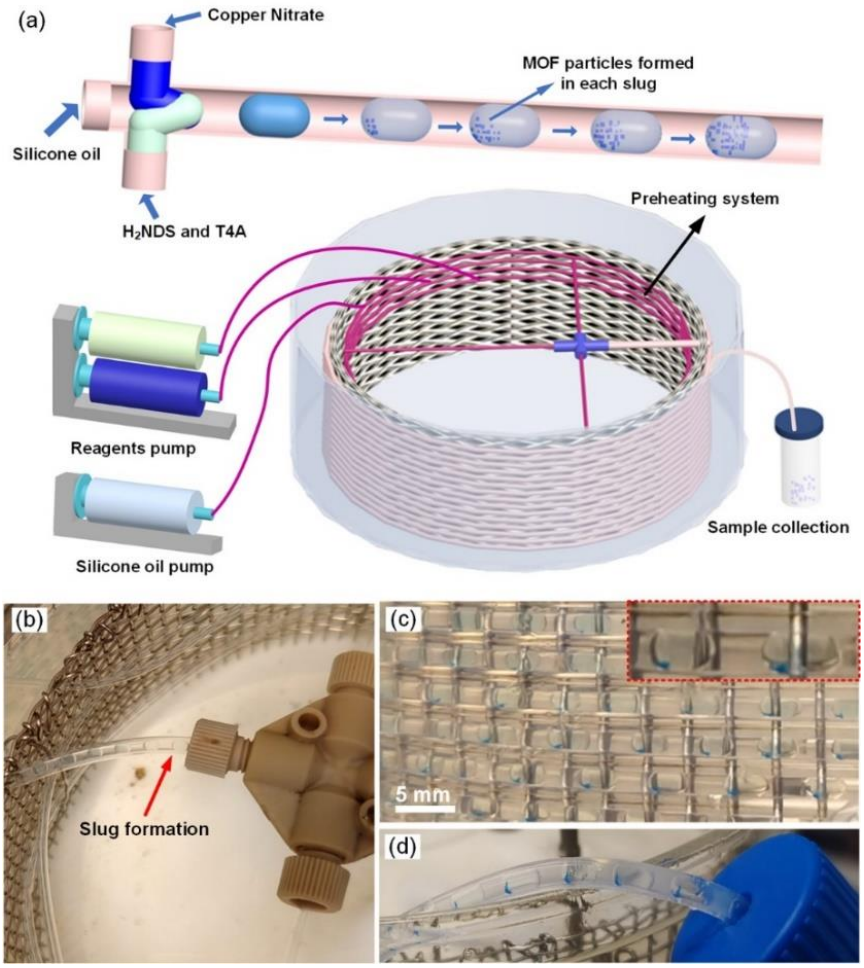

Figure 2.7 Transferring batch synthesis of Cu-SAT to continuous synthesis: (a) schematic diagram of the setup for two phase continuous synthesis of Cu-SAT MOFs, digital pictures of (b) slug formation at the inlet, (c) particle formation in the flow reactor and (d) sample collection at the reactor outlet.

CFD simulations were used to understand formation mechanism of slugs in the cross connector (Figure 2.8). In the double T-junction microtube (cross connector), as the dispersed phase continuously flowed into the main channel, the front of the two dispersed phases began to meet in the main channel, ultimately resulting in the head of the dispersed phase blocking the main channel. At 7 s, the dispersed phase had completely blocked the main channel (Figure 2.8a). Due to the viscous force and interfacial tension, the pressure in the main channel reached its maximum, indicating that the slug was growing, and its volume was increasing while continuing to move downstream (Figure 2.8b and c). Finally, at 9.5 s, the neck of the slug detached from the dispersed phase (Figure 2.8d). This process of slug generation is continuously repeated, and the slug size varies depending on the flow rate and flow rate ratio of the two phases.

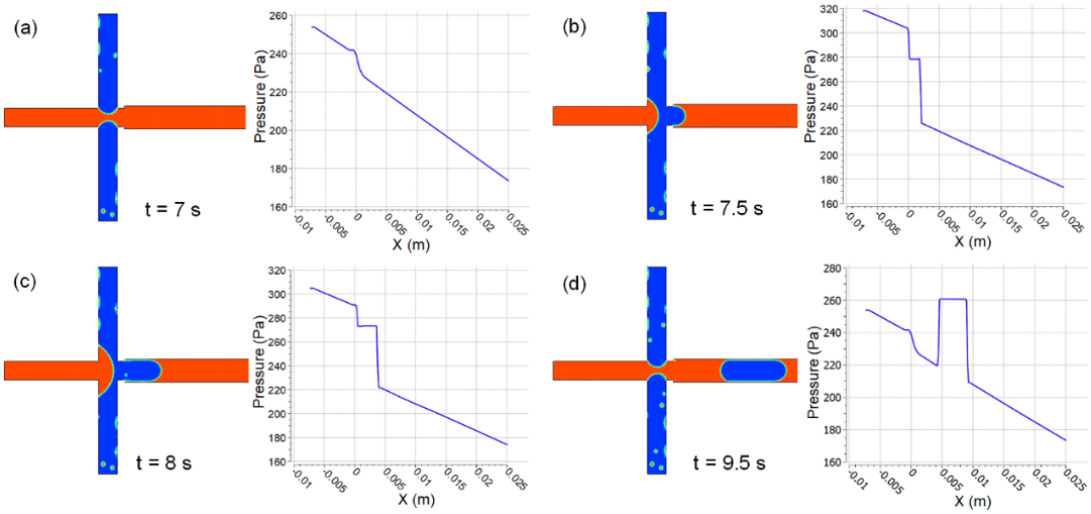

Figure 2.8 The simulations of the droplet generation and pressure plots on the XZ plane when generating a droplet: Generation of droplet at (a) 7 s, (b) 7.5 s, (c) 8 s, and (d) 9.5 s.

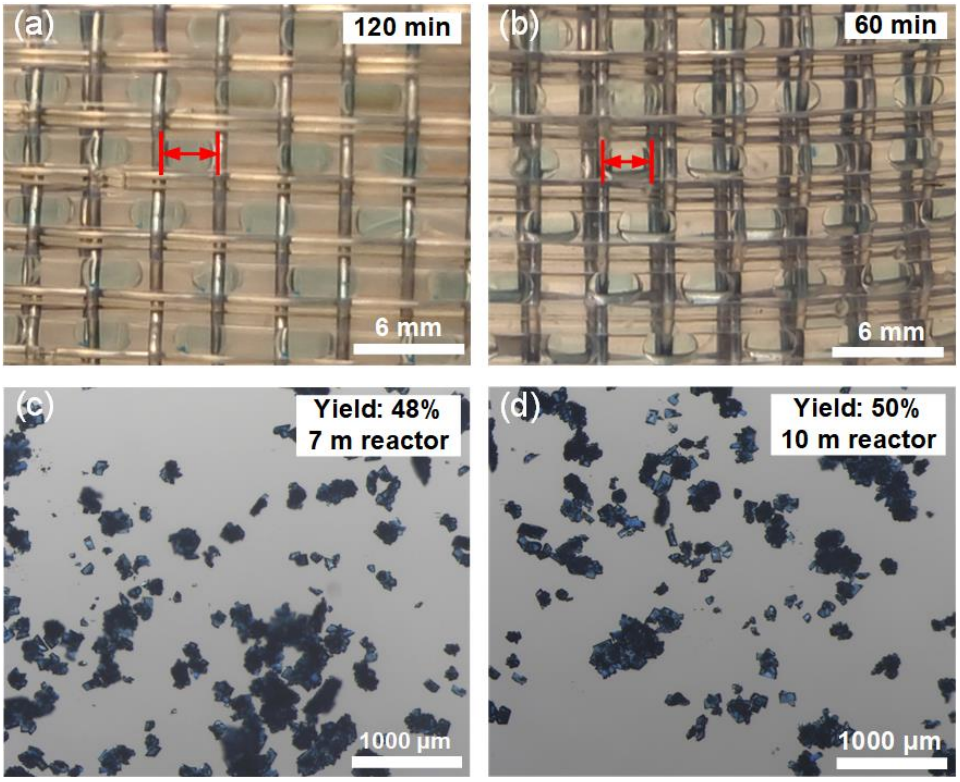

Figure 2.9 Digital photographs of slugs in a 10 m reactor with flow rates set to give a residence time of (a) 120 min and (b) 60 min. (c)-(d) Light micrographs of Cu-SAT particles made in (c) a 7 m reactor and (d) a 10 m reactor at 80 °C with a residence time of 120 min (matched experimental parameters, different reactor length).

At experimentally applied flow rates, the variation in slug size remained small. At flow rates giving a 120 min residence time, the slug length was approximately 3

mm or 5-10% longer than slugs at flow rates giving a 60 min residence time (Figure 2.9a and b). Furthermore, changes in flow rates with different reactor lengths (7 m or 10 m), produced similar samples (Figure 2.9c and d). Here, we used a 10 m reactor for stable, reproducible results within the range of flow rates used for Cu-SAT synthesis.

In experimental operation, blue crystals began to appear in each slug after one third of the residence time (40 min at 80 °C, and 20 min at 90 °C), with particles growing larger with increased reaction time. The slug pattern remained stable even as the product particles formed in the slugs and remained stable on leaving the reactor and moving to the collection vessel (Figure 2.7d).

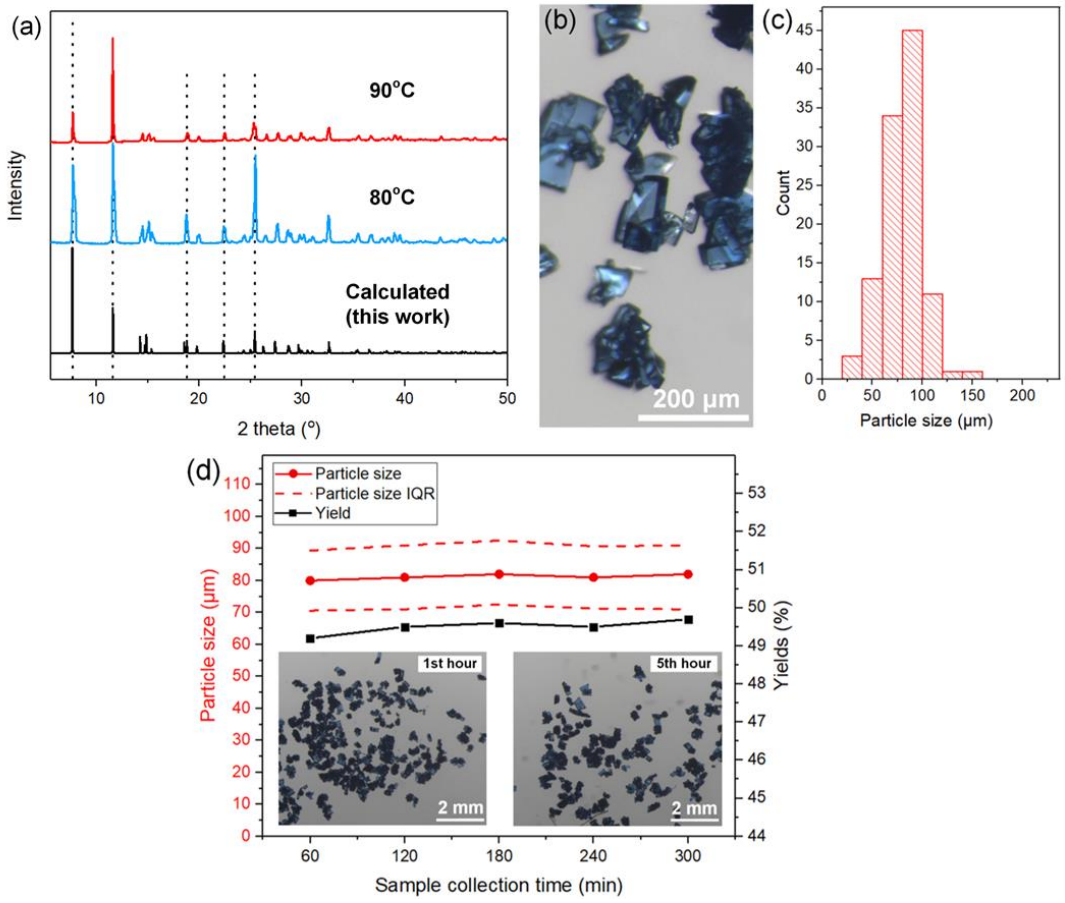

Figure 2.10 Results from of samples synthesized in the millifluidic system: (a) XRD patterns of samples made at different temperatures in the millifluidic system compared with the single crystal simulated result, (b) light micrograph of Cu-SAT made in flow with 120 min residence time at 80 °C and (c) associated histogram of the particle size distribution, and (d) reaction yield and average particle size results for different operational times in one synthesis with 120 min residence time at 80 °C, inset: light micrographs of Cu-SAT MOFs collected at the first hour (left) and the fifth hours (right).

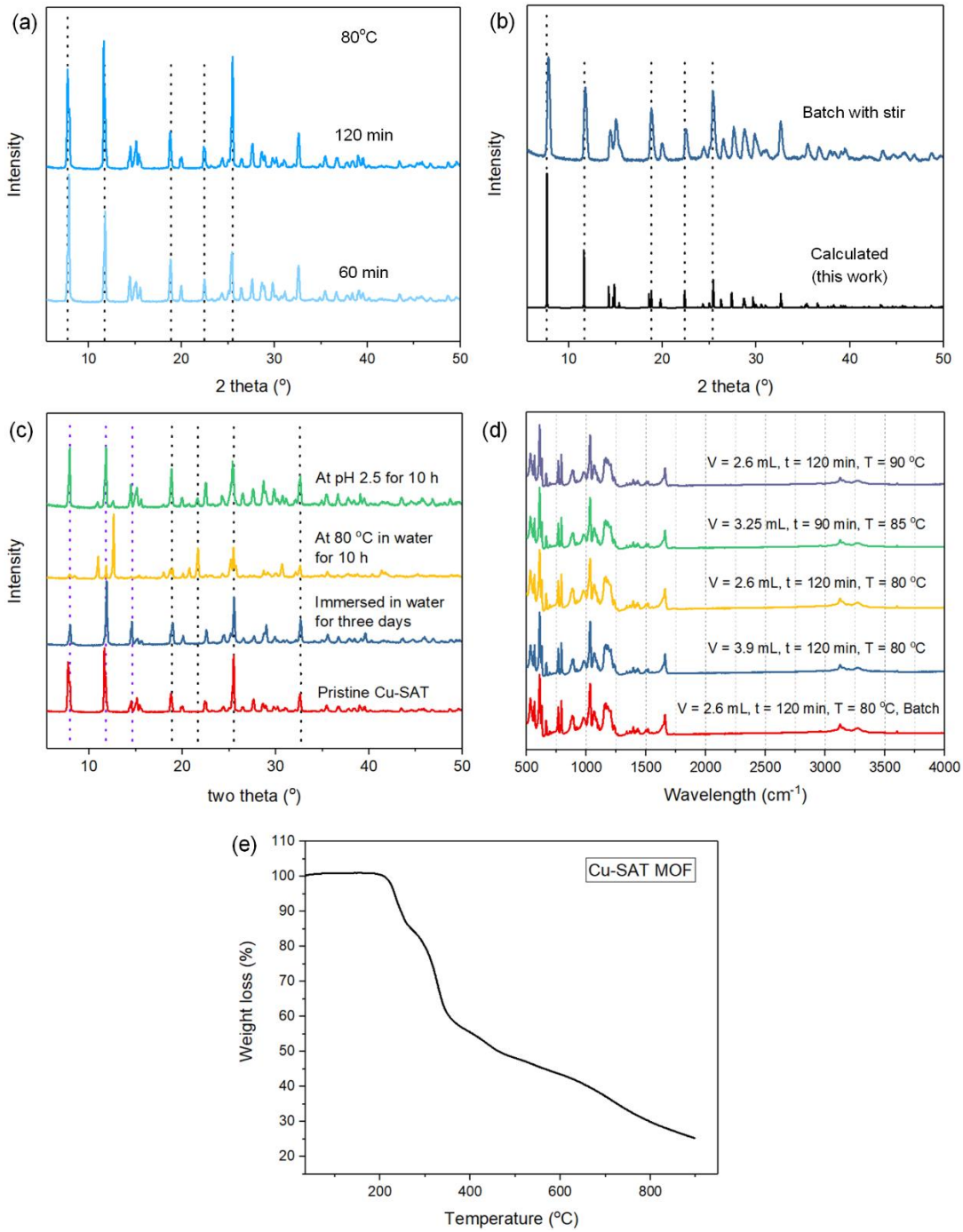

Figure 2.11 (a) XRD patterns of the Cu-SAT made in the millifluidic reactor at 80 °C with different residence times, (b) XRD pattern of the Cu-SAT made using stirred batch synthesis compared to the single crystal simulation, (c) XRD patterns of Cu-SAT made with a 120 min residence time in flow at 80 °C following different post synthesis treatment, (d) ATR-FTIR spectra of samples made by both batch and continuous synthesis, and (e) TGA of Cu-SAT under nitrogen.

XRD patterns from Cu-SAT samples made in flow with a residence time of 120 min under different reaction temperatures match with powder XRD patterns calculated from our single crystal structure (this work) and with samples made at 80 °C for different residence times (Figure 2.10a and Figure 2.11a), confirming the successful

continuous synthesis of Cu-SAT. Figure 2.10b presents a light micrograph of a continuously synthesized Cu-SAT sample made with 120 min residence time at 80 °C. As for batch reactions, continuously synthesized Cu-SAT appeared as uniformly blue crystals. Figure 2.10c presents the particle size distribution of this sample, with sizes ranging between 20 and 120 μm, which is half of the full range of the corresponding batch samples synthesized with the same reaction temperature and matched reaction time (Figure 2.3e). A continuous synthesis of Cu-SAT with 120 min residence time at 80 °C was operated for more than 5 h (equipped with syringe pumps with three syringes at a total flow rate of 0.16 mL min^{-1}, 0.08 mL min^{-1} for silicone oil and 0.04 mL/min for each of the aqueous phases using 24 mL silicone oil and 12 mL each of the aqueous phases from three 25 mL syringes) with no reduction in yield or change in particle size, as well as no evidence of reactor fouling (Figure 2.10d), demonstrating a sustained production rate of 59 mg h^{-1} with 78.6 kg m^{-3} day^{-1} space-time yield and consistent particle quality. The uniformity of particles collected for different reaction times is highlighted in the inset light micrographs.

The reaction yields of the batch and continuous reactions for different conditions are summarized in Table 2.6. The yields in continuous syntheses were typically 10-20% higher than those of the corresponding batch reactions under the same reaction parameters, indicating that the improved mass and heat transfer increase the rate of Cu-SAT formation in millifluidic synthesis. Batch synthesis with stirring was used to increase the heat and mass transfer in the batch process artificially. Using this method, an identical Cu-SAT crystal structure was observed (Figure 2.11b), with higher yields for the stirred batch reactions than was achieved in both unstirred batch and continuous syntheses. The stirring in batch synthesis further verified that the yield increases with better heat and mass transfer during the reaction, but without any particle size control in the case of stirred batch reactions. Extended unstirred reactions (Figure 2.3) and these stirred reactions (Table 2.6) suggested an upper limit of approximately 90% yield for Cu-SAT synthesis. The continuous synthesis approached this limit in the continuous reactor (>80% yield at 90 °C and 120 min residence time). Further enhancing mass transfer by refinements in the reactor design may offer improvements at shorter residence times and lower temperatures.

Table 2.6 Comparison of the yield (Y, %), production rate (PR, mg h^{-1}), and space-time yield (STY, kg m^{-3} day^{-1}) for batch and continuous millifluidic syntheses of Cu-SAT across selected temperature (T, °C), reaction (or residence) time (RT, min), and concentration of reagents (COR, mmol mL^{-1}). Yields of batch reaction at 80 and 90 °C with 60 min reaction time were too low to provide a precise value.

Parameters			Batch			Batch (stirred)			Continuous		
T	RT	COR	Y	PR	STY	Y	PR	STY	Y	PR	STY
80	60	0.038	-	-	-	64	22	26.5	13	31	41.3
90	60	0.038	-	-	-	67	23	27.7	41.5	99	131.7
80	120	0.038	36	6	7.45	82	14	16.9	49.5	59	78.6
90	120	0.038	62	11	12.8	92	16	19.0	81.5	97	129.3
85	90	0.032	39	9	10.8	67	15	18.5	58	92	122.7
85	90	0.032	41	9	11.3	73	17	20.1	58	92	122.7

Note: The standard deviation (SD) values of yield in continuous synthesis are lower than 1%, and SD values of yield in batch reaction with or without stirring are lower than 5%. SD values of PR and STY in continuous synthesis are lower than 3 mg h^{-1} and 6 kg m^{-3} day^{-1}, respectively. SD values of PR and STY in in batch reaction with or without stirring are lower than 1 mg h^{-1} and 1 kg m^{-3} day^{-1}, respectively.

The stability of Cu-SAT prepared in the millifluidic reactor in aqueous solutions was tested by soaking this sample in deionized water for 3 days at 25 °C and for 10 h at 80 °C, as well as in aqueous HCl (pH 2.5) for 10 h at 25 °C. XRD patterns obtained after each treatment presented similar profiles to the as-synthesized material (Figure 2.11c), with new peaks emerging at low pH or high temperature after extended exposure. These peaks, likely arising from degradation phases, match those reported under similar conditions for batch-synthesized Cu-SAT [15]. ATR-FTIR spectra of samples made by both batch and continuous syntheses present similar peaks and intensities (Figure 2.11d). There are strong absorption peaks at 1190, 1068, 620 and 530 cm^{-1}, which can be assigned to the main characteristic peaks of the sulfonate group [71]. The band around 1190 cm^{-1} is also attributed to the stretching vibration of the C-N bond [72]. The peak around 3300 cm^{-1} indicates amino groups in these samples [73]. Multiple absorption peaks in the range 1450 to 1650 cm^{-1} can be attributed to the skeleton vibration of the benzene rings [74], and absorption peaks in the range 650 to 900 cm^{-1} are assigned to the out-of-plane C-H bending vibration of the aromatic ring

[75] in these materials. TGA for Cu-SAT prepared in the millifluidic reactor indicated no mass loss below 200 °C (Figure 2.11e) followed by a series of mass losses, likely attributed to the initial release of DMF molecules between 218 to 254 °C followed by ligand decomposition.

Table 2.7 CHNS analysis by weight (wt%) for Cu-SAT. The elemental fractions (wt%) for the Cu-SAT unit cell (SC-XRD, Table 2.4) are included for comparison.

Sample	N (wt %)	C (wt %)	H (wt %)	S (wt %)	Ratio of N (wt %) to S (wt %)
Cu SAT batch a	16.49	30.15	2.99	9.85	1.67
Cu SAT batch b	15.80	28.68	2.82	9.60	1.65
Cu SAT flow a	16.29	29.50	2.96	8.88	1.83
Cu SAT flow b	16.36	29.24	2.95	9.55	1.71
AVG (wt %)	16.23 ± 0.30	29.39 ± 0.61	2.93 ± 0.07	9.47 ± 0.42	1.71 ± 0.06
Cu-SAT formula without DMF	18.21	27.31	2.61	10.39	1.75
Cu-SAT formula with DMF	18.35	28.68	2.54	9.86	1.86

Table 2.8 CHNS analysis as molar ratios (H = 1) for Cu-SAT. The elemental ratios for the Cu-SAT unit cell (SC-XRD, Table 2.4) are included for comparison.

Sample	N	C	H	S	Ratio of N to S
Cu SAT batch a	0.40	0.85	1.00	0.10	4.00
Cu SAT batch b	0.40	0.85	1.00	0.11	3.77
Cu SAT flow a	0.40	0.84	1.00	0.09	4.20
Cu SAT flow b	0.40	0.83	1.00	0.10	3.92
AVG	0.40	0.84 ± 0.01	1.00	0.10 ± 0.01	3.97 ± 0.18
Cu-SAT formula without DMF	0.50	0.88	1.00	0.13	4.00
Cu-SAT formula with DMF	0.52	0.94	1.00	0.12	4.25

To examine the elemental composition and chemical states in continuously synthesized Cu-SAT, CHNS and XPS analysis were carried out. Tables 2.7 and 2.8 present CHNS analysis results of batch and millifluidic synthesis products, confirming agreement with the molecular formula of Cu-SAT from SC-XRD ($C_{14}H_{16}N_8O_8S_2Cu_2$ including an additional retained DMF, C_3H_7NO, per formula unit). The ratio of N to S was 3.97 ± 0.18 compared to a ratio of 4 expected for Cu-SAT without any residual DMF.

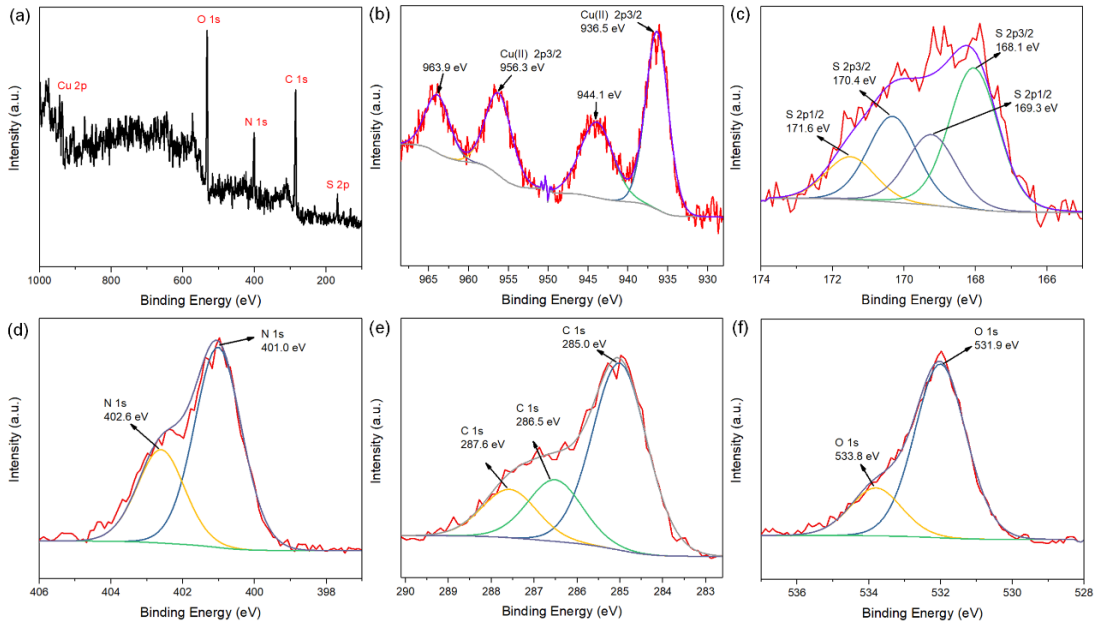

Figure 2.12 XPS results of the Cu-SAT synthesized with a residence time of 120 min at 80 °C in flow: (a) survey spectrum, and high resolution scans of: (b) Cu 2p, (c) S 2p, (d) N 1s, (e) C 1s and (f) O 1s photoelectron regions.

Figure 2.12a is the survey spectrum of the Cu-SAT synthesized with a residence time of 120 min at 80 °C in flow. The high resolution spectrum of the Cu 2p photoelectron region (Figure 2.12b) shows the presence of Cu(II), denoted by $2p_{3/2}$ - $2p_{1/2}$ peaks (at 936.5 and 956.3 eV respectively) as well as two highly distinctive satellite peaks (at 944.1 and 963.9 eV) [76]. The high resolution spectrum of the S 2p photoelectron region shows peaks at 168.1 and 169.3 eV belonging to the SO_3^{2-} group in this sample (Figure 2.12c) [77], and peaks at 170.4 and 171.6 eV associated with the SO_4^{2-} group, which may be oxidized SO_3^{2-} groups. The high resolution spectrum of the N 1s photoelectron region shows peaks at a binding energy of 401.0 eV for C–N bonds [78] and also 402.6 eV representing NO_3^- which might come from copper nitrate (Figure 2.12d) [79]. The C 1s photoelectron region shows peaks at 285 eV belonging to C-C and C-H bonds [80], whilst peaks at 286.5 eV and 287.8 eV are associated with C-OH and C=O bonds respectively, which may derive from the environment (Figure 2.12e) [81]. The O 1s photoelectron region shows peaks at binding energies of 531.9 eV, representing SO_3^{2-}/SO_4^{2-} groups in this sample [82], and also at 533.8 eV which can be assigned to either C=O groups [83] or H-O groups from environment water (Figure 2.12f) [84]. Minor features were attributed to either surface degradation, residual solvent or adventitious sources. Individual crystalline Cu-SAT particles prepared in flow were further characterized by SED and STEM-EDS. Figure

2.13 presents annular dark field STEM and corresponding electron diffraction patterns indexed to our reported Cu-SAT structure. Elemental mapping by STEM-EDS confirmed a homogeneous distribution of constituent elements Cu, S, O, N and C across individual single crystals (Figure 2.14).

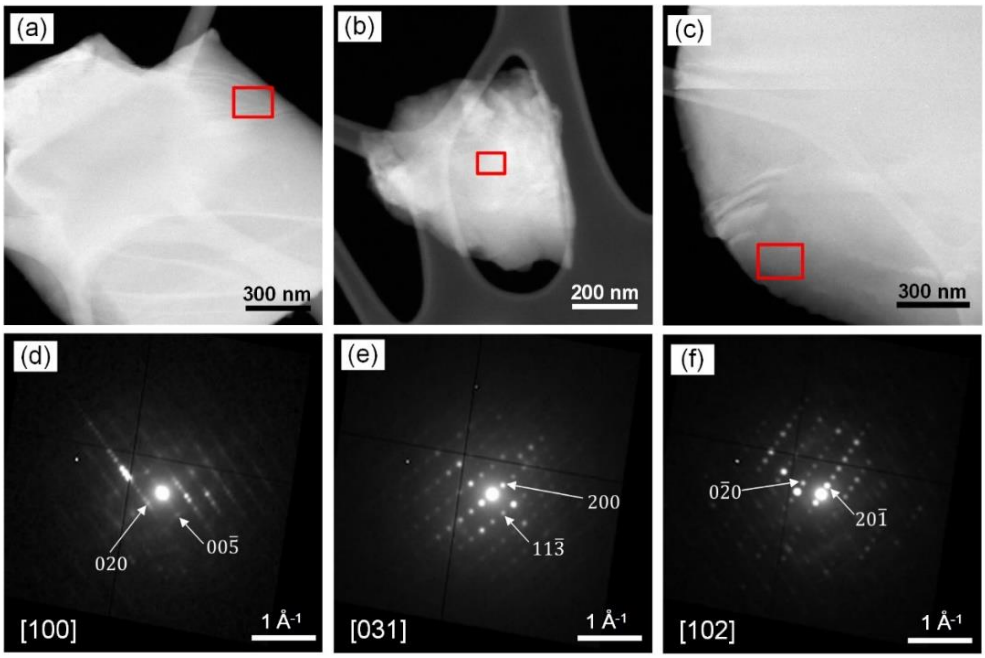

Figure 2.13 (a), (b) and (c) annular dark field STEM images of Cu-SAT particles synthesized in flow; (d), (e) and (f) are the corresponding diffraction patterns extracted from scanning electron diffraction data in the areas marked by the red rectangles.

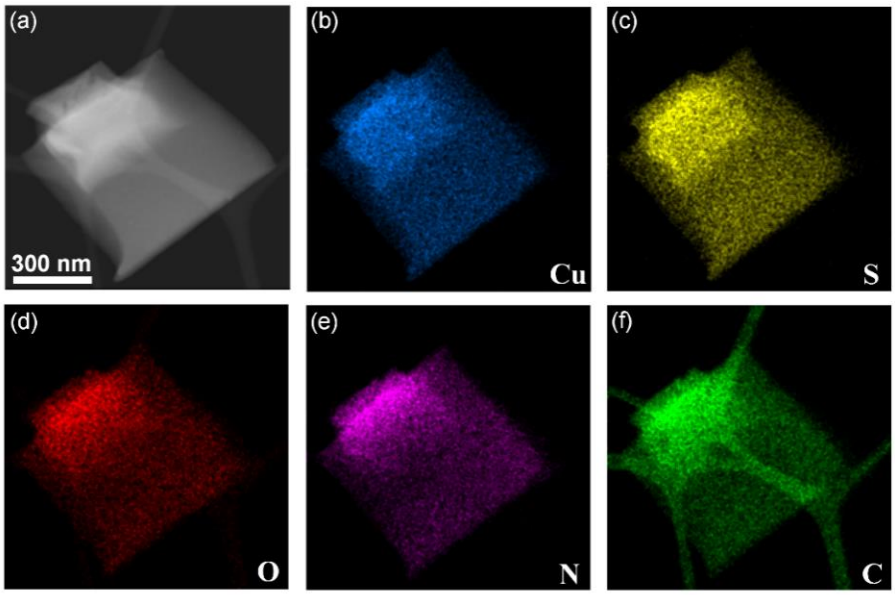

Figure 2.14 (a) STEM Annular Dark Field image of a Cu-SAT particle synthesized with a 120 min residence time at 80 °C in flow, and STEM-EDS elemental maps of: (b) Copper, (c) Sulphur, (d) Oxygen, (e) Nitrogen and (f) Carbon.

Table 2.9 Reaction parameters of 11 separate experiments used in a factorial design approach and the corresponding reaction results. Abbreviations in this table: Reaction temperature (T), Residence time (RT), Concentration of reagents (COR), Particle size (PS), Particle size interquartile range (PS IQR).

Experiments	Run order	T (°C)	RT (min)	COR (mmol/mL)	PS (μm)	PS IQR (μm)	Yield (%)
1	1	80	60	0.026	32	23	10.5
2	8	90	60	0.026	89	48	38.5
3	2	80	120	0.026	73	32	38
4	9	90	120	0.026	223	89	78
5	3	80	60	0.038	35	13	13
6	10	90	60	0.038	101	51	41.5
7	4	80	120	0.038	81	21	49.5
8	11	90	120	0.038	282	120	81.5
9	5	85	90	0.032	90	48	58
10	6	85	90	0.032	92	49	58
11	7	85	90	0.032	93	50	59

We next turned to a systematic exploration of the response of the millifluidic synthesis platform for Cu-SAT. Factorial experimental design enabled examination of all possible combinations of reaction parameters. The growth of MOF crystals is usually affected by reaction temperature, time, and concentration of reagents, with reaction yield and sample size being determined by these parameters. In our flow reactor, we can run continuous synthesis with reaction temperatures ranging between 80 and 90 °C, residences time from 60 to 120 min and reagent concentrations between 0.026 and 0.038 mmol mL^{-1}. In order to understand the trade-off between the continuous reaction parameters and the results, a factorial DoE with 8 experiments was created by varying each parameter between the lower and upper bounds and with 3 repeats at intermediate values. The standard deviations for yield, particle size, and particle size IQR in these 3 repeated experiments were 0.58%, 1.5 μm, and 1.4 μm, respectively. Figure 2.2 shows a visualization of this design. The designed experiments with the different reaction parameters and the corresponding results for reaction yield, particle size and particle size IQR are listed in Table 2.9.

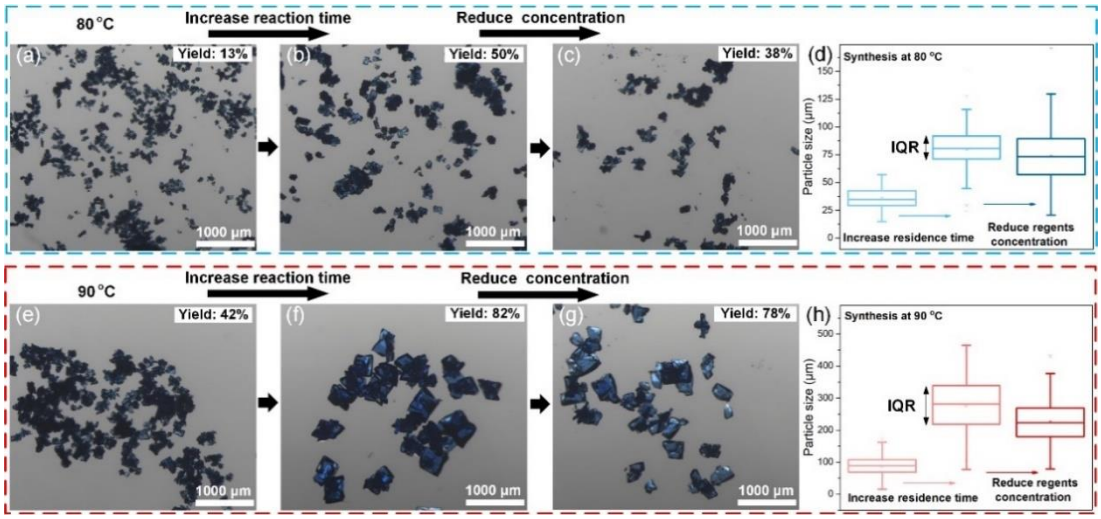

Figure 2.15 Cu-SAT particle size results for different continuous reaction conditions. Light micrographs of Cu-SAT made at 80 °C in flow: (a) 60 min residence time, (b) 120 min residence time, (c) 120 min residence time with a lower concentration of reagents, together with (d) a Box plot of the particle size in the three samples. Light Micrographs of Cu-SAT made at 90 °C in flow, (e) 60 min residence time, (f) 120 min residence time, (g) 120 min residence time with a lower concentration of reagents, together with (h) a Box plot of the particle size in the three samples.

Figure 2.15 presents light micrographs of continuously synthesized samples together with box plots of particle size. Keeping the temperature constant at 80 °C but increasing the reaction time from 60 to 120 minutes resulted in an increased yield from 13 to 50%. Particle sizes likewise increased with reaction time (Figure 2.15a and b) with the median particle size increasing from 35 to 81 µm but with an increase in the spread of particles sizes reflected in an increased particle size IQR from 13 to 21 µm. Reducing the reagent concentrations (from 0.038 to 0.026 mmol/mL) resulted in a reduced yield of 38% (Figure 2.15c) with a moderate reduction in median particle size (73 µm) and a substantially broadened particle size distribution (particle size IQR 32 µm).

Similar trends were observed at 90 °C (Figure 2.15e-h) with a doubling of the reaction time giving rise to an increased yield from 42% to 82%. Much larger particles were produced with median particle sizes at 90 °C recorded at 101 and 282 µm (particle size IQR 51 and 120 µm), respectively. As for the lower temperature synthesis, a small reduction in particle size (223 µm) and yield was observed when using a reduced concentration of reagents (Figure 2.15g). Notably, a change in the response of the particle size dispersity (particle size IQR) was observed when reducing reagent concentrations at 90 °C. Whereas at lower temperature, the spread of sizes increased

for reduced concentrations, the particle size IQR instead decreased at higher temperature for the more dilute reaction conditions.

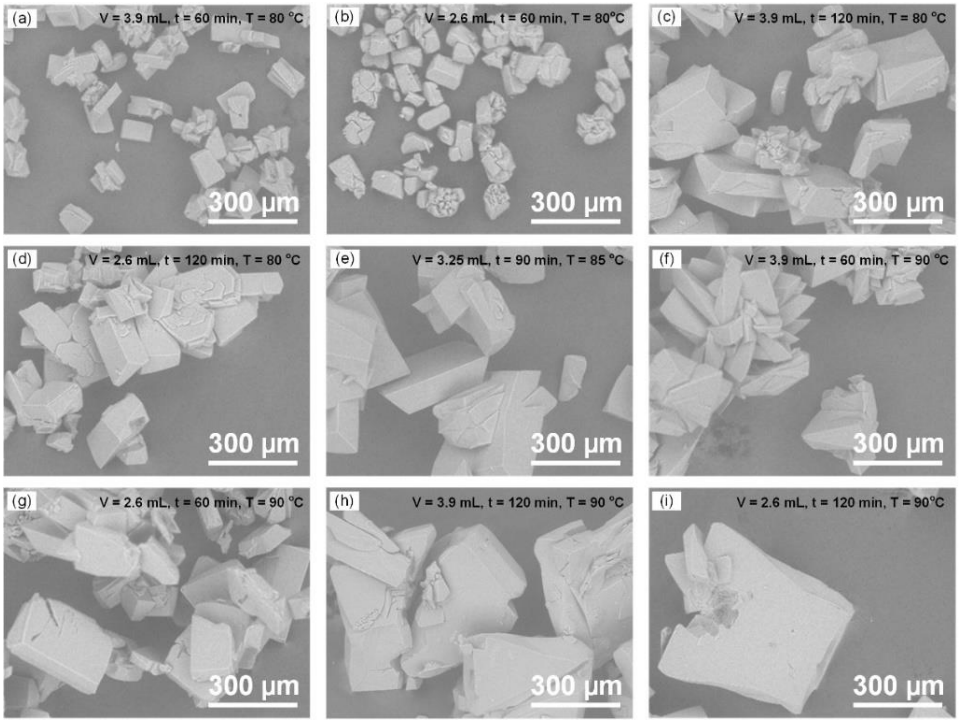

Figure 2.16 SEM micrographs of different samples made by continuous synthesis under different reaction conditions.

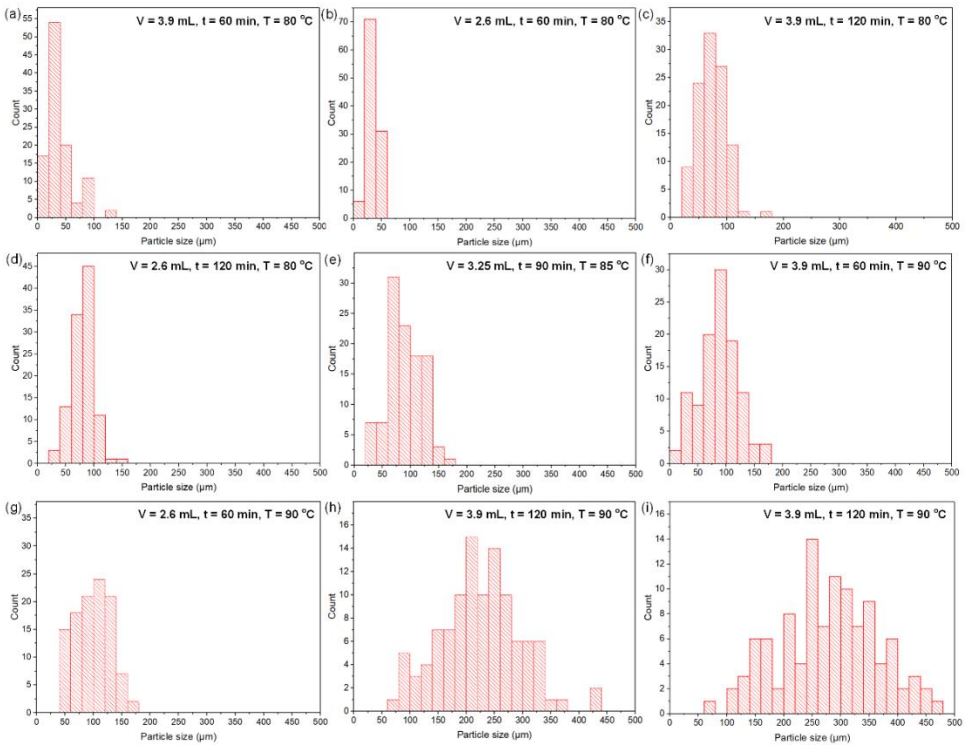

Figure 2.17 Histograms of particle size from different samples made by continuous synthesis using different reaction parameters.

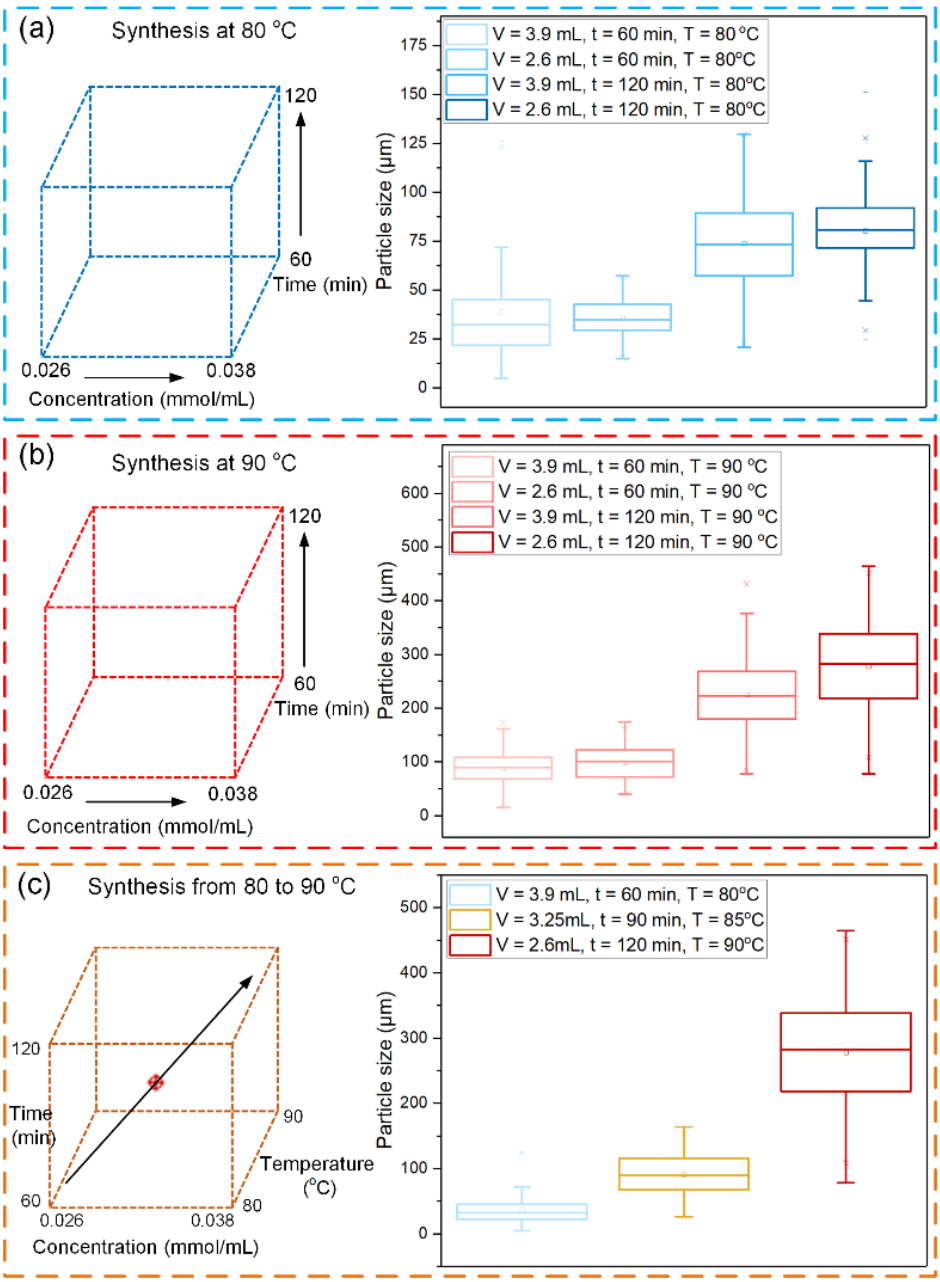

Figure 2.18 Box plot of particle size from different samples made by continuous synthesis at: (a) 80 °C, (b) 90 °C and (c) synthesized at three different temperatures.

Figure 2.16 presents SEM micrographs of samples made using the millifluidic reactor across a range of operating parameters. The crystals consistently presented smooth surfaces with sharp faceting. To aid in additional visualization, Figure 2.17 and 2.18 show histograms and box plots of particle size for millifluidic reaction products. Together, the observations on particle size consistently show that larger crystals were produced for longer reaction times and higher reaction temperatures.

Using the results from the 11 experiments of the DoE, linear response surface modelling was used to identify the trade-offs between the reaction parameters and the

reaction yield and particle size dispersity. The fitted regression equations for yield, particle size and particle size IQR are given in Table 2.3, here we focus on the key terms and trends. Figure 2.19a depicts the contour plot of the fitted response for reaction yield. The response is primarily affected by synthesis temperature and time in linear terms. The response of particle size was similarly found to depend on reaction time and temperature as well as one further statistically significant cross-term between time and temperature (Figure 2.19b). A more complex response was determined for particle size IQR (Figure 2.19c). The response of particle size IQR included significant contributions from reaction temperature, time, concentration of reagents and their cross terms. In these three equations, a minimal set of terms was used, keeping only terms that showed strong effects in an analysis of variance. The limited number of conditions constrains the model complexity, and there is potential for overfitting for a large number of coefficients as retained for the particle size IQR analysis. Nevertheless, our main finding in particle size IQR is that the response incorporates a more complex dependence.

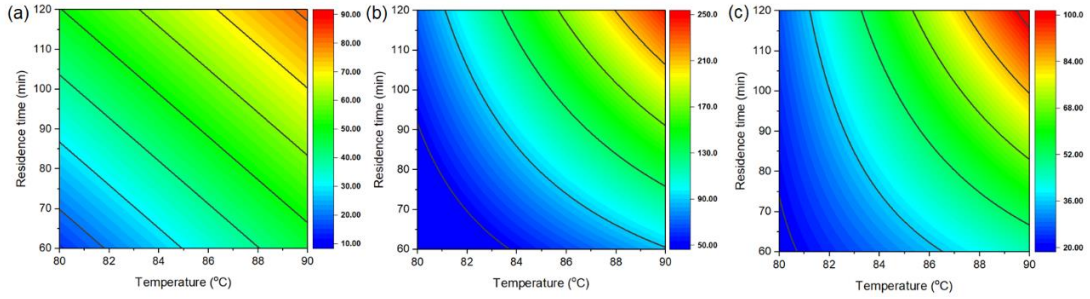

Figure 2.19 Linear response surface modelling results based on DoE. Contour plots of: (a) reaction yield (b) particle size and (c) particle size IQR as a function of synthesis temperature and time with concentration of reagents all equal to 0.032 mmol/ml.

The linear response modelling approach here is largely phenomenological, requiring wider refinement of MOF crystallization and growth models to gain additional mechanistic insights. However, this approach outlines a route for using a small number of experiments to rapidly identify characteristics of synthetic response. The contour plots exhibit a striking resemblance to a factorial DoE approach applied to the hydrothermal synthesis of MIL-88A(Fe), requiring the use of two-variable terms (cross-terms or quadratic terms) for particle size response characteristics [85]. Wider application to other systems will support the development of a library of similar and distinctive response characteristics for different MOF chemistries or reactors.

The shape of these response surfaces, nevertheless, do provide a qualitative method to assess prevailing MOF crystal growth theories. The dominant mechanism controlling crystal growth, whether determined by the rate of nucleation events (and whether homogeneous or autocatalytic [85-87]) or the rate of crystal growth, has often been a goal in MOF kinetics studies, whether applying Avrami- or Gualtieri-type kinetic models [88]. Many carboxylate-based MOFs including HKUST-1 [89], MIL-101(Al) [90], and MIL-88A(Fe) [85] show a dominant effect of the faster nucleation rate (i.e. a lower activation energy for nucleation than for growth). Similar characteristics are also seen in polymers, cast instead in terms of initiation and propagation rates [91], integral steps also identified in modelling MOF kinetics [87]. As for polymers, MOFs exhibiting a lower activation energy for nucleation (initiation) will see a broadened particle size (molecular weight) distribution or polydispersity at increased temperature. This is likewise the characteristic behavior observed in millifluidic synthesis of Cu-SAT, with more dilute conditions additionally reducing the driving force for nucleation and thereby reducing the dispersity (particle size IQR). We therefore infer that Cu-SAT exhibits the predominant characteristics of nucleation-dominated crystallization. Further kinetic studies exploring short-timescale crystallization in Cu-SAT may offer additional testing of this hypothesis, but this is beyond the focus of the millifluidic reactor parameter optimization for Cu-SAT production.

Instead, we apply the linear response modelling to a Pareto front determination. Controlled MOF crystal growth offers a route to the maximization of yield, but simultaneously supports minimization of particle size dispersity, outlining a multi-objective challenge. Figure 2.20 presents a plot highlighting the results in terms of these two objective axes, yield and particle size IQR. Light grey points are generated from the simulated equations for yield and particle size IQR, showing the linear response model values, and blue points mark the experimental data points. This plot further validates the model fit, with the distribution of the experimental data points captured by the shape of the predictions made by the response surface. Deviations between the experiment and model values reflects the precision offered in the analysis. The root mean square error (RMSE) of yield and particle size IQR comparing model and experimental DoE values were 4.9% and 2.5 μm, respectively. The Pareto front was, in turn, extracted from discrete evaluation of the linear response surface model,

with the maximum yield and minimum particle size IQR highlighted in red. These points establish the set of optima possible within the constraints of the reactor operating parameters, highlighting the trade-off between increasing yield and sacrificing a narrow particle size distribution. Alternative reactor designs supporting smaller slug sizes while retaining a stable slug flow pattern may present routes to modifying this trade-off.

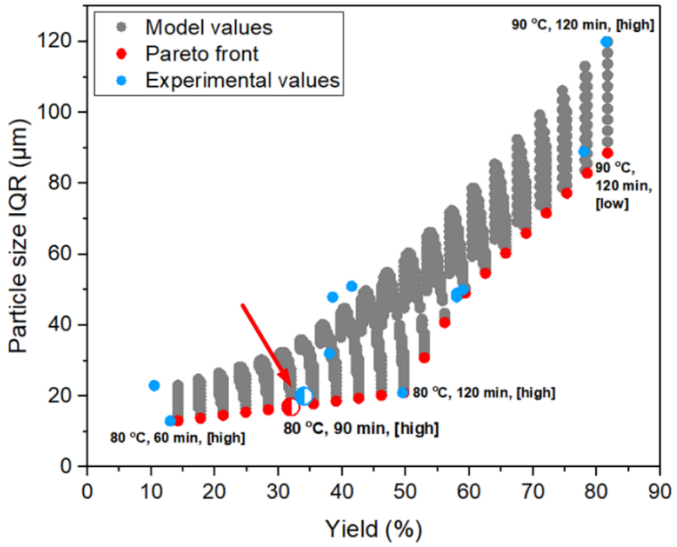

Figure 2.20 Pareto front plot of yield to particle size IQR. Experimental values are shown in blue. Model values are shown in gray with the Pareto front marked in red. Half-filled circles show selected conditions for comparing the model (red) and experimental response (blue).

To further establish the predictive value of the linear response model within the existing operating parameters, we selected a model value (Figure 2.20) on the Pareto front for reaction conditions of 90 min residence time at 80 °C with reagent concentration of 0.038 mmol mL^{-1}. The experimental reaction at these conditions exhibited matched yield and particle size IQR. The experimental yield differed from the model by 2% (34% for experimental yield compared to a 32% predicted yield), a small difference in the context of yields spanning approximately 15 to 85%. The experimental particle size IQR differed from the model by 3 µm (20 µm for experimental particle size IQR as compared with a 17 µm predicted IQR), likewise small relative to the range of particle size IQR values recorded from approximately 10 to 120 µm. The results of this validation experiment were also consistent with the variation expected from the RMSE for yield and particle size IQR (4.9% and 2.5 µm, respectively). This minimal, systematic DoE approach with robust interpolation across significant variation in yield and particle size distribution characteristics provides a

step toward benchmarking and comparison of the multi-parameter response of MOF growth between other sulfonate and non-sulfonate MOFs.

2.3.3 Membrane Fabrication and Proton Conductivity Measurements

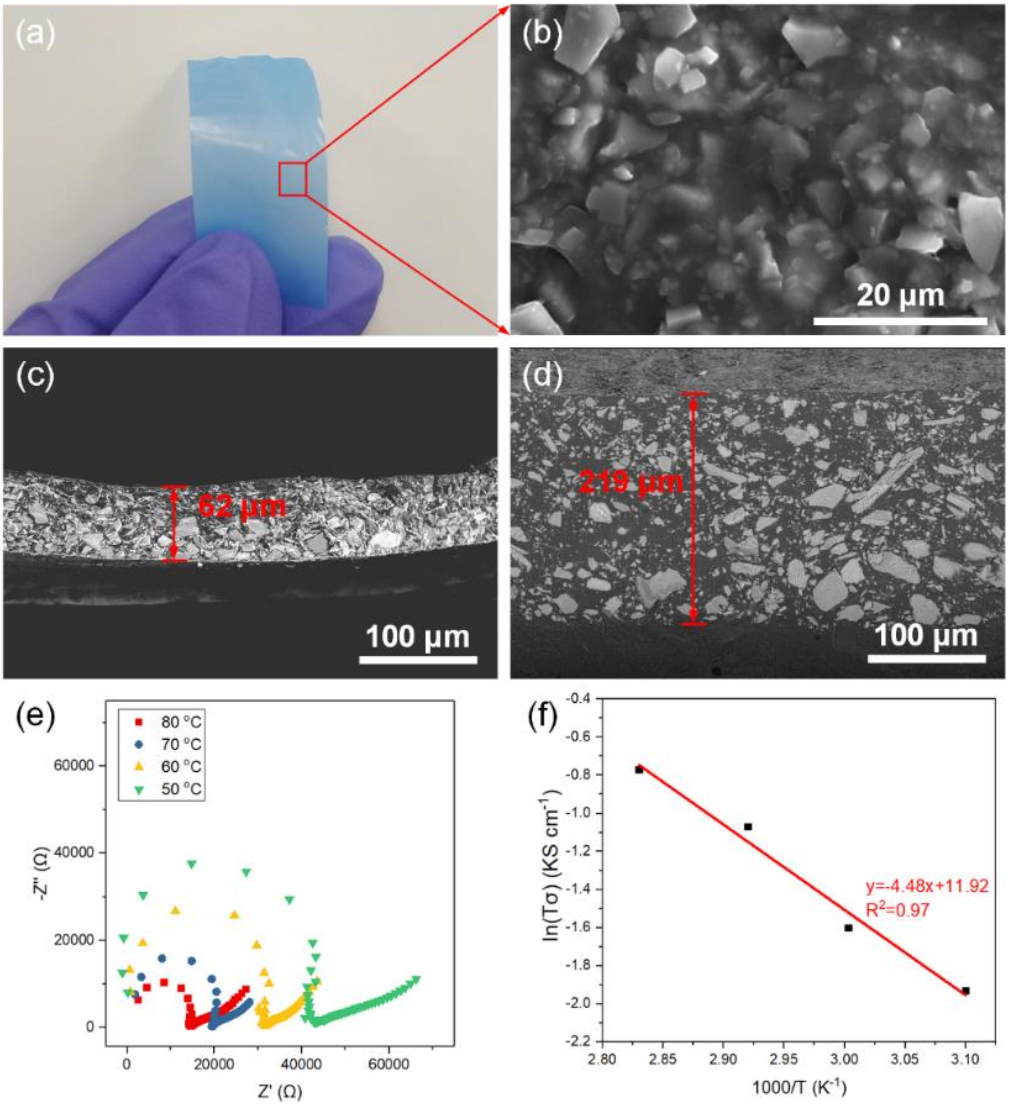

Figure 2.21 Results of proton conduction membrane fabrication using continuously synthesized Cu-SAT: (a) Digital and (b) SEM images of MMM-60 wt%, and cryo SEM micrographs of cross section of (c) the dry membrane and (d) the fully hydrated MMM-60 wt%, (e) Nyquist plots depicting the complex impedance as measured by electrochemical impedance spectroscopy and (f) Arrhenius plots of MMM-60 wt% conductivities for different temperatures at 95 % RH.

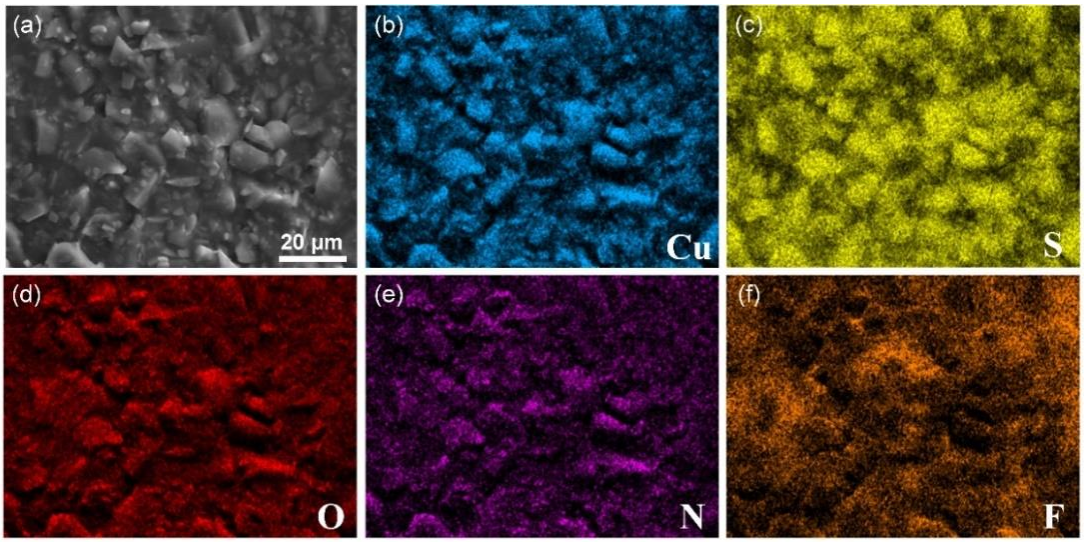

Figure 2.22 (a) SEM image of the MMM-60 wt% membrane, and SEM-EDS elemental maps of: (b) Copper, (c) Sulphur, (d) Oxygen, (e) Nitrogen and (f) Fluorine.

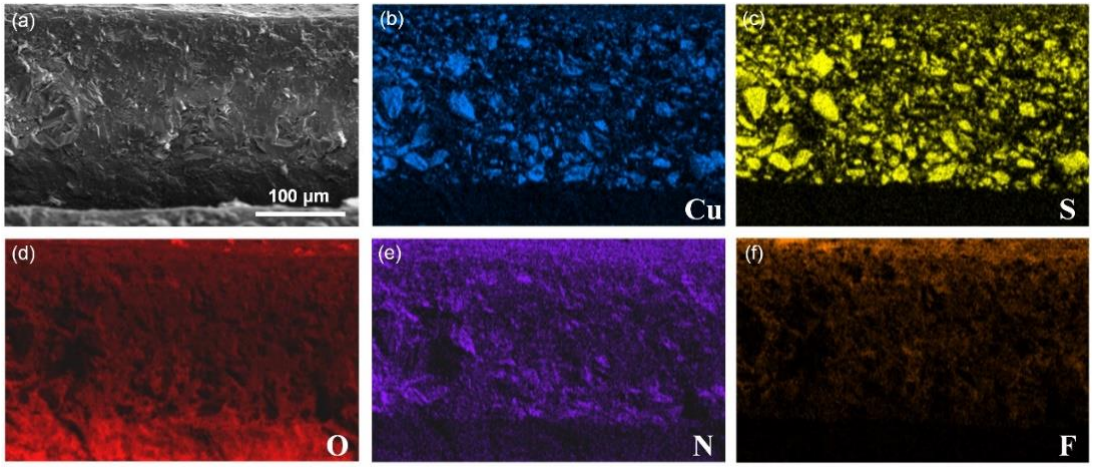

Figure 2.23 (a) Cryo-SEM cross-sectional image of the fully hydrated MMM-60 wt% membrane, and SEM-EDS elemental maps of: (b) Copper, (c) Sulphur, (d) Oxygen, (e) Nitrogen and (f) Fluorine.

MMMs were fabricated using Cu-SAT prepared by millifluidic synthesis in order to demonstrate the proton-conducting properties and potential use in fuel cell applications. MMMs were prepared using 60 wt% Cu-SAT and a blend of PVP and PVDF, matching previous MMM designs for Cu-SAT [15]. Figure 2.21a shows a digital photograph of MMM-60 wt%, exhibiting a similar blue color to Cu-SAT. The Cu-SAT particles were incorporated throughout the polymer matrix (Figure 2.21b). Cryo-SEM was used to determine the hydrated membrane thickness, as the polymer membrane swells during water uptake. As shown in Figures 2.21c and d, the thickness of dry membrane was approximately 62 µm and increased to approximately 219 µm

when fully hydrated, attributed to the hydrophilic behavior of PVP. Figures 2.22 and 2.23 show EDS mapping of the membrane both in plan view and in cross section, further confirming the dispersion of the MOF particles throughout the membrane. Figure 2.24 shows X-ray computed tomography of MMM-60 wt%, presented in orthogonal slices through the tomographic volume as well as in a volume rendering. 3D analysis indicated some asymmetry in the distribution of the largest particles but corroborates the distribution of Cu-SAT throughout the composite membrane. Further refinements of particle size control and membrane casting may enhance overall membrane performance further.

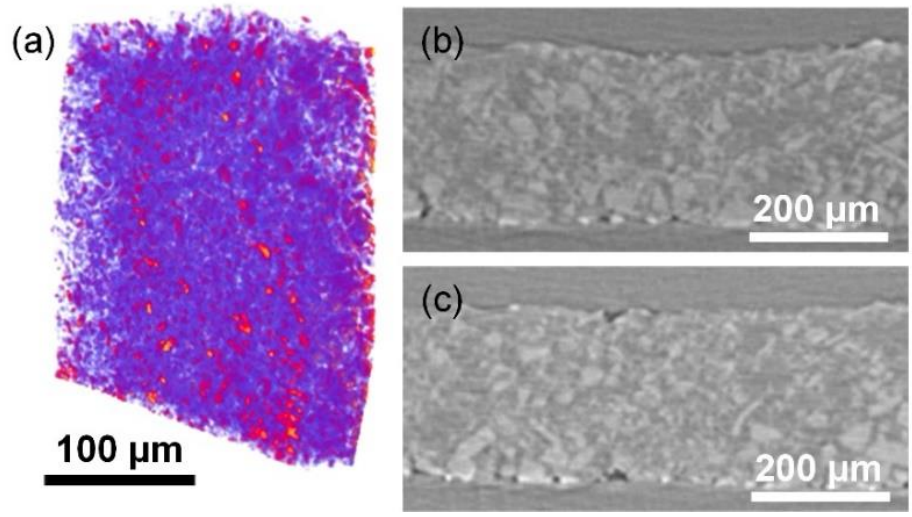

Figure 2.24 X-ray computed tomography images of: (a) the 3D structure of MMM-60%, (b) and (c) cross-sectional images of MMM-60 wt% from different areas.

Figure 2.21e shows the EIS results of MMM-60 wt% tested under different temperatures at 95% RH. The resistance decreased from 4.29×10^3 Ω to 1.45×10^3 Ω as the temperature increased from 50 to 80 °C, enabling determination of the activation energy E_a (Figure 2.21f). The activation energy of MMM-60 wt% was determined to be 37 ± 3 kJ mol^{-1} or 0.39 ± 0.04 eV (uncertainties given as the standard error), a value consistent with a predominantly Grotthuss mechanism, which ranges from 14 to 40 kJ mol^{-1} ($E_a < 0.4$ eV) [92]. The proton conductivity results of MMM-60 wt% determined using CV showed results similar to those by EIS, the highest proton conductivity recorded by CV as 1.26 mS cm^{-1} at 80 °C in 95% RH, and the E_a determined from CV (Figures 2.25c and d) was 35 ± 4 kJ mol^{-1} or 0.36 ± 0.04 eV (uncertainties given as the standard error).

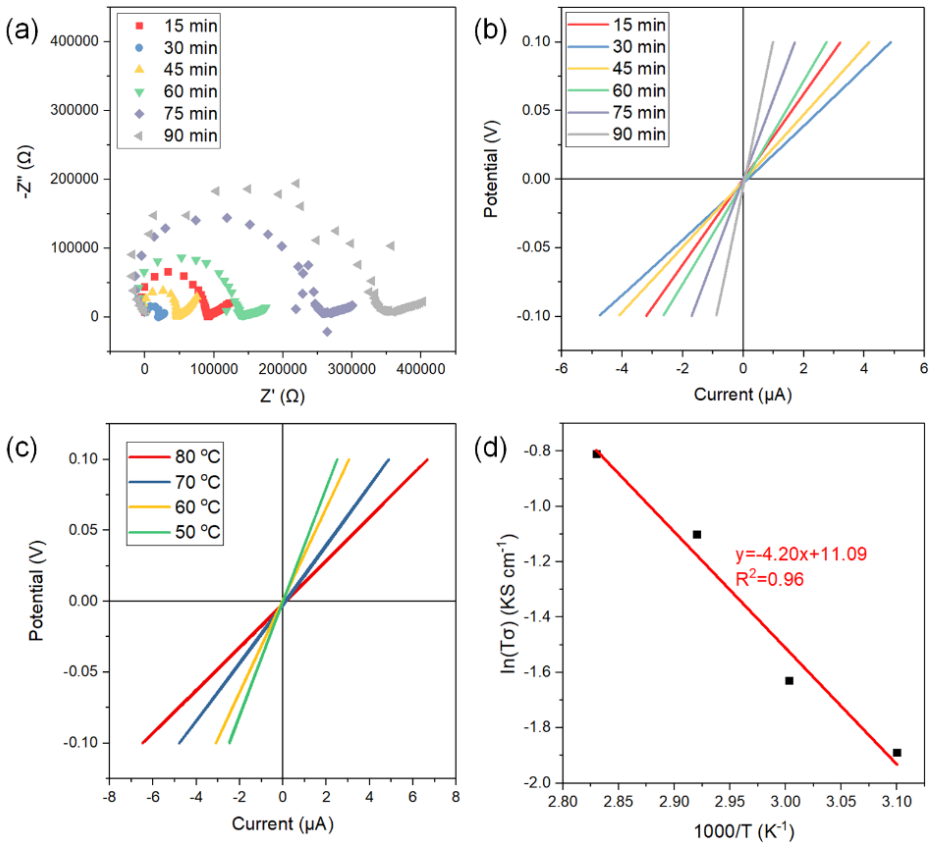

Figure 2.25 (a) EIS and (b) CV results of MMM-60 wt% membrane measured at different times after the temperature reached 70 °C in 95% RH, (c) CV and (d) Arrhenius plots of MMM-60% at different temperatures in 95% RH.

Table 2.10 Proton conductivities of MMM-60 wt% measured at different temperatures in 95 % RH.

Temperature (°C)	Conductivity from EIS (mS cm^{-1})	Conductivity from CV (mS cm^{-1})
80	1.33	1.26
70	0.98	0.97
60	0.62	0.59
50	0.45	0.47

Table 2.11 Replicate proton conductivities of MMM-60 wt% based on EIS tests at different temperatures in 95 % RH. Uncertainties are given as one standard deviation.

Temperature (°C)	Conductivity from EIS (mS cm^{-1})			AVG (mS cm^{-1})
80	1.33	1.29	1.39	1.34 ± 0.05
70	0.98	0.92	--	0.95 ± 0.04
60	0.62	0.65	--	0.64 ± 0.02
50	0.45	0.51	--	0.48 ± 0.04

The best proton conductivity of MMM-60 wt% determined by EIS was 1.34 ± 0.05 mS cm^{-1} at 80 °C and 95% RH, surpassing previous reports for Cu-SAT PVP/PVDF membranes of 0.8 mS cm^{-1} at 80 °C and 98% RH [15]. A full set of proton conductivities for MMM-60 wt% determined by EIS and CV in 95% RH and at different temperatures is given in Table 2.10 and 2.11. The MMM-60 wt% membrane reported here compares favorably to recently reported MOFs or MOF-based PEMs, such as phosphonate-based MOFs with a proton conductivity of 0.05 mS cm^{-1} at 90 °C and 98% RH [93], phenyl acyl thiourea carboxylate-based MOFs with a proton conductivity of 0.18 mS cm^{-1} at 100 °C and 98% RH [68], Ni-MOFs in a polyacrylonitrile nanofiber membrane with a proton conductivity of 0.06 mS cm^{-1} at 90 °C and 90% RH [94], and Cu-MOF/ PVP/PVDF composite membrane with a proton conductivity up to 0.44 mS cm^{-1} at 80 °C and 98% RH [95]. While these comparisons are not exhaustive and encompass many complex variables, millifluidic-synthesized Cu-SAT represents a competitive candidate material for further development of MMMs for fuel cell applications. Extending the stability of Cu-SAT and optimization of the interplay of mechanical and chemical properties of the Cu-SAT-polymer membrane offer routes to further improvements in composite performance. MOFs developed for these applications tend to be tested as pellets or as MMMs without reported particle size optimization [11, 15, 96, 97], and work on controlled particle size is underway to pursue this route to further advances in MMM design.

2.4 Conclusions

We have synthesized Cu-SAT, a mixed linker MOF incorporating both sulfonate and amine groups and carried out single crystal structure determination, significant materials characterization, and evaluation of synthetic parameters. Cu-SAT synthesis was transferred from batch solvothermal synthesis to a continuous synthesis using a millifluidic flow reactor, demonstrating more than five hours sustained production rate and consistent sample quality. The reactor parameters enable facile control of Cu-SAT particle size and particle size dispersity by adjusting residence time, temperature, and reagent concentration. We have employed a factorial DoE approach to quantify these trends, extracting a predictive linear response model indicating nucleation driven-growth processes. The reaction yields in the flow reactor were 10 to 20% higher than corresponding batch reactions using the same reaction parameters, indicating

improved mass and heat transfer in flow synthesis. These findings establish a new mode of sulfonate MOF synthesis in a generalizable, fouling-free slug-flow reactor.

Finally, the continuously synthesized Cu-SAT MOF was incorporated with PVP and PVDF polymers for PEMs application, and this membrane presented a proton conductivity of 1.34 ± 0.05 mS cm^{-1} at 80 °C and 95% RH. Further engineering of the membrane internal interfaces, mixed membrane composition, and optimization of particle size for MMMs, offer routes to the implementation of composite MOF materials for fuel cell applications, underpinned by reproducible sulfonate MOF crystal growth in continuous flow synthesis.

2.5 References

[1] T. Ghanbari, F. Abnisa, M. Wan, A Review on Production of Metal Organic Frameworks (MOF) for CO_2 Adsorption, Sci. Total Environ. 707 (2019) 135090.

[2] K. Wang, Y. Li, L.H. Xie, X. Li, J.R. Li, Construction and application of base-stable MOFs: a critical review, Chem. Soc. Rev. (2022) 6417-6441.

[3] X.L. Hu, K. Wang, X. Li, Q.Q. Pan, Z.M. Su, Two Anthracene Chromophores based Metal-Organic Frameworks for Gas Absorption and Promising Nitro Aromatic Sensing, New J. Chem. 44 (2020) 1249-1252.

[4] H. Li, K. Wang, Y. Sun, C.T. Lollar, J. Li, H.C. Zhou, Recent advances in gas storage and separation using metal-organic frameworks, Mater. Today 21 (2018) 108-121.

[5] D. Lv, P. Zhou, J. Xu, S. Tu, F. Xu, J. Yan, H. Xi, W. Yuan, Q. Fu, X. Chen, Q. Xia, Recent advances in adsorptive separation of ethane and ethylene by C_2H_6-selective MOFs and other adsorbents, Chem. Eng. J. 431 (2022) 133208-133230.

[6] L. Mitchell, B. Gonzalezsantiago, J.P.S. Mowat, M.E. Gunn, P. Williamson, N. Acerbi, M.L. Clarke, P.A. Wright, CCYG, Remarkable Lewis acid catalytic performance of the scandium trimesate metal organic framework MIL-100(Sc) for C–C and C-N bond-forming reactions, Catal. Sci. Technol. 3 (2012) 606-617.

[7] D. Yang, B.C. Gates, Catalysis by Metal Organic Frameworks: Perspective and Suggestions for Future Research, ACS Catal. 9 (2019) 1779-1798.

[8] D.W. Lim, H. Kitagawa, Proton Transport in Metal-Organic Frameworks, Chem. Rev. 120 (2020) 8416-8467.

[9] D.W. Lim, H. Kitagawa, Rational strategies for proton-conductive metal-organic frameworks, Chem. Soc. Rev. 50 (2021) 6349-6368.

[10] G.M. Wu, M.Y. Zhang, F.D. Wang, C.X. Zhang, Q.L. Wang, A dual-function Cd-MOF with high proton conduction and excellent fluorescence detection of pyridine, Dalton T. 51 (2022) 6687-6695.

[11] Y. Li, J. Feng, L. Wang, G. Li, High proton conduction in two highly stable phenyl imidazole dicarboxylate-based Cd(II)-MOFs, J. Solid State Chem. 319 (2023) 123828.

[12] K. Biradha, A. Goswami, R. Moi, S. Saha, Metal–organic frameworks as proton conductors: strategies for improved proton conductivity, Dalton T. 50 (2021) 10655-10673.

[13] H.A. Patel, N. Mansor, S. Gadipelli, D.J. Brett, Z. Guo, Superacidity in Nafion/MOF Hybrid Membranes Retains Water at Low Humidity to Enhance Proton Conduction for Fuel Cells, ACS Appl. Mater. Inter. 8 (2016) 30687-30691.

[14] G. Zhang, H. Fei, Synthesis and Applications of Porous Organosulfonate-Based Metal-Organic Frameworks, Top Curr. Chem. 377 (2019) 32.

[15] R. Moi, A. Ghorai, S. Banerjee, K. Biradha, Amino and Sulfonate Functionalized Metal-Organic Framework for Fabrication of Proton Exchange Membranes with Improved Proton Conductivity, Cryst. Growth Des. 20 (2020) 5557-5563.

[16] A.V. Desai, B. Joarder, A. Roy, P. Samanta, R. Babarao, S.K. Ghosh, Multifunctional Behavior of Sulfonate-Based Hydrolytically Stable Microporous Metal–Organic Frameworks, ACS Appl. Mater. Inter. 10 (2018) 39049-39055.

[17] Z. Li, G. He, Y. Zhao, Y. Cao, H. Wu, Y. Li, Z. Jiang, Enhanced proton conductivity of proton exchange membranes by incorporating sulfonated metal-organic frameworks, J. Power Sources 262 (2014) 372-379.

[18] X.Y. Dong, J.H. Wang, S.S. Liu, Z. Han, Q.j. Tang, Synergy between isomorphous acid and basic MOFs for anhydrous proton conduction of low-cost

hybrid membranes at high temperature, ACS Appl. Mater. Inter. 10 (2018) 38209-38216.
[19] V.V. Butova, A.P. Budnyk, E.A. Bulanova, C. Lamberti, A.V. Soldatov, Hydrothermal synthesis of high surface area ZIF-8 with minimal use of TEA, Solid State Sci. 69 (2017) 13-21.
[20] S.N. Tambat, P.K. Sane, S. Suresh, N. Varadan O, A.B. Pandit, S.M. Sontakke, Hydrothermal synthesis of NH_2-UiO-66 and its application for adsorptive removal of dye, Adv. Powder Technol. 29 (2018) 2626-2632.
[21] C.G. Lin, W. Zhou, X.T. Xiong, W. Xuan, P.J. Kitson, D.L. Long, W. Chen, Y.F. Song, L. Cronin, Digital Control of Multistep Hydrothermal Synthesis by Using 3D Printed Reactionware for the Synthesis of Metal-Organic Frameworks, Angew. Chem. Int. Ed. 57 (2018) 16716-16720.
[22] B. Zhang, Y. Luo, K. Kanyuck, N. Saenz, K. Reed, P. Zavalij, J. Mowery, G. Bauchan, Facile and template-free solvothermal synthesis of mesoporous/macroporous metal–organic framework nanosheets, RSC Adv. 8 (2018) 33059-33064.
[23] L.A. Lozano, C.M. Iglesias, B.M.C. Faroldi, M.A. Ulla, J.M. Zamaro, Efficient solvothermal synthesis of highly porous UiO-66 nanocrystals in dimethylformamide-free media, J. Mater. Sci. 53 (2017) 1862-1873.
[24] K. Kamal, M.A. Bustam, M. Ismail, D. Grekov, A. Mohd Shariff, P. Pre, Optimization of Washing Processes in Solvothermal Synthesis of Nickel-Based MOF-74, Materials 13 (2020) 2741.
[25] A.R. Abbasi, M. Rizvandi, Influence of the ultrasound-assisted synthesis of Cu-BTC metal-organic frameworks nanoparticles on uptake and release properties of rifampicin, Ultrason. Sonochem. 40 (2018) 465-471.
[26] A. Bakhshi, H. Saravani, G. Sargazi, M. Shahbakhsh, Ultrasound-assisted efficient synthesis of a novel Nd–MOF polymer as a new candidate for electrocatalytic activity in hydrogen storage, J. Appl. Electrochem. 51 (2020) 399-410.
[27] C. Forsyth, T. Taras, A. Johnson, J. Zagari, C. Collado, M.M. Hoffmann, C.R. Reed, Microwave Assisted Surfactant-Thermal Synthesis of Metal-Organic Framework Materials, Appl. Sci. 10 (2020) 4563.
[28] A. Laybourn, J. Katrib, R.S. Ferrari-John, C.G. Morris, S. Yang, O. Udoudo, T.L. Easun, C. Dodds, N.R. Champness, S.W. Kingman, Metal–organic frameworks in seconds via selective microwave heating, J. Mater. Chem. A 5 (2017) 7333-7338.
[29] I. Thomas Hillman, L.A. Stevens, M. Lange, J. Mllmer, W. Lewis, C. Dodds, S.W. Kingman, A. Laybourn, Developing a sustainable route to environmentally relevant metal–organic frameworks: ultra-rapid synthesis of MFM-300(Al) using microwave heating, Green Chem. 21 (2019) 5039-5045.
[30] D. Rambabu, S. Bhattacharyya, T. Singh, L.C. M, T.K. Maji, Stabilization of $MAPbBr_3$ Perovskite Quantum Dots on Perovskite MOFs by a One-Step Mechanochemical Synthesis, Inorg. Chem. 59 (2020) 1436-1443.
[31] J. Yang, X. Feng, G. Lu, Y. Li, C. Mao, Z. Wen, W. Yuan, NaCl as a solid solvent to assist the mechanochemical synthesis and post-synthesis of hierarchical porous MOFs with high I_2 vapour uptake, Dalton T. 47 (2018) 5065-5071.
[32] V. M. V, G. Nageswaran, Review—Direct Electrochemical Synthesis of Metal Organic Frameworks, J. Electrochem. Soc. 167 (2020) 155527.
[33] L.L. Jiang, X.z. Zeng, M.k. Li, M.Q. Wang, T.Y. Su, X.C. Tian, J. Tang, Rapid electrochemical synthesis of HKUST-1 on indium tin oxide, RSC Adv. 7 (2017) 9316-9320.

[34] A. Manz, J. Fettinger, E. Verpoorte, H. Lüdi, D.J. Harrison, Micromachining of monocrystalline silicon and glass for chemical analysis systems A look into next century's technology or just a fashionable craze?, Trac-Trend. Anal. Chem. 10 (2015) 144-149.
[35] J. Wang, Y. Song, Microfluidic Synthesis of Nanohybrids, Small 13 (2017) 1604084.
[36] I. Rossetti, M. Compagnoni, Chemical reaction engineering, process design and scale-up issues at the frontier of synthesis: Flow chemistry, Chem. Eng. J. 296 (2016) 56-70.
[37] O. Długosz, M. Banach, Inorganic nanoparticle synthesis in flow reactors – applications and future directions, React. Chem. Eng. 5 (2020) 1619-1641.
[38] C.T. Kung, H.Y. Gao, C.Y. Lee, Y.N. Wang, W.J. Dong, C.H. Ko, G. Wang, L.M. Fu, Microfluidic synthesis control technology and its application in drug delivery, bioimaging, biosensing, environmental analysis and cell analysis, Chem. Eng. J. 399 (2020) 125748.
[39] X. Wang, J. Liu, P. Wang, D. Andrew, L. Feng, X. Zhu, W. Wen, K. Rimantas, X. Gong, Synthesis of Biomaterials Utilizing Microfluidic Technology, Genes 9 (2018) 283.
[40] L. Falk, J.M. Commenge, Performance comparison of micromixers, Chem. Eng. Sci. 65 (2010) 405-411.
[41] R. Munirathinam, J. Huskens, W. Verboom, Supported Catalysis in Continuous-Flow Microreactors, Adv. Synth. Catal. 357 (2015) 1093-1123.
[42] C. Echaide-Górriz, C. Clément, F. Cacho-Bailo, C. Téllez, J. Coronas, New strategies based on microfluidics for the synthesis of metal–organic frameworks and their membranes, J. Mater. Chem. A 6 (2018) 5485-5506.
[43] J. Ren, X. Dyosiba, N.M. Musyoka, H.W. Langmi, M. Mathe, S. Liao, Review on the current practices and efforts towards pilot-scale production of metal-organic frameworks (MOFs), Coordin. Chem. Rev. 352 (2017) 187-219.
[44] P. Coliaie, R.R. Bhawnani, A. Prajapati, R. Ali, P. Verma, G. Giri, M.S. Kelkar, A. Korde, M. Langston, C. Liu, N. Nazemifard, D. Patience, T. Rosenbaum, D. Skliar, N.K. Nere, M.R. Singh, Patterned microfluidic devices for rapid screening of metal-organic frameworks yield insights into polymorphism and non-monotonic growth, Lab Chip 22 (2022) 211-224.
[45] M. Faustini, J. Kim, G.Y. Jeong, J.Y. Kim, H.R. Moon, W.S. Ahn, D.P. Kim, Microfluidic approach toward continuous and ultrafast synthesis of metal-organic framework crystals and hetero structures in confined microdroplets, J. Am. Chem. Soc. 135 (2013) 14619-14626.
[46] H. Lu, H. Wang, Y. Liu, M. Wang, J. Hu, Q. Yang, Substance transfer behavior controlled by droplet internal circulation, Chem. Eng. J. 393 (2020) 124657.
[47] A.M. Nightingale, T.W. Phillips, J.H. Bannock, J.C. de Mello, Controlled multistep synthesis in a three-phase droplet reactor, Nat. Commun. 5 (2014) 3777.
[48] T. Bailey, M. Pinto, N. Hondow, K.J. Wu, Continuous microfluidic synthesis of zirconium-based UiO-67 using a coiled flow invertor reactor, MethodsX 8 (2021) 101246.
[49] H. Wu, C. Wu, W. Liao, B.M. Matsagar, K. Chang, J. Huang, K.C.W. Wu, Continuous and ultrafast MOF synthesis using droplet microfluidic nanoarchitectonics, J. Mater. Chem. A 11 (2023) 9427-9435.
[50] N. Rohra, G. Gaikwad, P. Dandekar, R. Jain, Microfluidic Synthesis of a Bioactive Metal-Organic Framework for Glucose-Responsive Insulin Delivery, ACS Appl. Mater. Inter. 14 (2022) 8251-8265.

[51] Q. Fu, W. Niu, L. Yan, W. Xie, H. Jiang, S. Zhang, L. Yang, Y. Wang, Y. Xing, X. Zhao, A versatile microfluidic strategy using air–liquid segmented flow for continuous and efficient synthesis of metal–organic frameworks, Mater. Lett. 343 (2023) 134344.
[52] S. Kevat, B. Sutariya, V.N. Lad, Microfluidics-assisted, time-effective and continuous synthesis of bimetallic ZIF-8/67 under different synthesis conditions, J. Mater. Sci. 58 (2023) 5219-5233.
[53] S. Yamada, A. Hirano, Y. Tanaka, R. Akiyoshi, H. Yoshikawa, D. Tanaka, Synthesis of Mixed-Metal MIL-68 under Mild Conditions by Controlling Nucleation Using a Microfluidic System, Cryst. Growth Des. 22 (2022) 4139-4145.
[54] G. Xu, K. Otsubo, T. Yamada, S. Sakaida, H. Kitagawa, Superprotonic conductivity in a highly oriented crystalline metal-organic framework nanofilm, J. Am. Chem. Soc. 135 (2013) 7438.
[55] X.Y. Dong, J.J. Li, Z. Han, P.G. Duan, L.K. Li, S.Q. Zang, Tuning the functional substituent group and guest of metal–organic frameworks in hybrid membranes for improved interface compatibility and proton conduction, J. Mater. Chem. A 5 (2017) 3464-3474.
[56] S.M. Rezaei Niya, M. Hoorfar, Study of proton exchange membrane fuel cells using electrochemical impedance spectroscopy technique – A review, J. Power Sources 240 (2013) 281-293.
[57] N.A. Nazir, N. Kim, W.G. Iglesias, A. Jakli, T. Kyu, Conductive behavior in relation to domain morphology and phase diagram of Nafion/poly(vinylidene-co-trifluoroethylene) blends, Polymer 53 (2012) 196-204.
[58] M.A. Hickner, H. Ghassemi, Y.S. Kim, B.R. Einsla, J.E. McGrath, Alternative Polymer Systems for Proton Exchange Membranes (PEMs), Chem. Rev. 104 (2004) 4587-4612.
[59] J. Dechnik, J. Gascon, C.J. Doonan, C. Janiak, C.J. Sumby, Mixed-Matrix Membranes, Angew. Chem. Int. Ed. 56 (2017) 9292-9310.
[60] L. Fu, N.A. Hashim, Y. Liu, M. Abed, K. Li, Progress in the production and modification of PVDF membranes, J. Membrane. Sci. 375 (2011) 1-27.
[61] Y. Zhang, J. Li, L. Ma, W. Cai, H. Cheng, Recent Developments on Alternative Proton Exchange Membranes: Strategies for Systematic Performance Improvement, Energy Technol. 3 (2015) 675-691.
[62] C. Wu, S. Lu, H. Wang, X. Xu, S. Peng, Q. Tan, Y. Xiang, A novel polysulfone–polyvinylpyrrolidone membrane with superior proton-to-vanadium ion selectivity for vanadium redox flow batteries, J. Mater. Chem. A 4 (2016) 1174-1179.
[63] G.M. Sheldrick, SHELXT - integrated space-group and crystal-structure determination, Acta Crystallogr. A 71 (2015) 3-8.
[64] G.M. Sheldrick, Crystal structure refinement with SHELXL, Acta Crystallogr. C 71 (2015) 3-8.
[65] S. Li, S. Yu, S.M. Collins, D.N. Johnstone, C.W. Ashling, A.F. Sapnik, P.A. Chater, D.S. Keeble, L.N. McHugh, P.A. Midgley, D.A. Keen, T.D. Bennett, A new route to porous metal–organic framework crystal–glass composites, Chem. Sci. 11 (2020) 9910-9918.
[66] B.W. Veal, P.M. Baldo, A.P. Paulikas, J.A. Eastman, Understanding Artifacts in Impedance Spectroscopy, J. Electrochem. Soc. 162 (2014) 47-57.
[67] L. Ding, H. Zou, J. Lu, H. Liu, S. Wang, H. Yan, Y. Li, Enhancing Proton Conductivity of Nafion Membrane by Incorporating Porous Tb-Metal-Organic Framework Modified with Nitro Groups, Inorg. Chem. 61 (2022) 16185-16196.

[68] L.X. Xie, Z.J. Ye, X.D. Zhang, G. Li, Two stable phenyl acyl thiourea carboxylate-based MOFs: Syntheses, crystal structures and proton conductive properties, J. Solid State Chem. 311 (2022) 123154.
[69] M. Mamlouk, P. Ocon, K. Scott, Preparation and characterization of polybenzimidzaole/diethylamine hydrogen sulphate for medium temperature proton exchange membrane fuel cells, J. Power Sources 245 (2014) 915-926.
[70] A. Laybourn, A.M. López-Fernández, I. Thomas-Hillman, J. Katrib, W. Lewis, C. Dodds, A.P. Harvey, S.W. Kingman, Combining continuous flow oscillatory baffled reactors and microwave heating: Process intensification and accelerated synthesis of metal-organic frameworks, Chem. Eng. J. 356 (2019) 170-177.
[71] L. Zhong, S.F. Parker, Structure and vibrational spectroscopy of methanesulfonic acid, R. Soc. Open Sci. 5 (2018) 181363.
[72] Y. Ji, X. Yang, Z. Ji, L. Zhu, N. Ma, D. Chen, X. Jia, J. Tang, Y. Cao, DFT-Calculated IR Spectrum Amide I, II, and III Band Contributions of N-Methylacetamide Fine Components, ACS Omega 5 (2020) 8572-8578.
[73] N. Majoul, S. Aouida, B. Bessaïs, Progress of porous silicon APTES-functionalization by FTIR investigations, Appl. Surf. Sci. 331 (2015) 388-391.
[74] M. Staufer, U. Birkenheuer, T. Belling, F. Nörtemann, N. Rösch, W. Widdra, K.L. Kostov, T. Moritz, D. Menzel, The vibrational structure of benzene adsorbed on Si(001), J. Chem. Phys. 112 (2000) 2498-2506.
[75] Y. Ishida, T. Togashi, K. Yamamoto, M. Tanaka, T. Kiss, T. Otsu, Y. Kobayashi, S. Shin, Time-resolved photoemission apparatus achieving sub-20-meV energy resolution and high stability, Rev. Sci. Instrum. 85 (2014) 123904.
[76] G. Shi, W. Xu, J. Wang, Y. Yuan, S. Chaemchuen, F. Verpoort, A Cu-based MOF for the effective carboxylation of terminal alkynes with CO_2 under mild conditions, J. CO_2 Util. 39 (2020) 101177.
[77] D. Liu, Z. Jin, Y. Bi, Charge transmission channel construction between a MOF and rGO by means of Co–Mo–S modification, Catal. Sci. Technol. 7 (2017) 4478-4488.
[78] C. Gan, T. Liang, W. Li, X. Fan, M. Zhu, Amine-terminated ionic liquid modified graphene oxide/copper nanocomposite toward efficient lubrication, Appl. Surf. Sci. 491 (2019) 105-115.
[79] R. Ojeda-López, J.M. Esparza-Schulz, I.J. Pérez-Hermosillo, A. Hernández-Gordillo, A. Domínguez-Ortiz, Improve in CO_2 and CH_4 Adsorption Capacity on Carbon Microfibers Synthesized by Electrospinning of PAN, Fibers 7 (2019) 81.
[80] G.A. George, High resolution XPS of organic polymers—the scienta ESCA 300 data base, Polym. Int. 33 (1994) 439-440.
[81] A. Dolgov, D. Lopaev, C.J. Lee, E. Zoethout, V. Medvedev, O. Yakushev, F. Bijkerk, Characterization of carbon contamination under ion and hot atom bombardment in a tin-plasma extreme ultraviolet light source, Appl. Surf. Sci. 353 (2015) 708-713.
[82] J. Sicklinger, H. Beyer, L. Hartmann, F. Riewald, C. Sedlmeier, H.A. Gasteiger, SO_3 Treatment of Lithium- and Manganese-Rich NCMs for Li-Ion Batteries: Enhanced Robustness towards Humid Ambient Air and Improved Full-Cell Performance, J. Electrochem. Soc. 167 (2020) 130507.
[83] L. Zhang, L.Y. Tu, Y. Liang, Q. Chen, Z.S. Li, C.H. Li, Z.H. Wang, W. Li, Coconut-based activated carbon fibers for efficient adsorption of various organic dyes, RSC Adv. 8 (2018) 42280-42291.

[84] Y. Hu, J. Zhang, H. Huo, Z. Wang, X. Xu, Y. Yang, K. Lin, R. Fan, One-pot synthesis of bimetallic metal–organic frameworks (MOFs) as acid–base bifunctional catalysts for tandem reaction, Catal. Sci. Technol. 10 (2020) 315-322.
[85] E. Bagherzadeh, S.M. Zebarjad, H.R. Madaah Hosseini, P. Chagnon, Preparation, optimization and evolution of the kinetic mechanism of an Fe-MIL-88A metal–organic framework, CrystEngComm 21 (2019) 544-553.
[86] A.F. Gualtieri, Synthesis of sodium zeolites from a natural halloysite, Phys. Chem. Miner. 28 (2001) 719–728.
[87] A.V. Dighe, L. Huelsenbeck, R.R. Bhawnani, P. Verma, K.H. Stone, M.R. Singh, G. Giri, Autocatalysis and Oriented Attachment Direct the Synthesis of a Metal-Organic Framework, JACS Au 2 (2022) 453-462.
[88] N. Stock, S. Biswas, Synthesis of metal-organic frameworks (MOFs): routes to various MOF topologies, morphologies, and composites, Chem. Rev. 112 (2012) 933-969.
[89] E. Biemmi, S. Christian, N. Stock, T. Bein, High-throughput screening of synthesis parameters in the formation of the metal-organic frameworks MOF-5 and HKUST-1, Micropor. Mesopor. Mat. 117 (2009) 111-117.
[90] E. Stavitski, M. Goesten, J. Juan Alcaniz, A. Martinez-Joaristi, P. Serra Crespo, A.V. Petukhov, J. Gascon, F. Kapteijn, Kinetic control of metal-organic framework crystallization investigated by time-resolved in situ X-ray scattering, Angew. Chem. Int. Ed. 50 (2011) 9624-9628.
[91] N.A. Lynd, M.A. Hillmyer, Effects of Polydispersity on the Order−Disorder Transition in Block Copolymer Melts, Macromolecules 40 (2007) 8050-8055.
[92] J.T.W. Wang, S.L.C. Hsu, Enhanced high-temperature polymer electrolyte membrane for fuel cells based on polybenzimidazole and ionic liquids, Electrochim. Acta 56 (2011) 2842-2846.
[93] M. Rautenberg, B. Bhattacharya, C. Das, F. Emmerling, Mechanochemical Synthesis of Phosphonate-Based Proton Conducting Metal-Organic Frameworks, Inorg. Chem. 61 (2022) 10801-10809.
[94] Z.X. Bai, S.C. Liu, P. Chen, G.J. Cheng, G.Y. Wu, Y. Liu, Enhanced proton conduction of imidazole localized in one-dimensional Ni-metal-organic framework nanofibers, Nanotechnology 31 (2020) 125702.
[95] Y.L. Bao, J.Y. Zheng, H.P. Zheng, G.D. Qi, J.R. An, Y.P. Wu, Y.L. Liu, W.W. Dong, J. Zhao, D.S. Li, Cu-MOF@PVP/PVDF hybrid composites as tunable proton-conducting materials, J. Solid State Chem. 310 (2022) 123070.
[96] Z.Q. Shi, N.N. Ji, M.H. Wang, G. Li, A Comparative Study of Proton Conduction Between a 2D Zinc(II) MOF and Its Corresponding Organic Ligand, Inorg. Chem. 59 (2020) 4781-4789.
[97] X. Wang, Y. Rong, F. Wang, C. Zhang, Q. Wang, High performance proton exchange membranes with double proton conduction pathways by introducing MOF impregnated with protic ionic liquid into SPEEK, Micro. and Meso. Mater. 346 (2022) 112314.

Chapter 3 Modulating proton conductivity through crystal structure tuning in arenedisulfonate coordination polymers

3.1 Introduction

Metal–organic coordination polymers (CPs), encompassing one-dimensional (1D) chains, two-dimensional (2D) sheets, and three-dimensional (3D) frameworks built from the interconnection of metal ions or clusters and organic linkers [1], have been widely used in the fields of catalysis [2, 3], gas adsorption/separation [4, 5] and energy storage [6, 7]. Many CPs have been developed using carboxylate and N-donor ligands, including the now-widespread microporous CPs or metal-organic frameworks (MOFs) built from ditopic or tritopic carboxylates for UiO [8], HKUST [9], MIL [10], and IRMOF [11] families, imidazolate for the family of zeolitic imidazolate frameworks [12, 13], and pyridine- and pyrazine-based MOFs and CPs [14]. Phosphonates have also seen application in gas capture [15, 16] as well as for proton conduction [17]. Void structures in 2D or 3D frameworks, characteristic of MOFs, are not necessarily required for the targeted functional properties in proton and ionic conductivity where 1D and dense CPs have likewise shown considerable promise [18]. CPs built from sulfonate-metal coordination motifs have, however, seen significantly less exploration [19].

A number of sulfonate CPs have shown promising proton conductivity [20], attributed to the beneficial proton hopping sites incorporated in the form of sulfonic acid groups [21]. The sulfonate group has three O atoms, and the sulfonate unit can assemble metal ions into diverse structural frameworks, with 1D, 2D, and 3D arrangements reported [22]. The sulfonate group can coordinate with one O atom participating in coordination of the metal centre (designated η^1) or with two O atoms (designated η^2) or, alternatively, the sulfonate group can form bridging motifs (η^2, μ^2) [18]. In all cases, at least one other O atom provides further hydrogen-bond receptors to anchor proton carriers or to transfer protons [23]. As characteristically weakly coordinating groups, sulfonates tend to form CPs with soft metal ions (e.g. Cu^{2+}, Ca^{2+}, Ba^{2+}) [24].

Sulfonate CPs often appear as 1D or 2D layered structures [25], with far fewer 3D structures reported [26]. Combining sulfonate linkers together with N-donor

ligands as a structure-directing second ligand has provided a major guiding principle for sulfonate CP design. Kitagawa et al. reported porous 1D-ladder and 2D-sheet frameworks by using 5-sulfoisophthalate ligands with strongly coordinating N-donor ligands (e.g. 4,4′-bispyridylethylene and pyrazine) [27]. The 1,5-naphthalenedisulfonic acid (NDS) ligand has drawn particular attention [25, 28] as a ditopic linker that in this sense resembles the common benzenedicarboxylate (BDC) linker in MOFs [11].

Recently, a 2D sulfonate CP denoted Cu-SAT has been synthesized combining NDS and 1,2,4-triazol-4-amine (T4A) linkers and shows promising proton conductivity of the order of 10^{-3} S cm^{-1} at >95% relative humidity (RH) and 80 °C [20, 28], approaching the benchmark conductivities for Nafion proton conducting polymers (~10^{-2}-10^{-1} S cm^{-1}). In Cu-SAT, μ^2 OH groups and triazolate ligands connect Cu^{2+} ions in a chain with bridging η^2, μ^2 NDS linkers spanning the 1D Cu^{2+} chains to form a 2D structure. However, Cu-SAT, like many other MOFs, presents important limitations from a green chemistry perspective [29, 30] due to the use of dimethylformamide (DMF) in synthesis. Moreover, from a practical standpoint, Cu-SAT also exhibits limited stability on exposure to water, a critical challenge for proton conductivity under humid conditions. As such, we now turn to the role of the solvent in Cu-SAT synthesis and also examine a structurally analogous 2D CP built from only NDS and Ca^{2+} in aqueous solution [26]. The incorporation of coordinating solvent at Ca^{2+} sites likewise prompts exploration of the role of solvent choice in Ca^{2+} as well as Cu^{2+} NDS CPs, and motivates the examination of the as yet unreported proton conductivity of Ca-NDS CPs.

Figure 3.1 highlights the unified structural motifs across the Cu-SAT and Ca-NDS CPs. In Cu-SAT (Figure 3.1a), the neutral T4A ligands are shown in the axial positions and the anionic OH and NDS ligands are shown in the equatorial positions. The coordination environment in the Ca-NDS system is analogous with the bridging OH along the metal-metal 1D chain adopted by a further set of NDS ligands (Figure 3.1b, equatorial positions) and the structural position of the neutral T4A ligand adopted by solvent molecules (L) in the axial positions (L = H_2O in the reported Ca-NDS structure [26]). Figure 3.1c presents the molecular structure of the entire NDS and T4A ligands, and Figure 3.1d depicts how these components form a characteristic 2D layer structure in Cu-SAT and Ca-NDS CPs.

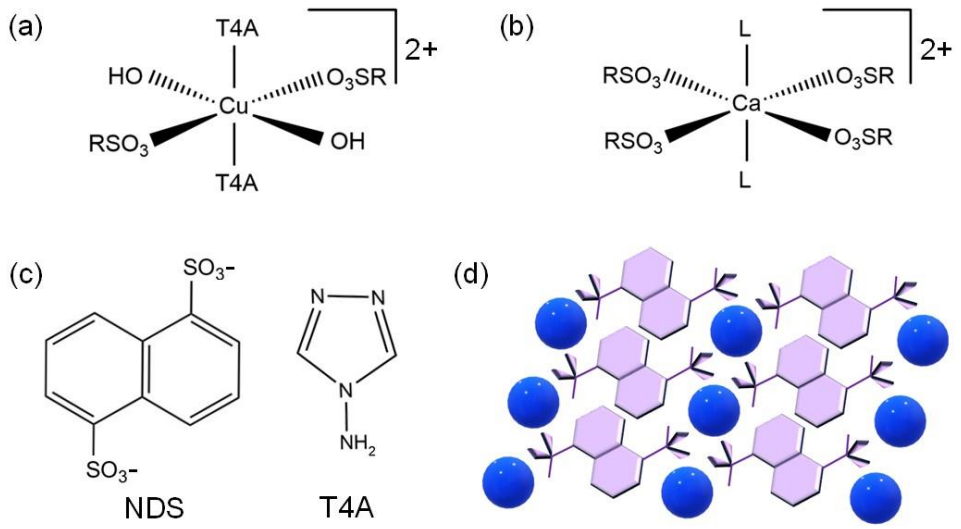

Figure 3.1 Coordination geometry of (a) Cu^{2+} in Cu-SAT and (b) Ca^{2+} in Ca-NDS CPs (L denotes coordinating solvent). (c) Molecular structure of the complete NDS and T4A ligands. (d) Schematic diagram of the characteristic 2D structure formed from NDS spanning between 1D metal chains. The blue spheres represent the metal ions separated by representations of the NDS ligand (purple).

The solvent in MOF and CP synthesis is known to play diverse roles including deprotonation of precursors as well as templating void spaces [31, 32]. The polarity of the solvent can also play a role in directing the final structure and associated topology and porosity [33]. The notable role of the solvent as a second ligand in Ca-NDS further invites exploration not only of the solvent choice but also the choice of the arenedisulfonate ligand. Principles of isoreticular chemistry are widespread in MOF synthesis [34, 35], and as such we now evaluate extended arenedisulfonate ligands as a further structural tuning parameter. The anthraquinone-2,6-disulfonate (2, 6-AQDS) ligand has been reported to form stable alkaline-earth sulfonate CPs with 3D structures, and the metal-to-metal distance of these samples are longer than 2,6-NDS synthesized CPs which also have 3D structures [26, 36, 37].

Here, to mimic the 1,5-NDS ligand we introduce the anthraquinone-1,5-disulfonate ligand (ADS) as a further structure-modifying element. By synthesising a systematic series of Cu^{2+} and Ca^{2+} NDS CPs, we now report solvent-directed single crystal structures of Cu-SAT (ethanol, EtOH), Ca-NDS (DMF), and Ca-NDS (dimethylsulfoxide, DMSO). By incorporating the 1,5-ADS ligand, we further introduce a hydrogen bonded network termed Cu-SQAT incorporating sulfonate, quinone, and aminotriazolate moieties as well as a 1D CP built from Ca and 1,5-ADS ligands, denoted Ca-ADS. We then test their proton conductivities to examine the

experimental structure-function relationship with a particular focus on changes in the relative positions of the electronegative functional groups along the major hydrogen bond acceptor chains common to the series. Taken together, these structures establish a correlation between proton conductivities and the tortuosity of the CP hydrogen bond acceptor site network. These findings in turn identify a general, cross-structure descriptor for tuning the sulfonate CP crystal structures to systematically modulate proton conductivity.

3.2 Experimental

3.2.1 Materials

1,5-Naphthalenedisulfonic acid tetrahydrate (H_2NDS, Molecular Weight: 360.36 g mol^{-1}), T4A (Molecular Weight: 84.08 g mol^{-1}), copper nitrate hemi(pentahydrate) (Molecular Weight: 232.59 g mol^{-1}), N, N-dimethylformamide (DMF, ≥ 99.9%), polyvinylpyrrolidone (PVP) [M_W 360,000], and polyvinylidene fluoride (PVDF) [M_W 534,000] were purchased from Sigma Aldrich (Merck Group). Calcium nitrate hemi(pentahydrate) (Molecular Weight: 236.15 g mol^{-1}) was purchased from Thermo Scientific, anthraquinone-1,5-disulfonic acid disodium salt (ADS, Molecular Weight: 422.31 g mol^{-1}) was purchased from Santa Cruz Biotechnology, dimethyl sulfoxide (DMSO, ≥ 99.5%) was purchased from Honeywell, and ethanol (EtOH, ≥ 99.5%) was purchased from VWR International. All chemicals were used as received. Deionized (DI) water (≥ 18.2 Mohm cm^{-1}) was used for all reactions.

3.2.2 Batch synthesis of the different CPs and membrane fabrication

3.2.2.1 Synthesis of Cu-SAT (EtOH)

Copper nitrate (23.2 mg, 0.1 mmol) was dissolved in DI water (0.3 mL), and EtOH (1.5 mL) was then added to form solution 1. T4A (8.4 mg, 0.1 mmol) and H_2NDS (36 mg, 0.1 mmol) were dissolved in DI water (0.3 mL) successively, and DMF (0.5 mL) was then added as precursor solution 2. Next, solutions 1 and 2 were mixed in a 20 mL glass vial and heated in an oil bath at 80 °C for 4 h. The reaction yield was determined gravimetrically and was recorded as 44% ± 3% (uncertainties in yields are given as one standard error).

3.2.2.2 Synthesis of Ca-NDS (water)

Calcium nitrate (47.2 mg, 0.2 mmol) was dissolved in DI water (0.3 mL) as

solution 1. H_2NDS (72 mg, 0.2 mmol) was dissolved in DI water (0.3 mL) as solution 2. Next, solutions 1 and 2 were mixed in a 20 mL glass vial and heated in a dry bath heater (Thermo Scientific) at 80 °C for 4 h. The reaction yield was determined gravimetrically and was recorded as 71% ± 3%.

3.2.2.3 Synthesis of Ca-NDS (DMF) and Ca-NDS (DMSO)

After evaluating yield and the solubility of precursors, the water:DMF and water:DMSO solvent ratios were set as 3:10. Calcium nitrate (47.2 mg, 0.2 mmol) was dissolved in DI water (0.3 mL), and DMF (1 mL) was then added as solution 1. H_2NDS (72 mg, 0.2 mmol) was dissolved in DI water (0.3 mL), and DMF (1 mL) was then added as solution 2. Next, solutions 1 and 2 were mixed in a 20 mL glass vial and heated in a dry bath heater at 80 °C for 4 h. Ca-NDS (DMSO) was synthesized by substituting DMSO for DMF in the above reaction (1 mL DMSO in each solution). The reaction yield was determined gravimetrically and was recorded as 42.3% ± 2% for Ca-NDS (DMF) and 40% ± 2% for Ca-NDS (DMSO).

3.2.2.4 Synthesis of Cu-SQAT

ADS (21 mg, 0.05 mmol) was dissolved in DI water (0.6 mL) in a 20 mL glass vial by sonicating for 10 minutes. T4A (4.2 mg, 0.05 mmol) and copper nitrate (11.6 mg, 0.05 mmol) were then added in the solution successively, followed by DMF (2 mL). The prepared solution was heated in a dry bath heater at 80 °C for 4 h. The reaction yield was determined gravimetrically and was recorded as 52% ± 2%.

3.2.2.5 Synthesis of Ca-ADS

ADS (42 mg, 0.1 mmol) was dissolved in DI water (2.6 mL) in a 20 mL glass vial by sonicating for 10 minutes. Calcium nitrate (23.6 mg, 0.1 mmol) was then dissolved in this solution. Next, the prepared chemical solution was heated in a dry bath heater at 80 °C for 4 h. The reaction yield was determined gravimetrically and was recorded as 35% ± 2%.

3.2.2.6 Membrane fabrication

The Ca-NDS (water) and Cu-SQAT based mixed matrix membranes (MMMs) were made using 60% by weight of these two CPs incorporated into PVP and PVDF (named as Ca-NDS (water)-MMM and Cu-SQAT-MMM). Typically, 30 mg PVDF and 90 mg PVP were dissolved in 1.8 mL DMF by stirring at room temperature for 180

min to obtain a homogeneous gel. Then, 180 mg of Ca-NDS (water) or Cu-SQAT were added and dispersed evenly in the above gel with vigorous stirring for 30 min. Next, this gel was poured onto a high-temperature resistant glass and cast with 60 μm thickness with using a BGO 209/2 adjustable applicator (Biuged Laboratory Instruments Co., Ltd). The membrane was then dried at 70 °C for 1 h in a vacuum oven to remove excess DMF. The solidified membrane was finally washed with deionized water three times and then dried at room temperature.

3.2.3 Materials Characterization

Powder X-ray diffraction patterns were recorded using a Bruker D2 diffractometer (Cu K_α λ = 1.54184 Å, 2θ scan range = 5-50°). Single crystal X-ray diffraction measurements were carried out at 100 K on a Rigaku SuperNova diffractometer equipped with an Atlas CCD detector and connected to an Oxford Cryostream low temperature device using Cu K_α radiation (λ = 1.54184 Å) for Cu-SAT (EtOH), Ca-NDS (DMSO), Cu-SQAT, and Ca-ADS and Mo K_α radiation (λ = 0.7103 Å, for larger crystals) for Ca-NDS (DMF). A microfocus X-ray source was used in all cases. The structure was solved by intrinsic phasing using SHELXT [38] and refined by a full matrix least squares technique based on the squared structure factor F^2 using SHELXL2014 [39]. Table 3.1 summarizes the crystallographic data for these five CPs. Vesta software (version 3.5.7) was employed to produce calculated XRD patterns from the single crystal structure.

Table 3.1 Crystallographic data for Cu-SAT (EtOH), Ca-NDS (DMF), Ca-NDS (DMSO), Cu-SQAT, and Ca-ADS. In the table, Z is the number of formula units in unit cell, ρ_{calc} is the calculated density, μ is the linear absorption coefficient, F(000) is the number of electrons in unit cell, N_{tot} is the total number of reflections, N_{obs} is the number of unique reflections with intensities $I > 2\sigma(I)$, N_{all} is the number of unique reflections, R_{int} is the merging error, R_1 is the conventional residual (R) factor for observed reflections, wR_2 is the weighted R value for all diffraction points, and F^2 is the squared structure factor.

Crystal data	**Cu-SAT (EtOH)**	**Ca-NDS (DMF)**	**Ca-NDS (DMSO)**	**Cu-SQAT**	**Ca-ADS†**
CCDC number	2336805	2336806	2336802	2336803	2336804
Formula	$C_{14}H_{16}Cu_2N_8O_8S_2$	$C_{16}H_{20}CaN_2O_8S_2$	$C_{14}H_{18}CaO_8S_4$	$C_{18}H_{16}Cu_2O_{10}S_2$	$C_{14}H_{12}CaO_{11}S_2$
Formula weight	615.55	472.54	482.60	695.59	460.44
Temperature/K	99.99(10)	100.01(10)	100.15(10)	100.00(10)	100.01(10)
Crystal system	monoclinic	triclinic	monoclinic	monoclinic	monoclinic
Space group	$P2_1/c$	$P\bar{1}$	$P2_1/n$	$P2_1/c$	$C2/c$
a/Å	6.7128(5)	9.4952(7)	5.4131(2)	13.7271(3)	20.1769(8)
b/Å	10.0239(7)	10.2875(7)	16.6724(6)	6.7154(2)	7.6697(3)
c/Å	14.5560(10)	11.0657(8)	10.7173(3)	12.1309(3)	10.7097(5)
α/°	90	74.765(6)	90	90	90
β/°	93.268(6)	79.328(6)	103.282(3)	91.407(2)	104.898(4)
γ/°	90	85.839(6)	90	90	90
Volume/Å^3	977.86(12)	1024.57(13)	941.36(6)	1117.93(5)	1601.62(12)
Z	2	2	2	2	4
ρ_{calc}/g cm^{-3}	2.091	1.532	1.703	2.066	1.909
μ/mm^{-1}	5.311	0.556	7.411	4.818	6.456
F(000)	620.0	492.0	500.0	700	944.0
Crystal size/mm^3	0.07 × 0.05 × 0.03	0.35 × 0.18 × 0.08	0.07 × 0.04 × 0.03	0.09 × 0.06 × 0.02	0.19 × 0.05 × 0.04
Radiation	Cu Kα	Mo Kα	Cu Kα	Cu Kα	Cu Kα
Index ranges	$-7 \le h \le 4$ $-11 \le k \le 12$ $-16 \le l \le 17$	$-10 \le h \le 13$ $-14 \le k \le 11$ $-14 \le l \le 14$	$-6 \le h \le 6$ $-19 \le k \le 20$ $-13 \le l \le 12$	$-16 \le h \le 16$ $-8 \le k \le 2$ $-15 \le l \le 14$	$-23 \le h \le 24$ $-9 \le k \le 9$ $-12 \le l \le 11$
N_{tot}	3711	8441	8897	4603	2341
N_{obs}/N_{all}	1519/1822	2467/4810	1656/1855	1848/2152	2107/2341
N_{par}	162	266	126	193	141
R_{int}	0.0427	0.0411	0.0524	0.0326	0.043
Goodness-of-fit on F^2	1.114	1.043	1.218	1.034	1.058
R_1 (observed)	0.0461	0.0550	0.0505	0.0364	0.0283
wR_2 (all data)	0.1212	0.1406	0.1276	0.1042	0.0770

†Ca-ADS was solved from a twinned crystal with two components relatively rotated by approximately 180° about the normal to (100).

The morphologies of the MOF pellet samples were characterized by light microscopy (LM, Olympus, BX51) and scanning electron microscopy (SEM, Hitachi/TM-3030Plus, equipped with a backscattered electron detector and operated at 15 kV accelerating voltage). An Oxford instruments 150 X-Max energy dispersive X-ray spectroscopy (EDS) detector was used to assess the elemental composition of pellet samples. The EDS analysis was conducted with an electron beam accelerated to 15 kV and using a probe current of 20 nA probe current and a working distance of 15 mm. Similar conditions were applied for EDS point analysis on the CPs powders to

verify their composition in comparison to empirical formula. Prior the EDS point analysis, the CPs powders were deposited on the carbon tape, and coated with 15 nm Pt to avoid the charging effect. For EDS point analysis, at least 5 areas were collected for each CP to ensure the statistical significance of the results. Cryo-SEM was carried out using an Tescan AmberX cryo-PFIBSEM, operated at 2 kV and equipped with a Quorum Technologies PP3010 cryo-stage and an Oxford instruments 150 X-Max energy dispersive X-ray spectroscopy (EDS) detector, to check the thickness, surface morphology, and elemental composition of the hydrated membrane. Thermogravimetric analyses (TGA) were carried out using a Netzsch STA 449F3 instrument with a heating rate of 10 °C min^{-1} in a nitrogen atmosphere (40 mL min^{-1}) and conducted from 50 to 850 °C. Characteristic temperatures for mass loss events were determined from the first derivative of the thermogravimetry curve (the DGT curve) by extracting the temperatures corresponding to maxima in the DGT curve. This temperature corresponds to the steepest change in mass loss. A Thermo Scientific Flash EA2000 elemental analyser was used to carry out carbon, hydrogen, nitrogen, and sulfur (CHNS) quantification. Briefly, this analysis entailed dropping samples into a furnace at 900 °C in a continual flow of helium. Pure oxygen was added for a few seconds to facilitate combustion. The combustion products pass through an oxidation/reduction reactor to convert them to CO_2, H_2O, N_2 and SO_2 which are then separated by gas chromatography and detected using thermal conductivity. X-ray photoelectron spectroscopy (XPS) was used to characterize the surface chemistry of the materials. CPs powders were pressed onto carbon tape and adhered to a standard omicron plate with a uniform flat sample. Cu-SAT (EtOH) and Cu-SQAT samples were sputtered with 500 V in 2 × 10^{-7} mbar of Argon for 2 minutes before XPS test. The experiment was carried out in UHV (<1×10^{-9} mbar) on a Specs FlexMod system. The illuminating X-ray source was a monochromatic Al Kα (hν = 1486.7 eV) anode at a power of 400 W and 15 kV. A Specs Phoibos 150 hemispherical analyzer with 1D delay line detectors was used to detect the photoelectrons. The powder is insulating so to reduce any differential charging at the surface which could distort the spectra, an electron flood gun (energy 4 eV and current 75 μA) was used to charge neutralize the sample. Survey spectra were obtained with a pass energy of 50 eV, a step width of 1 eV and a dwell time of 0.1 seconds. High resolution spectra were collected with a pass energy of 30 eV, a step width of 0.1 eV and a dwell time of 0.2 seconds. After collecting

the spectra, the data was analyzed using CasaXPS software. Binding energies were calibrated using the C-C C1s peak at 284.8 eV and the intensity was calibrated using a previously calculated transmission function for the specific instrument settings. All spectra were fitted with a Shirley background and the peak areas were determined. We quantified the relative atomic percentages using these peak areas and the respective relative sensitivity functions for each peak. Fourier Transform Infrared (FTIR) spectra of the CPs samples were obtained using a Bruker Vertex 80V FTIR spectrometer with a diamond prism Attenuated Total Reflection (ATR) crystal. Using a 6 mm aperture, data were collected for wavenumbers between 500 and 4000 cm^{-1} and averaged over 64 scans.

Scanning electron diffraction (SED) data were acquired using a JEOL ARM300CF transmission electron microscope (ePSIC, Diamond Light Source, UK) operated at 300 kV. This microscope was equipped with a high-resolution pole piece, a cold field emission gun, aberration-correctors in the probe- and image-forming optics, and a 4-chip Merlin-Medipix (512×512 pixels) electron counting detector. In SED, an electron nanobeam is scanned across a sample in an array *(x, y)* and a two-dimensional diffraction pattern (k_x, k_y) is recorded on the detector at each probe position (*x*, *y*). To achieve nanobeam diffraction, the electron optics were configured by deactivating the aberration corrector in the probe-forming optics and adjusting the condenser lens system to produce a convergence semi-angle of 0.8 mrad using a 10 μm condenser aperture. This configuration results in a diffraction-limited probe diameter of 3 nm at 300 kV. The beam current was measured at approximately 1 pA using a Faraday cup, with an exposure time set at 1 ms per probe position. In a single scan, the electron fluence was estimated to be roughly 8.8 e^{-} $Å^{-2}$, assuming a disk-like probe matching the diffraction-limited probe diameter. All measurements were performed across a scan size of 256×256 probe positions. For STEM-EDS, the same settings were employed, albeit with a 100 μm condenser aperture resulting in approximately 100-fold higher beam current for enhanced signal-to-noise ratio. Calibration data for both images and diffraction in SED dataset were acquired using a gold diffraction cross-grating with a 500 nm period (Ted Pella). Standard MoO_3 crystals from Agar Scientific were used to calibrate the relative rotation between the diffraction pattern and the scan pattern. SED data were processed, aligned, and calibrated using Pyxem-0.11.0 and

supporting tools from the HyperSpy package (1.6.5) [40] following previously reported procedures [41].

3.2.4 Proton Conductivity

Figure 3.2 Digital photograph of the pellet sample testing cell with two plate electrodes.

In order to test the proton conductivity of the synthesized sulfonate CPs, powder samples were pelletized under a pressure of 5 ton cm^{-2} for 2 minutes by using a 5 mm evacuable pellet die (Specac). Pellet samples were inserted in a cell consisting of two copper plates mounted on a polytetrafluoroethylene (PTFE) assembly (Figure 3.2). The contact between the copper electrodes and the pellet samples was secured by tightening screws on the cell. The proton conductivity (σ, mS cm^{-1}) was calculated according to:

$$\sigma = \frac{L}{AR} \quad (1)$$

where L is the thickness of pellet sample (cm), A is the cross-section area of pellet (cm^{-2}), and R is the resistance of pellet (Ω). R was measured by electrochemical impedance spectroscopy (EIS) in a two-electrode configuration between frequencies of 100 Hz and 1 MHz using a Gamry 1010E electrochemical workstation. The intercept at the axis corresponding to the real part of the complex impedance (Z′) was

taken as the resistance R [42].

All EIS measurements were performed 30 min after the testing temperatures (50-80 °C) reached the set value. Powder samples were placed in a 95% relative humidity (RH) chamber (Memmert HCP150) at room temperature overnight before pellet formation, and pellet samples were placed in a 95% RH chamber at room temperature overnight again to fully hydrate the sample, matching previous reports of RH equilibration conditions prior to testing [43, 44]. EIS measurements of Ca-NDS (water)-MMM and Cu-SQAT-MMM were carried out with using a BT-110 conductivity clamp (L = 0.425 cm). These membranes were held in a 95% RH chamber (Memmert HCP150) at room temperature over 12 h to fully hydrate before EIS test, testing method was followed with our previous work [28]. The activation energy (E_a) for membrane proton conduction was determined via the Arrhenius relationship [45]:

$$\mathrm{In}(\mathrm{T}\sigma) = \mathrm{In}(\sigma_0) - (\frac{E_a}{\mathrm{R}})(\frac{1000}{\mathrm{T}}) \quad (2)$$

where T is testing temperature (K), σ is the proton conductivity (S cm^{-1}), σ_0 is the pre-exponential factor (S (K cm) $^{-1}$) and R is the ideal gas constant (8.314 J (mol K) $^{-1}$). E_a was determined from linear fitting to estimate the slope from this Arrhenius plot.

3.3 Results and discussion

3.3.1 Single crystal structures of Cu^{2+} and Ca^{2+} arenedisulfonates

We first start with a brief evaluation of solvent effects in directing the structure of Cu-SAT as a 2D NDS-based CP with an established proton conductivity. Cu-SAT has been reported to exhibit structural changes after prolonged exposure to water [28]. In an attempt to reduce the DMF content in synthesis, we introduced EtOH to the solvent system. Notably, the powder XRD for this material, termed Cu-SAT (EtOH) exhibited the pattern characteristic for Cu-SAT after degradation following exposure to water (Figure 3.3). This synthesis appeared to offer a direct synthetic route to the degradation product after water exposure, with high quality single crystals recovered. In contrast, ageing Cu-SAT in water to form this degradation product did not offer crystals of sufficient quality for single crystal XRD (SC-XRD). We denote the direct synthesis product Cu-SAT (EtOH).

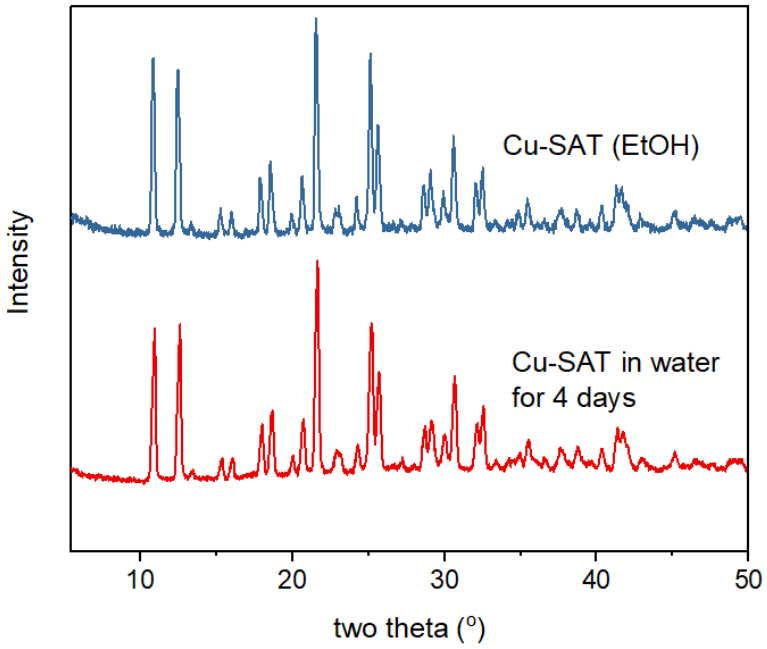

Figure 3.3 Powder XRD patterns of Cu-SAT after water degradation and the as-synthesized product of Cu-SAT (EtOH).

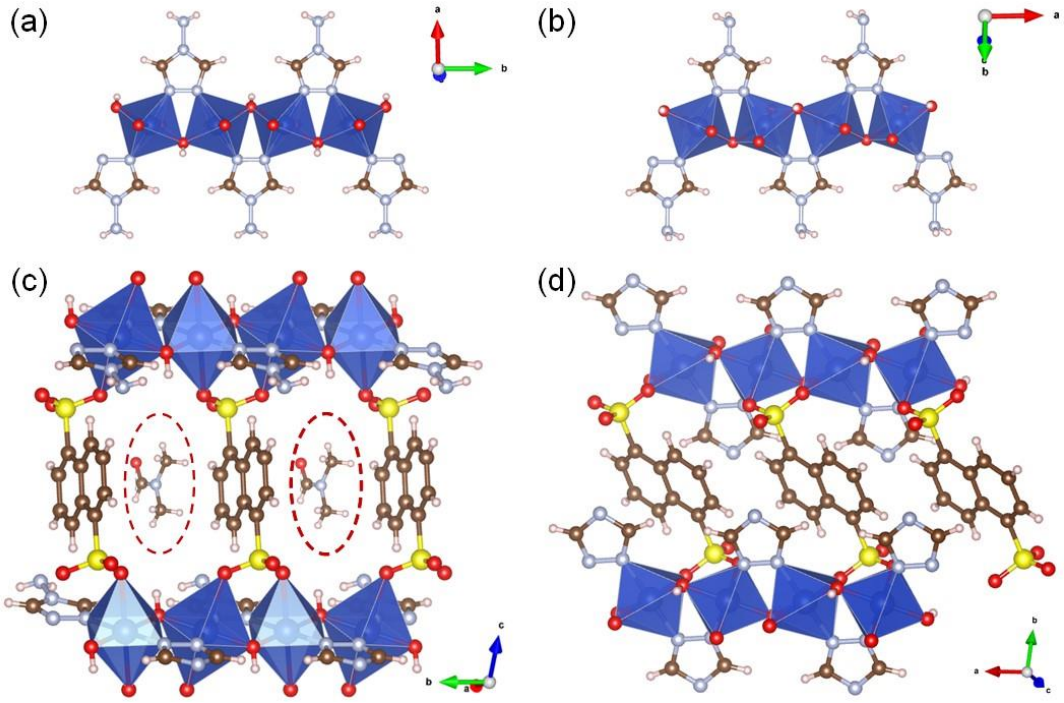

Figure 3.4 Polyhedral representation of the Cu^{2+} and T4A ligand chain in (a) Cu-SAT and (b) Cu-SAT (EtOH) as determined from SC-XRD. Polyhedral representation determined from SC-XRD showing the NDS ligand coordination with the Cu^{2+} chain in (c) Cu-SAT and (d) Cu-SAT (EtOH), red dashed ellipses mark the DMF molecule in the void space. Atoms are color-coded by element: S, yellow; Cu, blue; O, red; N, light blue; C, brown; H, beige.

Figure 3.4 presents a side-by-side comparison of the SC-XRD structures for Cu-SAT [28] and Cu-SAT (EtOH). As shown in Figure 3.4a and b, the Cu^{2+} centre in both Cu-SAT and Cu-SAT (EtOH) has an octahedral geometry with two coordination bonds to bridging OH moieties. There are a further two bonds to T4A ligands and also two η^2, μ^2 coordinating NDS ligands retained across both structures. These observations demonstrate that the water-aged Cu-SAT structure, as for directly synthesised Cu-SAT (EtOH) is not a decomposition product. Rather, the Cu-SAT (EtOH) structure indicates a more compact, DMF-free structure emerges with the loss of void spaces present in the Cu-SAT (Figure 3.4c and d). Notably, in Cu-SAT the chain of Cu^{2+} centres lies along the *b*-axis with 2D layers stacked approximately perpendicular to the *a*-axis whereas the Cu-SAT (EtOH) unit cell places the Cu^{2+} chain along the *a*-axis and 2D layers stacked perpendicular to the *c*-axis (Figures 3.5-3.6). Atomic displacement parameters (ADPs) of Cu-SAT (EtOH) indicate non-hydrogen atoms are well localised with minimal evidence of significant disorder in the structure (Figure 3.7). Details of a unit cell and the refinement for the Cu-SAT (EtOH) are given in Table 3.1.

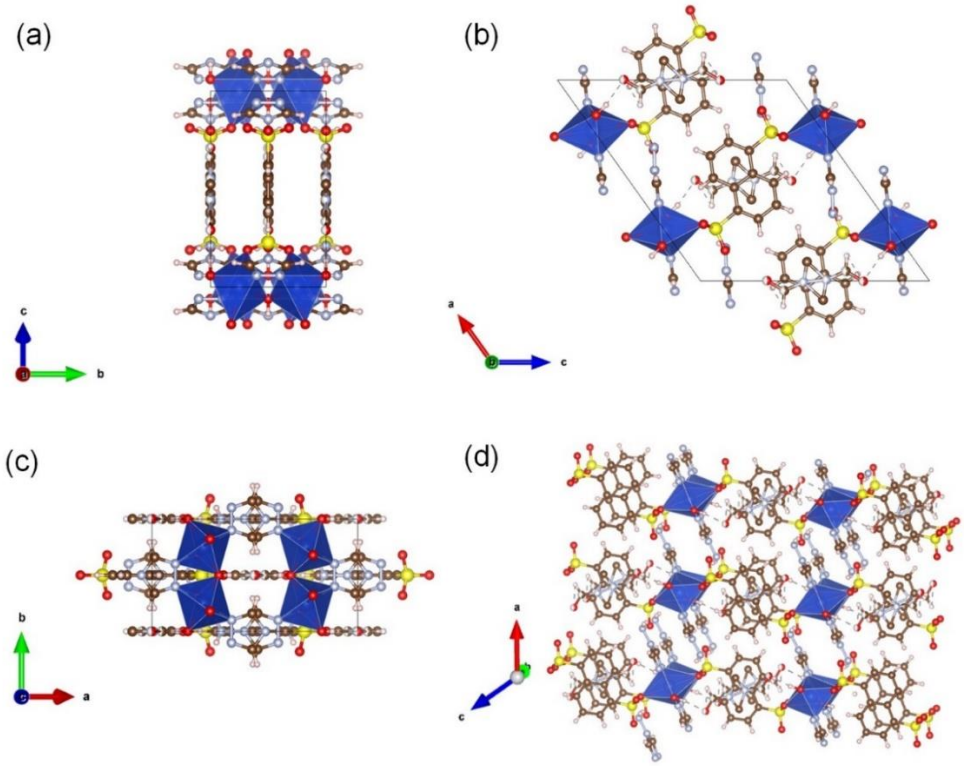

Figure 3.5 Polyhedral representations of the Cu-SAT unit cell determined by SC-XRD. The unit cell is depicted along (a) the *a*-axis, (b) the *b*-axis, (c) the *c*-axis, and (d) along a direction highlighting the stacked 2D layers formed by the NDS coordination of a Cu^{2+} chain. Atoms are color-coded by element: S, yellow; Cu, blue; O, red; N, light blue; C, brown; H, beige.

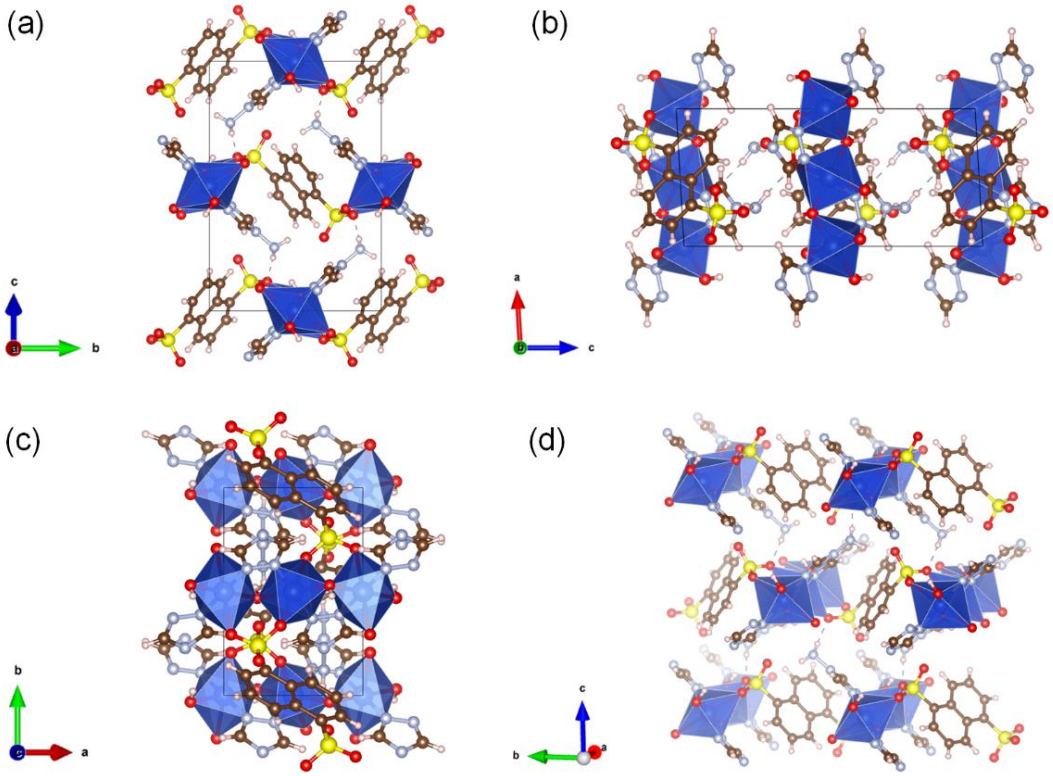

Figure 3.6 Polyhedral representations of the Cu-SAT (EtOH) unit cell as determined from SC-XRD. The unit cell is depicted along (a) the *a*-axis, (b) the *b*-axis, (c) the *c*-axis, and (d) along a direction highlighting the stacked 2D layers formed by NDS ligand coordination of a Cu^{2+} chain. Atoms are color-coded by element: S, yellow; Cu, blue; O, red; N, light blue; C, brown; H, beige.

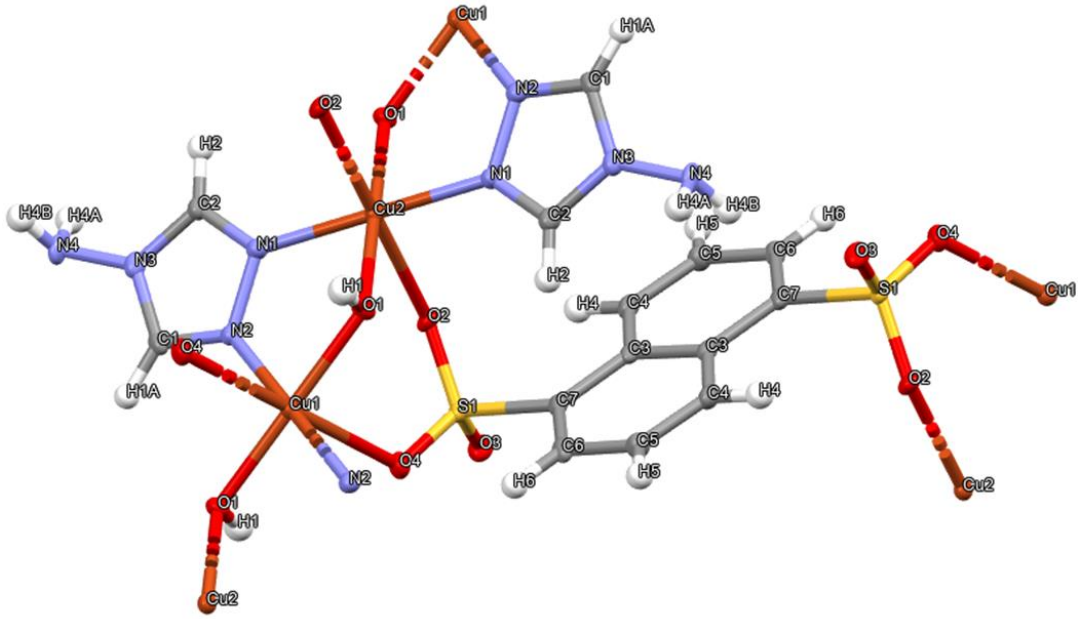

Figure 3.7 Visualisation of the atomic displacement parameters for the reported Cu-SAT (EtOH) structure showing the determined atoms depicted as ellipsoids (hydrogen atoms shown as spheres for reference).

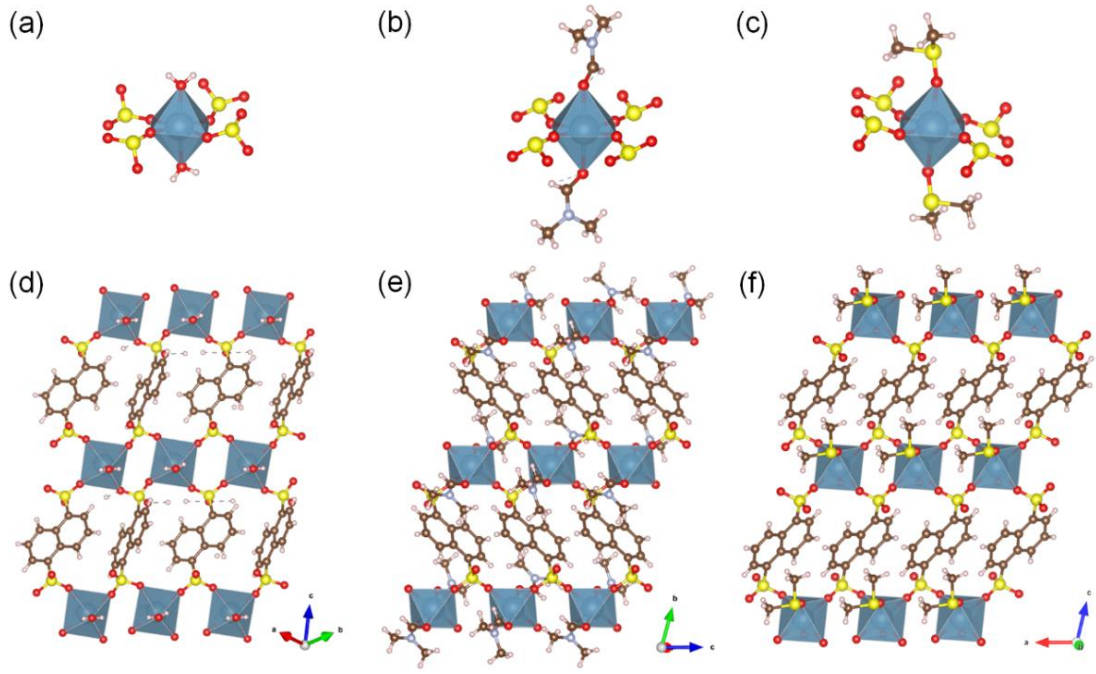

Figure 3.8 Polyhedral representations of the octahedral unit of Ca^{2+} in (a) Ca-NDS (water), (b) Ca-NDS (DMF) and (c) Ca-NDS (DMSO) as determined by SC-XRD. Polyhedral representations of the 2D layered structure of (d) Ca-NDS (water), (e) Ca-NDS (DMF) and (f) Ca-NDS (DMSO) as determined by SC-XRD. Atoms are color-coded by element: S, yellow; Ca, dusty blue; O, red; C, brown; N, light blue; H, beige.

We next turn to the structures of the Ca^{2+} CPs formed with NDS and water, DMF, and DMSO solvents. The metal centre, Ca^{2+}, exhibits a consistent octahedral geometry with four coordination bonds to sulfonate groups from the NDS ligands (Figure 3.8a-c). A further two coordination bonds are formed with water, DMF, or DMSO molecules in Ca-NDS (water), Ca-NDS (DMF), and Ca-NDS (DMSO) CPs, respectively. These three CPs present similar 2D sheet structures (Figure 3.8d-f). Notably, in Ca-NDS (water), the NDS molecules exhibit two orientations, producing alternating orientations of the aromatic rings. In contrast, in the Ca-NDS (DMF) and Ca-NDS (DMSO) structures, the aromatic ring systems are aligned in parallel. Consequently, there is greater tilting of Ca^{2+} octahedra relative to the plane of the 2D CP sheet in the Ca-NDS (DMF) and Ca-NDS (DMSO) structures. Due to different unit cell definitions, in Ca-NDS chains of Ca^{2+} run along $[1\bar{1}0]$ with 2D layers stacked along [110], while in Ca-NDS (DMF) Ca^{2+} chains follow the *b*-axis and 2D layers are stacked along the *a*-axis, and in Ca-NDS (DMSO) Ca^{2+} chains lie along the *a*-axis and 2D layers are stacked along the *b*-axis (Figures 3.8 and 3.11). ADPs of Ca-NDS (DMF) and Ca-NDS (DMSO) indicate all non-hydrogen atoms are well localised with minimal evidence of significant disorder in the structure (Figure 3.12). Further details of the unit cells of

the Ca-NDS (DMF) and Ca-NDS (DMSO) are presented in Table 3.1, whilst the unit cell of Ca-NDS (water) was reported previously by Cai et al. [26].

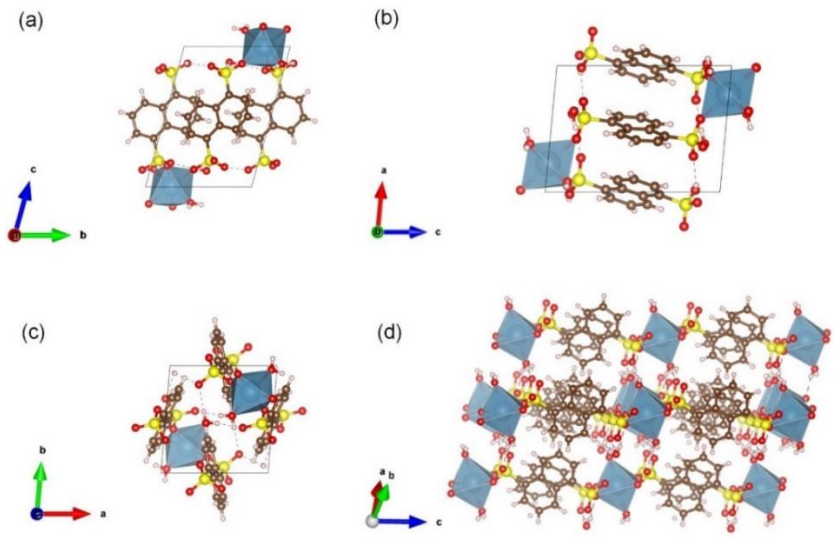

Figure 3.9 Polyhedral representations of the Ca-NDS (water) unit cell as determined from SC-XRD. The unit cell is depicted along (a) the *a*-axis, (b) the *b*-axis, (c) the *c*-axis, and (d) a direction highlighting the stacked 2D sheet structure formed by the NDS coordination of Ca^{2+}. Atoms are color-coded by element: S, yellow; Ca, dusty blue; O, red; C, brown; H, beige.

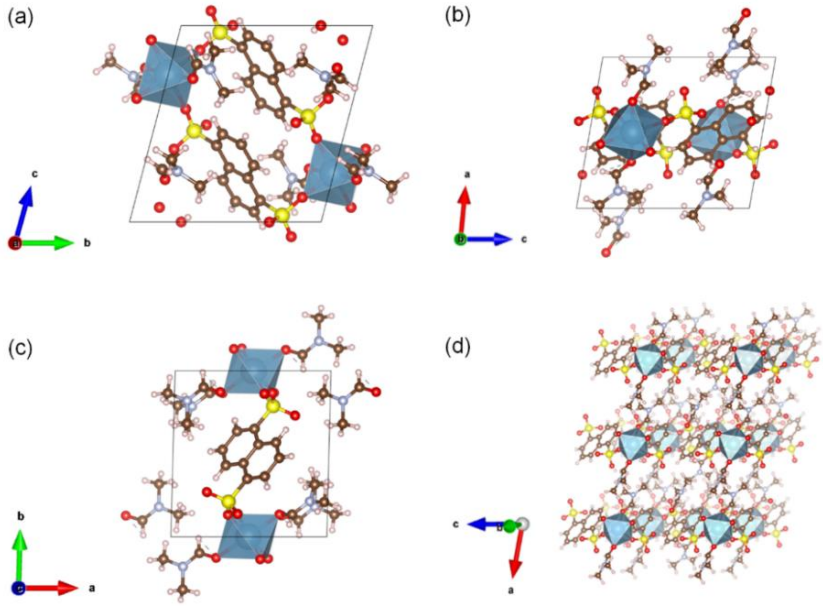

Figure 3.10 Polyhedral representations of the Ca-NDS (DMF) unit cell as determined from SC-XRD. The unit cell is depicted along (a) the *a*-axis, (b) the *b*-axis, (c) the *c*-axis, and (d) a direction highlighting the stacked 2D sheet structure formed by the NDS coordination of Ca^{2+}. Atoms are color-coded by element: S, yellow; Ca, dusty blue; O, red; C, brown; N, light blue; H, beige.

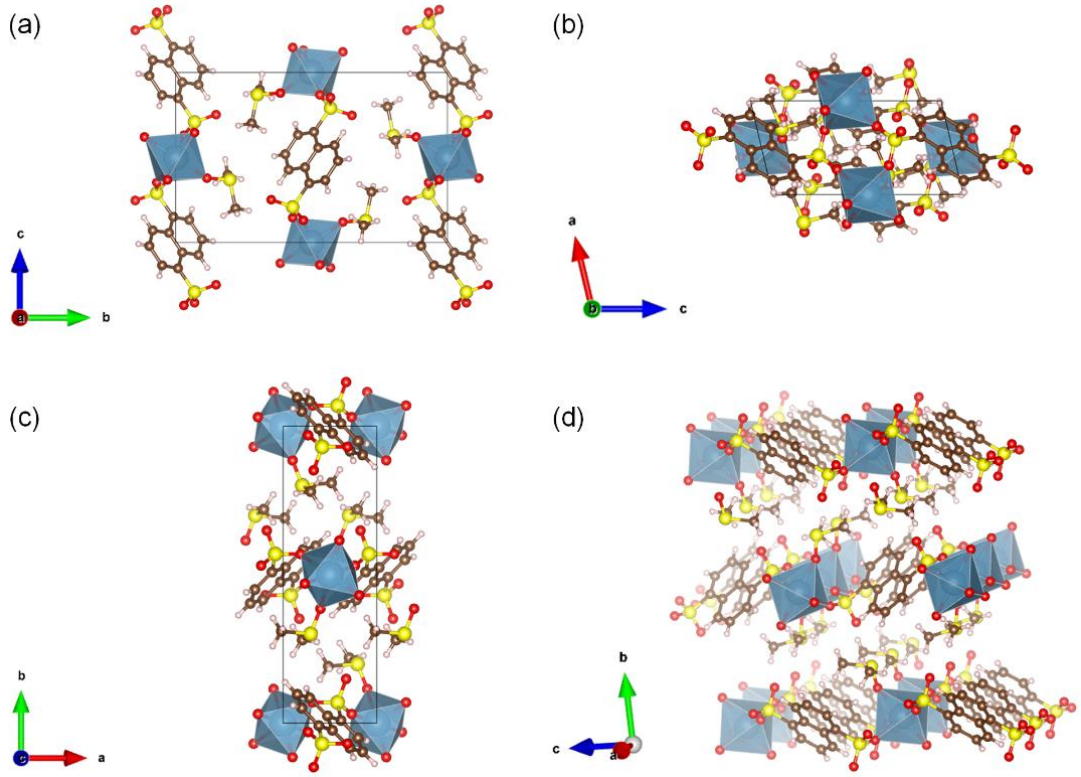

Figure 3.11 Polyhedral representations of the Ca-NDS (DMSO) structure as determined from SC-XRD. The unit cell is depicted along (a) the *a*-axis, (b) the *b*-axis, (c) the *c*-axis, and (d) a direction highlighting the stacked 2D sheet structure formed by NDS coordination of Ca^{2+}. Atoms are color-coded by element: S, yellow; Ca, dusty blue; O, red; C, brown; H, beige.

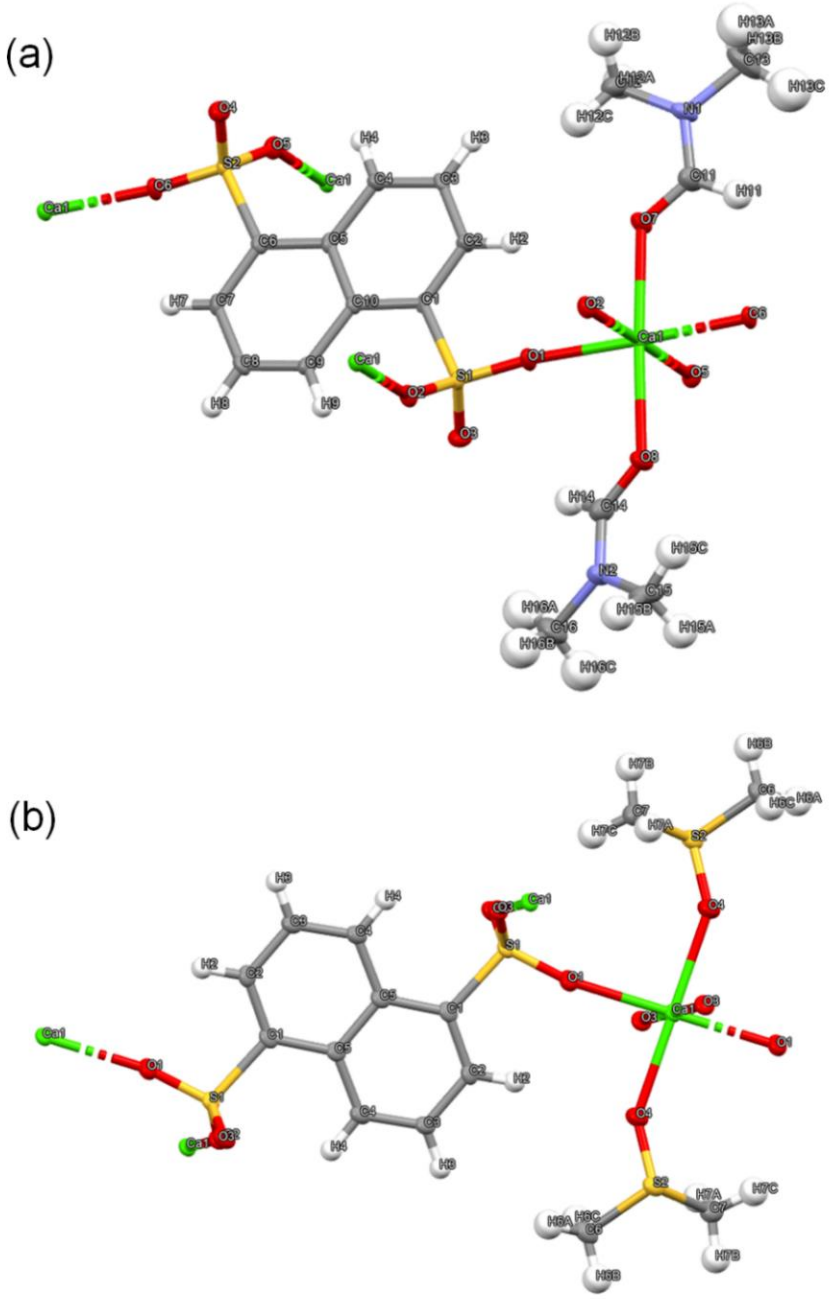

Figure 3.12 Visualisations of the atomic displacement parameters (a) for the reported Ca-NDS (DMF) structure and (b) for the reported Ca-NDS (DMSO) structure. The visualisations show the determined atoms depicted as ellipsoids (hydrogen atoms shown as spheres for reference).

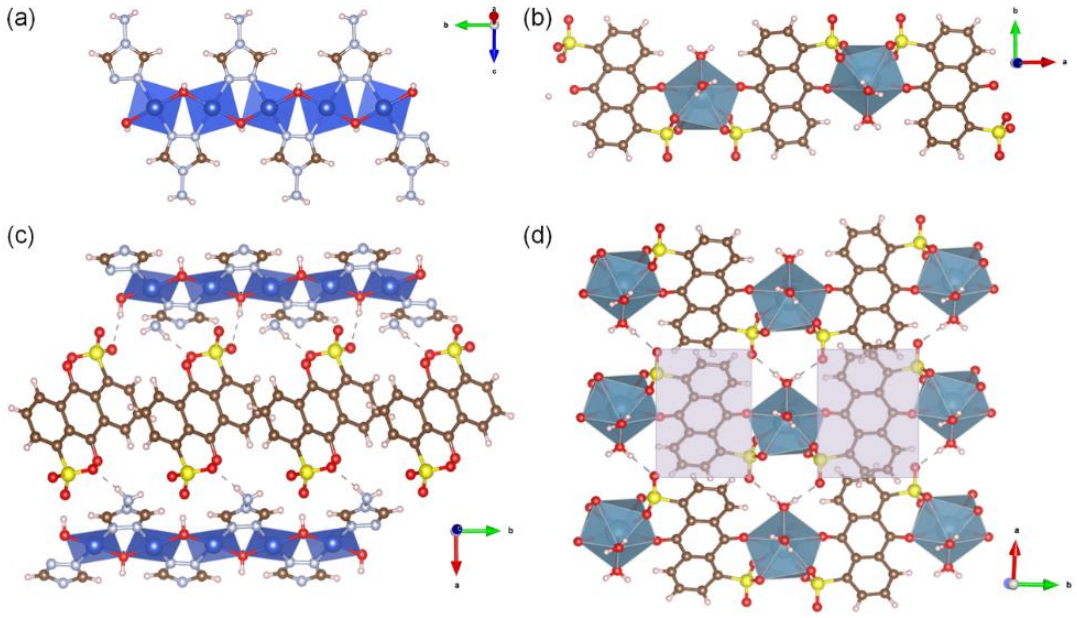

Figure 3.13 Polyhedral representations as determined by SC-XRD of (a) the Cu^{2+} and T4A ligand chain in Cu-SQAT, (b) the Ca^{2+} and NDS chain in Ca-ADS, (c) the interactions between ADS ligands and the Cu^{2+} chain in Cu-SQAT, and (d) the packing of 1D chains in Ca-ADS (the shading highlights two ADS ligands in the same chain). Atoms are color-coded by element: S, yellow; Cu, blue; O, red; N, light blue; C, brown; H, beige; Ca, dusty blue.

Structures resulting from analogous composition but substituting the ADS linker for NDS are shown in Figure 3.13, producing what we denote Cu-SQAT derived from Cu-SAT and producing Ca-ADS derived from Ca-NDS (water). Details of unit cells for the Cu-SQAT and Ca-ADS are provided in Table 3.1. In the Cu-SQAT structure (Figures 3.13a and c), Cu^{2+} exhibits distinctly different coordination to the octahedral ligand environment in Cu-SAT. Instead, a planar geometry is adopted around Cu^{2+} in what would resemble the equatorial positions in Cu-SAT but now in a corrugated 2D layer (see also Figure 3.14), with additional R-SO_3^- and R-NH_2 groups stabilising at a significantly longer distance in the axial positions from layers above and below. These could be considered 3D coordination between layers of the CP, but the distances and interactions between ligands and the metal centre are significantly larger in the axial positions in this structure at 2.496 Å for Cu-N (amino N) and 2.951 Å for Cu-O (sulfonate O) when compared to the characteristic distances in the planar (equatorial) positions at 2.004 Å for Cu-N (triazolate N) and 1.931 Å for Cu-O (hydroxyl O) or when compared with the distances in Cu-SAT at 2.009 Å for Cu-N (triazolate N), 2.473 Å for Cu-O (sulfonate O), and 1.947 Å for Cu-O (hydroxyl O). Moreover, the structure as shown in Figure 3.13c highlights the ADS ligands interact primarily through hydrogen bonding interactions with the bridging hydroxyl groups and the amino (T4A)

groups along the Cu^{2+} chains. Within the determined unit cell, the Cu^{2+} chains lie along the *b*-axis with corrugated 2D sheets stacked along the *c*-axis (Figure 3.15). ADPs of Cu-SQAT indicate all non-hydrogen atoms are well localised with ambiguity in atomic coordinates (Figure 3.16).

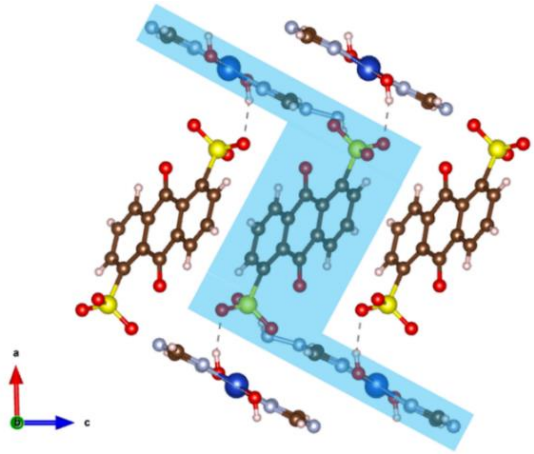

Figure 3.14 Polyhedral representation of Cu-SQAT depicting a side-on view along the crystallographic *b*-axis (the shading highlights 3D coordination between layers). Atoms are color-coded by element: S, yellow; Cu, blue; O, red; N, light blue; C, brown; H, beige.

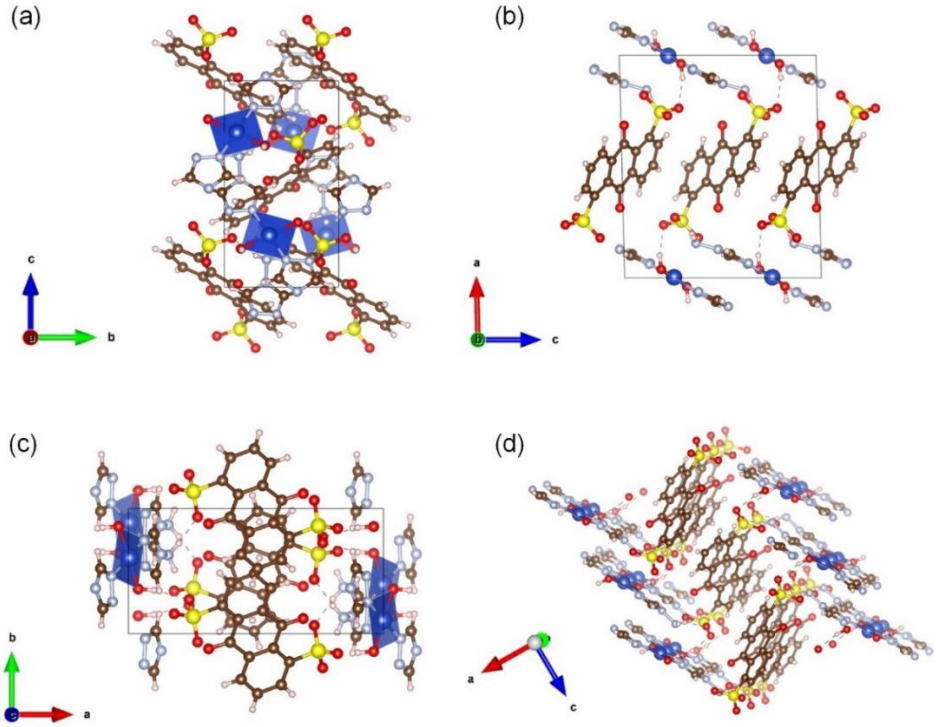

Figure 3.15 Polyhedral representations of the Cu-SQAT unit cell as determined from SC-XRD. The unit cell is depicted along (a) the *a*-axis, (b) the *b*-axis, (c) the *c*-axis, and (d) a direction highlighting the corrugated 2D sheet structure formed by the ADS coordination of the Cu^{2+} chain. Atoms are color-coded by element: S, yellow; Cu, blue; O, red; N, light blue; C, brown; H, beige.

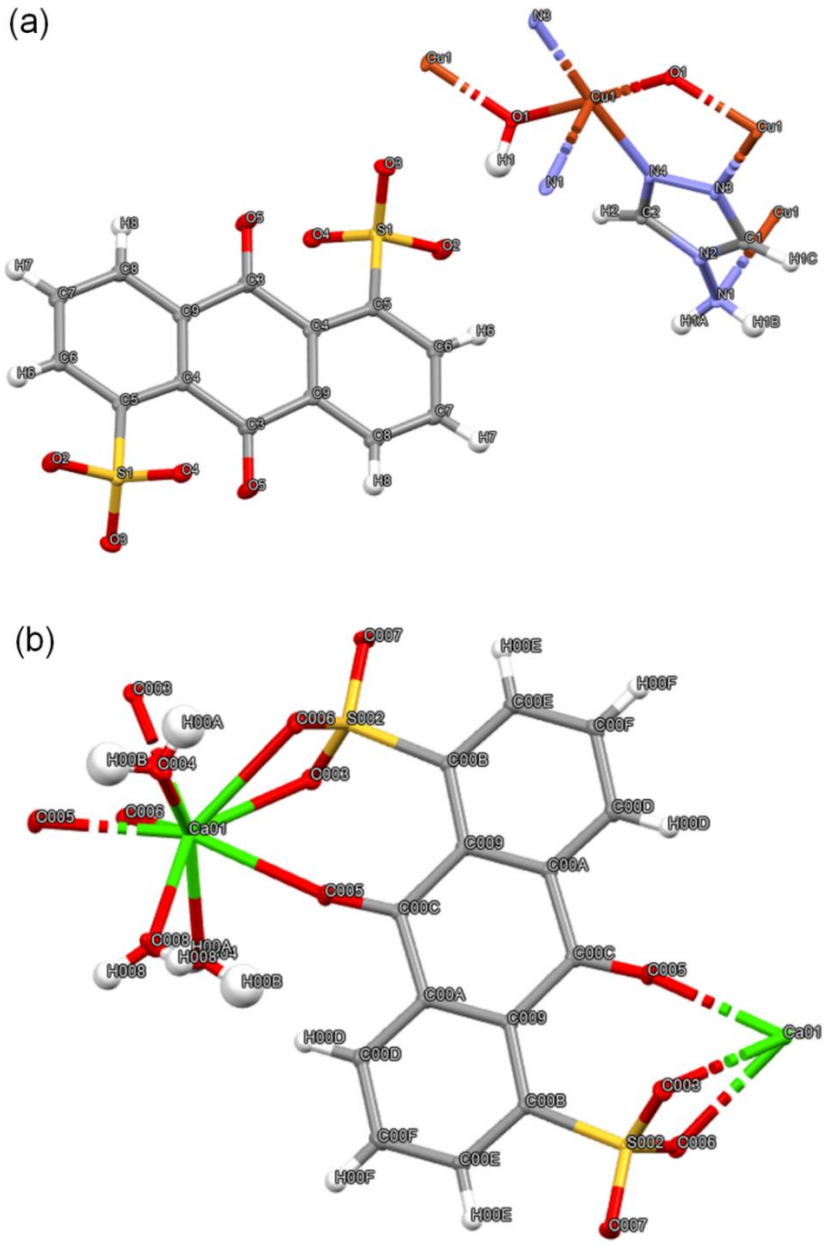

Figure 3.16 Visualisations of the atomic displacement parameters (a) for the reported Cu-SQAT structure and (b) for the reported Ca-ADS structure. The visualisations show the determined atoms depicted as ellipsoids (hydrogen atoms shown as spheres for reference).

The assembly of ligands and Ca^{2+} centres in Ca-ADS also shows a significant departure from the coordination motifs in the Ca-NDS structures (Figure 3.13b, d). The Ca^{2+} centre in Ca-ADS exhibits an apparent 9-fold coordination geometry about the Ca^{2+} centre, including three water molecules, two quinone carbonyl oxygens, and two pairs of η^2 non-bridging sulfonate ligands forming a distorted, approximately pentagonal bipyramidal coordination sphere. This coordination results in a 1D chain structure in Ca-ADS, with hydrogen bonding between the chains mediated by the free

sulfonate oxygens (hydrogen bond acceptors) and the nearest water ligands (hydrogen bond donors). The Ca-ADS unit cell places the 1D coordination polymer motif packed in sheets to form 2D layers stacked along the *c*-axis (Figure 3.17). ADPs of Ca-ADS indicate all non-hydrogen atoms are well localised with ambiguity in atomic coordinates (Figure 3.16b). Compared to the Ca-NDS structures, the quinone C=O groups show pronounced interaction with the Ca^{2+} atoms in Ca-ADS, seemingly precluding bridging coordination by the sulfonate groups to form a higher dimensional CP structure (Figure 3.18a and b). These single crystal structures suggest the 1,5-ADS ligand shows limited promise for isoreticular extension of the Cu-SAT and Ca-NDS CPs, in contrast to prior work with 2,6-ADS [37], but nevertheless introduces further modulation of the dense CP hydrogen bonding networks for proton conductivity applications.

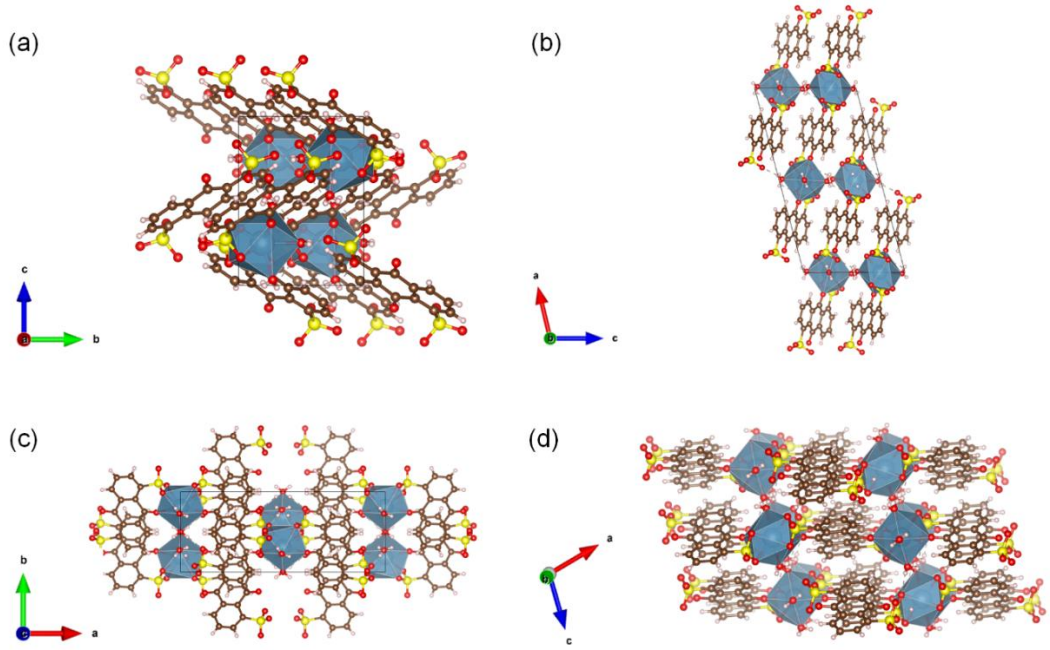

Figure 3.17 Polyhedral representations of the Ca-ADS unit cell as determined from SC-XRD. The unit cell is depicted along (a) the *a*-axis, (b) the *b*-axis, (c) the *c*-axis, and (d) a direction highlighting the stacked 2D sheet structure arising from ADS coordination of Ca^{2+} (2D sheet of 1D chains). Atoms are color-coded by element: S, yellow; Ca, dusty blue; O, red; C, brown; H, beige.

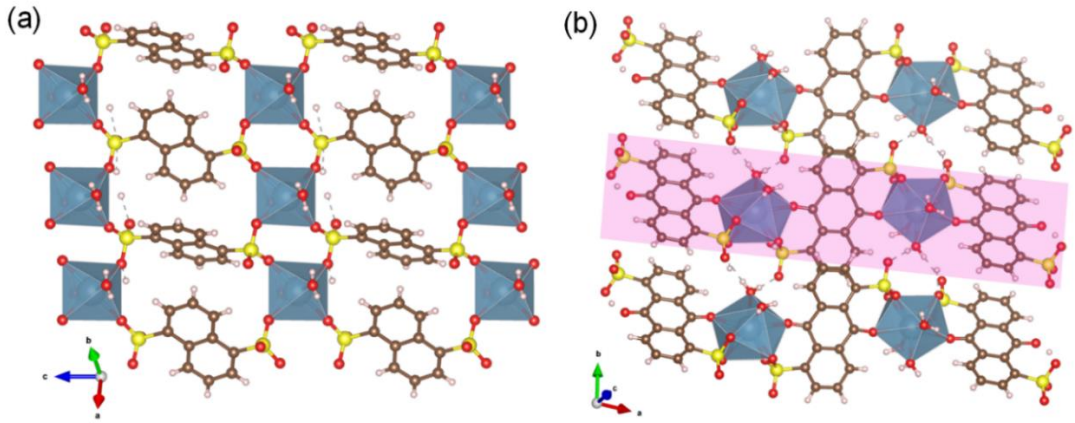

Figure 3.18 Polyhedral representation of (a) the 2D sheet structure of Ca-NDS (water) and (b) the 1D chain structure of Ca-ADS (the shading highlights the 1D chain). Atoms are color-coded by element: S, yellow; Ca, dusty blue; O, red; C, brown; H, beige.

Table 3.2 CHNS analysis as molar ratios (H = 1) for Cu-SAT and Cu-SAT (EtOH). The elemental ratios for the Cu-SAT and Cu-SAT (EtOH) unit cells (SC-XRD) are included for comparison. Uncertainties are given as one standard deviation.

Sample	N	C	H	S	Ratio of N to S
Cu-SAT a	0.40	0.85	1.00	0.10	4.00
Cu-SAT b	0.40	0.85	1.00	0.11	3.77
Cu-SAT c	0.38	0.80	1.00	0.11	3.45
AVG results of Cu-SAT	0.39 ± 0.01	0.83 ± 0.03	1.00	0.11 ± 0.01	3.74 ± 0.28
Unit cell formula Cu-SAT	0.52	0.94	1.00	0.12	4.25
Cu-SAT (EtOH) a	0.52	1.01	1.00	0.15	3.45
Cu-SAT (EtOH) b	0.52	1.01	1.00	0.15	3.45
Cu-SAT (EtOH) c	0.47	0.97	1.00	0.14	3.47
AVG results of Cu-SAT (EtOH)	0.50 ± 0.03	0.99 ± 0.02	1.00	0.14 ± 0.01	3.46 ± 0.01
Unit cell formula Cu-SAT (EtOH)	0.50	0.88	1.00	0.13	3.85

Table 3.3 CHNS analysis as molar ratios (H = 1) for Ca-NDS (water), Ca-NDS (DMF) and Ca-NDS (DMSO). The elemental ratios for the Ca-NDS (DMF) and Ca-NDS (DMSO) unit cells (SC-XRD) are included for comparison. Uncertainties are given as one standard deviation.

Sample	N	C	H	S	Ratio of N to S
Ca-NDS (water) a	0.02	1.15	1.00	0.23	--
Ca-NDS (water) b	0.02	0.87	1.00	0.16	--
Ca-NDS (water) c	0.03	1.10	1.00	0.26	
AVG results of Ca-NDS (water)	0.02 ± 0.01	1.04 ± 0.15	1.00	0.21 ± 0.05	--
Unit cell formula Ca-NDS (water)	--	1.00	1.00	0.20	--
Ca-NDS (DMF) a	0.11	1.10	1.00	0.19	0.08
Ca-NDS (DMF) b	0.09	1.11	1.00	0.19	0.07
Ca-NDS (DMF) c	0.13	1.12	1.00	0.29	0.07
AVG results of Ca-NDS (DMF)	0.11 ± 0.02	1.11 ± 0.01	1.00	0.22 ± 0.06	0.07 ± 0.01
Unit cell formula Ca-NDS (DMF)	0.10	0.80	1.00	0.10	1.00
Ca-NDS (DMSO) a	0.02	1.13	1.00	0.20	--
Ca-NDS (DMSO) b	0.01	0.68	1.00	0.12	--
Ca-NDS (DMSO) c	0.03	1.03	1.00	0.25	
AVG results of Ca-NDS (DMSO)	0.02 ± 0.01	0.94 ± 0.23	1.00	0.19 ± 0.07	--
Unit cell formula Ca-NDS (DMSO)	--	0.78	1.00	0.22	--

Table 3.4 CHNS analysis as molar ratios (H = 1) for Cu-SQAT and Ca-ADS. The elemental ratios for the Cu-SQAT and Ca-ADS unit cells (SC-XRD) are included for comparison. Uncertainties are given as one standard deviation.

Sample	N	C	H	S	Ratio of N to S
Cu-SQAT a	0.51	1.26	1.00	0.14	3.54
Cu-SQAT b	0.51	1.26	1.00	0.15	3.52
Cu-SQAT c	0.46	1.21	1.00	0.13	3.56
AVG results of Cu-SQAT	0.49 ± 0.03	1.24 ± 0.03	1.00	0.14 ± 0.01	3.54 ± 0.02
Unit cell formula Cu-SQAT	0.50	1.13	1.00	0.13	4.00
Ca-ADS a	0.02	1.20	1.00	0.16	--
Ca-ADS b	0.02	1.07	1.00	0.14	--
Ca-ADS c	0.04	1.29	1.00	0.21	
AVG results of Ca-ADS	0.03 ± 0.01	1.19 ± 0.11	1.00	0.17±0.04	--
Unit cell formula Ca-ADS	--	1.17	1.00	0.17	--

In addition to SC-XRD, we have further probed the powder-scale characteristics of the synthesised CPs. CHNS analysis showed similar ratios as determined by SC-XRD for Cu-SAT and Cu-SAT (EtOH) (Table 3.2), Ca-NDS (Table 3.3) and Cu-SQAT and Ca-ADS (Table 3.4). SEM-EDS further confirmed elemental content, composition, and homogeneity for the reported structures Cu-SAT (EtOH) and Cu-SQAT (Table 3.5, Figure 3.19-3.20), Ca-NDS (DMF), Ca-NDS (DMSO), and Ca-ADS (Table 3.6, Figures 3.21-3.23). XPS analyses likewise confirmed the elemental content, with small deviations observed from compositions expected in the SC-XRD molecular formula (Figures 3.24-3.25, Tables 3.7-3.8). These errors were attributed to surface degradation, residual solvent, or adventitious sources from the environment, though some missing metal centres, such as at the crystal surfaces in particular, cannot be ruled out from the XPS analyses. High resolution spectra further confirmed Cu (II) $2p_{3/2}$ and satellite peaks [46] in the reported Cu-based CP structures and a single calcium state of Ca (II) $2p_{3/2}$ and $2p_{1/2}$ [47] in the reported Ca-based CP structures. High resolution spectra of S $2p_{3/2}$ present two peaks around 168.0 and 169.2 eV belonging to the SO_3^{2-} [48] in all these reported structures, Ca-NDS (DMSO) shows two extra S 2p peaks associated with sulfinyl group from DMSO solvent [49].

Table 3.5 Elemental composition of Cu-SAT (EtOH) and Cu-SQAT from SEM-EDS analysis (Atomic %) determined using the Cliff-Lorimer method (manufacturer-supplied k-factors). The elemental ratios for the Cu-SAT (EtOH) and Cu-SQAT unit cells (SC-XRD) are included for comparison.

Sample	C %	O %	N %	S %	Cu %	Ratio of Cu/(Cu+S)
Cu-SAT (EtOH)	46.4	19.7	20.1	6.9	6.3	0.48
Unit cell formula Cu-SAT (EtOH)	41.2	23.5	23.5	5.9	5.9	0.5
Cu-SQAT	49.3	21.0	18.4	5.4	5.9	0.52
Unit cell formula Cu-SQAT	45	25	20	5	5	0.5

Table 3.6 Elemental composition of Ca-NDS (DMF), Ca-NDS (DMSO) and Ca-ADS from SEM-EDS analysis (Atomic %) determined using the Cliff-Lorimer method (manufacturer-supplied k-factors). The elemental ratios for the Ca-NDS (DMF), Ca-NDS (DMSO) and Ca-ADS unit cells (SC-XRD) are included for comparison.

Sample	C %	O %	N %	S %	Ca %	Ratio of Ca/(Ca+S)
Ca-NDS (DMF)	55.6	28.3	1.9	9.4	4.8	0.34
Unit cell formula Ca-NDS (DMF)	55.2	27.6	6.9	6.9	3.4	0.33
Ca-NDS (DMSO)	59.3	15.0	--	14.3	3.7	0.21
Unit cell formula Ca-NDS (DMSO)	51.9	29.6	--	14.8	3.7	0.2
Ca-ADS	58.0	29.0	--	8.6	4.4	0.34
Unit cell formula Ca-ADS	50	39.3	--	7.1	3.6	0.34

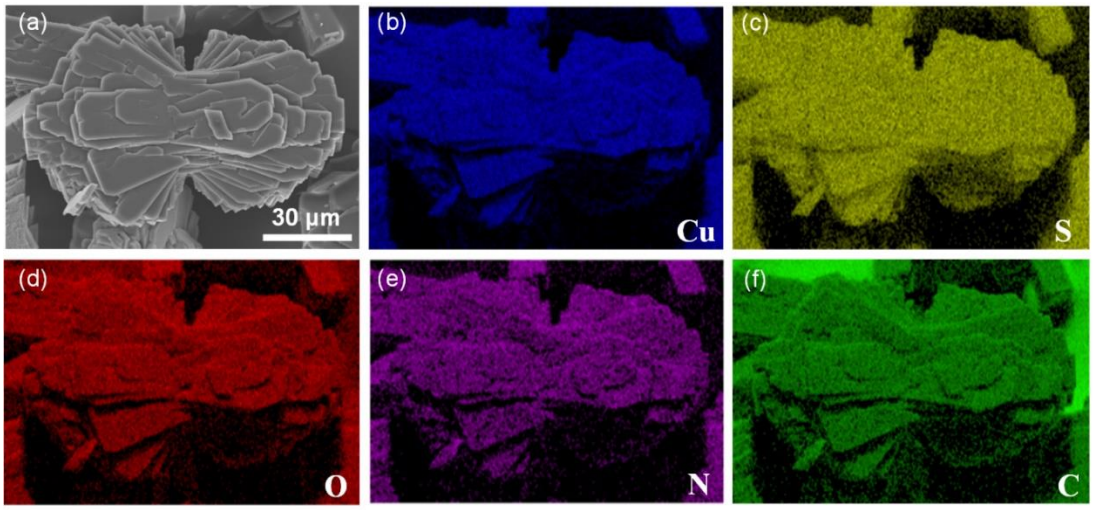

Figure 3.19 (a) SEM image of a Cu-SAT (EtOH) particle and SEM-EDS elemental maps of (b) copper, (c) sulfur, (d) oxygen, (e) nitrogen, and (f) carbon.

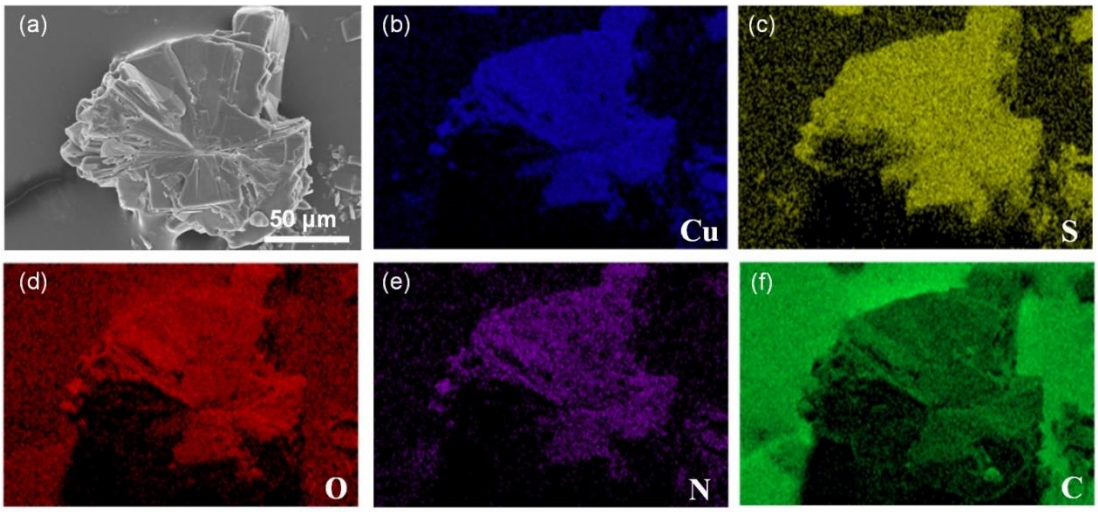

Figure 3.20 (a) SEM image of a Cu-SQAT particle and SEM-EDS elemental maps of (b) copper, (c) sulfur, (d) oxygen, (e) nitrogen, and (f) carbon.

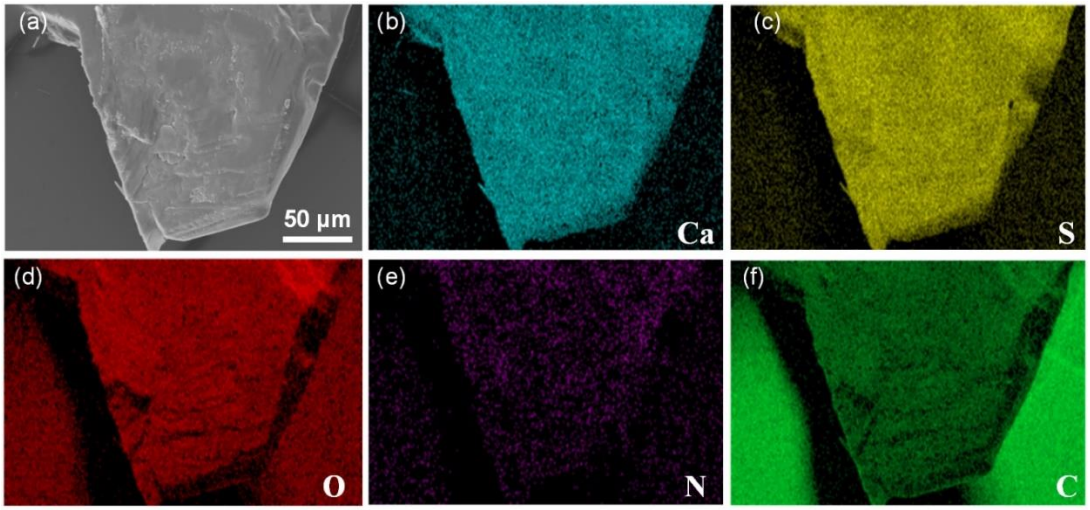

Figure 3.21 (a) SEM image of a Ca-NDS (DMF) particle and SEM-EDS elemental maps of (b) calcium, (c) sulfur, (d) oxygen, (e) nitrogen, and (f) carbon.

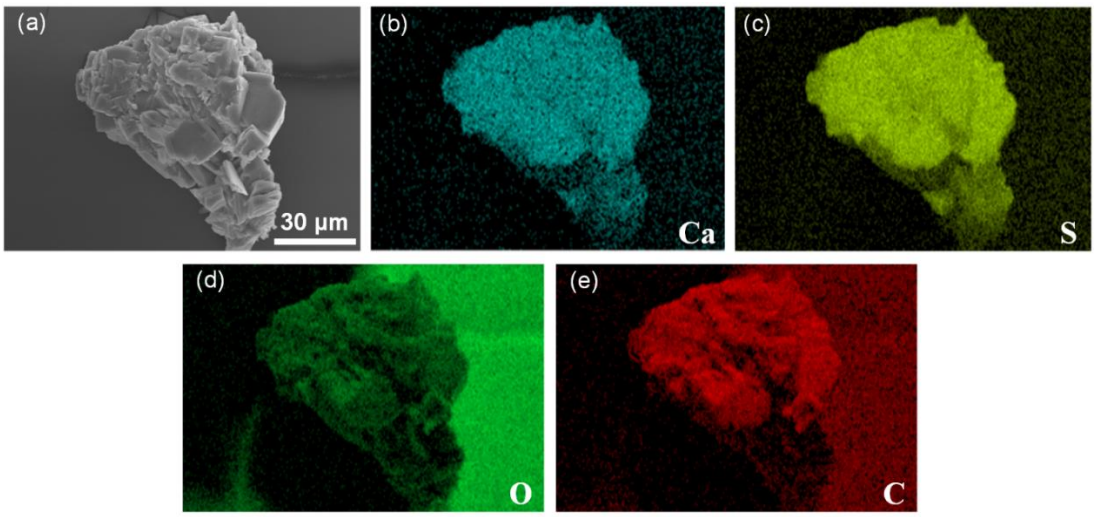

Figure 3.22 (a) SEM image of a Ca-NDS (DMSO) particle and SEM-EDS elemental maps of (b) calcium, (c) sulfur, (d) oxygen, and (e) carbon.

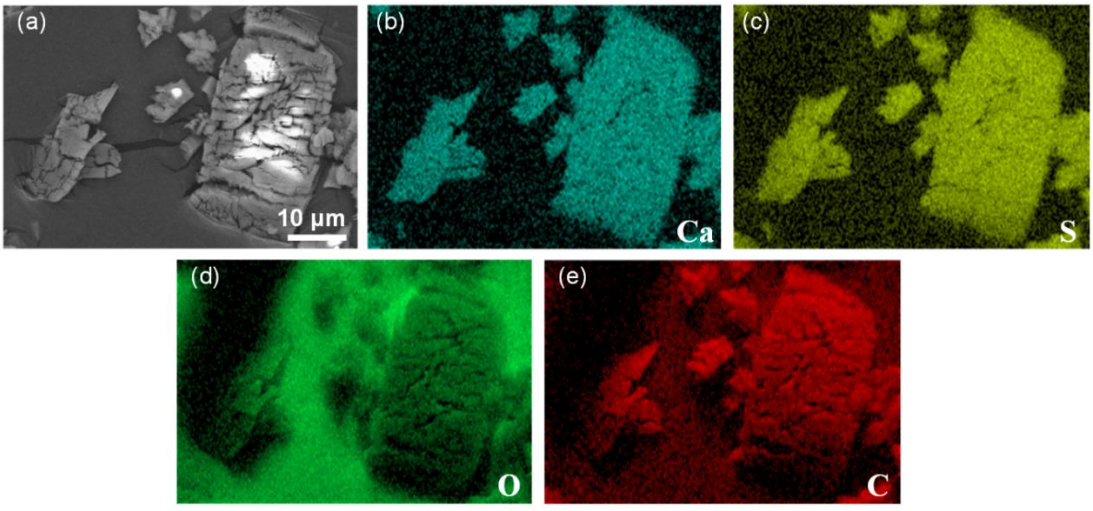

Figure 3.23 (a) SEM image of a Ca-ADS particle and SEM-EDS elemental maps of (b) calcium, (c) sulfur, (d) oxygen, and (e) carbon.

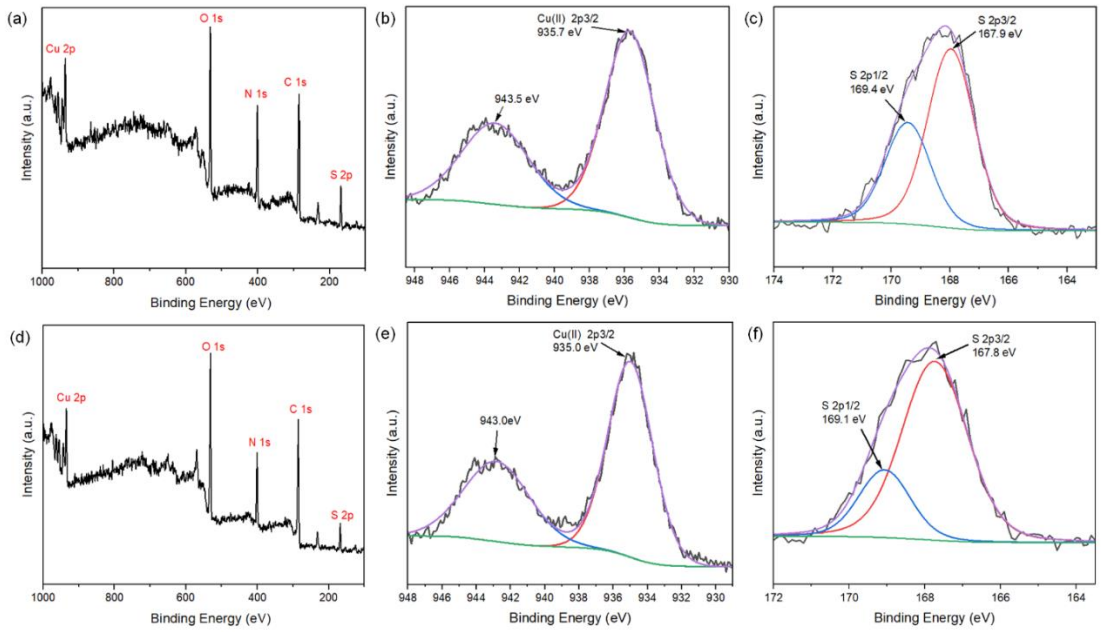

Figure 3.24 XPS analysis of Cu-SAT (EtOH) and Cu-SQAT, showing (a) survey spectra, (b) high resolution scans of Cu $2p_{3/2}$, and (c) high resolution scans of S $2p_{3/2}$ for Cu-SAT (EtOH), and (d) survey spectra, (e) high resolution scans of Cu $2p_{3/2}$, and (f) high resolution scans of S $2p_{3/2}$ for Cu-SQAT (Ar sputtering before analysis).

Table 3.7 Elemental composition analysis of Cu-SAT (EtOH) and Cu-SQAT by XPS (Ar sputtering before analysis). The elemental ratios for the Cu-SAT (EtOH) and Cu-SQAT unit cells (SC-XRD) are included for comparison.

Sample	C 1s %	O 1s %	N 1s %	S 2p %	Cu 2p %	Ratio of Cu/(Cu+S)
Cu-SAT (EtOH)	52.5	19.6	18.4	5.8	3.7	0.39
Unit cell formula Cu-SAT (EtOH)	41.2	23.5	23.5	5.9	5.9	0.5
Cu-SQAT	51.3	23.0	16.1	5.6	4.0	0.38
Unit cell formula Cu-SQAT	45	25	20	5	5	0.5

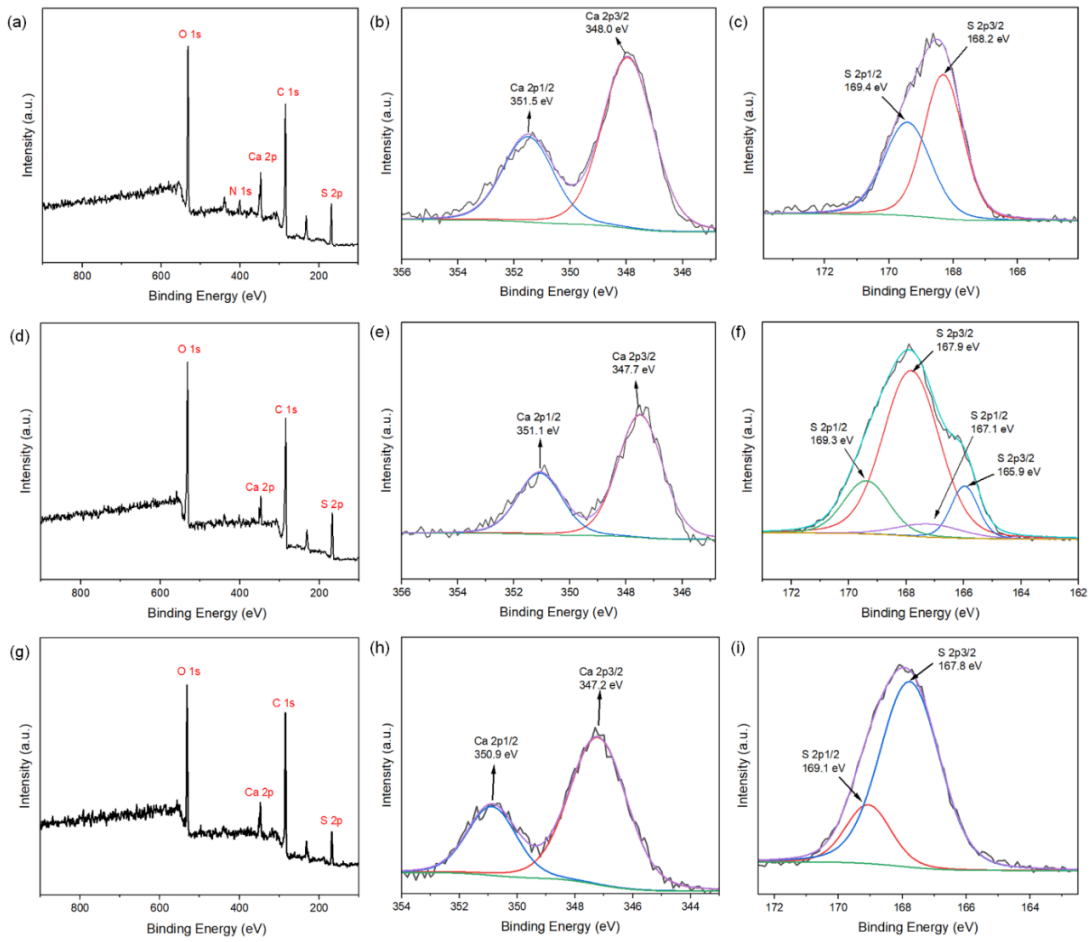

Figure 3.25 XPS analysis of Ca-NDS (DMF), Ca-NDS (DMSO), and Ca-ADS, showing (a) survey spectra, (b) high resolution scans of Ca $2p_{3/2}$, and (c) high resolution scans of S $2p_{3/2}$ for Ca-NDS (DMF), (d) survey spectra, (e) high resolution scans of Ca $2p_{3/2}$, and (f) high resolution scans of S $2p_{3/2}$ for Ca-NDS (DMSO), and (g) survey spectra, (h) high resolution scans of Ca $2p_{3/2}$, and (i) high resolution scans of S $2p_{3/2}$ for Ca-ADS.

Table 3.8 Elemental composition of Ca-NDS (DMF), Ca-NDS (DMSO) and Ca-ADS from XPS analysis. The elemental ratios for the Ca-NDS (DMF), Ca-NDS (DMSO) and Ca-ADS unit cells (SC-XRD) are included for comparison.

Sample	C 1s %	O 1s %	N 1s %	S 2p %	Ca 2p %	Ratio of Ca/(Ca+S)
Ca-NDS (DMF)	58	23.4	3.1	10.8	4.7	0.3
Unit cell formula Ca-NDS (DMF)	55.2	27.6	6.9	6.9	3.4	0.33
Ca-NDS (DMSO)	62.4	22.1	--	13.1	2.4	0.15
Unit cell formula Ca-NDS (DMSO)	51.9	29.6	--	14.8	3.7	0.2
Ca-ADS	65	21.8	--	9.8	3.5	0.26
Unit cell formula Ca-ADS	50	39.3	--	7.1	3.6	0.34

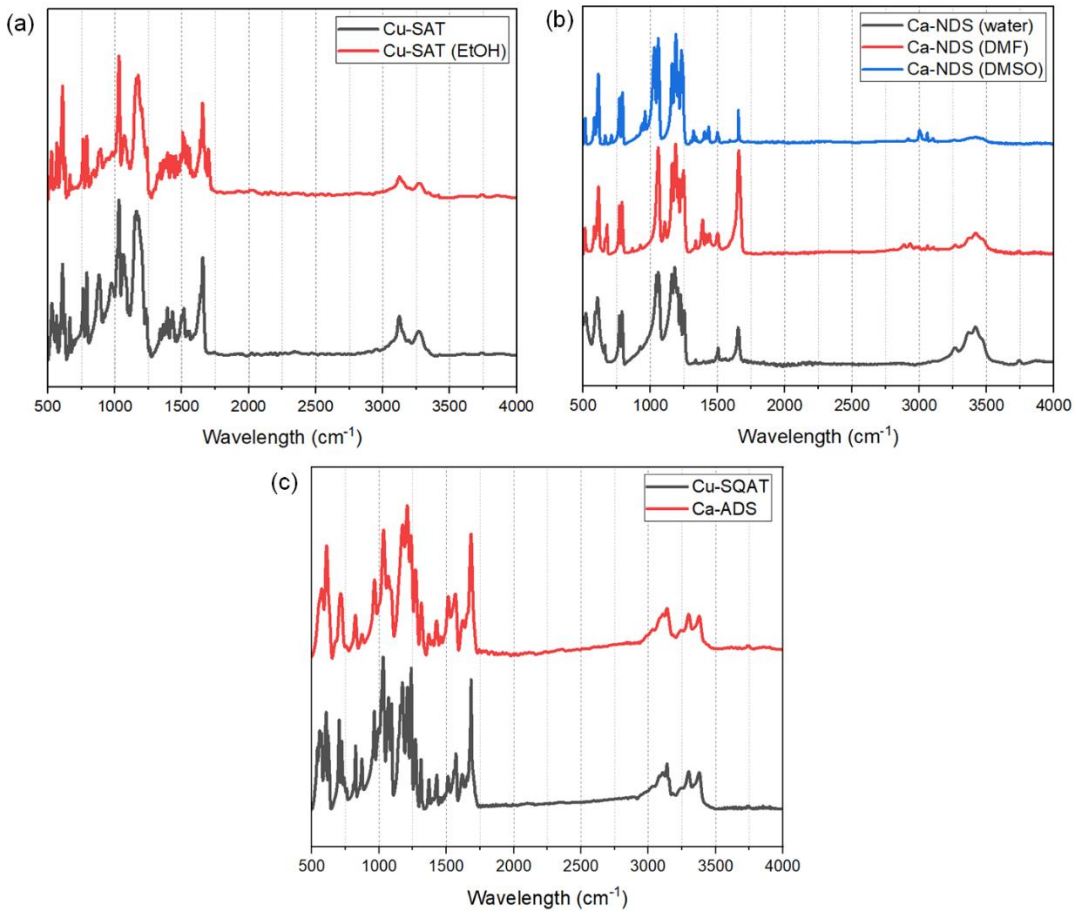

Figure 3.26 ATR-FTIR spectra of (a) Cu-SAT and Cu-SAT (EtOH), (b) Ca-NDS (water), Ca-NDS (DMF) and Ca-NDS (DMSO), and (c) Cu-SQAT and Ca-ADS samples.

ATR-FTIR spectra of all considered sulfonate CPs (Figure 3.26) consistently showed signatures attributable to the constituent ligands. Strong bands at approximately 530, 620, 1068 and 1190 cm^{-1}, were assigned as the major peaks of the

sulfonate group [50]. Multiple peaks across 1450 to 1650 cm^{-1} were attributed to the skeleton vibration of the benzene rings [51], and peaks in the range 650 to 900 cm^{-1} were assigned to the out-of-plane C-H bending vibration of the aromatic ring [52]. In Cu-SAT and Cu-SAT (EtOH), the stretching vibration of the C-N bond [53] and amino groups [54] from T4A contributed further bands at 1190 cm^{-1} and 3300 cm^{-1}. Ca-NDS (water) presents a wider and stronger band between 3000 to 3500 cm^{-1} relative to Ca-NDS (DMF) and Ca-NDS (DMSO), attributed to O-H band from water bound to Ca in the Ca-NDS (water) unit cell. In turn, the carbonyl group from the ADS ligand [55] contributes strong peaks at 1685 cm^{-1} in Cu-SQAT and Ca-ADS sample.

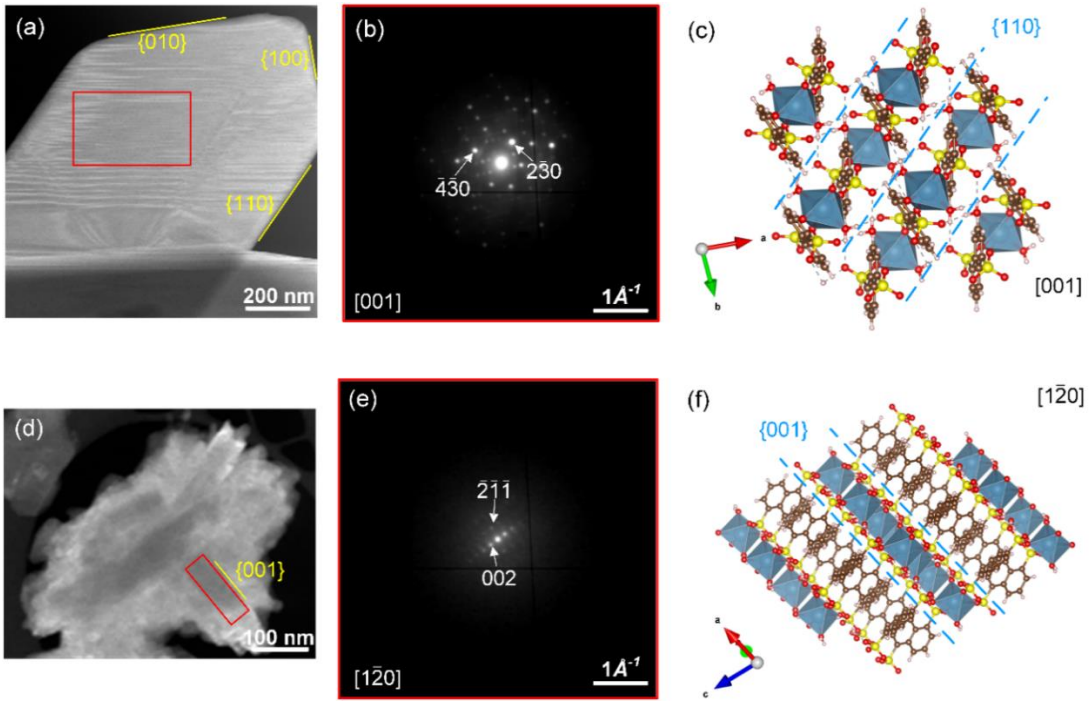

Figure 3.27 (a) and (d) Annular dark field STEM images of Ca-NDS (water) particles. (b) and (e) Corresponding diffraction patterns extracted from scanning electron diffraction data in the areas marked by the red rectangles. (c) and (f) Corresponding visualization of the crystal structures with major planes (facets) seen in (a) and (d) indexed on the real-space unit cell. Atoms are color-coded by element: S, yellow; Ca, dusty blue; O, red; C, brown; H, beige.

Building on previous nanobeam electron diffraction and elemental analysis on Cu-SAT [28], Ca-NDS (water) particles were further analysed by SED (Figure 3.27) and STEM-EDS (Figure 3.28 and 3.29). These STEM imaging and diffraction analyses revealed plate-like particle with four major facets indexed as {100}, {010}, {110}, and {001}. The prominent planes forming the top and bottom of plates appear to be {001} planes with the major side facets formed from {110} planes. We note the {110} planes

coincide with the inter-layer planes, and the larger {001} planes correspond to planes along the Ca-NDS-Ca direction. Under the assumption of thermodynamic or kinetic Wulff construction principles [56, 57], the larger {001} facets may be the planes with the lowest surface energies or growth velocities. This facet analysis also suggests that the surfaces terminate at either metal centres or ligand molecules, consistent with previous observations of metal centre termination in UiO-66 MOFs [58, 59]. Elemental mapping of Ca-NDS (water) by STEM-EDS analysis confirmed the expected elements within these microscopic single crystals (Figure 3.28 and 3.29).

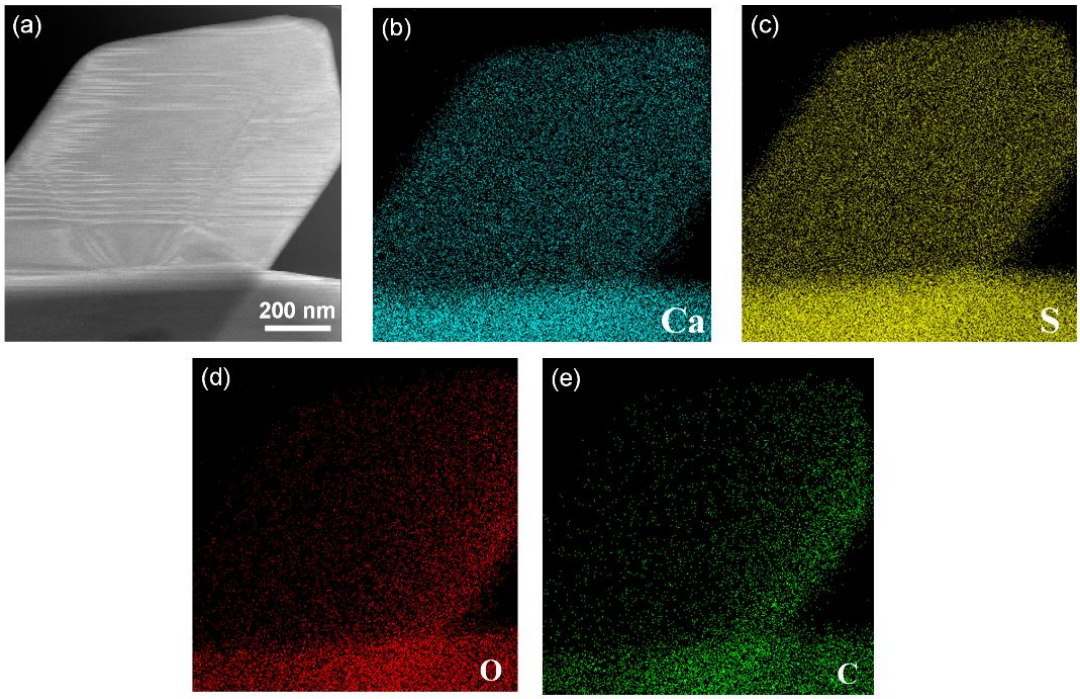

Figure 3.28 STEM Annular Dark Field image of Ca-NDS (water) sample, and STEM-EDS elemental maps of (b) calcium, (c) sulfur, (d) oxygen, and (e) carbon. The oxygen and carbon K_α emission occurs at low energy and is therefore affected by absorption effects within the sample, resulting in apparent inhomogeneities in the maps as a function of path from the source of X-ray emission to the X-ray detector.

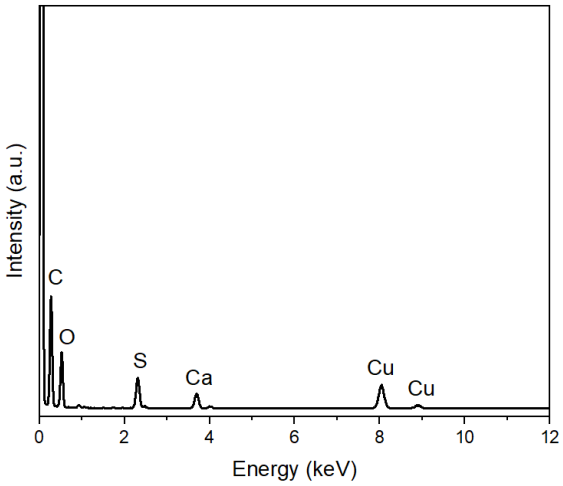

Figure 3.29 EDS spectra of the Ca-NDS (water) crystal shown in Figure 3.28.

3.3.2 Proton conductivity

To investigate the proton conductivities of the NDS- and ADS-based CPs, we have carried out EIS characterisation in pellet form under controlled temperature (50-80 °C) and humidity (95% RH). We first examined the thermal stability of the CPs by TGA and DTG analysis. Cu-SAT shows a series of mass losses from 235 °C, attributed to the release of DMF followed by ligand decomposition, whereas Cu-SAT (EtOH) showed mass losses from 282 °C due to ligand decomposition (Figure 3.30a and b). All temperatures were extracted from the maxima in the first derivative of the TGA curve (see Methods). Ca-NDS samples generally showed initial mass losses at 178 °C (water), 210 °C (DMF) and 320 °C (DMSO) followed by a second mass loss in each case above 500 °C (Figure 3.30c and d). The first mass losses follow the order of the solvent boiling points and may suggest this event involves loss of the coordinated solvent, followed by NDS decomposition above 500 °C. Ca-ADS similarly showed an initial mass loss from approximately 167 °C, and followed by subsequent mass loss above 500 °C. Cu-SQAT showed a first major mass loss from approximately 298 °C, consistent with its structural similarity to Cu-SAT (EtOH) (Figure 3.30e and f). In all cases, no major mass losses occur at temperatures of 80 °C or below. To further assess the stability of the samples under the pellet formation and EIS testing conditions, powder XRD characterisation was carried out to evaluate any significant changes in the crystal structure of the pellets. After exposuring Cu-SAT in high humidity and high temperature for a long time during EIS test, Cu-SAT presented a mixed crystal phase

with Cu-SAT (EtOH) (Figure 3.31a). No significant changes were observed for Cu-SAT (EtOH) (Figure 3.31b), for Ca-NDS (water, Ca-NDS (DMF), or Ca-NDS (DMSO) (Figure 3.32), or for Cu-SQAT or Ca-ADS (Figure 3.33).

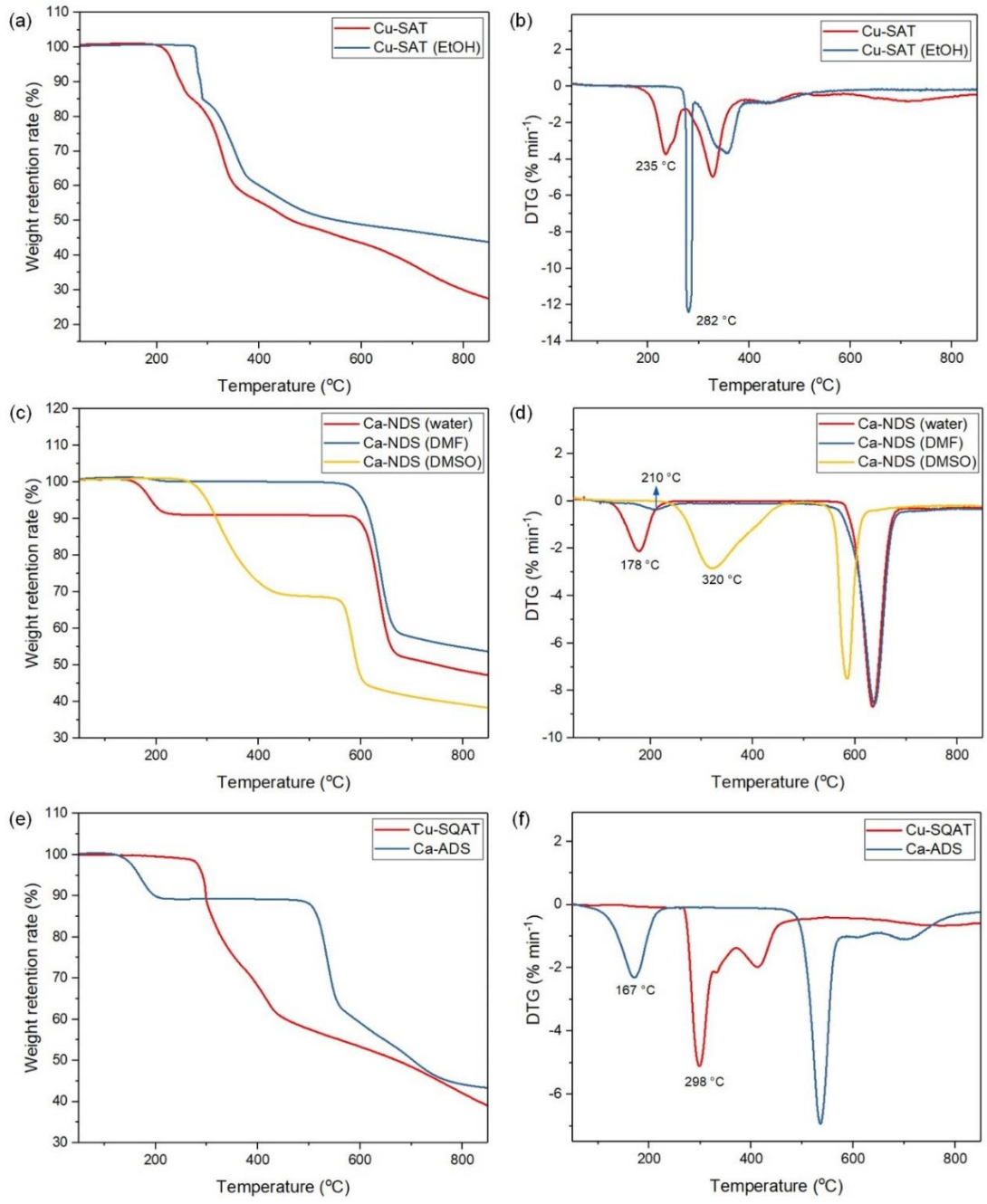

Figure 3.30 (a) TGA and (b) DTG results of Cu-SAT and Cu-SAT (EtOH) samples, (c) TGA and (d) DTG results of Ca-NDS (water), Ca-NDS (DMF) and Ca-NDS (DMSO) samples, and (e) TGA and (f) DTG results of Cu-SQAT and Ca-ADS samples.

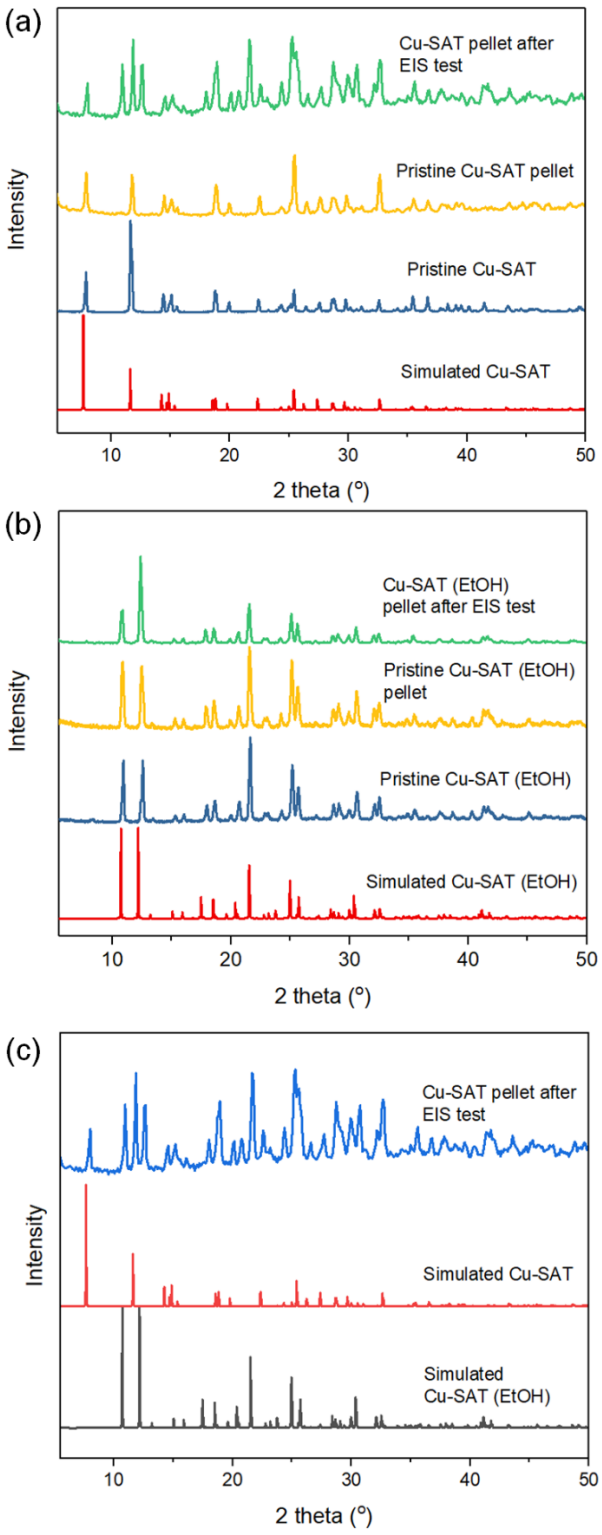

Figure 3.31 Experimental powder XRD patterns of (a) Cu-SAT and (b) Cu-SAT (EtOH) as a powder collected from synthesis (pristine), after pellet formation, and after EIS testing compared to powder XRD patterns simulated from the respective single crystal structures. (c) XRD patterns of Cu-SAT after EIS testing compared to powder XRD patterns simulated from Cu-SAT and Cu-SAT (EtOH).

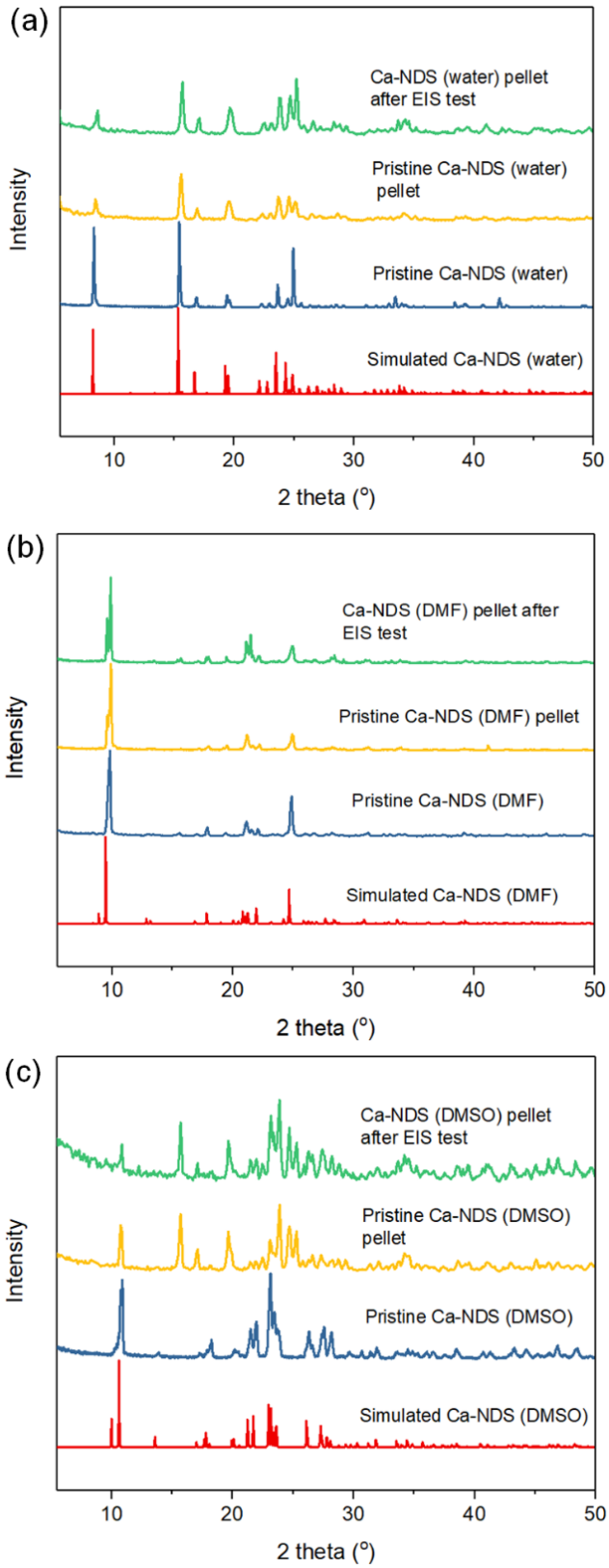

Figure 3.32 Experimental powder XRD patterns of (a) Ca-NDS (water), (b) Ca-NDS (DMF) and (c) Ca-NDS (DMSO) as a powder collected from synthesis (pristine), after pellet formation, and after EIS testing compared to powder XRD patterns simulated from the respective single crystal structures.

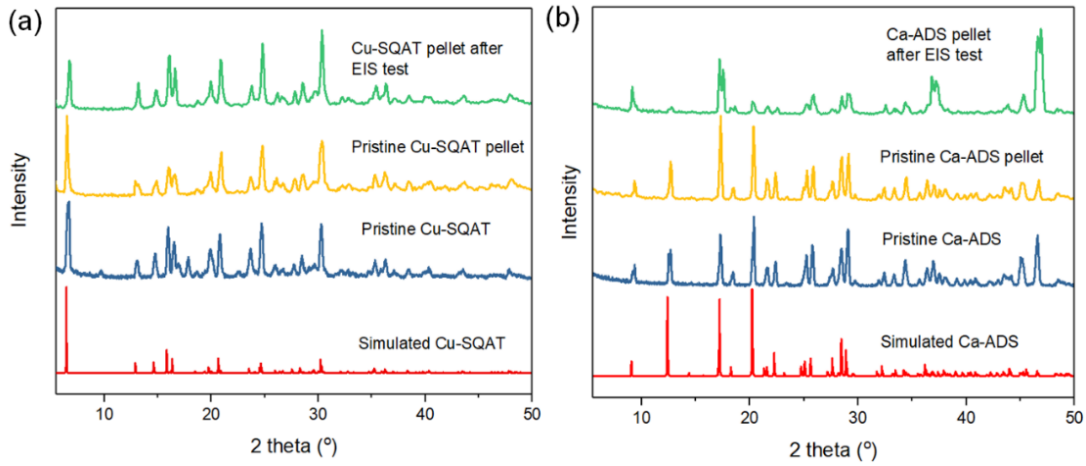

Figure 3.33 Experimental powder XRD patterns of (a) Cu-SQAT and (b) Ca-ADS as a powder collected from synthesis (pristine), after pellet formation, and after EIS testing compared to powder XRD patterns simulated from the respective single crystal structures.

After pellet making, inspection by light microscopy showed that the small particles formed during synthesis were pressed tightly together, and the surfaces of the resulting pellets were smooth and flat (Figure 3.34), suitable for testing in a plate-electrode EIS cell. Elemental mapping by SEM-EDS confirmed homogeneous distributions of Cu, S, O, N and C across the pellet surfaces of Cu-SAT and Cu-SQAT pellets and a homogeneous distribution of Ca, S, O, and C elements across the surface of Ca-NDS (water) pellets (Figure 3.35-3.38). We note that pellet densities were consistent and reproducible, and the pellet densities were generally >80% of the density calculated from their SC-XRD structures (Table 3.9-3.11).

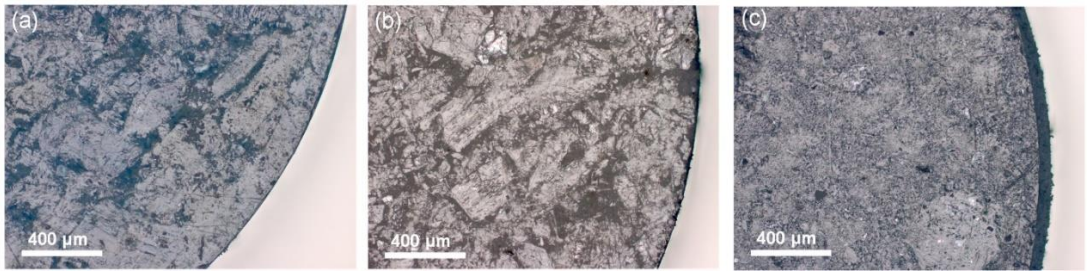

Figure 3.34 Light microscope images of (a) Cu-SAT, (b) Ca-NDS (water) and (c) Cu-SQAT pellets.

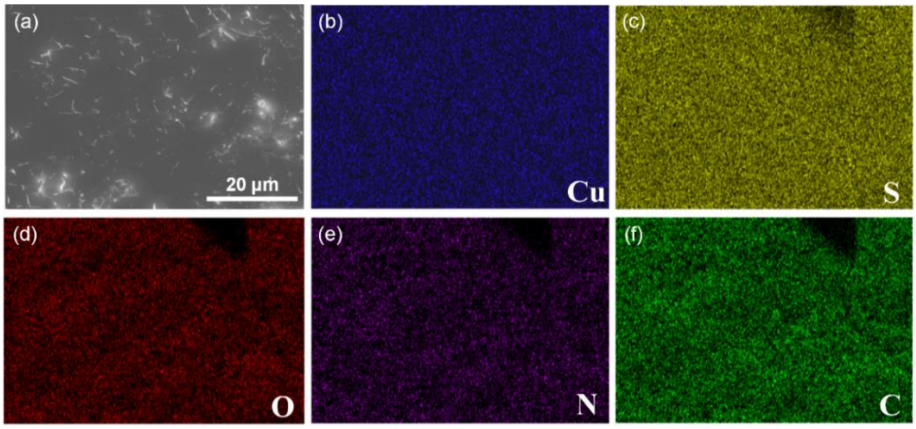

Figure 3.35 (a) SEM image of the Cu-SAT pellet, and SEM-EDS elemental maps of (b) copper, (c) sulfur, (d) oxygen, (e) nitrogen, and (f) carbon.

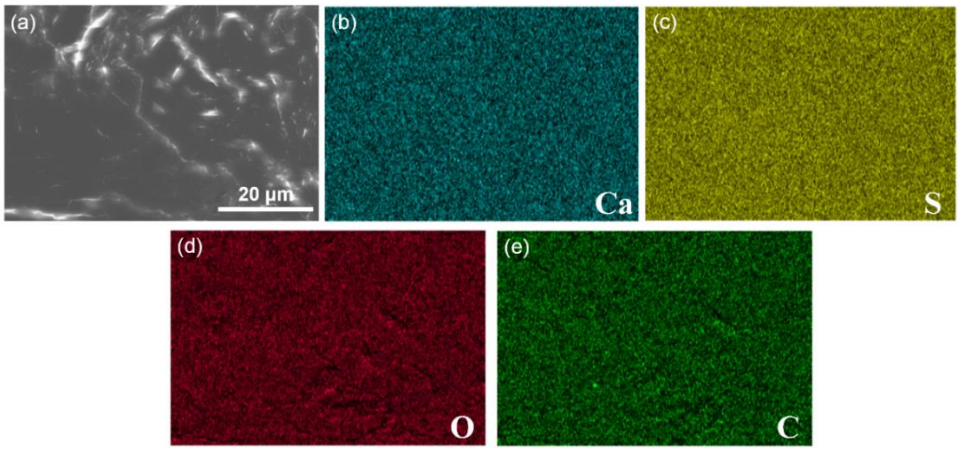

Figure 3.36 (a) SEM image of the Ca-NDS (water) pellet, and SEM-EDS elemental maps of (b) calcium, (c) sulfur, (d) oxygen, and (e) carbon.

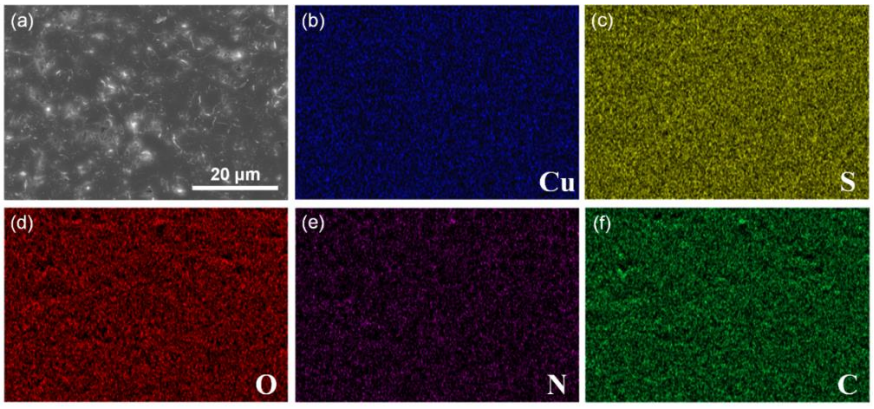

Figure 3.37 (a) SEM image of the Cu-SQAT pellet, and SEM-EDS elemental maps of (b) copper, (c) sulfur, (d) oxygen, (e) nitrogen, and (f) carbon.

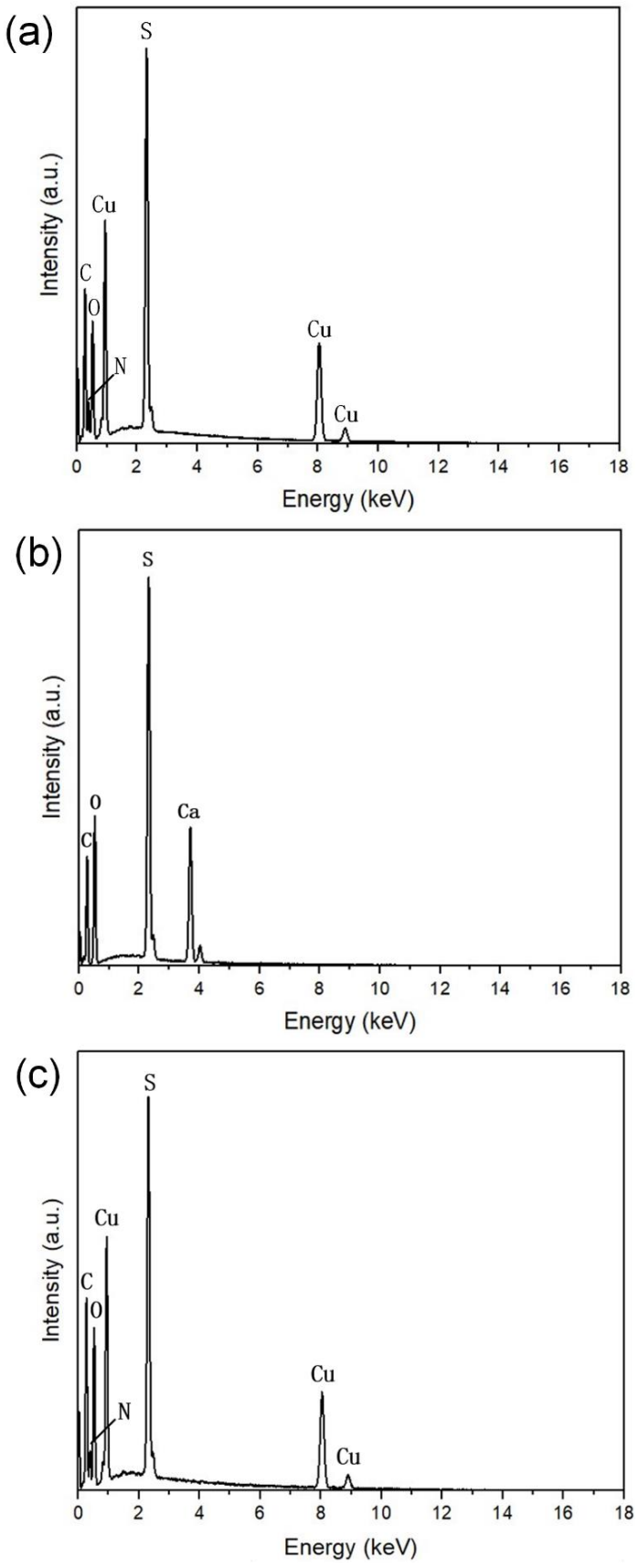

Figure 3.38 EDS spectra of (a) Cu-SAT, (b) Ca-NDS (water) and (c) Cu-SQAT pellets shown in Figure S31, S32, and S33, respectively.

Table 3.9 Density, resistance, and proton conductivities of Cu-SAT and Cu-SAT (EtOH) pellets. Uncertainties are given as one standard deviation.

Sample name	Density (g cm^{-3})	Calculated density (g cm^{-3})	Density as % of calculated density	Thickness (cm)	Resistance (ohm)	Proton conductivity (mS cm^{-1})
Cu-SAT a	1.708	1.899	89.94	0.104	230	2.31
Cu-SAT b	1.719		90.52	0.094	215	2.23
AVG of Cu-SAT	1.714 ± 0.008		90.23 ± 0.41	--	--	2.27 ± 0.06
Cu-SAT (EtOH) a	1.781	2.091	85.17	0.126	1950	0.33
Cu-SAT (EtOH) b	1.798		85.99	0.092	1269	0.37
AVG of Cu-SAT (EtOH)	1.790 ± 0.012		85.58 ± 0.57	--	--	0.35 ± 0.03

Note: Density as % of calculated density is the ratio of measured density to the calculated density of crystals from the SC-XRD (ρ_{calc}/g cm^{-3}), then times 100. Resistance and proton conductivity were measured at 80 °C in 95 % RH.

Table 3.10 Density, resistance, and proton conductivities of Ca-NDS (water), Ca-NDS (DMF) and Ca-NDS (DMSO) pellets. Uncertainties are given as one standard deviation.

Sample name	Density (g cm^{-3})	Calculated density (g cm^{-3})	Density as % of calculated density	Thickness (cm)	Resistance (ohm)	Proton conductivity (mS cm^{-1})
Ca-NDS (water) a	1.408	1.746	80.64	0.127	430	1.51
Ca-NDS (water) b	1.353		77.49	0.132	480	1.40
AVG of Ca-NDS (water)	1.381 ± 0.039		79.07 ± 2.22	--	--	1.46 ± 0.08
Ca-NDS (DMF) a	1.296	1.532	84.60	0.124	1750	0.36
Ca-NDS (DMF) b	1.332		86.95	0.110	1431	0.39
AVG of Ca-NDS (DMF)	1.314 ± 0.025		85.77 ± 1.66	--	--	0.38 ± 0.02
Ca-NDS (DMSO) a	1.449	1.703	85.09	0.127	900	0.72
Ca-NDS (DMSO) b	1.424		83.62	0.133	1030	0.66
AVG of Ca-NDS (DMSO)	1.437 ± 0.012		84.35 ± 1.04	--	--	0.69 ± 0.04

Note: Density as % of calculated density is the ratio of measured density to the calculated density of crystals from the SC-XRD (ρ_{calc}/g cm^{-3}), then times 100. Resistance and proton conductivity were measured at 80 °C in 95 % RH.

Table 3.11 Density, resistance, and proton conductivities of Cu-SQAT and Ca-ADS pellets. Uncertainties are given as one standard deviation.

Sample name	Density (g cm^{-3})	Calculated density (g cm^{-3})	Density as % of calculated density	Thickness (cm)	Resistance (ohm)	Proton conductivity (mS cm^{-1})
Cu-SQAT a	1.702	2.066	82.38	0.117	510	1.17
Cu-SQAT b	1.751		84.75	0.093	460	1.03
AVG of Cu-SQAT	1.727 ± 0.035		83.57 ± 1.68	--	--	1.11 ± 0.09
Ca-ADS a	1.699	1.910	88.95	0.110	1300	0.43
Ca-ADS b	1.731		90.63	0.102	1130	0.46
AVG of Ca-ADS	1.715 ± 0.023		89.79 ± 1.18	--	--	0.45 ± 0.02

Note: Density as % of calculated density is the ratio of measured density to the calculated density of crystals from the SC-XRD (ρ_{calc}/g cm^{-3}), then times 100. Resistance and proton conductivity were measured at 80 °C in 95 % RH.

Figure 3.39a presents the EIS results in the form of Nyquist plots for all seven CP pellets at 80 °C and 95% RH. The Cu-SAT material shows the smallest x-intercept value, reflecting the resistance, followed by Ca-NDS (water) and Cu-SQAT. Cu-SAT (EtOH) showed the highest intercept value. By accounting for the dimensions of the pellets, we determined conductivity values spanning 2.27 ± 0.06 mS cm^{-1} for Cu-SAT, 1.46 ± 0.08 mS cm^{-1} for Ca-NDS (water), and 1.11 ± 0.09 mS cm^{-1} for Cu-SQAT to 0.35 ± 0.03 mS cm^{-1} for Cu-SAT (EtOH). Here, uncertainties are given as one standard deviation. We note these conductivities take into the resistance (Figure 3.39) as well as the thickness of the sample (see also equation (1), Tables 3.9-3.11). Tables 3.9-3.11 further summarise the EIS measurements across all seven CPs at 80 °C and 95% RH. The Cu-SAT pellet measurement is of a similar order of magnitude to that reported in polymer-based mixed matrix membranes (1.35 ± 0.05 mS cm^{-1} at 80 °C and 95% RH) [20, 28], albeit somewhat higher. More broadly, these conductivities across the set reported here are promising amongst a number of CPs and MOFs (Table 3.12) [44, 60-65], often exhibiting proton conductivities under high humidity conditions of 10^{-4} to 10^{-5} S cm^{-1} in imidazolate and carboxylate MOFs [44, 60, 61].

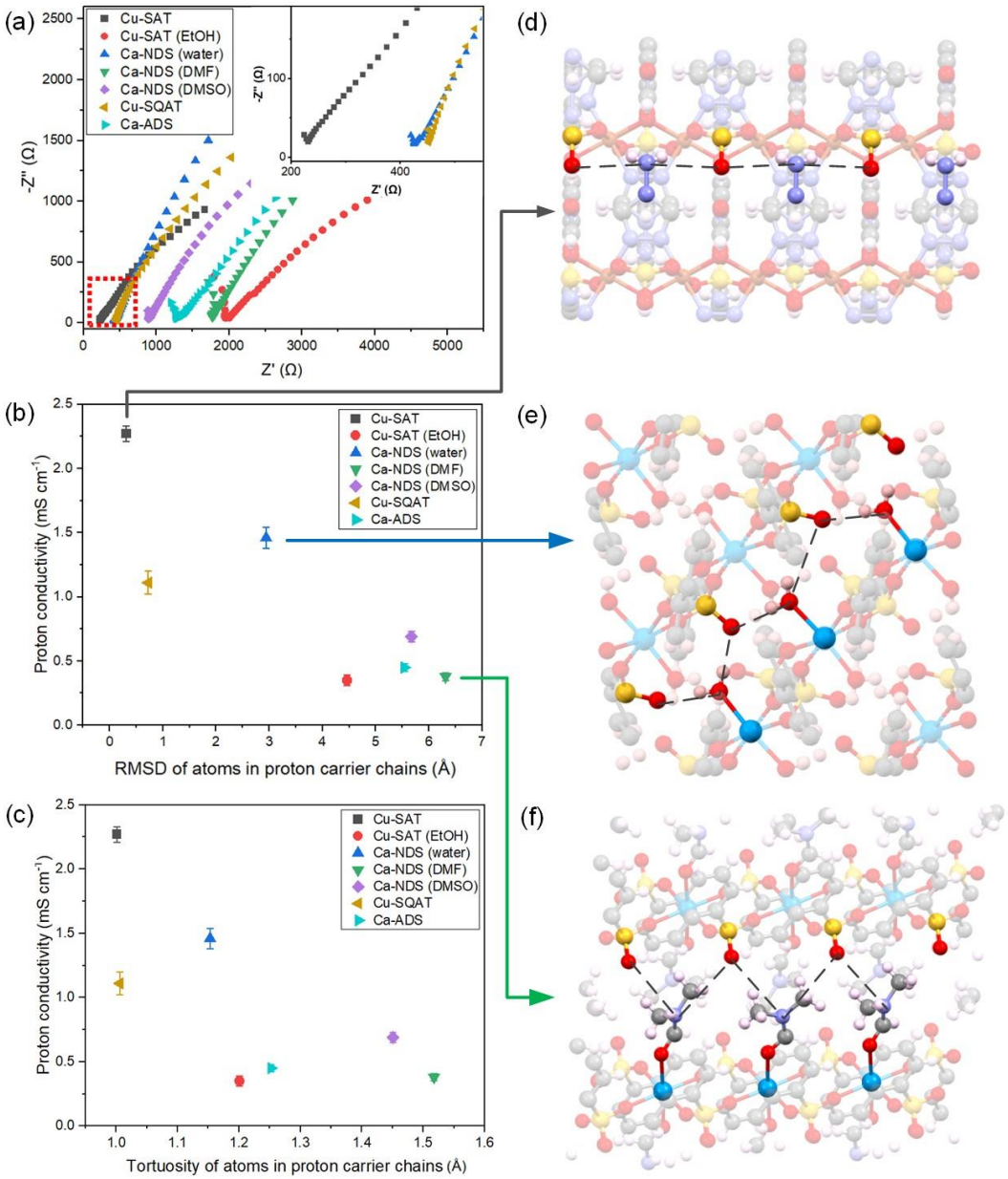

Figure 3.39 (a) EIS Nyquist plots for seven CPs synthesised in this work, prepared as pellets and measured at 80 °C and 95% RH. Correlation of recorded proton conductivities with (b) the RMSD and (c) the tortuosity of atoms in hydrogen bonding network within the synthesised CPs, determined from SC-XRD structures. The error bars indicate one standard deviation. Note: Tortuosity is the ratio of the full circuitous path-length along the chain to the distance between its ends. Illustration of the hydrogen bonding networks in (d) Cu-SAT, (e) Ca-NDS (water) and (f) Ca-NDS (DMF). The black dashed line marks the hydrogen bonding network between adjacent electronegative species.

Table 3.12 Proton conductivity and synthesis condition of CPs reported in this work compared with recent references.

Sample name	Proton conductivity (mS cm^{-1})	Synthesis condition	References
Cu-SAT	2.27 (80 °C, 95% RH)	80 °C for 3h	This work
Ca-NDS (water)	1.46 (80 °C, 95% RH)	80 °C for 3h	This work
Cu-SQAT	1.11 (80 °C, 95% RH)	80 °C for 3h	This work
MIL-68-In-OH	1.72 (100 °C, 98% RH)	125 °C for 5h	62
Tb-MOF	0.54 (100 °C, 98% RH)	95 °C for 72h	63
Sm-MOF	1.28 (100 °C, 98% RH)	95 °C for 72h	63
JUK-13- SO_3H-SO_2	0.23 (75 °C, 60% RH)	80 °C for 7 days	64
$[Cd(H_2BBT)_2]_n$	0.18 (100 °C, 98% RH)	20 °C for 7 days	44
$\{[Ni(p\text{-}IPhH_2IDC)_2]\cdot H_2O\}_n$	0.04 (100 °C, 98% RH)	150 °C for 96h	61
$[Sr(\mu_5\text{-}p\text{-}FPhHIDC)(H_2O)]_n$	0.04 (100 °C, 98% RH)	155 °C for 4 days	65
$[Ba(o\text{-}CPH_2IDC)]_n$	0.31 (100 °C, 98% RH)	150 °C for 96h	60

As Cu-SAT, Ca-NDS (water) and Cu-SQAT showed the most promising proton conductivities, temperature-dependent EIS measurements were used to estimate activation energies for proton transport (Figure 3.40). The activation energy E_a of Cu-SAT pellet was determined to be 62.3 ± 2.5 kJ mol^{-1} or 0.65 ± 0.03 eV (uncertainties given as the standard error), the E_a of the Ca-NDS (water) pellet was determined to be 65.26 ± 4.2 kJ mol^{-1} or 0.68 ± 0.04 eV, and the E_a of the Cu-SQAT pellet was determined to be 77.3 ± 5.0 kJ mol^{-1} or 0.81 ± 0.05 eV. These activation energies suggest that in pellet form these materials exhibit a predominantly vehicle mechanism ($E_a > 0.4$ eV) for proton transport, where the proton travels as a diffusing protonated group such as H_3O^+ [66]. In the pellet form, the overall transport behaviour contains contributions from both the transport within crystals and along or between grains.

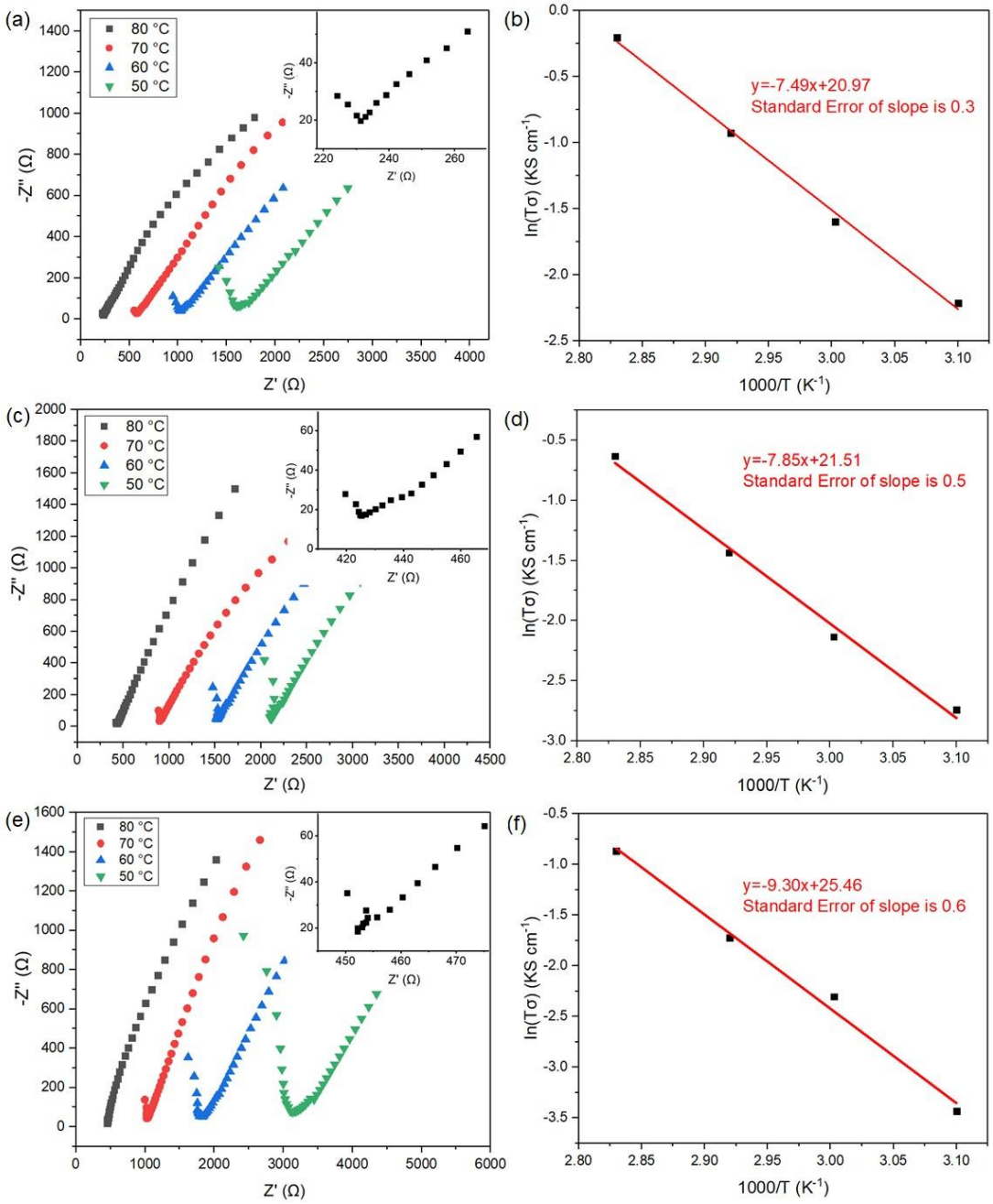

Figure 3.40 (a) EIS Nyquist plots and (b) Arrhenius plots of Cu-SAT pellet samples at 50-80 °C and 95% RH, (c) EIS Nyquist plots and (d) Arrhenius plots of Ca-NDS (water) pellet samples at 50-80 °C and 95% RH, (e) EIS Nyquist plots and (f) Arrhenius plots of Cu-SQAT pellet samples with temperature range 50-80 °C and 95% RH.

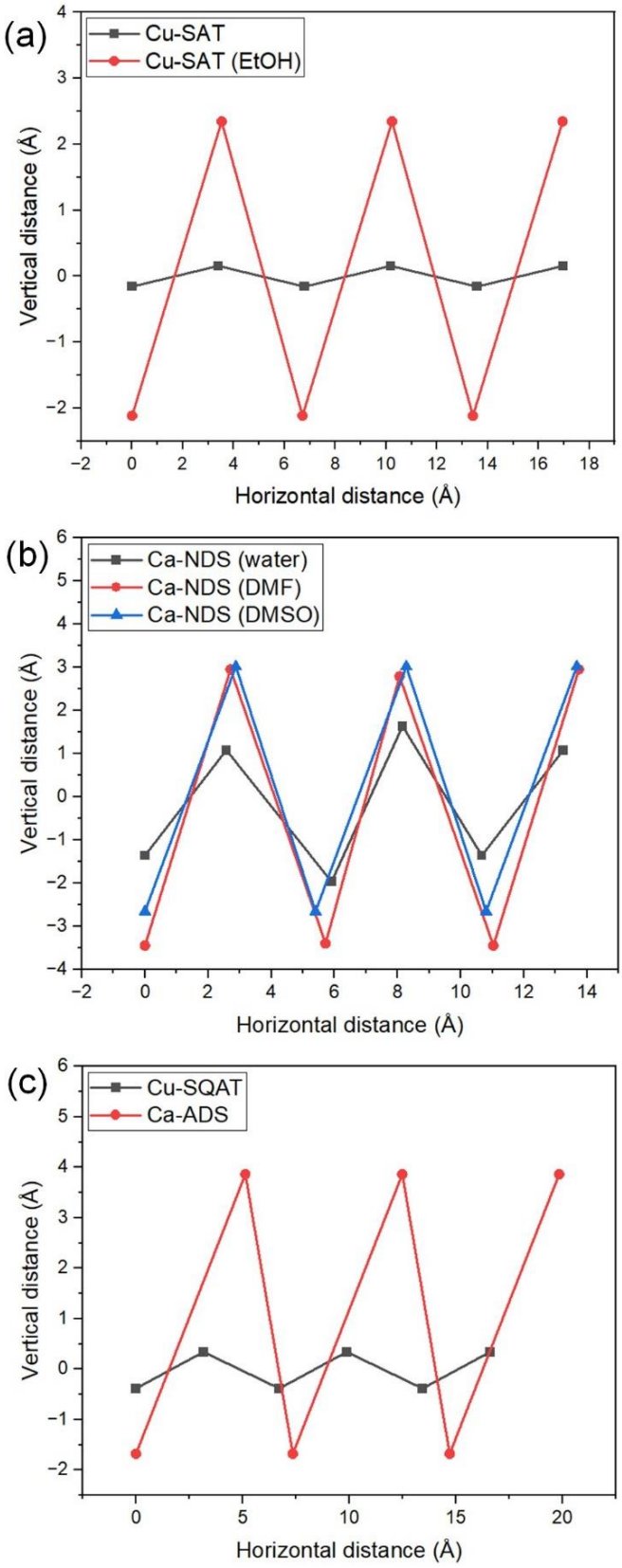

Figure 3.41 Distances between atoms in hydrogen bonding network chains in (a) Cu-SAT and Cu-SAT (EtOH), (b) Ca NDS samples, and (c) Cu-SQAT and Ca-ADS.

In order to further probe the structural and chemical origins of the spread of conductivities for these NDS- and ADS-based CPs, we return to the single-crystal structures. Given the prevailing understanding of the role of hydrogen bond donors and acceptors in MOF and CP proton conduction pathways, we have isolated the 1D shortest path routes through the seven synthesised CPs. By measuring the distances between proton carriers (taken as the most electronegative species along the chain), we have then extracted a root mean squared displacement (RMSD) as a general descriptor of the tortuosity of this hydrogen bonding and proton transport pathway. Figure 3.39b plots the recorded proton conductivities against the RMSD, showing more linear hydrogen bonding networks (smaller RMSD values) are correlated with higher proton conductivities. Figure 3.39c likewise depicts a consistent correlation between proton conductivities and the tortuosity of the chain, alternatively taken as the ratio of the full circuitous path-length along the chain to the distance between its ends. A clear trend emerges across the set of diverse structures exhibiting pronounced variation in the RMSD measure of the tortuosity, depicted in the unit cells in Figures 3.39d-f. The pathways mapped for all samples are shown in Figure 3.41.

Features specific to individual materials, such as differences in the electronegativity of the species involved in the hydrogen bonding network, differences in spacing between the 2D layers in each structure, and differences in the relative offset or packing between layers, may also impact proton conductivity. We note, however, that these structural features are intrinsically interlinked with the tortuosity of the lowest energy configuration. That is, species with stronger interactions between hydrogen bonding donors and acceptors are expected to favour more linear chains and, consequently, narrower gaps between layers. Cu-SQAT and Ca-ADS distinct network structures (a hydrogen bonding network and a 1D coordination polymer, respectively) and incorporate additional carbonyl moieties in their quinone functional groups, and Cu-SAT (EtOH) exhibits significantly corrugated layers in contrast to the quasi-planar 2D sheets observed in the other structures. Such differences may explain why these compounds show a deviation to lower conductivity relative to the trend in the other 2D arenedisulfonate coordination polymers. Possible missing metal clusters or excess ligands, either at the surface or the interior of crystals, could also modify proton conductivities, though XPS data would suggest higher incidence in Cu compounds (Figures 3.24-3.25, Tables 3.7-3.8) which do not consistently show a deviation from

the pattern in Figure 3.39. While there are undoubtedly numerous contributions to the overall conductivity in the pellet, including the specific chemical interactions beyond purely structural variations [67] and grain boundary pathways [68], the RMSD provides a practically useful classifier for proton conductivity within this set of chemically and structurally similar sulfonate CPs. Together, by experimentally deriving a set of CPs with sufficient chemical and structural inter-comparability, this analysis identifies a defining structure-function relationship for explaining and predicting variations in the proton conductivity of 2D sulfonate CPs.

To further demonstrate the utility of these coordination polymers for proton conducting membrane applications, Ca-NDS (water) and Cu-SQAT based MMMs were fabricated using a polymer matrix comprised of PVP and PVDF, two polymers that themselves show low proton conductivity but offer a favourable blend of hydrophilicity (PVP) and mechanical and thermal stability (PVDF) [69, 70]. This approach enables enhancing performance of membranes through the coordination polymer conductivity using alternative polymers to Nafion associated with high production costs and manufacturing hazards [71, 72]. The choice of Ca-NDS (water) and Cu-SQAT MMMs extends and complements our previous examination of Cu-SAT MMMs [28] as these sulfonate coordination polymers exhibit the next two top-performing pellet proton conductivities of the series considered here.

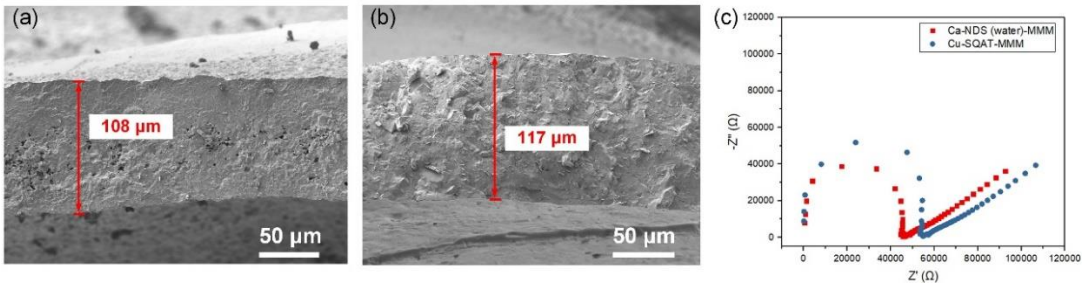

Figure 3.42 (a) Cryo-SEM micrographs of cross section of the fully hydrated (a) Ca-NDS (water)-MMM and (b) Cu-SQAT-MMM membranes, and (c) EIS Nyquist plots for Ca-NDS (water)-MMM and Cu-SQAT-MMM membranes measured at 80 °C and 95% RH.

Figure 3.42 shows cryo-SEM images of the membranes in the fully-hydrated state, used for accounting for thickness changes affected by swelling on hydration under electrochemical testing under high relative humidities (thicknesses of 108 µm and 117 µm for the Ca-NDS (water)-MMM and for the Cu-SQAT-MMM, respectively). Figure 3.43 and 3.44 present EDS mapping of the membranes in cross section, confirming the

dispersion of Ca-NDS (water) and Cu-SQAT particles throughout the membrane. Figure 3.39c presents EIS results of Ca-NDS (water)-MMM and Cu-SQAT-MMM, showing proton conductivities of Ca-NDS (water)-MMM and Cu-SQAT-MMM of 0.91 ± 0.04 and 0.68 ± 0.03 mS cm^{-1} at 80 °C and 95% RH, respectively. The proton conductivity of Cu-SAT based MMM, reported in our previous work [28], is 1.34 ± 0.05 mS cm^{-1}. As such, the MMMs prepared using Ca-NDS and Cu-SQAT follow the trend in pellet conductivities. Moreover, all three arenedisulfonate coordination polymer based MMMs (Cu-SAT, Ca-NDS (water) and Cu-SQAT) made in our work offer favourable conductivities in comparison with other recently reported MOF-based MMMs [44, 65, 73-75]. For the non-CPs materials, phosphine oxide- and pyridinyl-based fluoro-sulfonated PEMs exhibit a high proton conductivity between 10^{-3} to 10^{-2} S cm^{-1} at 80 °C [76], SPEEK usually has a proton conductivity from 10^{-3} to 10^{-2} S cm^{-1} depending on sulfonation degree and hydration [77]. Nafion has a much higher proton conductivities in the range of 10^{-2} to 10^{-1} S cm^{-1}, but its fabrication presents hazards as well as contributes to high production costs [71, 72]. Critically, record conductivity in this work is not the sole objective for optimizing these materials. Notably, reduced toxic solvent and a simplified set of precursors used in the preparation of Ca-NDS offers green chemical advantages for these MMMs while offering comparable proton conductivities to Cu-SAT prepared using DMF. The crystal structure trends identified (Figure 3.39) point to transferability through to membrane integration for improving materials selection and design for scalable MMMs in fuel cells and related technologies.

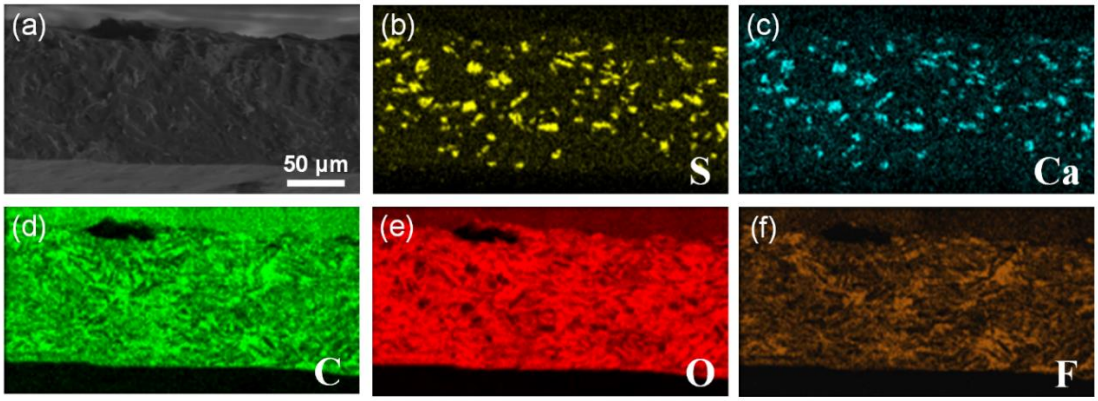

Figure 3.43 (a) Cryo-SEM cross-sectional image of the fully hydrated Ca-NDS (water)-MMM, and SEM-EDS elemental maps of: (b) sulfur, (c), calcium, (d) carbon, (e) oxygen, and (f) fluorine.

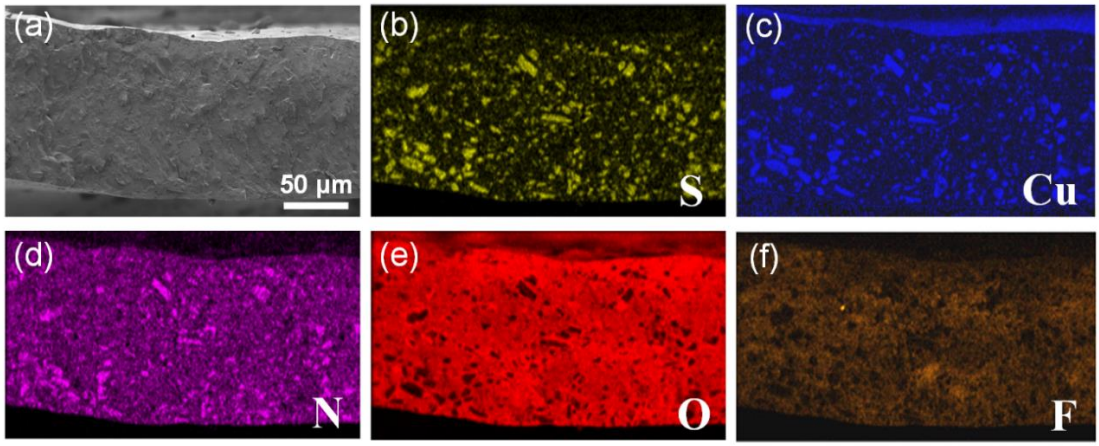

Figure 3.44 (a) Cryo-SEM cross-sectional image of the fully hydrated Cu-SQAT-MMM, and SEM

3.4 Conclusions

In summary, we have used NDS and ADS sulfonate ligands to synthesise a series of Cu^{2+} and Ca^{2+} CPs. By varying the solvent for a series of NDS-based structures, we have now reported unit cells for Cu-SAT (EtOH), Ca-NDS (DMF), and Ca-NDS (DMSO), all exhibiting a consistent 2D sheet structural motif. By using the ADS ligand, a hydrogen bonded network incorporating sulfonate, quinone, and aminotriazolate moieties named Cu-SQAT and a 1D CP built from Ca^{2+} denoted Ca-ADS have also been reported. We have assessed these materials' proton conductivity properties, of interest in fuel cell applications: Cu-SAT, Ca-NDS (water) and Cu-SQAT show promising proton conductivities of 2.27 ± 0.06, 1.46 ± 0.08 and 1.11 ± 0.09 mS cm^{-1} at 80 °C and 95% relative humidity, respectively. And the proton conductivities of Cu-SAT, Ca-NDS (water) and Cu-SQAT based MMMs present a similar order of magnitude to that their pellet samples. Finally, we have established an experimental structure-function relationship linking the tortuosity of the hydrogen bonding pathway with proton conductivities across the synthesised sulfonate CPs. These findings outline structural design principles of reducing the tortuosity of the hydrogen bonding pathway for sulfonate CPs and likely wider CP and MOF materials for optimising proton conductivity systematically.

3.5 References

[1] R. Sahoo, S.C. Pal, M.C. Das, Solid-State Proton Conduction Driven by Coordinated Water Molecules in Metal–Organic Frameworks and Coordination Polymers, ACS Energy Lett. 7 (2022) 4490-4500.

[2] W.X.W.X.H.H.J.W.C.Z.D. Mei, Morphology controlled synthesis of α-Fe_2O_3-x with benzimidazole-modified Fe-MOFs for enhanced photo-Fenton-like catalysis - ScienceDirect, Appl. Catal. B-Environ. 291 (2021) 120-129.

[3] D. Yang, B.C. Gates, Catalysis by Metal Organic Frameworks: Perspective and Suggestions for Future Research, ACS Catal. 9 (2019) 1779-1798.

[4] X.L. Hu, K. Wang, X. Li, Q.Q. Pan, Z.M. Su, Two Anthracene Chromophores based Metal-Organic Frameworks for Gas Absorption and Promising Nitro Aromatic Sensing, New J. Chem. 44 (2020) 1249-1252.

[5] H. Li, K. Wang, Y. Sun, C.T. Lollar, J. Li, H.C. Zhou, Recent advances in gas storage and separation using metal–organic frameworks, Mater. Today 21 (2018) 108-121.

[6] Y. Chen, L. Zheng, Y. Fu, R. Zhou, Y. Song, S. Chen, MOF-derived Fe_3O_4/carbon octahedral nanostructures with enhanced performance as anode materials for lithium-ion batteries, RSC Adv. 6 (2016) 85917-85923.

[7] X. Zhao, G. Niu, H. Yang, J. Ma, M. Sun, M. Xu, W. Xiong, T. Yang, L. Chen, C. Wang, MIL-88A@polyoxometalate microrods as an advanced anode for high-performance lithium ion batteries, CrystEngComm 22 (2020) 3588-3597.

[8] S. Tai, W. Zhang, J. Zhang, G. Luo, Y. Jia, M. Deng, Y. Ling, Facile preparation of UiO-66 nanoparticles with tunable sizes in a continuous flow microreactor and its application in drug delivery, Micropor. and Mesopor. Mat. 220 (2016) 148-154.

[9] Y.-K. Seo, G. Hundal, I.T. Jang, Y.K. Hwang, C.-H. Jun, J.-S. Chang, Microwave synthesis of hybrid inorganic–organic materials including porous $Cu_3(BTC)_2$ from Cu(II)-trimesate mixture, Micropor. and Mesopor. Mat. 119 (2009) 331-337.

[10] A. Grigoropoulos, A.I. McKay, A.P. Katsoulidis, R.P. Davies, A. Haynes, L. Brammer, J. Xiao, A.S. Weller, M.J. Rosseinsky, Encapsulation of Crabtree's Catalyst in Sulfonated MIL-101(Cr): Enhancement of Stability and Selectivity between Competing Reaction Pathways by the MOF Chemical Microenvironment, Angew Chem. Int. Ed. Engl. 57 (2018) 4532-4537.

[11] Z. Mai, D. Liu, Synthesis and Applications of Isoreticular Metal–Organic Frameworks IRMOFs-n (n = 1, 3, 6, 8), Cryst. Growth Des. 19 (2019) 7439-7462.

[12] X. Jiang, H. Li, J. Xiao, D. Gao, R. Si, F. Yang, Y. Li, G. Wang, X. Bao, Carbon dioxide electroreduction over imidazolate ligands coordinated with Zn(II) center in ZIFs, Nano Energy 52 (2018) 345-350.

[13] B. Huang, Y. Li, W. Zeng, Application status of zeolitic imidazolate framework in gas sensors, Nano Futures 6 (2022) 032003.

[14] S. Wang, M. Gong, X. Han, D. Zhao, J. Liu, Y. Lu, C. Li, B. Chen, Embedding Red Emitters in the NbO-Type Metal-Organic Frameworks for Highly Sensitive Luminescence Thermometry over Tunable Temperature Range, ACS Appl. Mater. Inter. 13 (2021) 11078-11088.

[15] S.S. Iremonger, J. Liang, R. Vaidhyanathan, I. Martens, G.K. Shimizu, T.D. Daff, M.Z. Aghaji, S. Yeganegi, T.K. Woo, Phosphonate monoesters as carboxylate-like linkers for metal organic frameworks, J. Am. Chem. Soc. 133 (2011) 20048-20051.

[16] S.S. Iremonger, J. Liang, R. Vaidhyanathan, G.K. Shimizu, A permanently porous van der Waals solid by using phosphonate monoester linkers in a metal organic framework, Chem. Commun (Camb) 47 (2011) 4430-4432.

[17] S. Horike, D. Umeyama, M. Inukai, T. Itakura, S. Kitagawa, Coordination-network-based ionic plastic crystal for anhydrous proton conductivity, J. Am. Chem. Soc. 134 (2012) 7612-7615.
[18] A.P. Côté, G.K.H. Shimizu, The supramolecular chemistry of the sulfonate group in extended solids, Coord. Chem. Rev. 245 (2003) 49-64.
[19] F. Yang, G. Xu, Y. Dou, B. Wang, H. Zhang, H. Wu, W. Zhou, J.-R. Li, B. Chen, A flexible metal–organic framework with a high density of sulfonic acid sites for proton conduction, Nat. Energy 2 (2017) 877-883.
[20] R. Moi, A. Ghorai, S. Banerjee, K. Biradha, Amino- and Sulfonate-Functionalized Metal–Organic Framework for Fabrication of Proton Exchange Membranes with Improved Proton Conductivity, Cryst. Growth Des. 20 (2020) 5557-5563.
[21] H.A. Patel, N. Mansor, S. Gadipelli, D.J. Brett, Z. Guo, Superacidity in Nafion/MOF Hybrid Membranes Retains Water at Low Humidity to Enhance Proton Conduction for Fuel Cells, ACS Appl. Mater. Inter. 8 (2016) 30687-30691.
[22] S.-N. Zhao, X.-Z. Song, M. Zhu, X. Meng, L.-L. Wu, S.-Y. Song, C. Wang, H.-J. Zhang, Assembly of three coordination polymers based on a sulfonic–carboxylic ligand showing high proton conductivity, Dalton T. 44 (2015) 948-954.
[23] P. Ramaswamy, R. Matsuda, W. Kosaka, G. Akiyama, H.J. Jeon, S. Kitagawa, Highly proton conductive nanoporous coordination polymers with sulfonic acid groups on the pore surface, Chem. Commun (Camb) 50 (2014) 1144-1146.
[24] G. Zhang, H. Fei, Synthesis and Applications of Porous Organosulfonate-Based Metal-Organic Frameworks, Top Curr. Chem. 377 (2019) 32.
[25] J. Cai, Structural chemistry and properties of metal arenesulfonates, Coord. Chem. Rev. 248 (2004) 1061-1083.
[26] J. Cai, C.H. Chen, C.Z. Liao, X.L. Feng, X.M. Chen, Solid-state structures of group 1 and group 2 metal 1,5-naphthalenedisulfonates: systematic investigation of lamellar three-dimensional networks constructed by metal arenedisulfonate, Acta Crystallogr. B 57 (2001) 520-530.
[27] D.K. Maity, K. Otake, S. Ghosh, H. Kitagawa, D. Ghoshal, Sulfonic Group Functionalized Mixed Ligand Coordination Polymers: Synthesis, Characterization, Water Sorption, and Proton Conduction Studies, Inorg. Chem. 56 (2017) 1581-1590.
[28] C. Sun, M. Barton, C.M. Pask, M. Edokali, L. Yang, A.J. Britton, S. Micklethwaite, F. Iacoviello, A. Hassanpour, M. Besenhard, R. Drummond-Brydson, K.-J. Wu, S.M. Collins, Droplet-based millifluidic synthesis of a proton-conducting sulfonate metal–organic framework, Chem. Eng. J. 474 (2023) 145892.
[29] J. Zhang, G.B. White, M.D. Ryan, A.J. Hunt, M.J. Katz, Dihydrolevoglucosenone (Cyrene) As a Green Alternative to N,N-Dimethylformamide (DMF) in MOF Synthesis, ACS Sustain. Chem. Eng. 4 (2016) 7186-7192.
[30] P. Marino, P.R. Donnarumma, H.A. Bicalho, V. Quezada-Novoa, H.M. Titi, A.J. Howarth, A Step toward Change: A Green Alternative for the Synthesis of Metal–Organic Frameworks, ACS Sustain. Chem. Eng. 9 (2021) 16356-16362.
[31] T. Kundu, M. Wahiduzzaman, B.B. Shah, G. Maurin, D. Zhao, Solvent-Induced Control over Breathing Behavior in Flexible Metal-Organic Frameworks for Natural-Gas Delivery, Angew. Chem. Int. Ed. Engl. 58 (2019) 8073-8077.
[32] G. Wen, B. Liu, D. Liu, F. Wang, L. Li, L. Zhu, D. Song, C. Huang, Y. Wang, Four congenetic zinc(II) MOFs from delicate solvent-regulated strategy: Structural diversities and fluorescent properties, Inorg. Chim. Acta 502 (2020) 119296.
[33] Q. Yang, X. Chen, Z. Chen, Y. Hao, Y. Li, Q. Lu, H. Zheng, Metal-organic frameworks constructed from flexible V-shaped ligands: adjustment of the

topology, interpenetration and porosity via a solvent system, Chem. Commun (Camb) 48 (2012) 10016-10018.
[34] W. Fan, X. Zhang, Z. Kang, X. Liu, D. Sun, Isoreticular chemistry within metal–organic frameworks for gas storage and separation, Coord. Chem.Rev. 443 (2021) 213968.
[35] O.M. Yaghi, M. O'Keeffe, N.W. Ockwig, H.K. Chae, M. Eddaoudi, J. Kim, Reticular synthesis and the design of new materials, Nature 423 (2003) 705-714.
[36] A.E. Platero-Prats, M. Iglesias, N. Snejko, Á. Monge, E. Gutiérrez-Puebla, From Coordinatively Weak Ability of Constituents to Very Stable Alkaline-Earth Sulfonate Metal−Organic Frameworks, Cryst. Growth Des. 11 (2011) 1750-1758.
[37] F. Gándara, A. García-Cortés, C. Cascales, B. Gómez-Lor, E. Gutiérrez-Puebla, M. Iglesias, A. Monge, N. Snejko, Rare earth arenedisulfonate metal− organic frameworks: An approach toward polyhedral diversity and variety of functional compounds, Inorg. chem. 46 (2007) 3475-3484.
[38] G.M. Sheldrick, SHELXT - integrated space-group and crystal-structure determination, Acta Crystallogr. A 71 (2015) 3-8.
[39] G.M. Sheldrick, Crystal structure refinement with SHELXL, Acta Crystallogr. C 71 (2015) 3-8.
[40] F. De La Peña, E. Prestat, V. Tonaas Fauske, P. Burdet, J. Lähnemann, T. Furnival, hyperspy/hyperspy: Release v1.6.5., Zenodo (2021).
[41] D.N. Johnstone, P. Crout, S. Høgås, T. Bergh, M. Danaie, C. Francis, S. Smeets, D. Weber, pyxem/pyxem-demos: pyxem-demos 0.11.0, 2020.
[42] S.M. Rezaei Niya, M. Hoorfar, Study of proton exchange membrane fuel cells using electrochemical impedance spectroscopy technique – A review, J. Power Sources 240 (2013) 281-293.
[43] L. Ding, H. Zou, J. Lu, H. Liu, S. Wang, H. Yan, Y. Li, Enhancing Proton Conductivity of Nafion Membrane by Incorporating Porous Tb-Metal-Organic Framework Modified with Nitro Groups, Inorg. Chem. 61 (2022) 16185-16196.
[44] L.X. Xie, Z.J. Ye, X.D. Zhang, G. Li, Two stable phenyl acyl thiourea carboxylate-based MOFs: Syntheses, crystal structures and proton conductive properties, J. Solid State Chem. 311 (2022) 123154.
[45] M. Mamlouk, P. Ocon, K. Scott, Preparation and characterization of polybenzimidzaole/diethylamine hydrogen sulphate for medium temperature proton exchange membrane fuel cells, J. Power Sources 245 (2014) 915-926.
[46] G. Shi, W. Xu, J. Wang, Y. Yuan, S. Chaemchuen, F. Verpoort, A Cu-based MOF for the effective carboxylation of terminal alkynes with CO_2 under mild conditions, J. CO_2 Util. 39 (2020) 101177.
[47] Q. Liu, J. Li, Z. Zhou, J. Xie, J.Y. Lee, Hydrophilic Mineral Coating of Membrane Substrate for Reducing Internal Concentration Polarization (ICP) in Forward Osmosis, Sci. Rep. 6 (2016) 19593.
[48] D. Liu, Z. Jin, Y. Bi, Charge transmission channel construction between a MOF and rGO by means of Co–Mo–S modification, Catal. Sci. Technol. 7 (2017) 4478-4488.
[49] P. Gobbo, Z. Mossman, A. Nazemi, A. Niaux, M.C. Biesinger, E.R. Gillies, M.S. Workentin, Versatile strained alkyne modified water-soluble AuNPs for interfacial strain promoted azide-alkyne cycloaddition (I-SPAAC), J Mater. Chem. B 2 (2014) 1764-1769.
[50] L. Zhong, S.F. Parker, Structure and vibrational spectroscopy of methanesulfonic acid, R. Soc. Open Sci. 5 (2018) 181363.
[51] M. Staufer, U. Birkenheuer, T. Belling, F. Nörtemann, N. Rösch, W. Widdra, K.L.

Kostov, T. Moritz, D. Menzel, The vibrational structure of benzene adsorbed on Si(001), J. Chem. Phys. 112 (2000) 2498-2506.
[52] Y. Ishida, T. Togashi, K. Yamamoto, M. Tanaka, T. Kiss, T. Otsu, Y. Kobayashi, S. Shin, Time-resolved photoemission apparatus achieving sub-20-meV energy resolution and high stability, Rev. Sci. Instrum. 85 (2014) 123904.
[53] Y. Ji, X. Yang, Z. Ji, L. Zhu, N. Ma, D. Chen, X. Jia, J. Tang, Y. Cao, DFT-Calculated IR Spectrum Amide I, II, and III Band Contributions of N-Methylacetamide Fine Components, ACS Omega 5 (2020) 8572-8578.
[54] N. Majoul, S. Aouida, B. Bessaïs, Progress of porous silicon APTES-functionalization by FTIR investigations, Appl. Surf. Sci. 331 (2015) 388-391.
[55] D. Grime, I.M. Ward, The assignment of infra-red absorptions and rotational isomerism in polyethylene terephthalate and related compounds, Trans. Faraday Soc. 54 (1958) 959-971.
[56] G. Wulff, XXV. Zur Frage der Geschwindigkeit des Wachsthums und der Auflösung der Krystallflächen, Z Krist-Cryst. Mater. 34 (1901) 449-530.
[57] E. Ringe, R.P. Van Duyne, L.D. Marks, Kinetic and Thermodynamic Modified Wulff Constructions for Twinned Nanoparticles, J. Phys. Chem. C 117 (2013) 15859–15870.
[58] L. Liu, Z. Chen, J. Wang, D. Zhang, Y. Han, Imaging defects and their evolution in a metal–organic framework at sub-unit-cell resolution, Nat. Chem. 11 (2019) 1.
[59] D.N. Johnstone, F.C.N. Firth, C.P. Grey, P.A. Midgley, S.M. Collins, Direct Imaging of Correlated Defect Nanodomains in a Metal-Organic Framework, J. Am. Chem. Soc. 142 (2020) 13081−13089.
[60] Z. Guo, Y. Zhang, J. Liu, B. Han, G. Li, Two imidazole multicarboxylate-based MOFs: syntheses, structures and proton conductive properties, New J. Chem. 45 (2021) 16971-16977.
[61] H. Zhao, Z.H. Du, C.Y. Mu, G. Li, Proton conductive properties of a substituted imidazole dicarboxylate-based hydrogen-bonded organic framework and a related nickel-organic framework, J. Solid State Chem. 315 (2022) 123550.
[62] Y.J. Song, Y.L. Sang, K.Y. Xu, H.L. Hu, Q.Q. Zhu, G. Li, Ligand-Functionalized MIL-68-type Indium(III) Metal-Organic Frameworks with Prominent Intrinsic Proton Conductivity, Inorg. Chem. 63 (2024) 4233-4248.
[63] Y.L. Hong, S.W. Zuo, H.Y. Du, Z.Q. Shi, H. Hu, G. Li, Four Lanthanide(III) Metal-Organic Frameworks Fabricated by Bithiophene Dicarboxylate for High Inherent Proton Conduction, ACS Appl. Mater. Interfaces 16 (2024) 13745-13755.
[64] M. Szufla, A. Krawczuk, G. Jajko, P. Kozyra, D. Matoga, Flattening of a Bent Sulfonated MOF Linker: Impact on Structures, Flexibility, Gas Adsorption, CO(2)/N(2) Selectivity, and Proton Conduction, Inorg. Chem. 63 (2024) 151-162.
[65] R.L. Liu, J. Li, Y.L. Zhao, Y.R. Wang, X.H. Fan, G. Li, D.Y. Wang, Two-in-one: Proton-conductive and luminescence properties of one strontium(II)-organic framework bearing imidazole dicarboxylate, J. Solid State Chem. 332 (2024) 124557.
[66] J.T.W. Wang, S.L.C. Hsu, Enhanced high-temperature polymer electrolyte membrane for fuel cells based on polybenzimidazole and ionic liquids, Electrochim. Acta 56 (2011) 2842-2846.
[67] A. Gupta, S. Goswami, S.M. Elahi, S. Konar, Role of Framework–Carrier Interactions in Proton-Conducting Crystalline Porous Materials, Cryst. Growth Des. 21 (2021) 1378-1388.
[68] K. Zhang, G.H. Wen, S.S. Bao, L.Q. Wu, J.G. Jia, Studying the Proton Conduction through the Grain Surface of UiO-66-NH₂, ACS Appl. Energy Mater.

3 (2020) 8198-8204.
[69] L. Fu, N.A. Hashim, Y. Liu, M. Abed, K. Li, Progress in the production and modification of PVDF membranes, J. Membrane. Sci. 375 (2011) 1-27.
[70] Y. Zhang, J. Li, L. Ma, W. Cai, H. Cheng, Recent Developments on Alternative Proton Exchange Membranes: Strategies for Systematic Performance Improvement, Energy Technol. 3 (2015) 675-691.
[71] N.A. Nazir, N. Kim, W.G. Iglesias, A. Jakli, T. Kyu, Conductive behavior in relation to domain morphology and phase diagram of Nafion/poly(vinylidene-co-trifluoroethylene) blends, Polymer 53 (2012) 196-204.
[72] M.A. Hickner, H. Ghassemi, Y.S. Kim, B.R. Einsla, J.E. McGrath, Alternative Polymer Systems for Proton Exchange Membranes (PEMs), Chem. Rev. 104 (2004) 4587-4612.
[73] M. Rautenberg, B. Bhattacharya, C. Das, F. Emmerling, Mechanochemical Synthesis of Phosphonate-Based Proton Conducting Metal-Organic Frameworks, Inorg. Chem. 61 (2022) 10801-10809.
[74] Y.L. Bao, J.Y. Zheng, H.P. Zheng, G.D. Qi, J.R. An, Y.P. Wu, Y.L. Liu, W.W. Dong, J. Zhao, D.S. Li, Cu-MOF@PVP/PVDF hybrid composites as tunable proton-conducting materials, J. Solid State Chem. 310 (2022) 123070.
[75] S. Luo, N. Deng, H. Wang, Q. Zeng, Y. Li, W. Kang, B. Cheng, Facilitating Li^+ conduction channels and suppressing lithium dendrites by introducing Zn-based MOFs in composite electrolyte membrane with excellent thermal stability for solid-state lithium metal batteries, Chem. Eng. J. 474 (2023) 145683.
[76] B. Ghanti, R. Kamble, H. Komber, B. Voit, S. Banerjee, High proton-conducting phosphine oxide-and pyridinyl-based fluoro-sulfonated proton exchange membranes with enhanced chemical stability, J. Power Sources 631 (2025) 236201.
77] M. Segale, T. Seadira, R. Sigwadi, T. Mokrani, G. Summers, A New Frontier Towards Development of Efficient SPEEK Polymer Membranes for PEM Fuel Cells Applications: A Review, Mater. Adv. 5 (2024) 7979-8006.

Chapter 4 Ultrasound-assisted continuous aqueous synthesis of sulfonate, imidazolate, and carboxylate MOFs with high space time yield

4.1 Introduction

The scalable production of metal-organic frameworks (MOFs) underpins the technological realisation of the promise that they have shown in applications ranging from gas storage [1], chemical separations [2], and catalysis [3] to proton conduction [4]. Intensification of MOF production, however, risks deleterious environmental impact without green chemical synthesis implemented in scalable reactor designs. The vast majority of MOFs have been reported using syntheses lasting several hours or days and using toxic solvents, impeding scale-up and sustainable production [5, 6]. These synthetic approaches, frequently employing dimethylformamide (DMF) or diethylformamide (DEF) as the solvent or in the solvent system, support diverse metal-based secondary building units and diverse chemistries of organic ligands [7], such as sulfonates for proton conduction MOFs [8], carboxylates for UiO [9], HKUST [10], MIL [11], and IRMOF [12] families, and imidazolates for the zeolitic imidazolate frameworks (ZIFs) [13]. While aqueous syntheses have been reported in a number of cases, the solvent system alone addresses only part of the challenge. Minimising waste overall also demands non-fouling reactors for scalable, green chemical, and (ideally) continuous MOF production.

Reactor fouling in wet-chemical nanoparticle synthesis encompasses several mechanisms where material is deposited on reactor surfaces [14]. Flow reactors are likely to foul when solid particles formed in solution adhere to reactor walls resulting in local accumulation (i.e. fouling) and potentially clogging. Both impede the reactor operation, disturb controlled synthetic conditions, and reduce the yield. Reactors that can inhibit fouling by design, e.g. reactors featuring high shear or external forces [15, 16], reactors with low surface to volume ratios [17, 18], jet reactors [19], two-phase and multiple-phase segmented flow reactors [8, 20], or reactors tuning particle and wall surface chemistry [19, 21], have not seen widespread application in green chemical MOF production approaches.

Hydrothermal or solvothermal methods implemented in batch reactors are the

most common means for synthesizing large and high-quality MOF crystals in research environments [22, 23]. However, these methods have disadvantages of long reaction times, batch-to-batch variations, and generally make use of toxic solvents (e.g. DMF and DEF) [24]. Water [25], ethanol [6], isopropyl alcohol [26], STEPOSOL MET-10U (*N*,*N*-dimethyl-9-decenamide) [27] and Cyrene (dihydrolevoglucosenone) [28] have been reported as green solvents for MOF synthesis. Among these solvents, water has advanced as the most promising for green chemical production of MOFs because of its low toxicity and safety, independence of fossil fuel feedstocks, and limited side-reactions [29-31]. Emerging synthetic approaches, i.e., sono-chemical [32], microwave [33], electrochemical [30], and mechanochemical synthesis [34], have been reported for faster syntheses of MOFs in batch. However, integration and translation of batch processes to reactors delivering continuous synthetic operation remains a nontrivial objective.

Microfluidic and millifluidic methods have seen particular success offering routes to tighten control over synthetic conditions, continuous operation, and production scale-up for nanomaterials fabrication [35, 36] and biopharmaceutical engineering [37]. Flow reactors have higher mass and heat transfer compared with batch reactors because of their high surface area to volume (SAV) ratios, the SAV of a microreactor is normally between 10,000 to 50,000 m^{-1} (100-1000 m^{-1} for traditional reactors), fostering higher reaction rates and increased reaction space time yields (STY) [8, 14]. In the MOF synthesis, STY more than 500-1000 kg m^{-3} day^{-1} could be considered as high STY [38]. Among these microfluidic and millifluidic approaches, two-phase droplet flow can impede channel clogging, and short residence times can enhance particle size control relative to single-phase flow designs [39]. In addition, two-phase flow systems provide a promising method for the fast synthesis of MOF particles, as vortices within the droplet flow further increase the mixing and the heat and mass transfer [40]. However, MOF synthesis often remains plagued by slow nucleation rates and many two-phase flow setups require post-synthetic phase separation steps, presenting a persistent challenge for the scale-up of MOF synthesis.

The sono-chemical synthesis technique has proven advantageous for the production of MOFs, attributed to ultrasound-enhanced crystal nucleation rates [32, 41]. Ultrasonic waves induce cavitation as a secondary effect when applied in a liquid medium, creating microbubbles throughout the liquid medium and producing

improved MOF crystallization rates compared to conventional heating [42, 43]. The oscillation and collapse of the cavitation bubbles also serve to break-up agglomerates [44]. Moreover, acoustophoretic effects direct microparticles to the centre of reactor, inhibiting sedimentation [45], thereby preventing clogging. In batch processes however, control of the reactor temperature can produce poor reproducibility in addition to the extended reaction times and batch-to-batch variations typical of solvothermal approaches. We posit that integrating ultrasound and continuous, two-phase water/gas reactor concepts offers key advantages of both sono-chemical and flow synthesis without additional separations or toxic solvents, whilst also offering well-controlled MOF particle size and enhanced STY for both rapid feedback during process development and, ultimately, scalable production [46, 47].

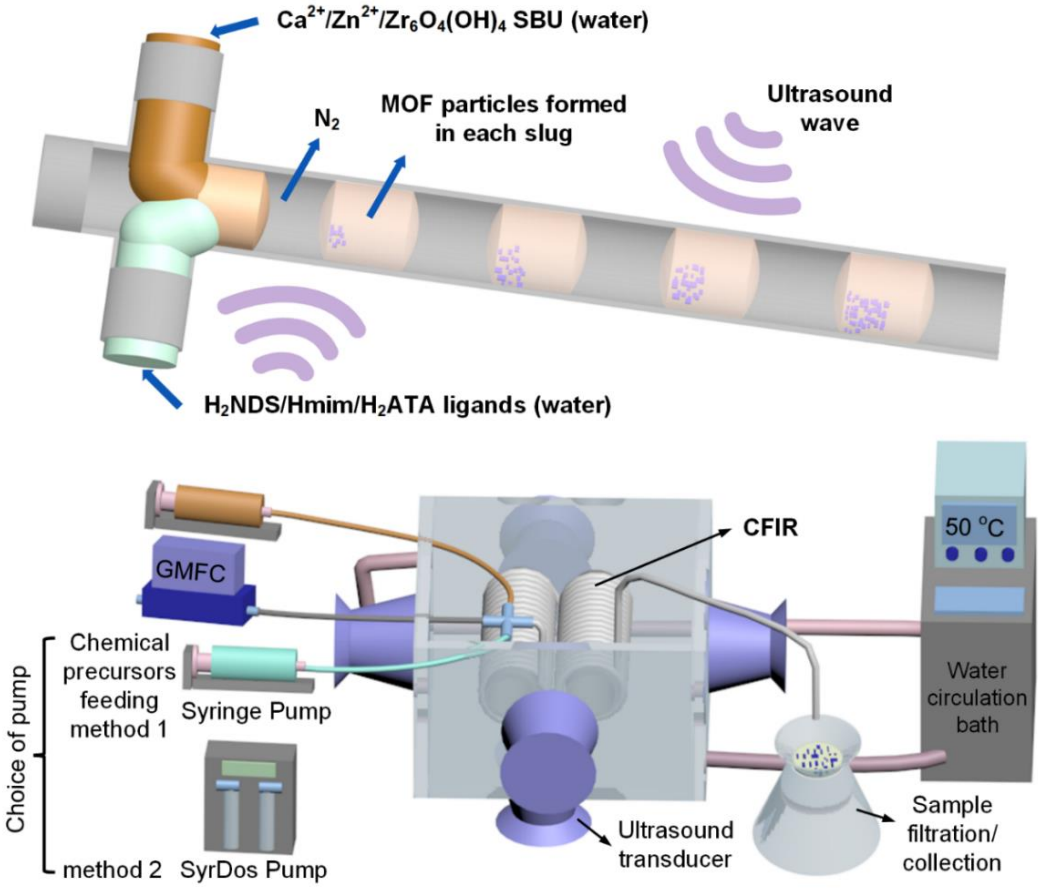

Figure 4.1 Schematic diagram of the ultrasound-assisted two-phase flow reaction platform for the synthesis of different MOFs.

In this work, we first report the continuous, ultrasound-assisted, single-phase flow synthesis of Ca-NDS (water), a Ca-based naphthalenedisulfonate coordination polymer with promising proton conductivity [29]. Then, following on from a parameter-space exploration for Ca-NDS (water) in single-phase flow, we report a

second-generation reactor in the form of an ultrasound-assisted, two-phase flow reactor using N_2 gas as the carrier phase for use as a universal and non-fouling MOF reactor. Figure 4.1 presents a schematic of this reactor, providing a conceptual overview and highlighting the simultaneous mixing of separately introduced metal and ligand precursor solutions and solvent slug formation as well as the integration of two-phase flow within a coiled flow inverter reactor (CFIR) design with ultrasonic transducers positions on five sides under dynamic temperature control (circulating water). We demonstrate this reactor's capabilities for the aqueous synthesis of Ca-NDS (water) as well as aqueous syntheses of ZIF-8 and UiO-66-NH_2 MOFs. The reactor, operating at stable temperature, offers a reliable, rapidly transferable reaction platform for diverse MOF chemistries and unambiguously demonstrates the significant role of ultrasound power in increasing STYs.

4.2 Experimental

4.2.1 Materials

1,5-Naphthalenedisulfonic acid tetrahydrate (H_2NDS, Molecular Weight, M_W, 360.36 g mol^{-1}), methanol (≥ 99.9%), polyvinylpyrrolidone (PVP, M_W 360,000 g mol^{-1}), and polyvinylidene fluoride (PVDF, M_W 534,000 g mol^{-1}) were purchased from Sigma Aldrich (Merck Group). Calcium nitrate hemi(pentahydrate) (M_W 236.15 g mol^{-1}), 2-aminoterephthalic acid (99%, H_2ATA, M_W 181.15 g mol^{-1}), zirconyl chloride octahydrate (98%, M_W 322.25 g mol^{-1}) were purchased from Thermo Fisher Scientific. Zinc acetate dihydrate (M_W 219.5 g mol^{-1}) and 2-methylimidazole (99%, Hmim, M_W 82.11 g mol^{-1}) were ordered from Fluorochem. Sodium hydroxide (NaOH, M_W 40 g mol^{-1}) and glacial acetic acid were purchased from Fisher Chemical.

4.2.2 Batch synthesis

4.2.2.1 Synthesis of Ca-NDS (water)

The synthetic procedure was similar to our previously reported study [29]. Briefly, calcium nitrate (165 mg, 0.7 mmol) was dissolved in deionised (DI) water (between 1 and 1.7 mL) as solution 1. H_2NDS (252 mg, 0.7 mmol) was dissolved in DI water (between 1 and 1.7 mL) as solution 2. Next, for solvothermal synthesis, solutions 1 and 2 were mixed in a 20 mL glass vial and heated in a dry bath heater (Thermo Fisher Scientific) at 50 °C for 30 min. Alternately, for sono-chemical batch synthesis, the 20

mL glass vial containing the mixed solution was immersed in an ultrasonic bath (GT SONIC-D3, 40 kHz, 100 W) at a temperature of 50 °C for 2 min. After the reaction, white solids were recovered by vacuum filtration and oven dried overnight at 80 °C.

4.2.2.2 Synthesis of ZIF-8

The synthesis process followed reported procedures [48]. Zinc acetate dihydrate (286 mg, 1.3 mmol) was dissolved in DI water (15 mL) as solution 1. Hmim (3736 mg, 45.5 mmol) was dissolved in DI water (15 mL) as solution 2. Next, for solvothermal synthesis, solutions 1 and 2 were mixed in a 40 mL glass vial and heated in a dry bath heater at 50 °C for 180 min. Alternately, for sono-chemical synthesis, the 40 mL glass vial containing the mixed solution was immersed in an ultrasonic bath at a temperature of 50 °C for 5 min. After the reaction, white precipitates were separated via centrifugation at 6800 rpm for 2 min. Collected samples were soaked in methanol for two days before drying overnight in an oven at 80 °C.

4.2.2.3 Synthesis of UiO-66-NH_2

The synthesis process followed previously reported procedures [49]. Zirconyl chloride octahydrate (1288 mg, 4 mmol) was dissolved in DI water (12 mL) and glacial acetic acid (5 mL) as solution 1. This solution was heated at 60 °C for 2 h and allowed to cool down to room temperature before carrying out subsequent reactions. H_2ATA (724 mg, 4 mmol) and NaOH (320 mg, 8 mmol) were dissolved in DI water (20 mL) as solution 2. Next, for solvothermal synthesis, solutions 1 and 2 were mixed in a 40 mL glass vial and heated in a dry bath heater at 50 °C for 180 min. Alternately, for sono-chemical synthesis, the mixed solution was immersed in an ultrasonic bath at a temperature of 50 °C for 5 min reaction time. After the reaction, yellow precipitates were separated via centrifugation at 6800 rpm for 2 min. Collected samples were soaked in methanol for two days before drying overnight in an oven at 80 °C.

4.2.3 Ultrasound-assisted continuous single-phase flow synthesis

4.2.3.1 Ultrasound-assisted single-phase flow synthesis of Ca-NDS (water) in an ultrasonic bath

Glass syringes (25 mL, SGE) were used to deliver chemical precursors (chemical solutions are reported in 3.2.1). A T-mixer (P-713, IDEX) was used to mix all precursors in the inlet of CFIR which used 4.5 m tubing (PFA, outer diameter 1/8 inch,

inner diameter 1/16 inch, Adtech) coiled around a plastic tube (diameter ~ 2 cm). The reactor volume was accordingly taken as 9 mL. The CFIR was immersed in an ultrasonic bath (GT SONIC-D3, 40 kHz, ultrasonic power 100 W). The solution 1 and flows were initiated once the water bath reached the set temperature. The reaction temperature was varied between 20 and 80 °C, the residence time (determined by the flow rates) was varied between 0.5 and 2 min, and the concentration of precursors was varied between 0.2 to 0.35 M. Ca-NDS (water) particles were collected directly in the outlet of CFIR reactor through filtration and then dried overnight in an oven at 80 °C. A schematic diagram of this single-phase flow synthesis is shown in Figure 4.2.

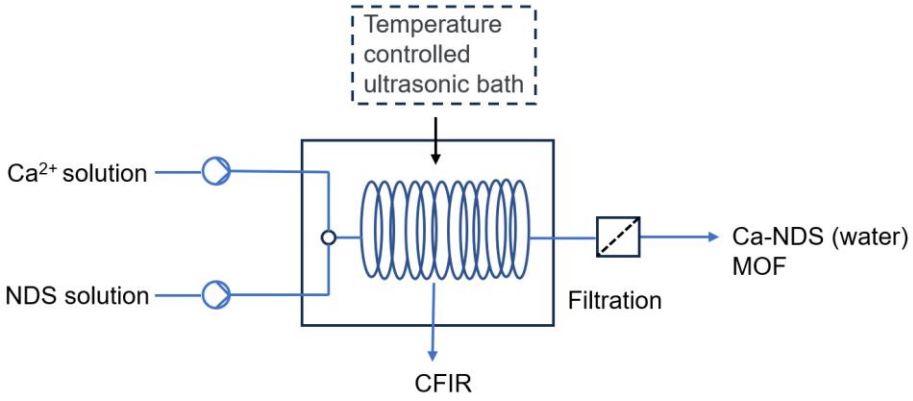

Figure 4.2 Schematic diagram of the ultrasound-assisted continuous synthesis of Ca-NDS (water) in single-phase flow.

4.2.3.2 Ultrasound-assisted single-phase flow synthesis of Ca-NDS (water) in a dedicated reactor

To better control reaction temperature and explore the effect of ultrasonic power (varied between 50 and 150 W), a dedicated stainless steel reaction vessel (12 × 12 × 7 cm) with an acrylic lid was constructed. Five ultrasonic transducers (Beijing Yongda Ultrasonic Co., Ltd.) were mounted on each of the walls (other than the lid), powered by an ultrasonic generator (BJV 300, Beijing Yongda Ultrasonic Co., Ltd.). The reaction temperature was controlled by a water circulation bath with refrigeration and heating functions (Fisherbrand™ Isotemp™ R20). The same CFIR (4.2.3.1) was placed inside the ultrasound chamber. The temperature was varied between 20 and 80 °C, the residence time (determined by the flow rates) was varied between 0.5 and 2 min, the concentration of precursors was 0.275 M, and the ultrasonic power was varied between 50 and 150 W.

4.2.3.3 Ultrasound-assisted continuous two-phase flow synthesis

A two-phase flow reactor was constructed from the single-phase setup (4.2.3.2) using N_2 gas as the second phase. Figures 4.1 and 4.3 are schematic diagrams of the ultrasound-assisted two-phase flow setup. Chemical precursors (chemical solutions for synthesising Ca-NDS (water), ZIF-8, and UiO-66-NH_2 reported in sections 4.2.2.1, 4.2.2.2 and 4.2.2.3, respectively) were delivered by glass syringes (25 mL, SGE) or a continuous pump (SyrDos^{TM} 2XLP). The flow rate of N_2 gas was controlled precisely by a gas mass flow controller (GMFC, FG-201AV, Bronkhorst). A cross connector (P-723, IDEX) was used to mix the precursors and form stable slugs in the inlet of the CFIR (the same reactor as used in section 4.2.3.1), forming slugs of consistent volume and concentration. The ratio of flow rates of the chemical precursors to N_2 gas was 1:1 in order to form a stable slug pattern. The residence time for the synthesis of Ca-NDS (water) and ZIF-8 was 0.75 min, using flow rates for each chemical precursor of 3 mL min^{-1} and a N_2 gas flow rate of 6 mL min^{-1}. The residence time for the synthesis of UiO-66-NH_2 was 1 min, using flow rates for each chemical precursor of 2.25 mL min^{-1} and a N_2 gas flow rate of 4.5 mL min^{-1}. Both solutions were allowed to flow once the temperature in reaction vessel reached 50 °C, more than 1 reactor volume of solution was allowed to pass through for achieving stable slug flow before the collection of samples for yield calculations. Ca-NDS (water) was collected directly at the CFIR outlet by filtration. For ZIF-8 and UiO-66-NH_2, solid products and the reaction solution were collected in a centrifuge tube containing excess water (in order to dilute reaction solutions and avoid further crystal growth during sample collection). The suspension was then centrifuged to isolate the solid product. Sample activation and drying processes were carried out following the same procedures as used for batch synthesis.

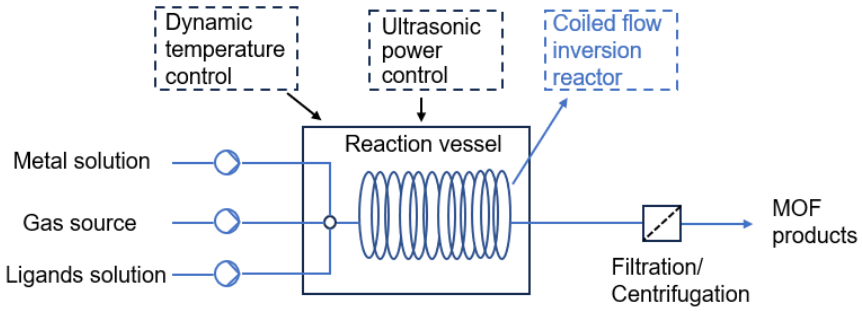

Figure 4.3 A general schematic diagram of the ultrasound-assisted two-phase flow reactor for MOF synthesis.

4.2.4 Fabrication of pellets and membranes with Ca-NDS (water)

Proton conductivity measurements of the Ca-NDS (water) synthesized in flow were carried out using both pellet and membrane testing following our previous work [29]. Ca-NDS (water) powders made in the two-phase flow reactor were pelletized under a pressure of 5 ton cm^{-2} for 2 minutes by using a 5 mm pellet die (Specac). For membrane measurements, Ca-NDS (water) powders were used directly to make mixed matrix membranes (MMMs) without further processing (i.e. no further grinding required). To form membranes, Ca-NDS (water) particles were incorporated into PVP and PVDF at a weight percent of 60% Ca-NDS (water). Typically, PVDF (45 mg) and PVP (135 mg) were first dissolved in DMF (2.7 mL) by stirring at room temperature for 3 h to obtain a homogeneous gel. Next, Ca-NDS (water) particles (270 mg) were added and dispersed evenly in the gel by vigorous stirring for 1 h at room temperature. The prepared gel was then poured onto a high-temperature resistant glass and cast using an adjustable applicator (BGO 209/2, Biuged Laboratory Instruments Co., Ltd) to form a film of 60 μm thickness. The resulting membranes were dried at 70 °C for 1 h in a vacuum oven to remove excess DMF. Finally, the solidified membranes were washed with DI water 3 times and then dried at room temperature. MMMs made using Ca-NDS (water) synthesized in single-phase flow and two-phase flow were denoted Ca-NDS (water)-MMM-1 and Ca-NDS (water)-MMM-2, respectively.

4.2.5 Materials characterization

The surface morphologies of the samples were characterized by light microscopy (LM, Olympus, BX51) and scanning electron microscopy (SEM, Hitachi TM-3030Plus, equipped with a backscattered electron detector and operated at 15 kV accelerating voltage). High resolution SEM images were collected using a Hitachi SU8230 SEM equipped with a cold field emission electron source. An Oxford instruments 150 X-Max energy dispersive X-ray spectroscopy (EDS) detector, in the Hitachi SU8230 SEM, was used to assess the elemental composition of MOF particles. EDS analysis was conducted with an electron beam accelerated to 10 kV, a probe current of 20 nA, a working distance of 15 mm, and a pixel dwell time of 10 μs. Similar conditions were applied for EDS point analysis on the MOF particles to verify their composition in comparison to their empirical formula. Before the EDS point analysis, MOF particles were drop-cast onto carbon tape and coated with 10 nm Pt to avoid

sample charging. For EDS point analysis, at least 5 areas were collected for each particle to assess the statistical significance of the results. Cryo-SEM was used to measure the thickness, surface morphology, and elemental composition of the hydrated membrane using a Tescan AmberX cryo-PFIBSEM, equipped with a Quorum Technologies PP3010 cryo-stage and an Oxford instruments 150 X-Max energy dispersive EDS detector and operated at a 2 keV electron beam energy. Particle sizes of Ca-NDS (water) and ZIF-8 were measured from SEM images using ImageJ: The average of the length taken as the longest dimension of the particle and the width perpendicular to the length was used as a descriptor of particle size. More than 200 particles were measured for each sample.

Powder X-ray diffraction (XRD) patterns were acquired using a Bruker D2 diffractometer (Cu K_α λ = 1.54184 Å, 2θ scan range = 5-50°). Fourier Transform Infrared (FTIR) spectra were recorded using a Bruker Vertex 80V FTIR spectrometer with a diamond prism Attenuated Total Reflection crystal. Spectra were collected for wavenumbers between 500 and 4000 cm^{-1} and averaged over 32 scans. Thermogravimetric analyses (TGA) were conducted using a Netzsch STA 449F3 instrument with a heating rate of 10 °C min^{-1} from 30 to 900 °C in a nitrogen atmosphere. The first derivative of the thermogravimetry curve (the DGT curve) was calculated numerically to extract the temperatures at which there was the steepest change in mass loss. X-ray photoelectron spectroscopy (XPS) was employed to characterize the surface chemistry of the synthesized MOFs. MOF particles were pressed onto carbon tape and adhered to a standard omicron plate. The experiment was conducted in UHV ($<1\times10^{-9}$ mbar) on a Specs FlexMod system. The illuminating X-ray source was a monochromatic Al Kα (hν = 1486.7 eV) anode at a power of 400 W and 15 kV. A Specs Phoibos 150 hemispherical analyzer with 1D delay line detectors was used to detect the photoelectrons. The powders were insulating, and so, to reduce any differential charging at the surface which could distort the spectra, an electron flood gun (energy 4 kV and current 75 µA) was used to charge neutralize the sample. Survey spectra were obtained with a pass energy of 50 eV, a step width of 1 eV and a dwell time of 0.1 seconds. High resolution spectra were collected with a pass energy of 30 eV, a step width of 0.1 eV and a dwell time of 0.2 seconds. After collecting the spectra, the data were analyzed using CasaXPS software. Binding energies were calibrated using the C-C C1s peak at 284.8 eV and the intensity was calibrated using

a previously calculated transmission function for the specific instrument settings. All spectra were fitted with a Shirley background and the peak areas were used to quantify the relative atomic percentages using the respective relative sensitivity functions for each peak. N_2 adsorption-desorption isotherms were measured using a Nova 800 (Anton Paar) BET surface area analyzer. Prior to measurements, ZIF-8 was degassed for 3 h at 300 °C and UiO-66-NH_2 was degassed for 5 h at 250 °C. The specific area was determined using the BETSI method [50]. The total pore volume was determined using the adsorption branch of the N_2 isotherm at $P/P_0 = 0.99$ from Nova Anton Paar Kaomi software.

4.2.6 Linear response surface modelling

Linear response modelling was conducted using Minitab (version 21.3). An analysis of variance was carried out to identify statistically significant terms for linear response model fitting. Terms associated with low probability values (p-values) were excluded from model fitting. The p-values, together with an inspection of the distribution of contributions of all terms, were used to select retained terms, targeting the minimum number of terms to describe the response. Linear response surface modelling was carried out for STY, particle size, and particle size IQR. Equations were used to fit the results across the parameter space: 20 °C ≤ Temperature (T) ≤ 80 °C, 0.5 min ≤ Residence time (t) ≤ 2 min, and 0.2 mol/L ≤ Reagent Concentrations (C) ≤ 0.35 mol L^{-1}.

The values of R^2, the predicted R^2 (R^2 (pred), a calculation involving the removal of each experimental measurement and estimating the quality of the model's prediction of the removed measurements), and the root mean squared deviation (RMSD) for both the Box-Behnken experimental design points and additional verification points (see Figure 4.4a, Tables 4.1 and 4.2) were considered in selecting the optimized regression equations for STY, particle size, and particle size IQR. The optimized regression equations were chosen based on assessing the relative increase in R^2 for increasing the number of terms, maximizing the predicted R^2 (R^2 (pred)) values, and minimizing the RMSD values. These metrics were balanced with the aim to minimize the number of terms used in each equation. As summarized in Tables 4.3-4.5, the optimized regression equations for STY, particle size, and particle size IQR contained 6, 8 and 7 terms, respectively. The coefficients for the corresponding equations are given in

Table 4.6. Contour plots for STY and particle size as well as for STY and particle size IQR were then created using these optimized regression equations.

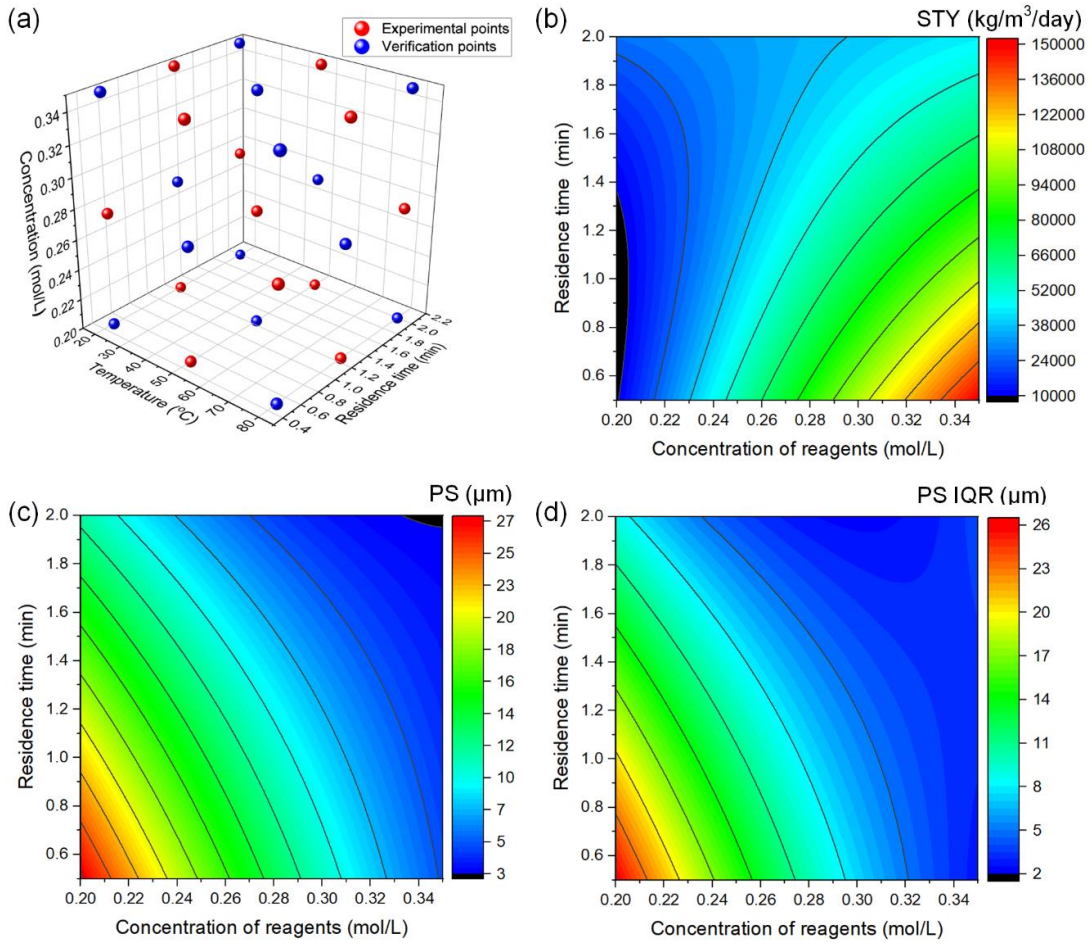

Figure 4.4 (a) Overview of the Box-Behnken factorial design of experiments. The red points mark the conditions used for experimental input for response surface modelling and the blue points mark additional points used for verification of the model. The corresponding coefficients of the response surface modelling are given in Table S6. The response surfaces are represented as contour plots for (b) STY, (c) PS, and (d) PS IQR as a function of the concentration of reagents and the reaction time with the reaction temperature fixed at 50 °C. Abbreviations in this figure: Space time yield (STY), Particle size (PS), Particle size interquartile range (PS IQR).

Table 4.1 Reaction parameters of 15 separate experiments used in the Box-Behnken design and the corresponding reaction results of the ultrasound-assisted single-phase synthesis of Ca-NDS (water). Abbreviations in this table: Reaction temperature (T), Residence time (RT), Concentration of reagents (COR), Space time yield (STY), Particle size (PS), Particle size interquartile range (PS IQR).

Experiment No.	T (°C)	RT (min)	COR (mmol mL^{-1})	Yield (%)	STY (kg m^{-3} day^{-1})	PS (µm)	PS IQR (µm)
1	20	0.5	0.275	8.7	24998	25.1	14.9
2	20	2	0.275	48.9	35072	6.9	3.9
3	20	1.25	0.2	2.3	1929	31.2	23.9
4	20	1.25	0.35	46.1	67372	5.9	2.7
5	50	0.5	0.2	0.5	1044	26.1	27.3
6	50	2	0.2	27.9	14554	11.4	8.2
7	50	0.5	0.35	44.3	161892	5.1	3.6
8	50	2	0.35	56.7	51733	4.5	3.1
9	50	1.25	0.275	46.4	53257	9.1	6.1
10	50	1.25	0.275	48.2	55335	9.7	6.3
11	50	1.25	0.275	45.3	52005	8.8	5.3
12	80	0.5	0.275	46.4	133228	9.3	6.6
13	80	2	0.275	56.7	40669	6.2	4.5
14	80	1.25	0.2	31.7	26484	12.9	10.4
15	80	1.25	0.35	56.7	82875	4.7	3.6

Note: Experiments are run in the same order as the experiment number.

Table 4.2 Reaction parameters of 14 verification experiments for the Box-Behnken design and the corresponding reaction results of the ultrasound-assisted single-phase synthesis of Ca-NDS (water). Abbreviations in this table: Reaction temperature (T), Residence time (RT), Concentration of reagents (COR), Space time yield (STY), Particle size (PS), Particle size interquartile range (PS IQR).

Experiment No.	T (°C)	RT (min)	COR (mmol mL^{-1})	Yield (%)	STY (kg m^{-3} day^{-1})	PS (µm)	PS IQR (µm)
1	20	0.5	0.35	18.1	66006	5.1	3.1
2	20	1.25	0.275	43.7	50180	7.5	3.3
3	20	2	0.2	10.6	5542	11.4	8.7
4	20	2	0.35	51.8	47276	5.3	3.5
5	50	0.5	0.275	22.6	64892	6.2	4.1
6	50	1.25	0.2	16.1	13417	13.5	11.1
7	50	1.25	0.35	54.9	80259	4.3	2.9
8	50	2	0.275	51.3	36830	7.4	4.4
9	80	0.5	0.2	24.5	51118	14.6	11.2
10	80	0.5	0.35	52.3	191114	9.1	6.7
11	80	1.25	0.275	51.6	59238	7.2	4.8
12	80	2	0.2	36.3	18958	12.1	7.9
13	80	2	0.35	59.8	54627	5.4	2.5

Note: Experiments are run in the same order as the experiment number.

Table 4.3 Evaluation of fitting quality for linear response surface equations for space time yield (STY) by varying the number of coefficients. The selected number of terms, exhibiting a limiting gain in R^2 for increasing the number of terms, among the highest R^2 (pred), and a minimum in the RMSD for the verification points, is highlighted in bold.

Term number	R^2 (%)	R^2 (pred %)	RMSD for STY	RMSD for STY of verification points
4	79.57	51.14	19580	19300
5	93.15	75.34	11334	15258
6	**94.33**	**73.6**	**10311**	**13435**
7	94.63	63.19	10039	15905
8	94.82	48.28	9856	15779

Table 4.4 Evaluation of fitting quality for linear response surface equations for particle size (PS) by varying the number of coefficients. The selected number of terms, exhibiting limiting gain in R^2 for increasing the number of terms, the highest R^2 (pred), and a minimum in the RMSD for the verification points, is highlighted in bold**.**

Term number	R^2 (%)	R^2 (pred %)	RMSD for PS	RMSD for PS of verification points
6	95.67	85.36	1.72	7.72
7	97.29	83.94	1.36	5.31
8	**98.97**	**89.67**	**0.84**	**5.13**
9	99.03	85.01	0.82	5.14

Table 4.5 Evaluation of fitting quality for linear response surface equations for particle size IQR (PS IQR) by varying the number of coefficients. The selected number of terms, exhibiting limiting gain in R^2 for increasing the number of terms, the highest R^2 (pred), and a minimum in the RMSD for the verification points, is highlighted in bold.

Term number	R^2 (%)	R^2 (pred %)	RMSD for PS IQR	RMSD for PS IQR of verification points
6	95.87	86.83	1.49	4.7
7	**98.33**	**89.7**	**0.95**	**4.41**
8	98.74	87.7	0.82	4.41
9	98.89	83.27	0.77	4.43

The retained terms for each regression equation are given below (coefficients differ between equations as a result of independent fitting for each measured response), with coefficients in lower case *a, b, c,…* etc. and reaction parameters denoted as temperature *T*, residence time *t*, and concentration of reagents *C*:

$$STY = -a + bT + ct + dC + e(t^2) - f(Tt) - g(tC)$$

$$particle\ size = a - bT - ct - dC + e(T^2) + f(C^2) + g(Tt) + h(TC) + i(tC)$$

$$particle\ size\ IQR = a - bT - ct - dC + e(C^2) + f(Tt) + g(TC) + h(tC)$$

Table 4.6 Coefficients determined from response surface fitting (equations above).

Equations	Coefficient values								
	a	b	c	d	e	f	g	h	i
STY	326885	2067	136387	1220152	16771	1140	549641	-	-
Particle size	146.1	1.133	31.72	486.6	0.002509	384	0.1678	1.9	62.7
Particle size IQR	148.2	0.6482	33.13	625.1	631	0.0989	1.6	82.7	-

Note: No transformations of the data were used during the modelling.

4.2.7 Proton conductivity testing

Electrochemical impedance spectroscopy (EIS) was carried out on Ca-NDS (water) pellets and MMMs as reported previously [8]. A temperature-controlled humidity chamber (Memmert HCP150) was used for testing between 50 to 80 °C with 95% relative humidity (RH). The proton conductivity (σ, mS cm^{-1}) was calculated according to:

$$\sigma = \frac{L}{AR} \tag{1}$$

where L represents the thickness of the pellet or membrane sample (cm), A refers to the cross-sectional area of the tested sample (cm^{-2}), and R is the resistance of the sample (Ω). R was measured by EIS in a two-electrode configuration between frequencies of 100 Hz and 1 MHz using a Gamry 1010E electrochemical workstation.

4.3 Results and discussion

4.3.1 Ultrasound-assisted single-phase flow synthesis of Ca-NDS (water)

The Ca-NDS (water) coordination polymer has been reported by Cai *et al*. [51], as well as in our previous work [29] using a solvothermal batch synthesis. However, the large Ca-NDS (water) particles generated by the batch reaction limits their direct use in proton exchange membranes (PEMs), because only small and uniform MOF particles can be used to make homogenous PEMs. Ultrasound-assisted flow synthesis offers a promising route to achieve small and uniform particles in high yield. Firstly, we implemented a synthesis in a single-phase flow reactor placed in an ultrasonic bath to explore the effects of the main parameters of reaction temperature, time, and concentration of precursors.

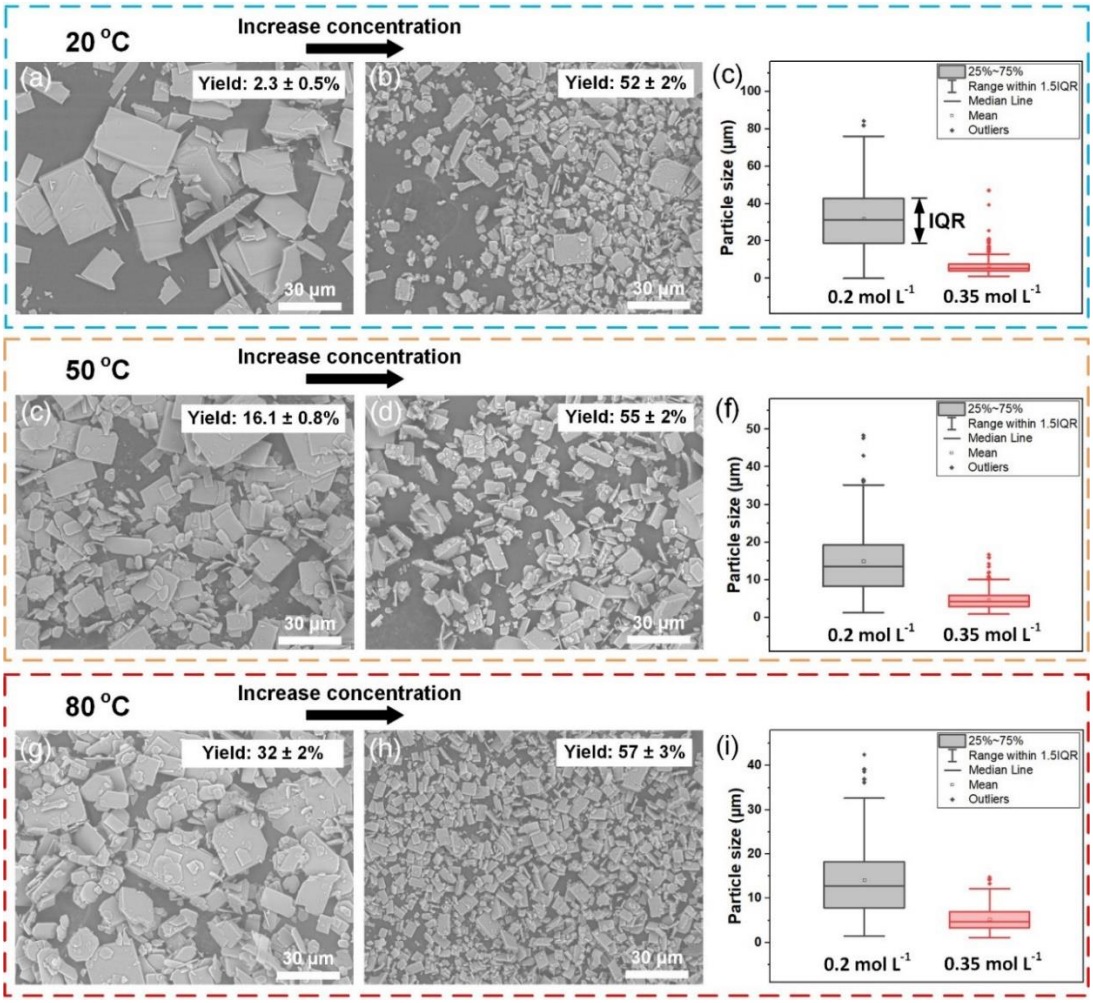

Figure 4.5 SEM images of Ca-NDS (water) made in single-phase ultrasound-assisted flow with different parameters and box plots of particle sizes. The horizontal lines in the box plots are the minimum, first quartile, median, third quartile, and maximum. The mean is shown as a square. Outliers (greater than 1.5 times the interquartile range) are shown as additional points. The concentrations of precursor solutions with the same metal-to-ligand ratio were increased from 0.2 to 0.35 M. The residence time of these reactions was 1.25 min.

Figure 4.5 presents the SEM images of Ca-NDS (water) particles made in this reactor. For a reaction temperature fixed at 20 °C, increasing the concentration of precursors from 0.2 to 0.35 M results in a significantly increased reaction yield from 2.3 to 51.8% and a reduction in particle size (median particle size decreased from 31.2 to 5.9 μm, Figure 4.5a-b). The distribution of particle sizes also narrowed, with the particle size interquartile range (IQR) reduced from 23.9 to 2.7 μm (Figure 4.5c). Similar trends were observed for reaction temperatures fixed at 50 and 80 °C (Figure 4.5c-i). Comparing the temperature response, yield increased with temperature while particle size and particle size IQR decreased with increasing temperature.

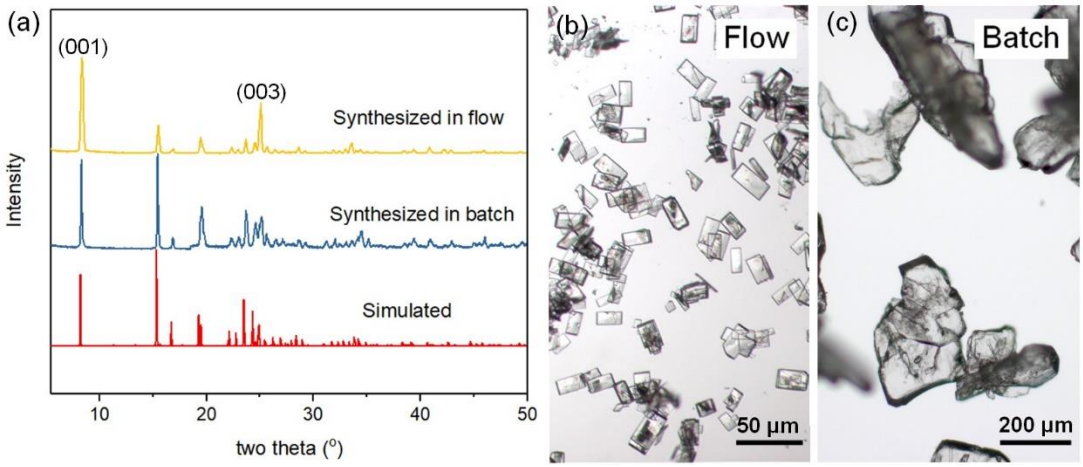

Figure 4.6 (a) Powder XRD patterns of Ca-NDS (water) synthesized in flow and batch alongside a simulated pattern from the reported unit cell [51]. (b)-(c) Light micrographs of Ca-NDS (water) made in (b) flow and (c) batch reactions.

The XRD pattern of Ca-NDS (water) synthesized in single-phase flow (Figure 4.6a) exhibited identical peak positions as for the batch synthesis and as for the pattern calculated from the single-crystal structure. The intensities of the (001) and (003) reflections were enhanced for Ca-NDS (water) synthesized in flow, consistent with preferred orientation in the fine powder sample comprised of plates with top and bottom {001} surface terminations, a habit observed previously in batch-synthesized crystals [29]. Compared with batch-synthesized Ca-NDS (water) particles, the ultrasound-assisted flow synthesis produced much smaller and more uniform particles (Figure 4.6b-c).

To probe the interactions between key parameters (reaction temperature, time, and concentration of precursors), we employed a factorial experimental design. Specifically, we implemented a Box-Behnken design (BBD), because it is a 3-level and 3-factor design this design that reduces the number of experiments while effectively modeling quadratic interactions. BBD avoids extreme conditions, minimizes prediction errors at the center, and is particularly useful when working with three or more factors. The BBD comprises 12 different experiments varying each parameter and three repeats at intermediate values (15 total experiments). Figure 4.4a shows a visualization of this design. All reaction parameters from the Box-Behnken design and the corresponding reaction results are listed in Table 4.1. The standard deviations for yield, STY, particle size, and particle size IQR in these 3 repeated experiments were 1.2%, 1.4×10^3 kg m^{-3} day^{-1}, 0.4 µm and 0.4 µm, respectively. These results were in turn used for linear response surface modelling to document the

trade-offs between reaction parameters and STY, particle size, and particle size IQR (Tables 4.2-4.6, Figures 4.4 and 4.7).

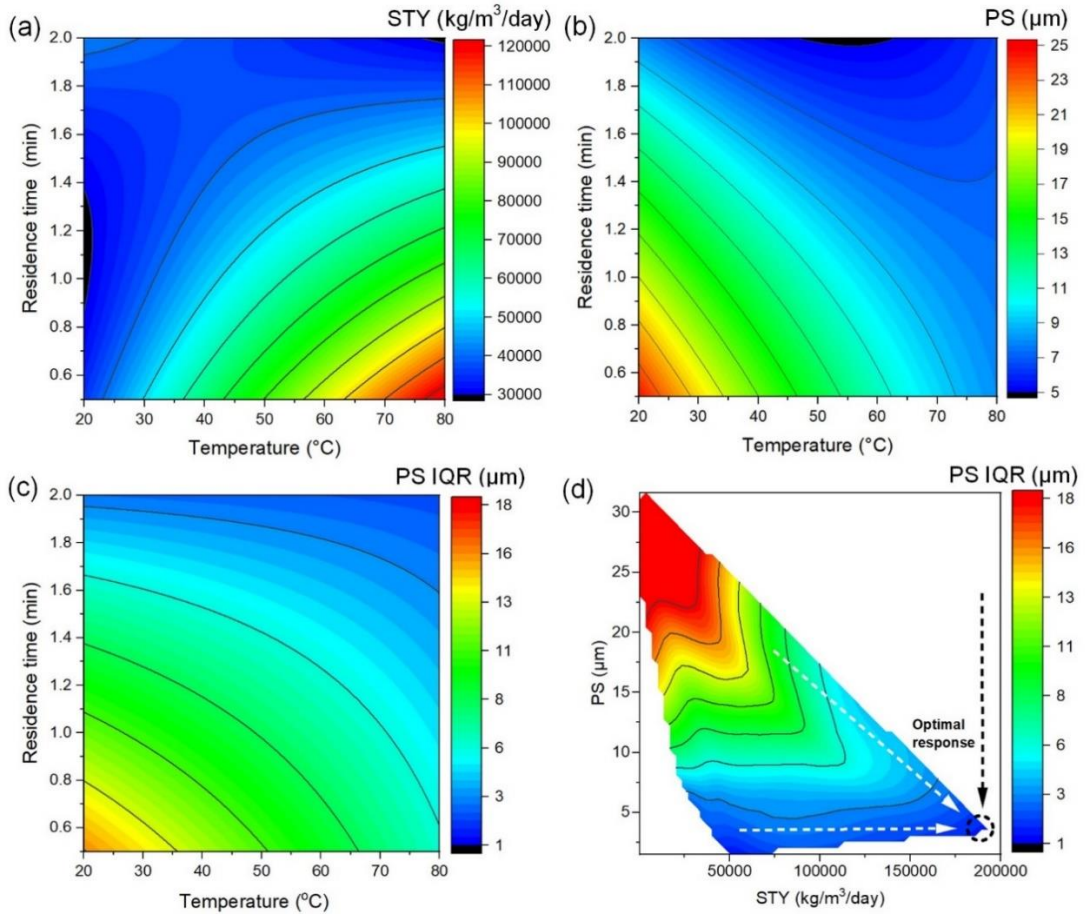

Figure 4.7 Linear response surface modelling results based on a factorial design of experiments. The response surface models are depicted as contour plots of (a) STY, (b) PS, and (c) PS IQR as a function of synthesis temperature and time at a fixed concentration of reagents (0.275 mol L^{-1}). (d) Contour plot depicting the simultaneous optimisation of maximum STY and minimum PS and PS IQR. Abbreviations in this figure: Space time yield (STY), Particle size (PS), Particle size interquartile range (PS IQR).

Figure 4.7a-c present contour plots depicting the response surface modelling as a function of temperature and residence time at a fixed reagent concentration of 0.275 mol L^{-1}. Figure 4.4b-d presents additional contour plots as a function of the concentration of reagents and residence time at a fixed temperature (50 °C). These findings highlight that increasing temperature, reducing residence time, and increasing the concentration of reagents maximize the STY (Figure 4.7a, Figure 4.4b). In contrast, the smallest particle sizes and particle size IQRs are achieved at high temperature, long residence times, and high concentrations of reagents (Figure 4.7b-c, Figure 4.4c-d). The apparent trade-off in short residence times for high STY and long residence times for small particle sizes and particle size IQRs, however, can be resolved by the

compensating control of particle size and particle size IQR via the concentration of reagents. That is, considering the combinations accessible in the reactor for the simultaneous objectives of maximum STY and minimum particle size and particle size IQR (Figure 4.7d), a single optimum condition was determined offering high STYs accompanied by small and uniform particle sizes. This characteristic association indicates conditions dominated by crystal nucleation. In contrast, low STYs coincident with larger particle sizes and particle size IQRs reflect a more crystal growth-dominated evolution of the particulate reaction products. The optimal conditions observed experimentally corresponded to the highest STY of 1.6×10^5 kg m^{-3} day^{-1} with a production rate of 59 g h^{-1} for an intermediate reaction temperature of 50 °C, the shortest reaction time (30 s), and the highest concentration (0.35 M) used in the Box-Behnken design, with a correspondingly small particle size and particle size IQR of 5.1 and 3.6 µm, respectively.

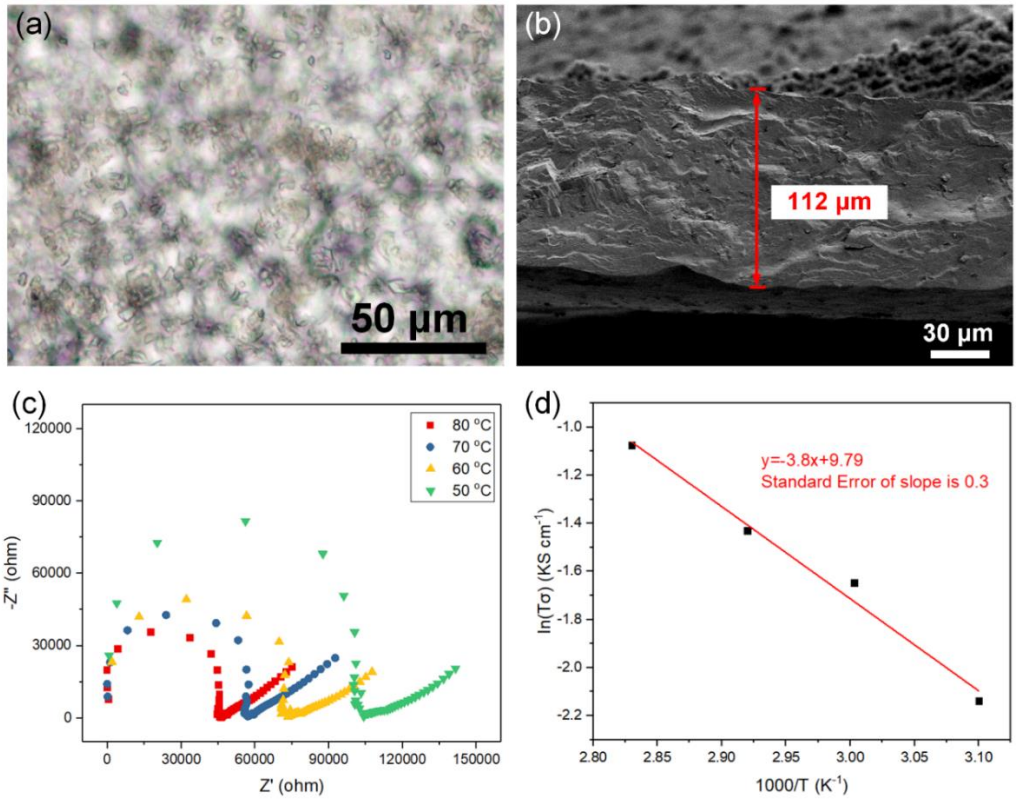

Figure 4.8 (a) Light microscope image of Ca-NDS (water)-MMM; (b) Cryo-SEM micrograph of a cryo-FIB cross section of the fully hydrated (a) Ca-NDS (water); (c) EIS Nyquist plots and (d) Arrhenius plot of Ca-NDS (water)-MMM-1 between 50-80 °C and 95% RH.

To verify the preservation of functional properties, MMMs were prepared for proton conductivity testing. Figures 4.8a and b show a homogeneous dispersion of the

Ca-NDS (water) crystals in the MMM (denoted Ca-NDS (water)-MMM-1) by light microscopy and cryo-SEM. A cross-section observed by cryo-SEM was used to estimate the thickness of the hydrated membrane at approximately 112 μm. Figures 4.9 and 4.10 present EDS mapping of the membrane both in cross section and in plan view, confirming the dispersion of Ca-NDS (water) particles throughout the membrane. EIS (Figure 4.8c) confirmed the proton conductivity of Ca-NDS (water)-MMM-1 as 0.97 ± 0.05 mS cm^{-1} at 80 °C in 95 % RH. Using EIS across multiple temperature conditions, an Arrhenius plot (Figure 4.8d) was used to determine the activation energy, E_a, for proton conduction in the membrane as 32 ± 3 kJ mol^{-1} or 0.33 ± 0.03 eV, a value consistent with a predominantly Grotthuss mechanism (E_a < 0.4 eV) [52].

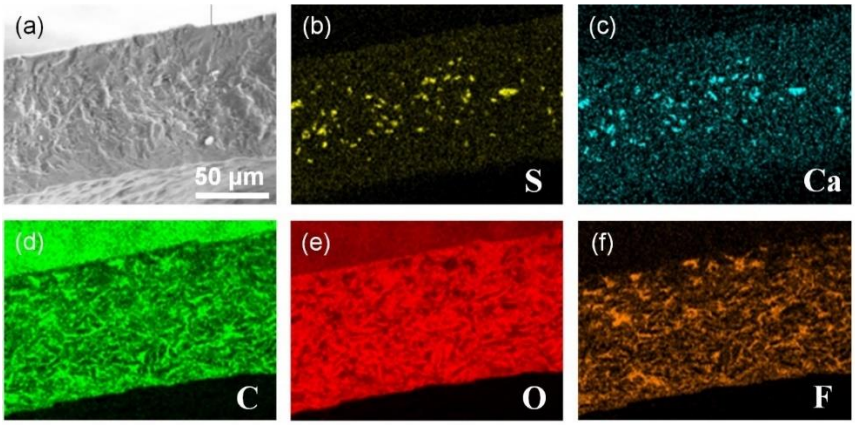

Figure 4.9 (a) Cryo-SEM cross-sectional image of the fully hydrated Ca-NDS (water)-MMM-1 and SEM-EDS elemental maps of (b) sulfur, (c), calcium, (d) carbon, (e) oxygen, and (f) fluorine.

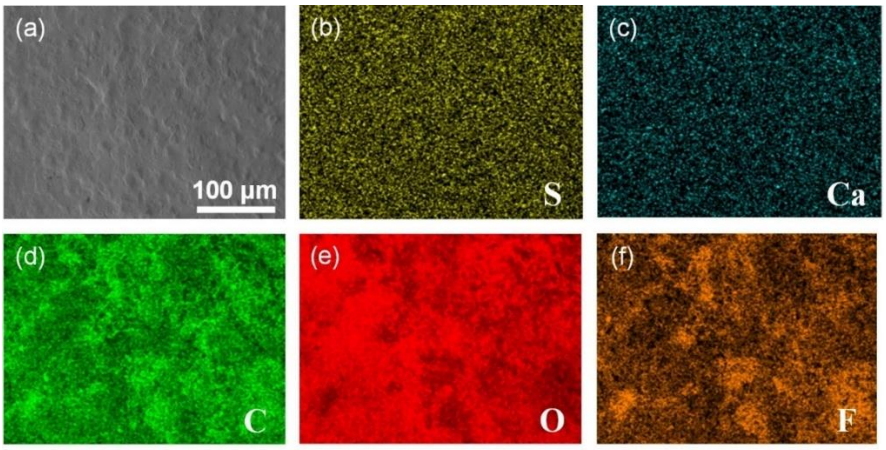

Figure 4.10 (a) Cryo-SEM image of the surface of the fully hydrated Ca-NDS (water)-MMM-1 and SEM-EDS elemental maps of (b) sulfur, (c), calcium, (d) carbon, (e) oxygen, and (f) fluorine.

4.3.2 Ultrasound-assisted continuous MOF reactor: Two-phase flow

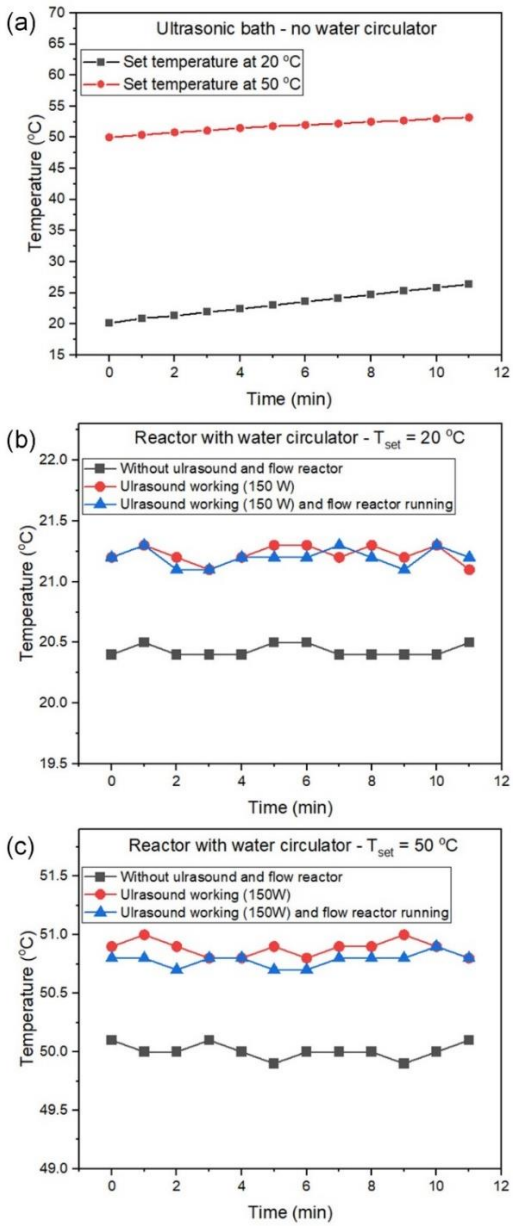

Figure 4.11 (a) Temperature records of the ultrasonic bath when set at temperatures of 20 °C and 50 °C with exposure to ultrasound; temperature records of the updated reaction platform with a water circulation bath when set at temperatures of (b) 20 °C and (c) 50 °C.

We next developed a second-generation setup in order to better control the reaction parameters in ultrasound-assisted flow synthesis and to generalise the reactor to the aqueous synthesis also of ZIF-8 and UiO-66-NH_2. This setup added a water circulation bath to control the reaction temperature dynamically. The ultrasonic bath used in the initial single-phase flow synthesis showed linear temperature increases with increasing reaction times (Figure 4.11a) for set temperatures of 20 and 50 °C,

consistent with the addition of heat to the bath from the ultrasound exposure. In contrast, the second-generation platform preserved temperature stability to within 0.25 °C (Figures 4.11b and c). This second-generation reactor also supported changing the ultrasound power to further probe the effect of this key parameter on the aqueous syntheses of Ca-NDS (water), ZIF-8, and UiO-66-NH_2.

Table 4.7 Yield and space time yield (STY) comparison between reactions using different ultrasound powers in the single-phase synthesis of Ca-NDS (water).

Power (W)	20 °C 1.25 min 0.275 M		50 °C 0.5 min 0.275 M		50 °C 2 min 0.275 M		80 °C 1.25 min 0.275 M	
	Yield (%)	STY (kg m^{-3} day^{-1})	Yield (%)	STY (kg m^{-3} day^{-1})	Yield (%)	STY (kg m^{-3} day^{-1})	Yield (%)	STY (kg m^{-3} day^{-1})
50	32 ± 1	$3.7\times10^4 \pm 1\times10^3$	20 ± 2	$5.4\times10^4 \pm 5\times10^3$	47 ± 3	$3.4\times10^4 \pm 2\times10^3$	47 ± 2	$5.3\times10^4 \pm 2\times10^3$
100	44 ± 2	$5.0\times10^4 \pm 2\times10^3$	23 ± 2	$6.5\times10^4 \pm 4\times10^3$	51 ± 2	$3.7\times10^4 \pm 2\times10^3$	52 ± 2	$6.0\times10^4 \pm 2\times10^3$
150	47 ± 2	$5.4\times10^4 \pm 2\times10^3$	24 ± 2	$7.0\times10^4 \pm 5\times10^3$	53 ± 2	$3.8\times10^4 \pm 2\times10^3$	53 ± 2	$6.1\times10^4 \pm 2\times10^3$

Table 4.8 Particle size (PS) and particle size interquartile range (PS IQR) comparison between reactions using different ultrasound powers in the single-phase synthesis of Ca-NDS (water).

Power (W)	20 °C 1.25 min 0.275 M		50 °C 0.5 min 0.275 M		50 °C 2 min 0.275 M		80 °C 1.25 min 0.275 M	
	PS (μm)	PS IQR (μm)	PS (μm)	PS IQR (μm)	PS (μm)	PS IQR (μm)	PS (μm)	PS IQR (μm)
50	16.0	7.8	14.8	6.6	11.4	7.3	9.4	6.1
100	7.5	4.3	6.2	4.1	7.4	4.4	7.2	4.8
150	6.3	3.7	5.7	2.7	6.7	3.3	6.5	3.5

First, we replicated the single-phase flow synthesis of Ca-NDS (water) in the second-generation reactor. Under matched conditions of temperature, time, and concentration of precursors (now variable ultrasound power), the yield and STY of Ca-NDS (water) increased with increasing ultrasonic power (Table 4.7), while particle size and particle size IQR decreased with increasing ultrasonic power (Table 4.8). We attribute these observations to the vigorous microscale mixing and diffusion of the solute and increased nucleation rates under sonication [41]. Although this updated reaction platform was promising, clogging was observed during the single-phase

synthesis of Ca-NDS (water) after running the reaction for more than 10 min.

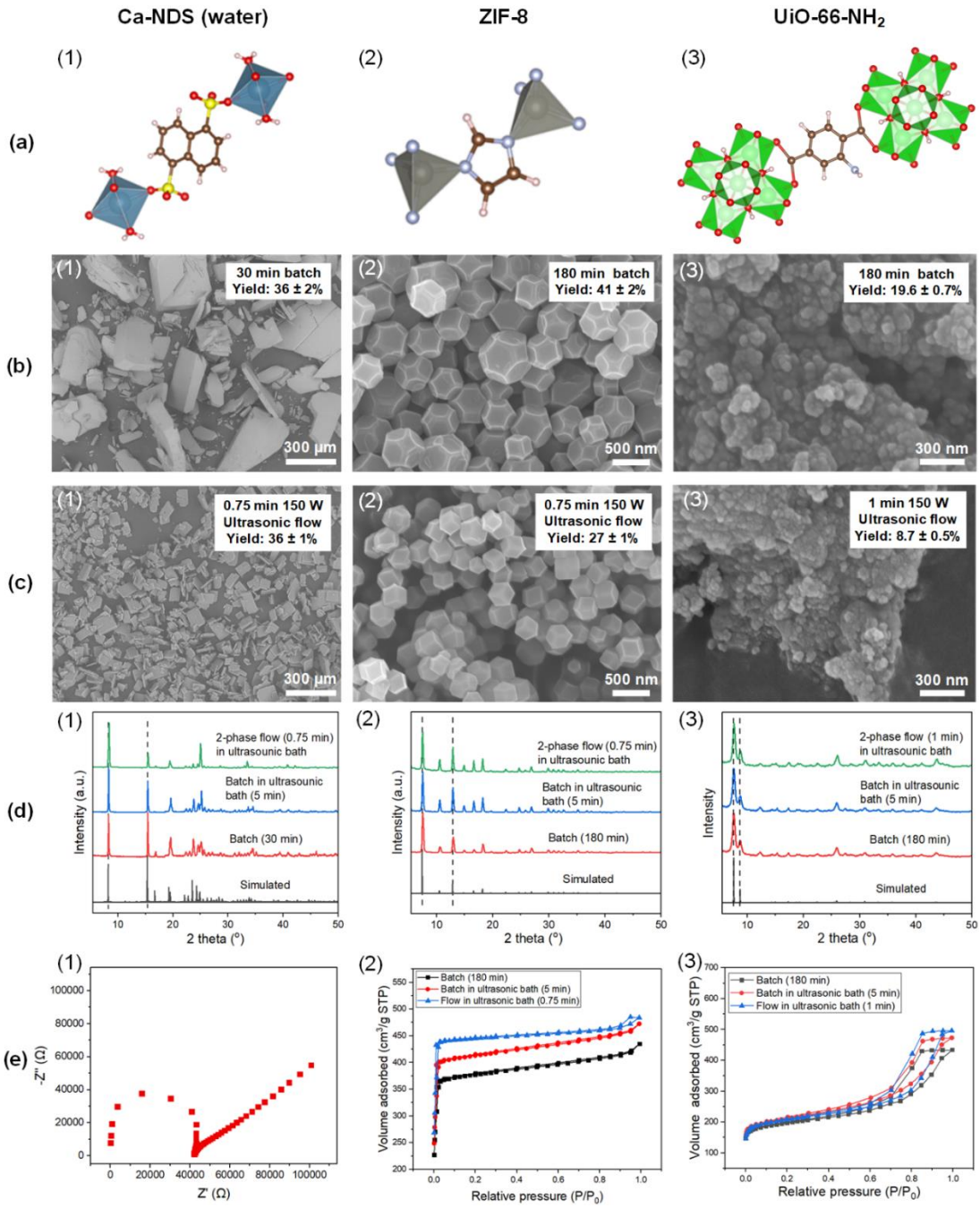

Figure 4.12 (a) Polyhedral representations of Ca-NDS (water), ZIF-8 and UiO-66-NH_2. (b)-(c) SEM images of Ca-NDS (water), ZIF-8, and UiO-66-NH_2 particles made in (b) batch and (c) ultrasound-assisted two-phase flow. (d) XRD patterns of Ca-NDS (water), ZIF-8, and UiO-66-NH_2 powders made in batch and ultrasound-assisted two-phase flow compared with simulated patterns. For the simulated patterns, the unit cells were taken from published structures deposited in the Cambridge Crystallographic Data Centre (CCDC) for Ca-NDS (water) [51] (CCDC 152303), ZIF-8 [69] (CCDC 864312), and UiO-66-NH_2 [70] (CCDC: 1405751). (e) EIS Nyquist plot of Ca-NDS (water)-MMM-2 measured at 80 °C and 95% RH, and N_2 adsorption-desorption isotherms of ZIF-8 and UiO-66-NH_2 made in batch and in ultrasound-assisted two-phase flow.

In order to overcome this limitation arising from clogging and thereby achieve a more than ten-fold increase in the continuous operation time (albeit with a five-fold reduction in production rate, see below), we further added N_2 gas as the second phase for ultrasound-assisted two-phase flow synthesis. In addition to Ca-NDS (water), we also demonstrate this two-phase flow reactor for the synthesis of ZIF-8 and UiO-66-NH_2 in aqueous solvent. These MOFs were selected to encompass diverse functional group chemistries, from the sulfonate linkers of Ca-NDS (water) to the imidazolate linkers in ZIF-8 and carboxylate linkers in UiO-66-NH_2 (Figure 4.12a). Figures 4.12b-c present the corresponding SEM images for these three MOFs, comparing the products prepared in batch and in ultrasound-assisted two-phase flow. Compared with the batch samples, smaller and more uniform particles were obtained from the two-phase flow for all three materials.

Batch and two-phase flow syntheses produced products with the same peak positions in XRD as expected from unit cell calculations (Figure 4.12d), confirming that ultrasound did not alter the crystal structures produced. The functional group chemistry of each material synthesized in the ultrasound-assisted two-phase flow reactor (Ca-NDS (water), ZIF-8, and UiO-66-NH_2 MOFs) was further confirmed by ATR-FTIR (Figure 4.12). For Ca-NDS (water), strong bands at approximately at 530, 620, 1068 and 1190 cm^{-1} were assigned as the major peaks of the sulfonate group [53]. Multiple peaks across 1450 to 1650 cm^{-1} were attributed to the skeleton vibration of the benzene rings [54], and peaks in the range 650 to 900 cm^{-1} were assigned to the out-of-plane C-H bending vibration of the aromatic ring [55]. A wider and stronger band between 3000 to 3500 cm^{-1} was attributed to O-H band from water bound to Ca in the Ca-NDS (water) unit cell. For ZIF-8, the bands at 687 and 754 cm^{-1} in the fingerprint region were associated with out-of-plane bending of the imidazole ring, whereas peaks in the region of between 900 and 1350 cm^{-1} arose from the in-plane bending [56]. The peaks at 1581 and 1678 cm^{-1} were attributed to the bending and stretching N-H vibrations of the imidazole group [57]. Two weak peaks at 2930 and 3124 cm^{-1} are assigned to the aliphatic and aromatic C-H stretching of the imidazole, respectively [58]. For UiO-66-NH_2, the characteristic peak at 768 cm^{-1} was associated with Zr-O stretching vibration [59]. The peak at 1425 cm^{-1} was associated with the C-C vibrational bond, and the peaks at 1382 and 1572 cm^{-1} were attributed to symmetric and asymmetric C-O stretching bonds respectively, resulting from aromatic and

carboxylic groups [60]. The bonding between aromatic carbon and nitrogen (C-N) could be observed at 1258 and 1338 cm^{-1}, and the peak at 1619 cm^{-1} was assigned as the bending vibration of N-H, and the wide band between 3200 and 3500 cm^{-1} were derived from the amine group [59].

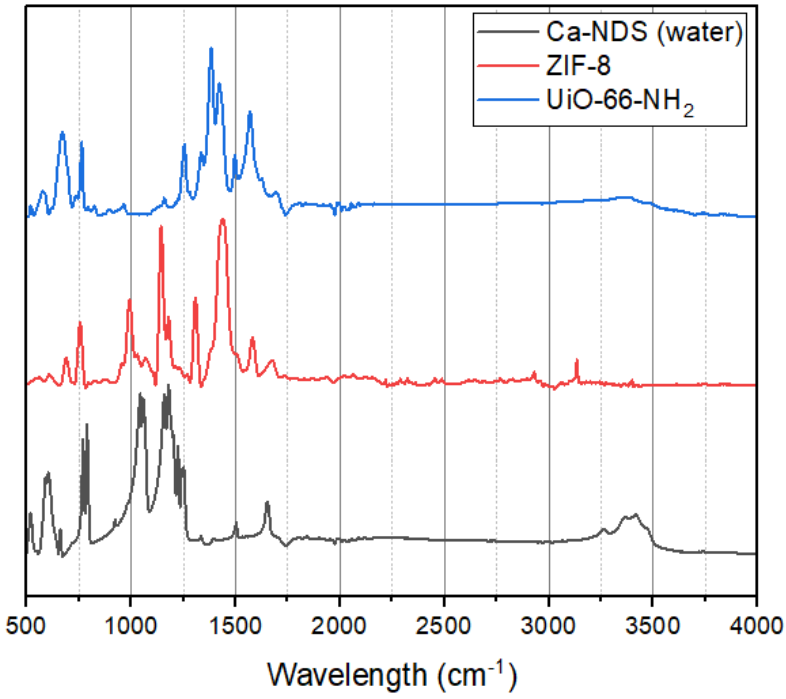

Figure 4.13 ATR-FTIR spectra of Ca-NDS (water), ZIF-8, and UiO-66-NH_2 samples synthesized in two-phase flow.

The thermal response characteristics were examined by TGA (Figure 4.13). The TGA curve of the as-synthesized Ca-NDS (water) showed an initial mass loss from approximately 170 °C, indicating loss of coordinated water molecules, followed by NDS decomposition above 600 °C (a and b). ZIF-8 similarly showed the first weight-loss step around 170 °C corresponding to the release of the absorbed water, a sharp weight loss at approximately 620 °C was caused by structural degradation and decomposition of Hmim ligands (c and d). The TGA curve of UiO-66-NH_2 featured a mass decrease at around 90 °C caused by the loss of surface water molecules (e and f), the second small weight decrease around 200 °C corresponded to the loss of water molecules coordinated in the cage within MOFs, followed by the collapse the structure of MOF and decomposition of H_2ATA ligands [61]. All temperatures were extracted from the maxima in the first derivative of the TGA curve (the DTG curve). SEM-EDS and XPS analyses were used to confirm the elemental composition, homogeneity, and chemical states relative to the reported unit cell structures of Ca-NDS (water) (Figures

4.15 and 4.16a-c, Tables 4.9 and 4.10), ZIF-8 (Figures 4.17 and 4.16d-f, Tables 4.11 and 4.12), and UiO-66-NH_2 (Figures 4.18 and 4.16g-i, Tables 4.13 and 4.14). Together, this structural and chemical characterisation confirmed the reliable synthesis of the target materials.

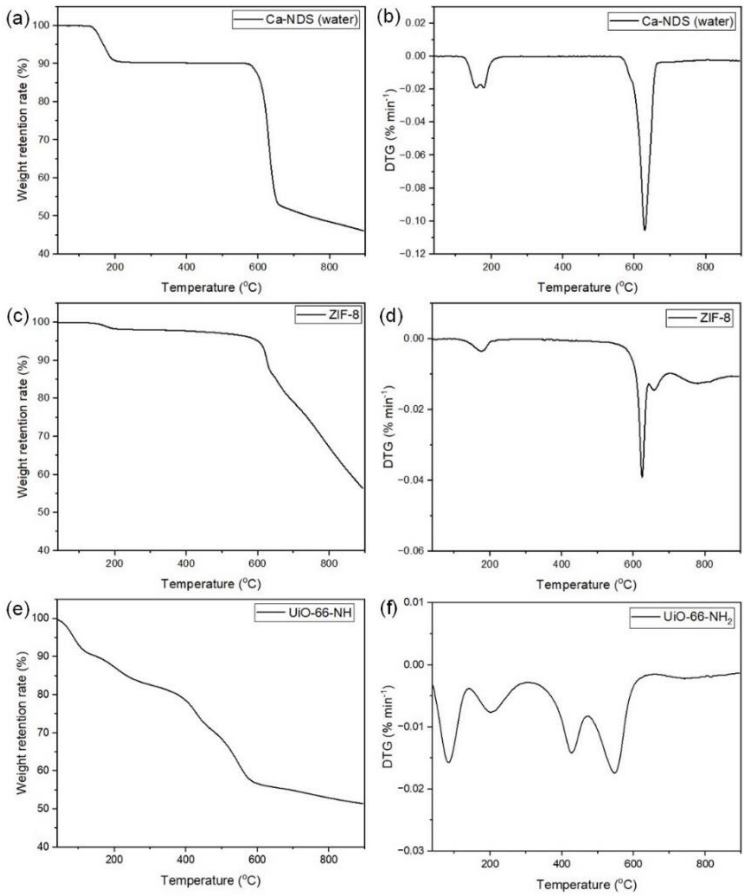

Figure 4.14 TGA and the corresponding differential thermogravimetry (DTG) curves obtained on (a-b) Ca-NDS (water), (c-d) ZIF-8, and (e-f) UiO-66-NH_2 samples synthesized in two-phase flow.

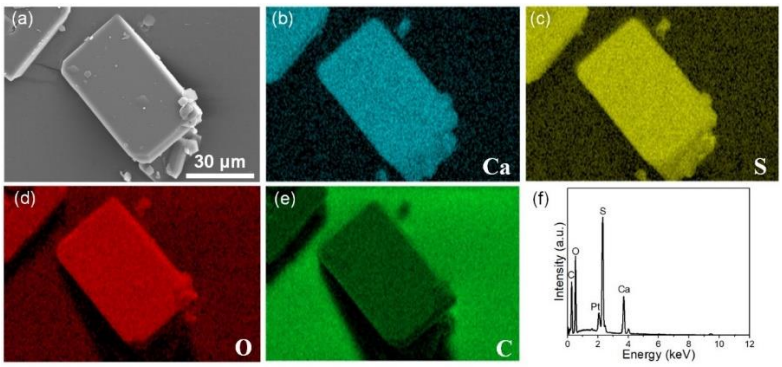

Figure 4.15 (a) SEM image of Ca-NDS (water) particles synthesized in two-phase flow and SEM-EDS elemental maps of (b) calcium, (c) sulfur, (d) oxygen, and (e) carbon. (f) Integrated EDS spectrum from the entire field of view.

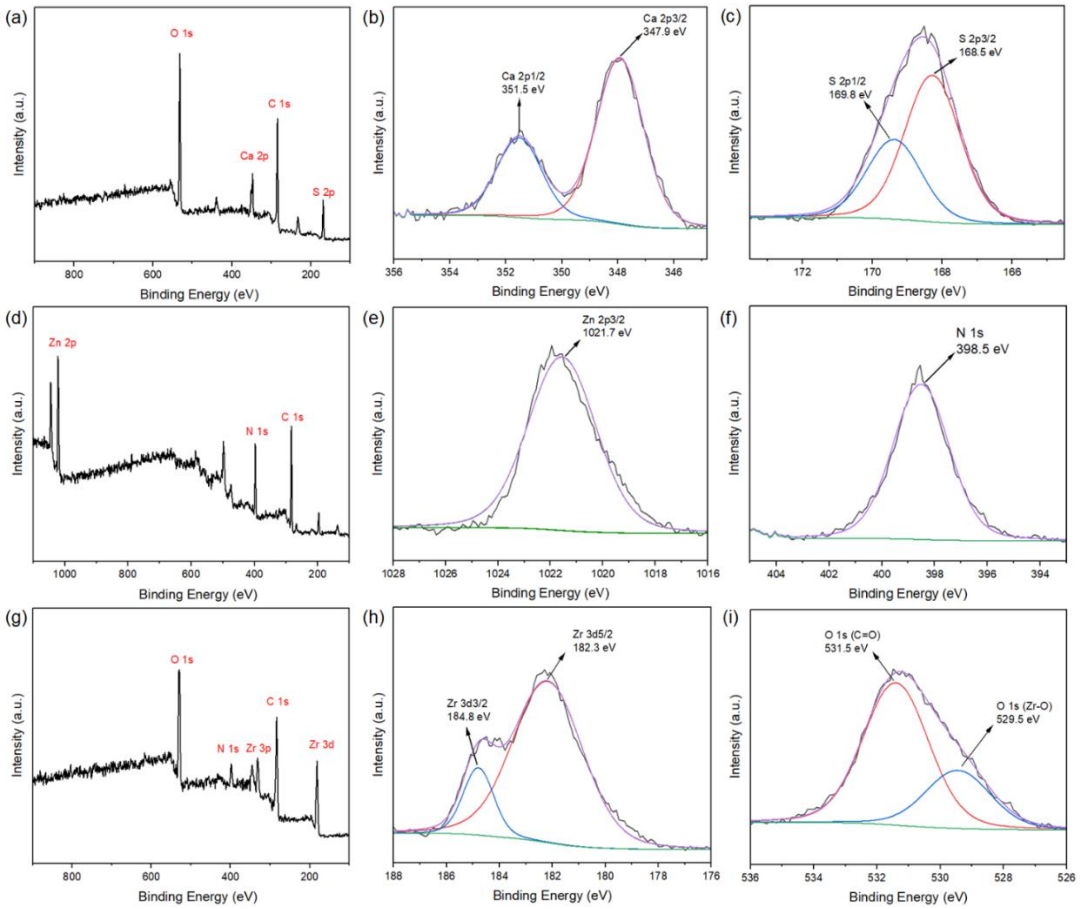

Figure 4.16 XPS analyses of Ca-NDS (water), ZIF-8, and UiO-66-NH_2 synthesized in two-phase flow. (a) Survey spectra and high resolution scans of (b) the Ca 2p peak corresponding to Ca^{2+} $2p_{3/2}$ and $2p_{1/2}$ [62] in the Ca-NDS (water) structure and (c) the S 2p peak for Ca-NDS (water) showing $2p_{3/2}$ and $2p_{1/2}$ peaks at 168.5 and 169.8 eV. These S 2p features were attributed to the SO_3^{2-} group [63] in the Ca-NDS (water) structure. (d) Survey spectra and high resolution scans of (e) the Zn^{2+} $2p_{3/2}$ peak (1021.7 eV [64]) and (f) the N 1s for ZIF-8 with a peak at 398.5 eV attributed to the imidazole groups in ZIF-8 [65]. (g) Survey spectra and (h) high resolution scan of Zr 3d peak showing two peaks at 182.3 and 184.8 eV assigned to Zr^{4+} $3d_{5/2}$ and $3d_{3/2}$, respectively [66]. These features indicate the formation of Zr-O bonds in the metal cluster of UiO-66-NH_2. (i) High resolution scan of O 1s peak for UiO-66-NH_2 showing peaks at binding energies of 531.5 and 529.5 eV, attributed to C=O [67] and Zr-O bonds [66, 68], respectively.

Table 4.9 Elemental composition by SEM-EDS analysis (atomic %) of Ca-NDS (water) synthesized in two-phase flow. The quantification was carried out using the Cliff-Lorimer method with manufacturer-supplied k-factors. The theoretical elemental ratios for the Ca-NDS (water) unit cell [51] are included for comparison.

Elements	C %	O %	S %	Ca %	Ratio of Ca/(Ca+S)
Ca-NDS (water)	51.1	32.8	10.8	5.3	0.33
Unit cell formula Ca-NDS (DMF)	47.6	38.1	9.5	4.8	0.34

Table 4.10 Elemental composition by XPS (atomic%) of Ca-NDS (water) synthesized in two-phase flow. The theoretical elemental ratios for the Ca-NDS (water) unit cell [51] are included for comparison.

Elements	C 1s %	O 1s %	S 2p %	Ca 2p %	Ratio of Ca/(Ca+S)
Ca-NDS (water)	55.6	28.2	10.8	5.4	0.33
Unit cell formula Ca-NDS (DMF)	47.6	38.1	9.5	4.8	0.34

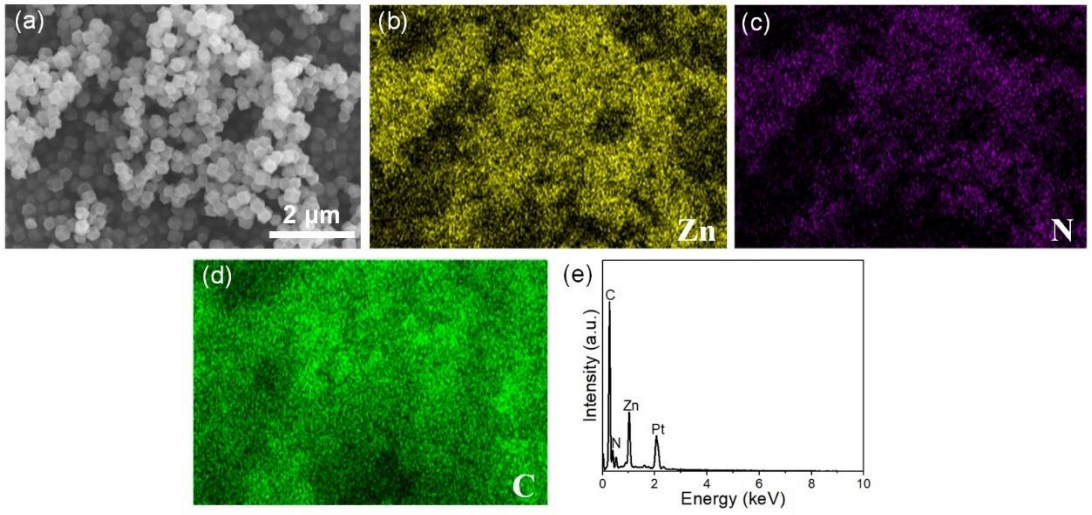

Figure 4.17 (a) SEM image of ZIF-8 particles synthesized n two-phase flow and SEM-EDS elemental maps of (b) zinc, (c) nitrogen, and (d) carbon. (e) Integrated EDS spectrum from the entire field of view.

Table 4.11 Elemental composition by SEM-EDS analysis (atomic %) of ZIF-8 synthesized in two-phase flow. The quantification was carried out using the Cliff-Lorimer method with manufacturer-supplied k-factors. The theoretical elemental ratios for the ZIF-8 unit cell [69] are included for comparison.

Elements	C %	N %	Zn %	Ratio of Zn/(Zn+N)
ZIF-8	74.2	21.4	4.4	0.17
Unit cell formula ZIF-8	61.5	30.8	7.7	0.2

Table 4.12 Elemental composition by XPS (atomic %) of ZIF-8 synthesized in two-phase flow. The theoretical elemental ratios for the ZIF-8 unit cell [69] are included for comparison.

Elements	C 1s %	N 1s %	Zn 2p %	Ratio of Zn/(Zn+N)
ZIF-8	70.6	25.3	4.1	0.14
Unit cell formula ZIF-8	61.5	30.8	7.7	0.2

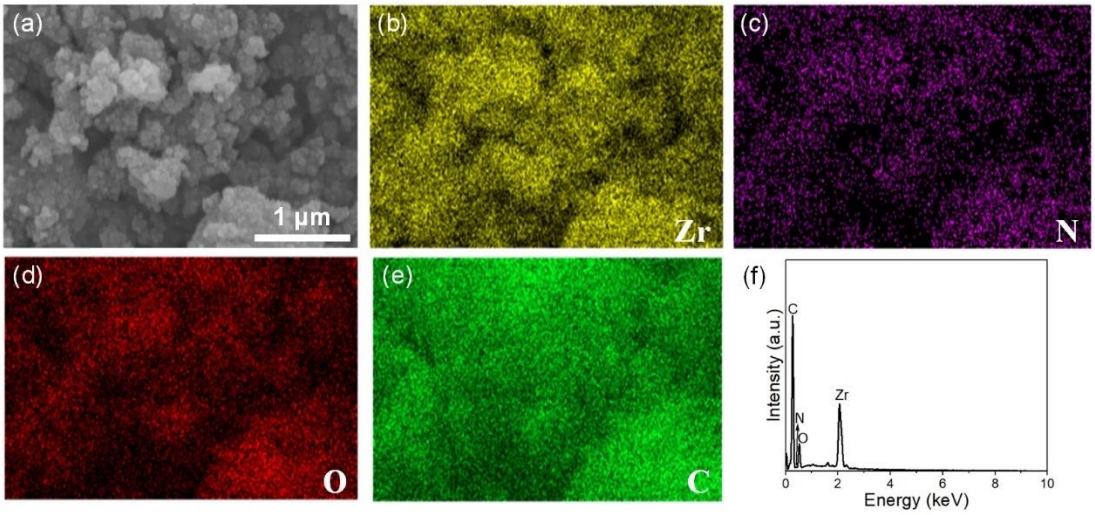

Figure 4.18 (a) SEM image of UiO-66-NH_2 particles flow synthesized in two-phase flow and SEM-EDS elemental maps of (b) zirconium, (c) nitrogen, (d) oxygen, and (e) carbon. (f) Integrated EDS spectrum from the entire field of view.

Table 4.13 Elemental composition by SEM-EDS analysis (atomic %) of UiO-66-NH_2 synthesized in two-phase flow. The quantification was carried out using the Cliff-Lorimer method with manufacturer-supplied k-factors. The theoretical elemental ratios for the UiO-66-NH_2 unit cell [70] are included for comparison.

Elements	C %	O %	N %	Zr %	Ratio of Zr/(Zr+O)	Ratio of Zr/(Zr+N)
UiO-66-NH_2	85.7	11.6	1.0	1.8	0.13	0.64
Unit cell formula UiO-66-NH_2	43.6	44.4	5.5	6.6	0.13	0.55

Table 4.14 Elemental composition by XPS (atomic%) of UiO-66-NH_2 synthesized in two-phase flow. The theoretical elemental ratios for the UiO-66-NH_2 unit cell [70] are included for comparison.

Elements	C 1s %	O 1s %	N 1s %	Zr 3d %	Ratio of Zr/(Zr+O)	Ratio of Zr/(Zr+N)
NH_2-UIO-66	60.6	27.7	5.7	6.0	0.18	0.51
Unit cell formula NH_2-UiO-66	43.6	44.4	5.5	6.6	0.13	0.55

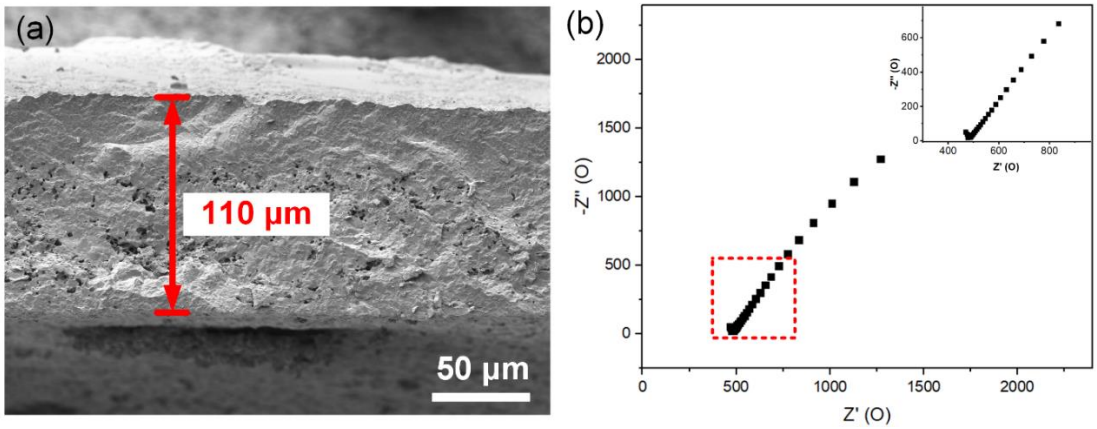

Figure 4.19 (a) Cryo-SEM micrograph of a cross section of the fully hydrated Ca-NDS (water)-MMM-2; and (b) EIS Nyquist plot for Ca-NDS (water) based pellet measured at 80 °C and 95% RH.

Each of the materials also showed matched or superior functional performance properties compared to the samples prepared using batch syntheses. A membrane prepared using Ca-NDS (water) prepared in two-phase flow denoted Ca-NDS (water)-MMM-2 (Figure 4.12e-1, thickness measured by cryo-SEM in Figure 4.19a), exhibited a proton conductivity from EIS of 0.94 ± 0.03 mS cm^{-1} at 80 °C in 95 % RH.

Corresponding pellets exhibited a proton conductivity of 1.48 ± 0.05 mS cm^{-1} at 80 °C in 95 % RH (Figure 4.19b and Table 4.15). These proton conductivity results of Ca-NDS (water) made in two-phase flow were slightly higher than those reported in our previous work [29]. We attribute this improvement to the smaller and more uniform Ca-NDS (water) particles made in the two-phase flow which assist in the preparation of homogenous membranes and pellets with reduced void space.

Table 4.15 Density, resistance, and proton conductivities of Ca-NDS (water) pellets prepared from material synthesized in two-phase flow. Uncertainties are given as one standard deviation.

Sample name	Density (g cm^{-3})	Calculated density (g cm^{-3})	Density as % of calculated density	Thickness (cm)	Resistance (ohm)	Proton conductivity (mS cm^{-1})
Ca-NDS (water) a	1.44	1.746	82.63	0.145	485	1.53
Ca-NDS (water) b	1.52		86.94	0.121	432	1.43
AVG of Ca-NDS (water)	1.48 ± 0.04		85 ± 2	--	--	1.48 ± 0.05

Table 4.16 BET surface area and pore volume of ZIF-8 synthesized by batch, ultrasound-assisted batch, and two-phase flow in ultrasonic bath approaches.

Synthesis methods and median particle size	Batch (600 nm)	Batch in ultrasonic bath (500 nm)	Two-phase flow in ultrasonic bath (330 nm)
BET surface area (m^2 g^{-1})	1587	1735	1886
Pore volume (cm^3 g^{-1})	0.644	0.670	0.721

Table 4.17 BET surface area and pore volume of UiO-66-NH_2 synthesized by batch, ultrasound-assisted batch, and two-phase flow in ultrasonic bath approaches.

Synthesis methods and particle size	Batch	Batch in ultrasonic bath	Two-phase flow in ultrasonic bath
BET surface area (m^2 g^{-1})	743	795	787
Pore volume (cm^3 g^{-1})	0.663	0.720	0.756

For the MOFs ZIF-8 and UiO-66-NH_2, we assessed their properties by N_2

adsorption-desorption isotherms. ZIF-8 isotherms presented a rapid increase at low relative pressure ($P/P_0 < 0.1$) and typical type-I isotherm behavior [71, 72] (Figure 4.12e-2), consistent with the microporous structure of ZIF-8. ZIF-8 synthesized in the second-generation ultrasound-assisted two-phase flow reactor exhibited a surface area of 1886 $m^2 g^{-1}$ and a pore volume of 0.721 $cm^3 g^{-1}$. The specific surface area is very close to the theoretical maximum of 1947 $m^2 g^{-1}$ [73]. Both surface area and pore volume values were higher than for the corresponding batch-synthesized samples (Table 4.16), consistent with the formation of high quality ZIF-8 crystals with significant accessible pore space [73]. The N_2 isotherms recorded on UiO-66-NH_2 samples were classified as type IV isotherms with a clear hysteresis loop [60] (Figure 4.12e-3). UiO-66-NH_2 synthesized in two-phase flow exhibited a surface area of 787 $m^2 g^{-1}$ and a pore volume of 0.756 $cm^3 g^{-1}$. These values were similar to those recorded on samples made in an ultrasonic bath but were higher than batch synthesized samples without ultrasound (Table 4.17). Together, the EIS and N_2 isotherms indicated that the Ca-NDS (water), ZIF-8, and UiO-66-NH_2 crystals prepared by ultrasound-assisted two-phase flow exhibit equal or superior quality to matched aqueous-phase batch synthesis products.

Our reactor design specifically targets the flexible adjustment of ultrasound power between 50 and 150 W allowing the study of this parameter across all three materials Ca-NDS (water), ZIF-8, and UiO-66-NH_2. Figure 4.20a depicts the dependence of STY on ultrasound power, normalised to the STY at 100 W for consistent comparison independent of differences in overall reactivity of the three syntheses at the available flow rates. These STYs were calculated from the total weight of the collected products, justified by the phase purity and the retained or improved properties (Figure 4.20). The STY and production rate results are also summarised in Tables 4.18-20. We note that the STYs in two-phase flow are calculated using the total reactor volume; the yields per volume of solvent used per unit time are approximately double the reported STYs. We observed a consistent trend of increasing STY with increasing ultrasound power across all three linker functional group families. With increasing ultrasound power, smaller particles of Ca-NDS (water) and ZIF-8 were also produced (Figures 4.21 and 4.22), further supporting the enhanced nucleation effects of the ultrasound power. As UiO-66-NH_2 particles were too aggregated to distinguish easily primary particle size, we have not included particle size result for UiO-66-NH_2

(Figure 4.23). We also note that the reaction yields of synthesizing these three MOFs in the ultrasound-assisted two-phase flow are relative lower than batch reaction using a longer time. However, this work is more focused on achieving high STY, so quite short residence times were used for these reactions. In the future, we can optimize reaction parameters to improve yield and STY while also recycling chemical precursors to maximize reagent utilization and minimize environmental pollution.

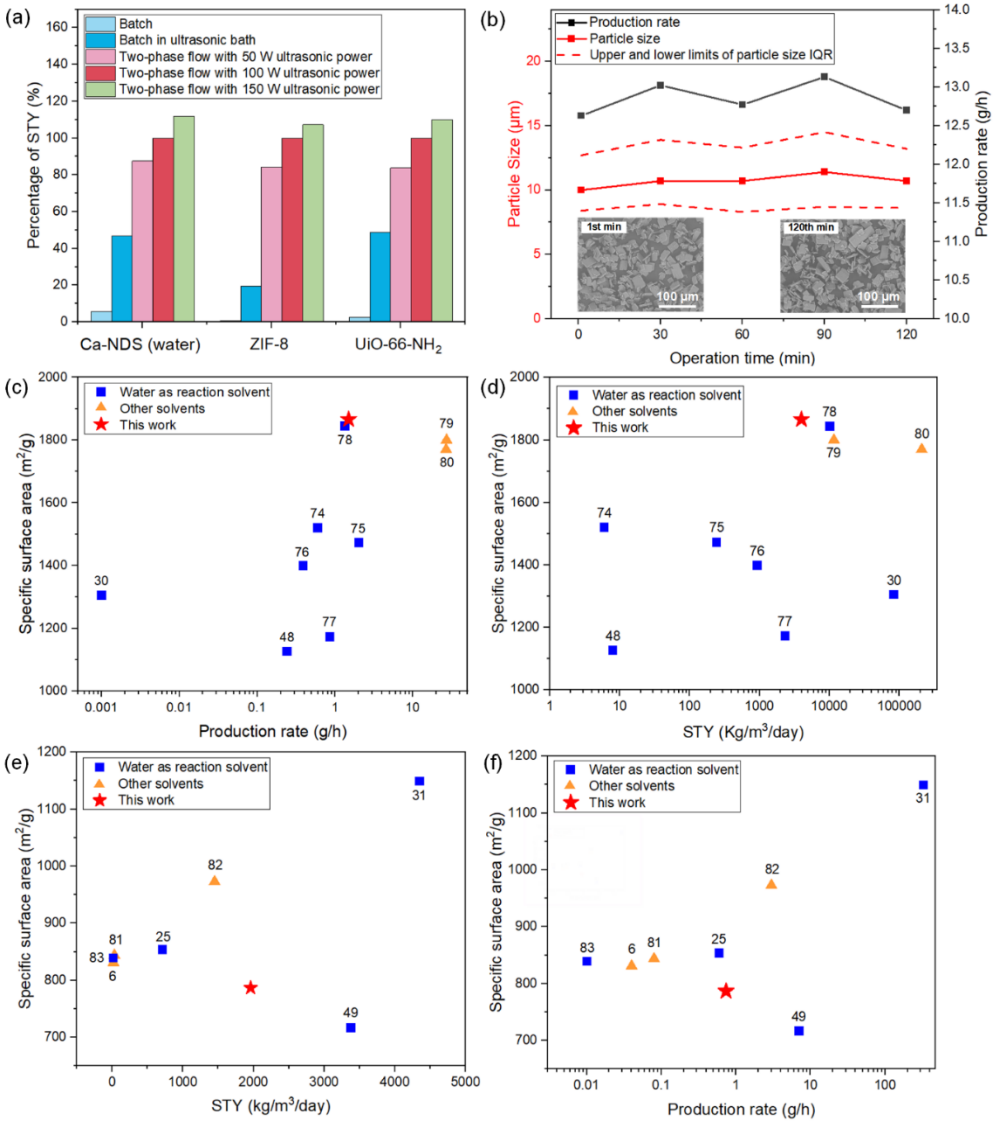

Figure 4.20 (a) Normalised STYs of MOFs made in batch and two-phase flow (100% STY is taken as the STY in two-phase flow with 100 W ultrasonic power). (b) Production rate and particle size for continuous operation of the ultrasound-assisted two-phase flow reactor, showing sustained production of Ca-NDS (water) across 120 min with a 0.75 min residence time and 150 W ultrasonic power at 50 °C. Specific surface area of ZIF-8 made in the two-phase flow as a function of (c) production rate and (d) STY in comparison with previously reported syntheses. Specific surface area of UiO-66-NH_2 made in ultrasound-assisted two-phase flow (this work) as a function of (e) production rate and (f) STY in comparison with previously reported syntheses.

Table 4.18 STY of Ca-NDS (water) synthesized by batch, ultrasound-assisted batch, and ultrasound-assisted two-phase flow methods at 50 °C.

Reaction parameters	30 min batch	2 min batch (100 W)	0.75 min two-phase flow 50 W	0.75 min two-phase flow 100 W	0.75 min two-phase flow 150 W
Yield %	36 ± 2	38 ± 2	28 ± 2	32 ± 2	36 ± 1
STY ($kg\ m^{-3}\ day^{-1}$)	$1.7\times10^{3} \pm 1\times10^{2}$	$1.4\times10^{4} \pm 1\times10^{3}$	$2.7\times10^{4} \pm 2\times10^{3}$	$3.1\times10^{4} \pm 1\times10^{3}$	$3.4\times10^{4} \pm 1\times10^{3}$
Production rate ($g\ h^{-1}$)	1.06 ± 0.06	8.8 ± 0.6	10.0 ± 0.7	11.5 ± 0.4	12.6 ± 0.4

Table 4.19 STY of ZIF-8 synthesized by batch, ultrasound-assisted batch, and ultrasound-assisted two-phase flow methods at 50 °C.

Reaction parameters	180 min batch	5 min batch (100 W)	0.75 min two-phase flow 50 W	0.75 min two-phase flow 100 W	0.75 min two-phase flow 150 W
Yield %	41 ± 2	25 ± 2	21 ± 1	25.2 ± 0.9	27 ± 1
STY ($kg\ m^{-3}\ day^{-1}$)	$3.1\times10^{1} \pm 6$	$7.2\times10^{2} \pm 5\times10^{1}$	$3.1\times10^{3} \pm 2\times10^{2}$	$3.7\times10^{3} \pm 1\times10^{2}$	$4.0\times10^{3} \pm 2\times10^{2}$
Production rate ($g\ h^{-1}$)	0.02 ± 0.01	0.45 ± 0.03	1.15 ± 0.07	1.37 ± 0.04	1.49 ± 0.07

Table 4.20 STY of UiO-66-NH_2 synthesized by batch, ultrasound-assisted batch, and ultrasound-assisted two-phase flow methods at 50 °C.

Reaction parameters	180 min batch	5 min batch (100 W)	1 min two-phase flow 50 W	1 min two-phase flow 100 W	1 min two-phase flow 150 W
Yield %	19.6 ± 0.7	10.3 ± 0.4	6.6 ± 0.4	7.9 ± 0.6	8.7 ± 0.5
STY ($kg\ m^{-3}\ day^{-1}$)	$4.6\times10^{1} \pm 2$	$8.7\times10^{2} \pm 4\times10^{1}$	$1.5\times10^{3} \pm 1\times10^{2}$	$1.8\times10^{3} \pm 1\times10^{2}$	$2.0\times10^{3} \pm 1\times10^{2}$
Production rate ($g\ h^{-1}$)	0.029 ± 0.001	0.54 ± 0.03	0.56 ± 0.04	0.67 ± 0.04	0.74 ± 0.04

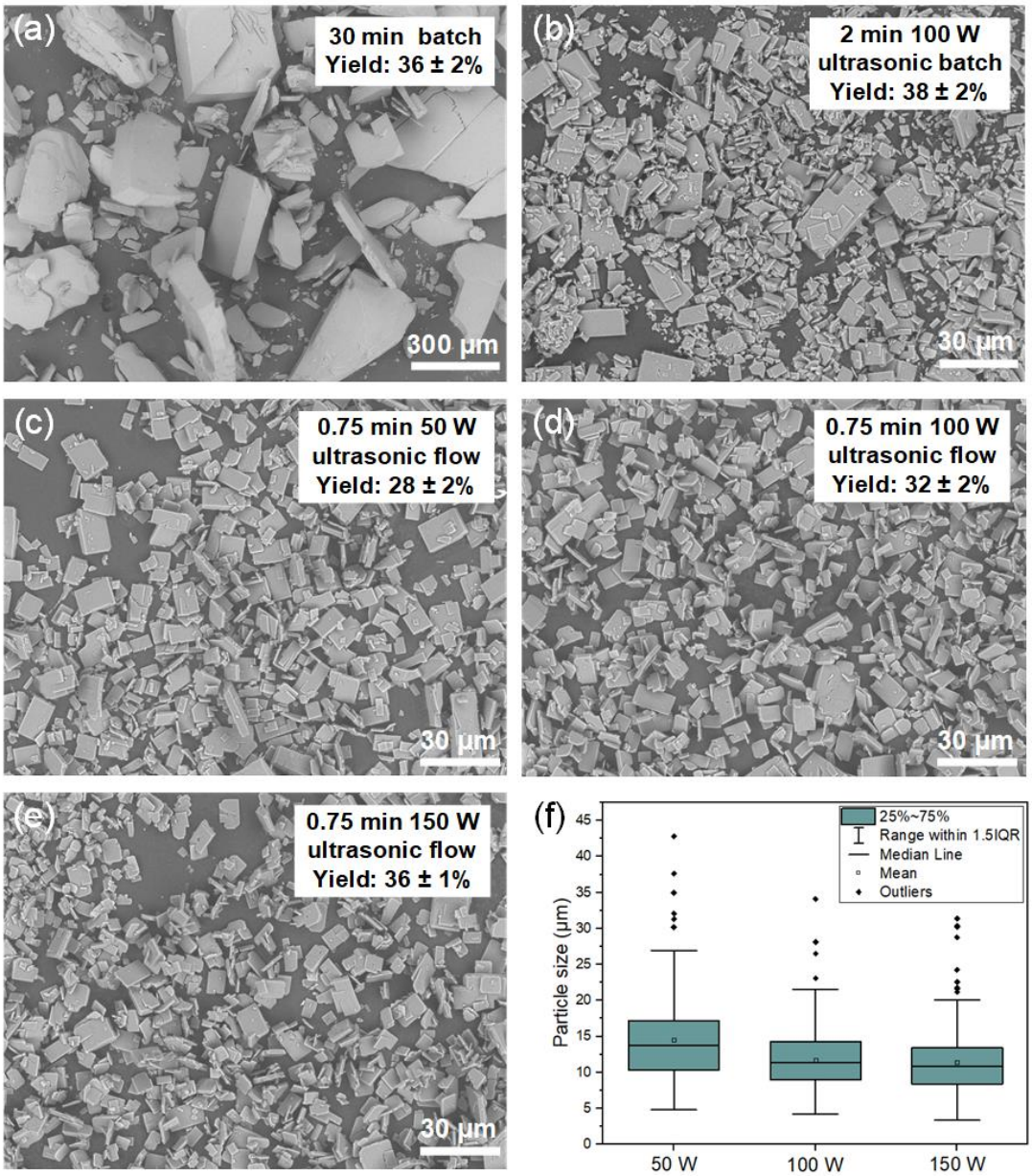

Figure 4.21 SEM images of Ca-NDS (water) particles synthesized in (a) batch with a reaction time of 30 min; (b) ultrasonic batch with a reaction time of 2 min; (c)-(e) two-phase flow (0.75 min or 45 s residence time) using an ultrasonic power of (c) 50 W, (d) 100 W, and (e) 150 W. (f) Box charts of particle size for the samples made in two-phase flow shown in (c)-(e).

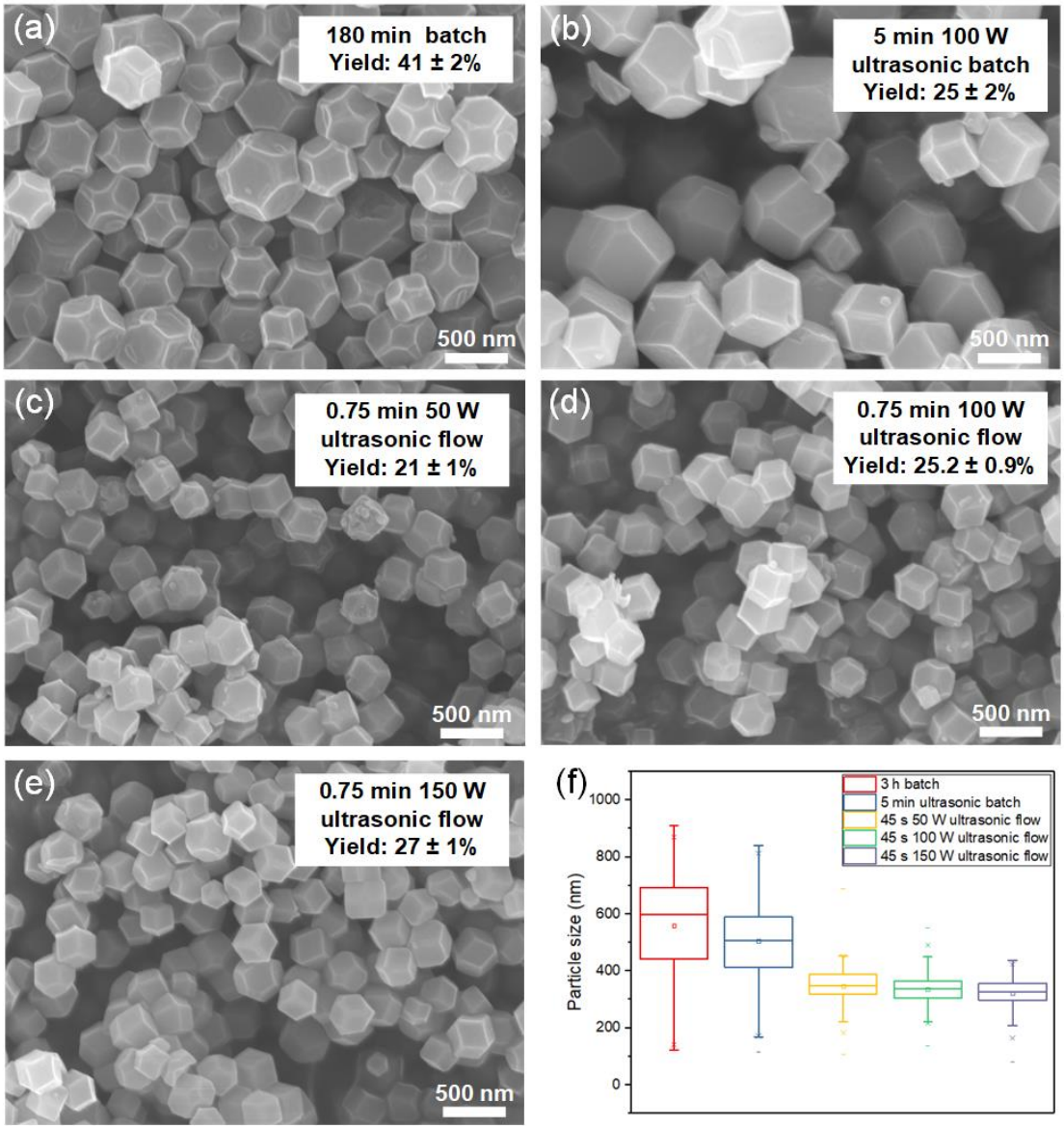

Figure 4.22 SEM images of ZIF-8 particles synthesized in: (a) batch with a reaction time of 180 min (3 h); (b) ultrasonic batch with a reaction time of 5 min; (c)-(e) two-phase flow (0.75 min or 45 s residence time) using ultrasonic powers of (c) 50 W, (d) 100 W, and (e) 150 W. (f) Box charts of particle size of the samples shown in (a)-(e).

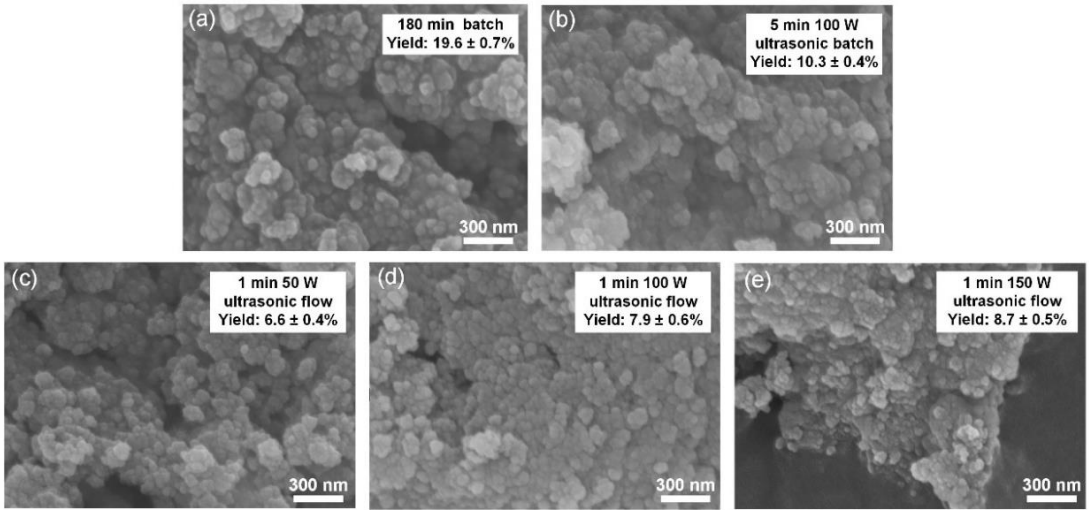

Figure 4.23 SEM images of UiO-66-NH_2 samples synthesized in: (a) batch with a reaction time of 180 min (3 h); (b) ultrasonic batch within 5 min; (c)-(e) two-phase flow (1 min residence time) using ultrasonic powers of (c) 50 W, (d) 100 W, and (e) 150 W.

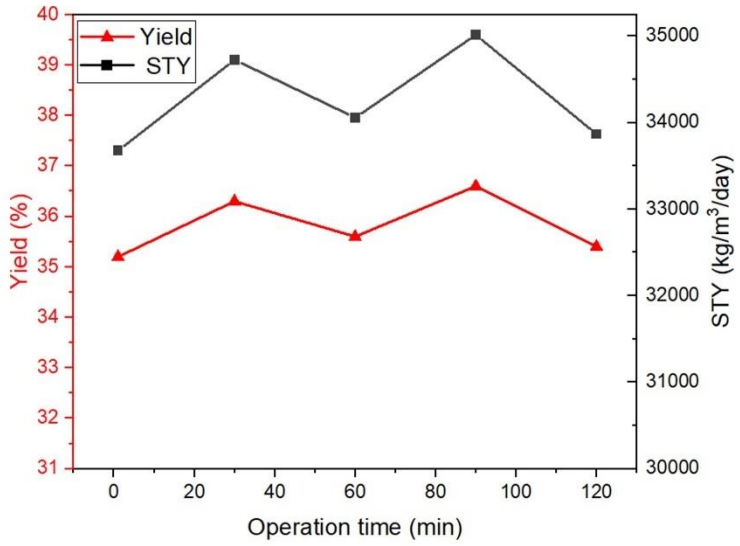

Figure 4.24 Yields and STYs for continuous operation of two-phase flow synthesis of Ca-NDS (water). The reaction platform supports sustained production for over 120 min in ultrasound-assisted two-phase flow with a 0.75 min residence time and a 150 W ultrasonic power at 50 °C.

Finally, to highlight this reactor's capabilities for a fully continuous mode of operation, the syringe pumps were further replaced by two SyrDos pumps to continuously feed precursors (total flow rate of 6 mL min^{-1}, flow rate of N_2 gas was 6 mL min^{-1}). Returning to the ultrasound-assisted two-phase flow continuous synthesis of Ca-NDS (water) with 0.75 min residence time at 50 °C under 150 W ultrasonic power, we operated the reactor for more than 120 minutes without interruption. As shown in Figure 4.20b, this reaction platform demonstrated a sustained production rate

of 12.9 ± 0.4 g h^{-1} in the synthesis of Ca-NDS (water) with no reduction in the production rate or change in particle size observed during this extended continuous operation. Moreover, we observed no evidence of reactor fouling. The reaction yield remained constant at 35.8 ± 0.5 % and the STY was consistently $3.43\times10^4 \pm 5\times10^2$ kg m^{-3} day^{-1}, exhibiting smaller deviations than the errors estimated from three separate flow syntheses using syringe pumps under otherwise identical reaction conditions (Figure 4.24 and Table 4.18). Not only does the reactor platform offer rapid transferability across different aqueous-phase synthesis, but this evidence on continuous operation additionally highlights the suitability of this reaction platform design for scalable production.

The highest STYs (using syringe pumps) for Ca-NDS (water), ZIF-8, and UiO-66-NH_2 MOFs were $3.4\times10^4 \pm 1\times10^3$, $4.0\times10^3 \pm 2\times10^2$, and $2.0\times10^3 \pm 1\times10^2$ kg m^{-3} day^{-1}, respectively. To contextualise these results, we have drawn together other previously reported aqueous-phase syntheses of ZIF-8 [30, 48, 74-80] and UiO-66-NH_2 [6, 25, 31, 49, 81-83] that report the necessary details for comparison of production rate, STY, and specific surface area (Figure 4.20c-f and Tables 4.21 and 4.22). Only two previous reports, including one of our own, have reported the synthesis of Ca-NDS (water) with previous work focused on the structure rather than production rate. Nevertheless, STYs of the order of 10^3-10^5 kg m^{-3} day^{-1} and production rates of the order 10^1 g h^{-1} have been considered of scalable and commercial interest in other systems [84, 85]. Our ZIF-8 synthesis stands out as delivering specific surface areas and production rates among the highest reported to date, excluding approaches with different solvents or additives (Figure 4.20c and d). Polyzoidis and co-workers reported a much higher STY for ZIF-8 that synthesized in flow, but they used methanol and NH_3(aq) as solvent [80], while our work used water as green solvent to reduce the environmental impact. Our UiO-66-NH_2 synthesis is within the spread of previous reports (Figure 4.20e and f).

Table 4.21 Comparison of surface areas, yields, space time yields (STYs), production rates, and surface area production rate (SAPR) for aqueous ZIF-8 syntheses reported in the literature and this work. RT denotes room temperature.

Solvent	Temp (°C)	Synthesis method	BET surface area ($m^2\ g^{-1}$)	Yield (%)	STY ($kg\ m^{-3}\ day^{-1}$)	Production rate ($g\ h^{-1}$)	SAPR ($m^2\ m^{-3}\ day^{-1}$)	Ref.
water	25	Hydro-thermal batch	1126	90	8	0.24	9.0×10^6	48
water	RT	Hydro-thermal batch	1520	97.5	6	0.6	9.1×10^6	74
water	RT	Hydro-thermal batch	1472	90	244	2.03	3.6×10^8	75
water	RT	Hydro-thermal batch	1398.7	84.5	930	0.39	1.3×10^9	76
water	RT	Hydro-thermal batch	1173	80	2337	0.86	2.7×10^9	77
water	RT	AC electrokinetic assisted continuous flow	1305	49	83623	0.001	1.1×10^{11}	30
water	RT	Continuous flow	1844	--	10132	1.34	1.9×10^{10}	78
water + NH_4OH	RT	Continuous flow	1800	--	11625	27	2.1×10^{10}	79
MeOH + NH_3	RT	Continuous flow	1770	54	210000	26.67	3.7×10^{11}	80
water	50	Ultrasound-assisted two-phase flow	1886	27.1	4000	1.49	7.5×10^9	This work

Note: the specific surface area can vary depending on the calculation method, references in this table are from the main text.

The surface area production rate (SAPR) has also been put forward as an important figure of merit [86, 87]. At 7.5×10^9 $m^2\ m^{-3}\ day^{-1}$ for ZIF-8 and 1.6×10^9 $m^2\ m^{-3}\ day^{-1}$ for UiO-66-NH_2, our reactor offers competitive SAPR values for both ZIF-8 and UiO-66-NH_2 (maximum prior values of 10^6-10^{11} $m^2\ m^{-3}\ day^{-1}$ for ZIF-8 and 10^6-10^9 $m^2\ m^{-3}\ day^{-1}$ for UiO-66-NH_2, Tables 4.21 and 4.22). These figures of merit underscore the rapid transferability to other systems, i.e. the generalisation of the

reactor platform, without substantial re-optimisation of each synthesis. We also note that our reactor is a small laboratory scale flow reactor with 9 mL volume in our reaction platform, and so the competitive production of high-quality crystals and generalisation across distinct functional group chemistries highlights the advantages for larger or parallelised reactors of ultrasound-assisted aqueous synthesis in two-phase flow. Using N_2 as the carrier phase, moreover, ensures facile separation and reduced waste (offering an oil- and organic solvent-free two-phase reactor solution).

Table 4.22 Comparison of surface areas, yields, space time yields (STYs), production rates, and surface area production rate (SAPR) for aqueous UiO-66-NH_2 syntheses reported in the literature and this work. RT denotes room temperature.

Solvent	Temp (°C)	Synthesis method	BET surface area (m^2 g^{-1})	Yield (%)	STY (kg m^3 day^{-1})	Production rate (g h^{-1})	SAPR (m^2 m^{-3} day^{-1})	Ref.
water + acetic acid	RT	Hydro-thermal batch	854	40	716	0.6	6.1×10^8	25
water + acetic acid	RT	Hydro-thermal batch	717	37	3381	7.04	2.4×10^9	49
EtOH + formic acid	110	Hydro-thermal in vacuum	831	75	20	0.04	1.7×10^7	6
DMF	RT	Electro-chemical	844	62	32	0.08	2.7×10^7	81
water + acetic acid	85	Continuous synthesis	1150	74	4346	325	5.0×10^9	31
DMF + trifluoracetic acid	175	Microwave assisted	973	86	1450	3	1.4×10^9	82
water + acetic acid	90	Continuous flow spray-drying	840	70	10	0.01	8.4×10^6	83
water + acetic acid	50	Ultrasound-assisted two-phase flow	787	8.7	2000	0.74	1.6×10^9	This work

Note: the specific surface area can vary depending on the calculation method, references in this table are from the main text.

A core motivation in scale-up synthesis is to produce chemicals at the lowest cost possible, so costs comparison between batch and flow systems are worth considering. Batch systems typically have lower initial capital costs but higher operating costs due

to labor and downtime, whereas flow processing systems need higher upfront investments but offer lower long-term costs because of automation, efficiency, and waste reduction [88]. The flow systems are more generalizable for synthesizing different types of materials, while further changing of machine settings are needed when switching between product types in batch systems [89]. Flow systems usually consume less energy by maintaining steady-state conditions, whereas batch processes involve frequent heating and cooling cycles [90]. Batch systems tend to be less efficient in terms of material usage, resulting in higher reagent consumption and waste, whereas flow systems allow precise control, reducing costs [91]. Finally, safety and compliance costs for batch systems are typically higher due to variability and the risk of runaway reactions, whereas flow systems offer better control and fewer hazards, making them a cost-effective option for continuous production [90]. Based on these information, the ultrasound-assisted flow reaction systems reported in this work is more cost-effective and is more promising for scale-up synthesis than batch systems.

4.4 Conclusions

In summary, we report an ultrasound-assisted two-phase flow reactor for the aqueous-phase continuous production of the sulfonate coordination polymer Ca-NDS (water), as well the imidazolate MOF ZIF-8 and the carboxylate MOF UiO-66-NH_2. By using N_2 gas as the carrier phase, this reactor eliminates steps for the chemical or mechanical separation of a liquid carrier phase. The reactor supports adjustable ultrasound power, enabling the isolation of the effects of this parameter. Ultrasound power consistently increases yield and reduces particle size and the width of the particle size distribution, outlining a consistent enhancement in the rate of nucleation. The reactor nevertheless produces highly faceted Ca-NDS (water) and ZIF-8 crystals with high quality proton conductivities (1.48 ± 0.05 mS cm^{-1} in pellet form and 0.94 ± 0.03 mS cm^{-1} in MMM form at 80 °C in 95 % RH) and gas sorption (1886 m^2 g^{-1}), respectively. Using the reactor, we record STYs for Ca-NDS (water), ZIF-8, and UiO-66-NH_2 of $3.4\times10^4 \pm 1\times10^3$, $4.0\times10^3 \pm 2\times10^2$ and $2.0\times10^3 \pm 1\times10^2$ kg m^{-3} day^{-1}, respectively. Moreover, we have demonstrated that the reactor can be operated with continuous precursor feeds and without fouling for more than 2 hours with a sustained production rate and crystal product quality. Together, these results demonstrate the generalizable and scalable green chemical synthesis of coordination polymers and MOFs using ultrasound-assisted continuously operable reactors. The ultrasound-

assisted design may, in turn, boost production rates further in application to reactors with scaled up volumes for efficient MOF synthesis with reduced environmental impact.

4.5 References

[1] X.L. Hu, K. Wang, X. Li, Q.Q. Pan, Z.M. Su, Two Anthracene Chromophores based Metal-Organic Frameworks for Gas Absorption and Promising Nitro Aromatic Sensing, New J. Chem. 44 (2020) 1249-1252.

[2] D. Lv, P. Zhou, J. Xu, S. Tu, F. Xu, J. Yan, H. Xi, W. Yuan, Q. Fu, X. Chen, Q. Xia, Recent advances in adsorptive separation of ethane and ethylene by C_2H_6-selective MOFs and other adsorbents, Chem. Eng. J. 431 (2022) 133208-133230.

[3] D. Yang, B.C. Gates, Catalysis by Metal Organic Frameworks: Perspective and Suggestions for Future Research, ACS Catal. 9 (2019) 1779-1798.

[4] Y. Li, J. Feng, L. Wang, G. Li, High proton conduction in two highly stable phenyl imidazole dicarboxylate-based Cd(II)-MOFs, J. Solid State Chem. 319 (2023) 123828.

[5] H.N. Abdelhamid, G.A. Mahmoud, W. Sharmouk, A cerium-based MOFzyme with multi-enzyme-like activity for the disruption and inhibition of fungal recolonization, J. Mater. Chem. B 8 (2020) 7548-7556.

[6] X. Zhang, S. Zhang, G. Ouyang, R. Han, Removal of Cr(VI) from solution using UiO-66-NH_2 prepared in a green way, Korean J. Chem. Eng. 39 (2022) 1839-1849.

[7] R. Sahoo, S.C. Pal, M.C. Das, Solid-State Proton Conduction Driven by Coordinated Water Molecules in Metal–Organic Frameworks and Coordination Polymers, ACS Energy Lett. 7 (2022) 4490-4500.

[8] C. Sun, M. Barton, C.M. Pask, M. Edokali, L. Yang, A.J. Britton, S. Micklethwaite, F. Iacoviello, A. Hassanpour, M. Besenhard, R. Drummond-Brydson, K.-J. Wu, S.M. Collins, Droplet-based millifluidic synthesis of a proton-conducting sulfonate metal–organic framework, Chem. Eng. J. 474 (2023) 145892.

[9] S. Tai, W. Zhang, J. Zhang, G. Luo, Y. Jia, M. Deng, Y. Ling, Facile preparation of UiO-66 nanoparticles with tunable sizes in a continuous flow microreactor and its application in drug delivery, Micropor. and Mesopor. Mat. 220 (2016) 148-154.

[10] Y.-K. Seo, G. Hundal, I.T. Jang, Y.K. Hwang, C.-H. Jun, J.-S. Chang, Microwave synthesis of hybrid inorganic–organic materials including porous $Cu_3(BTC)_2$ from Cu(II)-trimesate mixture, Micropor. and Mesopor. Mat. 119 (2009) 331-337.

[11] A. Grigoropoulos, A.I. McKay, A.P. Katsoulidis, R.P. Davies, A. Haynes, L. Brammer, J. Xiao, A.S. Weller, M.J. Rosseinsky, Encapsulation of Crabtree's Catalyst in Sulfonated MIL-101(Cr): Enhancement of Stability and Selectivity between Competing Reaction Pathways by the MOF Chemical Microenvironment, Angew Chem. Int. Ed. Engl. 57 (2018) 4532-4537.

[12] Z. Mai, D. Liu, Synthesis and Applications of Isoreticular Metal–Organic Frameworks IRMOFs-n (n = 1, 3, 6, 8), Cryst. Growth Des. 19 (2019) 7439-7462.

[13] B. Huang, Y. Li, W. Zeng, Application status of zeolitic imidazolate framework in gas sensors, Nano Futures 6 (2022) 032003.

[14] M.O. Besenhard, S. Pal, G. Gkogkos, Non-fouling flow reactors for nanomaterial synthesis, React. Chem. Eng. 8 (2023) 955-977.

[15] S. Mohammadi, A. Harvey, K.V.K. Boodhoo, Synthesis of TiO_2 nanoparticles in a spinning disc reactor, Chem. Eng. J. 258 (2014) 171-184.

[16] X. Chen, N.M. Smith, K.S. Iyer, C.L. Raston, Controlling nanomaterial synthesis, chemical reactions and self assembly in dynamic thin films, Chem. Soc. Rev. 43 (2014) 1387-1399.

[17] K. Simeonidis, A. Makridis, M. Angelakeris, I. Kellartzis, S. Veintemillas-Verdaguer, Continuous production of magnetic iron oxide nanocrystals by oxidative precipitation, Chem. Eng. J. 393 (2020) 124593.

[18] I. Lignos, Y. Mo, L. Carayannopoulos, M. Ginterseder, M.G. Bawendi, K.F. Jensen, A high-temperature continuous stirred-tank reactor cascade for the multistep synthesis of InP/ZnS quantum dots, React. Chem. Eng. 6 (2021).
[19] L. Chen, H. Zeng, Y. Guo, X. Yang, B. Chen, A comparative analysis of micro-mixing process in a confined impinging jet reactor with/without applying ultrasound, Chem. Eng. Process. 177 (2022) 108991.
[20] M.O. Besenhard, S. Pal, L. Storozhuk, S. Dawes, N.T.K. Thanh, L. Norfolk, S. Staniland, A. Gavriilidis, A versatile non-fouling multi-step flow reactor platform: demonstration for partial oxidation synthesis of iron oxide nanoparticles, Lab Chip 23 (2023) 115-124.
[21] C. Howell, A. Grinthal, S. Sunny, M. Aizenberg, J. Aizenberg, Designing Liquid-Infused Surfaces for Medical Applications: A Review, Adv. Mater. 30 (2018) 1802724.
[22] V.V. Butova, A.P. Budnyk, E.A. Bulanova, C. Lamberti, A.V. Soldatov, Hydrothermal synthesis of high surface area ZIF-8 with minimal use of TEA, Solid State Sci. 69 (2017) 13-21.
[23] L.A. Lozano, C.M. Iglesias, B.M.C. Faroldi, M.A. Ulla, J.M. Zamaro, Efficient solvothermal synthesis of highly porous UiO-66 nanocrystals in dimethylformamide-free media, J. Mater. Sci. 53 (2017) 1862-1873.
[24] X. Zhang, Z. Chen, X. Liu, S.L. Hanna, X. Wang, R. Taheri-Ledari, A. Maleki, P. Li, O.K. Farha, A historical overview of the activation and porosity of metal–organic frameworks, Chem. Soc. Rev. 49 (2020) 7406-7427.
[25] I. Pakamor, J. Rousseau, C. Rousseau, E. Monflier, P.g. Szilágyi, An ambient-temperature aqueous synthesis of zirconium-based metal–organic frameworks, Green Chem. 20 (2018).
[26] P.B. So, P.-H. Tang, B.-S. Liao, N. Sathishkumar, H.-T. Chen, C.-H. Lin, Sustainable scale-up synthesis of MIL-68 (Al) using IPA as solvent for acetic acid capture, Micropor. Mesopor. Mat. 316 (2021) 110943.
[27] P. Marino, P.R. Donnarumma, H.A. Bicalho, V. Quezada-Novoa, H.M. Titi, A.J. Howarth, A step toward change: a green alternative for the synthesis of metal–organic frameworks, ACS Sustain. Chem. Eng. 9 (2021) 16356-16362.
[28] J. Zhang, G.B. White, M.D. Ryan, A.J. Hunt, M.J. Katz, Dihydrolevoglucosenone (Cyrene) as a green alternative to N, N-dimethylformamide (DMF) in MOF synthesis, ACS Sustain. Chem. Eng. 4 (2016) 7186-7192.
[29] C. Sun, C.M. Pask, S.T. Pham, E. Rapaccioli, A.J. Britton, S. Micklethwaite, A. Bell, M.O. Besenhard, R. Drummond-Brydson, K.-J. Wu, Modulating proton conductivity through crystal structure tuning in arenedisulfonate coordination polymers, J. Mater. Chem. A 12 (2024) 18440-18451.
[30] S. Chen, X. Zhou, G. Li, F. Yang, Controlled synthesis of metal-organic frameworks via AC electrokinetic mixing-assisted microfluidics: A case study of ZIF-8, Chem. Eng. J. 480 (2024) 148208.
[31] H. Reinsch, S. Waitschat, S.M. Chavan, K.P. Lillerud, N. Stock, A Facile "Green" Route for Scalable Batch Production and Continuous Synthesis of Zirconium MOFs, Eur. J. Inorg. Chem. 2016 (2016) 4490-4498.
[32] J. Cao, X. Peng, H. Li, L. Ren, T. Xu, K. Sun, Y. Zhang, D. Li, Ultrasound-assisted continuous-flow synthesis of PEGylated MIL-101(Cr) nanoparticles for hematopoietic radioprotection, Mater. Sci. Eng. C 129 (2021) 112369.
[33] C. Forsyth, T. Taras, A. Johnson, J. Zagari, C. Collado, M.M. Hoffmann, C.R. Reed, Microwave Assisted Surfactant-Thermal Synthesis of Metal-Organic Framework Materials, Appl. Sci. 10 (2020) 4563.

[34] D. Rambabu, S. Bhattacharyya, T. Singh, L.C. M, T.K. Maji, Stabilization of $MAPbBr_3$ Perovskite Quantum Dots on Perovskite MOFs by a One-Step Mechanochemical Synthesis, Inorg. Chem. 59 (2020) 1436-1443.
[35] I. Rossetti, M. Compagnoni, Chemical reaction engineering, process design and scale-up issues at the frontier of synthesis: Flow chemistry, Chem. Eng. J. 296 (2016) 56-70.
[36] O. Długosz, M. Banach, Inorganic nanoparticle synthesis in flow reactors – applications and future directions, React. Chem. Eng. 5 (2020) 1619-1641.
[37] N. Hao, Y. Nie, J.X.J. Zhang, Microfluidic synthesis of functional inorganic micro-/nanoparticles and applications in biomedical engineering, Int. Mater. Rev. 63 (2018) 461-487.
[38] M. Rubio-Martinez, C. Avci-Camur, A.W. Thornton, I. Imaz, D. Maspoch, M.R. Hill, New synthetic routes towards MOF production at scale, Chem. Soc. Rev. 46 (2017) 3453-3480.
[39] M. Faustini, J. Kim, G.Y. Jeong, J.Y. Kim, H.R. Moon, W.S. Ahn, D.P. Kim, Microfluidic approach toward continuous and ultrafast synthesis of metal-organic framework crystals and hetero structures in confined microdroplets, J. Am. Chem. Soc. 135 (2013) 14619-14626.
[40] H. Lu, H. Wang, Y. Liu, M. Wang, J. Hu, Q. Yang, Substance transfer behavior controlled by droplet internal circulation, Chem. Eng. J. 393 (2020) 124657.
[41] V.V. Banakar, S.S. Sabnis, P.R. Gogate, A. Raha, Saurabh, Ultrasound assisted continuous processing in microreactors with focus on crystallization and chemical synthesis: A critical review, Chem. Eng. Res. Des. 182 (2022) 273-289.
[42] A. Dastbaz, J. Karimi-Sabet, M.A. Moosavian, Sonochemical synthesis of novel decorated graphene nanosheets with amine functional Cu-terephthalate MOF for hydrogen adsorption: Effect of ultrasound and graphene content, International Journal of Hydrogen Energy 44 (2019) 26444-26458.
[43] B. Pollet, The Use of Power Ultrasound for the Production of PEMFC and PEMWE Catalysts and Low-Pt Loading and High-Performing Electrodes, Catalysts 9 (2019) 246.
[44] Z. Dong, C. Delacour, K.M. Carogher, A.P. Udepurkar, S. Kuhn, Continuous Ultrasonic Reactors: Design, Mechanism and Application, Materials 13 (2020) 344.
[45] Z. Dong, D.F. Rivas, S. Kuhn, Acoustophoretic focusing effects on particle synthesis and clogging in microreactors, Lab Chip 19 (2019) 316-327.
[46] R.J. Eder, S. Schrank, M.O. Besenhard, E. Roblegg, H. Gruber-Woelfler, J.G. Khinast, Continuous sonocrystallization of acetylsalicylic acid (ASA): Control of crystal size, Cryst. Growth Des. 12 (2012) 4733-4738.
[47] D. Rossi, R. Jamshidi, N. Saffari, S. Kuhn, A. Gavriilidis, L. Mazzei, Continuous-flow sonocrystallization in droplet-based microfluidics, Cryst. Growth Des. 15 (2015) 5519-5529.
[48] Jian, Meipeng, Wang, Huanting, Liu, Bao, Jiuhui, Zhang, Xiwang, Ruiping, Water-based synthesis of zeolitic imidazolate framework-8 with high morphology level at room temperature, RSC Adv. 5 (2015) 48433.
[49] L. Huelsenbeck, H. Luo, P. Verma, J. Dane, R. Ho, E. Beyer, H. Hall, G.M. Geise, G. Giri, Generalized Approach for Rapid Aqueous MOF Synthesis by Controlling Solution pH, Cryst. Growth Des. 20 (2020) 6787-6795.
[50] J.W. Osterrieth, J. Rampersad, D. Madden, N. Rampal, L. Skoric, B. Connolly, M.D. Allendorf, V. Stavila, J.L. Snider, R. Ameloot, How reproducible are surface areas calculated from the BET equation?, Adv. Mater. 34 (2022) 2201502.

[51] J. Cai, C.H. Chen, C.Z. Liao, X.L. Feng, X.M. Chen, Solid-state structures of group 1 and group 2 metal 1,5-naphthalenedisulfonates: systematic investigation of lamellar three-dimensional networks constructed by metal arenedisulfonate, Acta Crystallogr. B 57 (2001) 520-530.
[52] J.T.W. Wang, S.L.C. Hsu, Enhanced high-temperature polymer electrolyte membrane for fuel cells based on polybenzimidazole and ionic liquids, Electrochim. Acta 56 (2011) 2842-2846.
[53] L. Zhong, S.F. Parker, Structure and vibrational spectroscopy of methanesulfonic acid, R. Soc. Open Sci. 5 (2018) 181363.
[54] M. Staufer, U. Birkenheuer, T. Belling, F. Nörtemann, N. Rösch, W. Widdra, K.L. Kostov, T. Moritz, D. Menzel, The vibrational structure of benzene adsorbed on Si(001), J. Chem. Phys. 112 (2000) 2498-2506.
[55] Y. Ishida, T. Togashi, K. Yamamoto, M. Tanaka, T. Kiss, T. Otsu, Y. Kobayashi, S. Shin, Time-resolved photoemission apparatus achieving sub-20-meV energy resolution and high stability, Rev. Sci. Instrum. 85 (2014) 123904.
[56] M. Jian, B. Liu, G. Zhang, R. Liu, X. Zhang, Adsorptive removal of arsenic from aqueous solution by zeolitic imidazolate framework-8 (ZIF-8) nanoparticles, Colloids Surf. A 465 (2015) 67-76.
[57] M. He, J. Yao, Q. Liu, K. Wang, F. Chen, H. Wang, Facile synthesis of zeolitic imidazolate framework-8 from a concentrated aqueous solution, Microporous and Mesoporous Mater. 184 (2014) 55-60.
[58] Z.-X. Low, J. Yao, Q. Liu, M. He, Z. Wang, A.K. Suresh, J. Bellare, H. Wang, Crystal Transformation in Zeolitic-Imidazolate Framework, Cryst. Growth Des. 14 (2014) 6589-6598.
[59] X. Zhang, Y. Zhang, T. Wang, Z. Fan, G. Zhang, A thin film nanocomposite membrane with pre-immobilized UiO-66-NH(2) toward enhanced nanofiltration performance, RSC Adv. 9 (2019) 24802-24810.
[60] S. Wu, Y. Ge, Y. Wang, X. Chen, F. Li, H. Xuan, X. Li, Adsorption of Cr(VI) on nano UiO-66-NH_2 MOFs in water, Environ. Technol. 39 (2018) 1937-1948.
[61] M. Aghajanzadeh, M. Zamani, H. Molavi, H. Khieri Manjili, H. Danafar, A. Shojaei, Preparation of Metal–Organic Frameworks UiO-66 for Adsorptive Removal of Methotrexate from Aqueous Solution, J. Inorg. Organomet. Polym. Mater. 28 (2017) 177-186.
[62] Q. Liu, J. Li, Z. Zhou, J. Xie, J.Y. Lee, Hydrophilic Mineral Coating of Membrane Substrate for Reducing Internal Concentration Polarization (ICP) in Forward Osmosis, Sci. Rep. 6 (2016) 19593.
[63] D. Liu, Z. Jin, Y. Bi, Charge transmission channel construction between a MOF and rGO by means of Co–Mo–S modification, Catal. Sci. Technol. 7 (2017) 4478-4488.
[64] F. Kumbetlioglu, K.O. Oskay, Z. Ciplak, A. Ates, Preparation, Characterization, and Application of Metal Oxide-Doped Zeolitic Imidazolate Framework, ACS Omega 8 (2023) 27650-27662.
[65] F. Tian, A.M. Cerro, A.M. Mosier, H.K. Wayment-Steele, R.S. Shine, A. Park, E.R. Webster, L.E. Johnson, M.S. Johal, L. Benz, Surface and Stability Characterization of a Nanoporous ZIF-8 Thin Film, J. Phys. Chem. C 118 (2014) 14449-14456.
[66] M. Peñas-Garzón, M.J. Sampaio, Y.L. Wang, J. Bedia, J.J. Rodriguez, C. Belver, C.G. Silva, J.L. Faria, Solar photocatalytic degradation of parabens using UiO-66-NH_2, Sep. Purif. Technol. 286 (2022) 120467.

[67] A. Dolgov, D. Lopaev, C.J. Lee, E. Zoethout, V. Medvedev, O. Yakushev, F. Bijkerk, Characterization of carbon contamination under ion and hot atom bombardment in a tin-plasma extreme ultraviolet light source, Appl. Surf. Sci. 353 (2015) 708-713.
[68] J. Ren, S. Lv, S. Wang, M. Bao, X. Zhang, Y. Gao, Y. Liu, Z. Zhang, L. Zeng, J. Ke, Construction of efficient g-C_3N_4/NH_2-UiO-66 (Zr) heterojunction photocatalysts for wastewater purification, Sep. Purif. Technol. 274 (2021) 118973.
[69] W. Morris, C.J. Stevens, R.E. Taylor, C. Dybowski, O.M. Yaghi, M.A. Garcia-Garibay, NMR and X-ray Study Revealing the Rigidity of Zeolitic Imidazolate Frameworks, J. Phys. Chem. C 116 (2012) 13307-13312.
[70] C.A. Trickett, K.J. Gagnon, S. Lee, F. Gandara, H.B. Burgi, O.M. Yaghi, Definitive molecular level characterization of defects in UiO-66 crystals, Angew.Chem. Int. Ed 54 (2015) 11162-11167.
[71] W. Morris, C.J. Stevens, R. Taylor, C. Dybowski, O.M. Yaghi, M.A. Garcia-Garibay, NMR and X-ray study revealing the rigidity of zeolitic imidazolate frameworks, J. Phys. Chem. C 116 (2012) 13307-13312.
[72] J. Liu, J. He, L. Wang, R. Li, P. Chen, X. Rao, L. Deng, L. Rong, J. Lei, NiO-PTA supported on ZIF-8 as a highly effective catalyst for hydrocracking of Jatropha oil, Sci. Rep. 6 (2016) 23667.
[73] M. Taheri, I.D. Bernardo, A. Lowe, D.R. Nisbet, T. Tsuzuki, Green Full Conversion of ZnO Nanopowders to Well-Dispersed Zeolitic Imidazolate Framework-8 (ZIF-8) Nanopowders via a Stoichiometric Mechanochemical Reaction for Fast Dye Adsorption, Cryst. Growth Des. 20 (2020) 2761-2773.
[74] K. Kida, M. Okita, K. Fujita, S. Tanaka, Y. Miyake, Formation of high crystalline ZIF-8 in an aqueous solution, CrystEngComm 15 (2013) 1794.
[75] I.U. Khan, M.H.D. Othman, A.F. Ismail, N. Ismail, J. Jaafar, H. Hashim, M.A. Rahman, A. Jilani, Structural transition from two-dimensional ZIF-L to three-dimensional ZIF-8 nanoparticles in aqueous room temperature synthesis with improved CO_2 adsorption, Mater. Charact. 136 (2018) 407-416.
[76] M.U.A. Prathap, S. Gunasekaran, Rapid and Scalable Synthesis of Zeolitic Imidazole Framework (ZIF-8) and its Use for the Detection of Trace Levels of Nitroaromatic Explosives, Adv. Sustain. Syst. 2 (2018) 1800053.
[77] Y. Pan, Y. Liu, G. Zeng, L. Zhao, Z. Lai, Rapid synthesis of zeolitic imidazolate framework-8 (ZIF-8) nanocrystals in an aqueous system, Chem. Commun. 47 (2011) 2071-2073.
[78] H. Wu, C. Wu, W. Liao, B.M. Matsagar, K. Chang, J. Huang, K.C.W. Wu, Continuous and ultrafast MOF synthesis using droplet microfluidic nanoarchitectonics, J. Mater. Chem. A 11 (2023) 9427-9435.
[79] A.S. Munn, P.W. Dunne, S.V. Tang, E.H. Lester, Large-scale continuous hydrothermal production and activation of ZIF-8, Chem. Commun. 51 (2015) 12811-12814.
[80] A. Polyzoidis, T. Altenburg, M. Schwarzer, S. Loebbecke, S. Kaskel, Continuous microreactor synthesis of ZIF-8 with high space–time-yield and tunable particle size, Chem. Eng. J. 283 (2016) 971-977.
[81] J.Z. Wei, F.X. Gong, X.J. Sun, Y. Li, T. Zhang, X.J. Zhao, F.M. Zhang, Rapid and Low-Cost Electrochemical Synthesis of UiO-66-NH_2 with Enhanced Fluorescence Detection Performance, Inorg. Chem. 58 (2019) 6742-6747.
[82] R.M. Guerrero, I.D. Lemir, S. Carrasco, C. Fernandez-Ruiz, S. Kavak, P. Pizarro, D.P. Serrano, S. Bals, P. Horcajada, Y. Perez, Scaling-Up Microwave-Assisted

Synthesis of Highly Defective Pd@UiO-66-NH_2 Catalysts for Selective Olefin Hydrogenation under Ambient Conditions, ACS Appl. Mater. Interfaces 16 (2024) 24108-24121.
[83] C. Avci-Camur, J. Troyano, J. Pérez-Carvajal, A. Legrand, D. Farrusseng, I. Imaz, D. Maspoch, Aqueous production of spherical Zr-MOF beads via continuous-flow spray-drying, Green Chem. 20 (2018) 873-878.
[84] M. Rubio-Martinez, T.D. Hadley, M.P. Batten, K. Constanti-Carey, T. Barton, D. Marley, A. Mönch, K.S. Lim, M.R. Hill, Scalability of continuous flow production of metal–organic frameworks, ChemSusChem 9 (2016) 938-941.
[85] M. Rubio-Martinez, M.P. Batten, A. Polyzos, K.-C. Carey, J.I. Mardel, K.-S. Lim, M.R. Hill, Versatile, high quality and scalable continuous flow production of metal-organic frameworks, Sci. Rep. 4 (2014) 5443.
[86] A. Laybourn, A.M. López-Fernández, I. Thomas-Hillman, J. Katrib, W. Lewis, C. Dodds, A.P. Harvey, S.W. Kingman, Combining continuous flow oscillatory baffled reactors and microwave heating: Process intensification and accelerated synthesis of metal-organic frameworks, Chem. Eng. J. 356 (2019) 170-177.
[87] C. McKinstry, E.J. Cussen, A.J. Fletcher, S.V. Patwardhan, J. Sefcik, Scalable continuous production of high quality HKUST-1 via conventional and microwave heating, Chem. Eng. J. 326 (2017) 570-577.
[88] C. Holtze, R. Boehling, Batch or flow chemistry?–a current industrial opinion on process selection, Curr. Opin. Chem. Eng. 36 (2022) 100798.
[89] G. Steiner, W.G. Truscott, Batch scheduling to minimize cycle time, flow time, and processing cost, IIE transactions 25 (1993) 90-97.
[90] D. Dallinger, C.O. Kappe, Why flow means green–Evaluating the merits of continuous processing in the context of sustainability, Curr. Opin. Green Sustain. Chem. 7 (2017) 6-12.
[91] T.A. Phung Hai, A.A. Samoylov, B.S. Rajput, M.D. Burkart, Laboratory ozonolysis using an integrated Batch–DIY flow system for renewable material production, ACS omega 7 (2022) 15350-15358.

Chapter 5 Conclusions and Future work

5.1 Conclusions

The overall aim of this thesis was to explore the crystal growth processes, encompassing solvent- and ligand-metal interactions, of sulfonate MOFs, the effects on their proton conductivities, and the potential for scalable and generalisable green chemical synthesis platforms for MOFs. These aims took shape through the lenses of tuning crystal structures by using different metal ions and sulfonate ligands as well as green solvents as well as the development of continuous and ultrasound-assisted synthesis methods.

In Chapter 2, the focus was on exploring the possibility of transferring the batch-synthesized a sulfonate MOF to millifluidic continuous synthesis and to interrogate optimal reaction conditions and trade-offs in particle size control and yield. In this research, the sulfonate MOF denoted Cu-SAT [1] was first synthesized in a two-phase millifluidic flow reactor. Reaction yields in the flow reactor were typically 10-20% higher than those obtained in the batch reactor under the matched reaction parameters, because of the higher mass and heat transfer in the flow reactor. The fouling-free multiphase flow reactor synthesis was operated for more than 5 h with no reduction in yield or change in the particle size distribution, and demonstrated a sustained STY up to 10^2 kg m^{-3} day^{-1} with consistent particle quality. These results indicated that the flow synthesis method reported in this work is promising for scaled-up fabrication of other sulfonate MOFs. In contrast, STYs for hydrothermal or solvothermal synthesis are often in the range of 0.1-10 kg m^{-3} day^{-1} with inferior particle size control [2, 3].

A factorial DoE approach was used to investigate how reaction parameters affect reaction results in the flow synthesis in this work. The DoE and modelling results revealed a Pareto front for trade-offs in particle size control and yield in the continuous synthesis of Cu-SAT. These analyses also indicated that Cu-SAT presented the predominant characteristics of nucleation-dominated crystallization, a characteristic similar to reports on HKUST-1 [4], MIL-101(Al) [5], and MIL-88A(Fe) [6]. The DoE approach reported in this work outlined a route for using a small number of experiments to rapidly identify characteristics of synthetic response. In addition, the proton conductivity of the flow synthesized Cu-SAT MOF can reach up to 10^{-3} S cm^{-1} at 80 °C and 95% RH. This proton conductivity was higher than many reported MOFs

[7-9] often with conductivities between 10^{-6} and 10^{-4} S cm^{-1}. Nafion exhibits a much higher proton conductivities than our work in the range of 10^{-2} to 10^{-1} S cm^{-1} [10]. However, Nafion manufacturing depends on toxic precursors and highly reactive intermediates, presenting hazards as well as contributing to high production costs [11, 12].

In Chapter 3, the focus was on synthesizing sulfonate CPs with simplified method and following green chemistry principles, in turn exploring how the solvent-directed crystal structure affects their proton conductivities. Side reactions between precursors in the form of gel formation was a significant challenge in the Cu-SAT synthesis when the ligands are not dissolved in the right sequence and mixed in the right way. Given that the NDS ligand used to prepare Cu-SAT presented promising proton conductivity (Chapter 2), in Chapter 3 a simplified single ligand strategy was used to synthesize different sulfonate CPs using NDS as well as ADS ligands. Drawing inspiration from the consistent 2D sheet structured Ca-NDS CP [13], this work reported 7 solvent-directed crystal structures for sulfonate CPs using Cu^{2+} and Ca^{2+} as metal ions and DMF as well as green solvents (EtOH, water and DMSO). These reaction solvents served as both ligands (water, DMSO, DMF) and pore-templating agents (DMF) that provided a means for tuning the hydrogen bonding network structure in sulfonate CPs. Proton conductivities of pellets made from these sulfonate CPs were from 10^{-4} to 10^{-3} S cm^{-1} at 80 °C and 95% RH, prompting further investigation for their use in PEMs as proton conductivities in the range of 10^{-3} to 10^{-1} S cm^{-1} are considered promising for MOFs [14]. To further probe the structural and chemical origins of the observed spread in conductivities, structural similarities and differences of these sulfonate CPs were analysed. This study showed that reduced tortuosity in the proton transport pathway was correlated with higher proton conductivities, outlining a structural design principle for optimising proton conductivity systematically in sulfonate CPs and likely wider CP and MOF materials.

Degradation products are rarely well described; in this work, by developing a direct synthesis route by introducing EtOH to the solvent system together with single-crystal X-ray diffraction, the structure of the degradation product of the Cu-SAT MOF after water exposure was determined. In the beginning of this research, EtOH was used to mix with water and DMF as solvents in the synthesis of Cu-SAT for reducing the amount of DMF, following green chemical synthesis principles. XRD results indicated

that a new structure (Cu-SAT (EtOH)) was formed in this greener synthesis compared with Cu-SAT, but this XRD results were the same with water-aged Cu-SAT structure. The structure analysis indicated that the water-aged Cu-SAT structure, as for directly synthesised Cu-SAT (EtOH) was not a simple decomposition product. Instead, the Cu-SAT (EtOH) structure presented a more compact, DMF-free structure with the loss of void spaces present in the Cu-SAT. This structure change resulted in a higher RMSD value of proton transport pathway in the Cu-SAT (EtOH) compared with Cu-SAT, which explained why Cu-SAT presented better proton conductivity than Cu-SAT (EtOH). This finding elucidates the why and the how of sulfonate CPs lost the proton conduction performance. Cyrene and STEPOSOL MET-10U were also studied as greener solvents for sulfonate CP synthesis but did not result in coordination polymers under the conditions examined, which may be caused by the steric hindrance of these two solvents. I have noticed that EtOH did not coordinate and integrate with the Cu-SAT (EtOH) crystal structures, maybe because EtOH does not has strong donor or long-pairs that can effectively combine with active sites in the crystal structure.

In Chapter 4, the focus was on scalable and green chemical (aqueous solvent) synthesis of the sulfonate CP Ca-NDS (water) as well as the imidazolate MOF ZIF-8 and the carboxylate MOF UiO-66-NH_2. Ultrasound-assisted flow synthesis was used for MOF fabrication, as ultrasound energy can increase nucleation rate during crystal synthesis [15, 16]. Ca-NDS (water) was chosen for the ultrasound-assisted flow synthesis at first, as this MOF presented a good proton conductivity of 1.46 ± 0.08 mS cm^{-1} at 80 °C and 95% RH using water as solvent (Chapter 3). Moreover, Ca-NDS (water) can be synthesized readily at room temperature and can form crystals quite rapidly compared with Cu-SAT and other MOFs which need days or many hours, indicating this MOF is more promising for scalable, green chemical synthesis. At the beginning, a Box-Behnken experimental design, providing more data points than a simple design used Chapter 2, and was used for linear RSM to optimize reaction parameters for maximising the STY while minimising the particle size and particle size dispersity. These analyses also provided insights into the nucleation mechanisms in the ultrasound-assisted continuous synthesis of Ca-NDS (water) in a single-phase flow reactor. As Ca-NDS (water) can be formed in several minutes in the ultrasound-assisted synthesis, a 4.5 m CFIR reactor was used for the continuous synthesis. DoE results indicated that higher yield arose from elevated rates of crystal nucleation, while

lower yield arose from slower nucleation tipping the balance toward particle sizes dominated by crystal growth. In this case, and in contrast to work on Cu-SAT in Chapter 2, there was only a single optimum condition for increasing STY and controlling particle size in the ultrasound-assisted continuous synthesis of Ca-NDS (water). I attribute these differences in the ultrasound-assisted case to the significantly enhanced nucleation rates driving high yield with low particle size dispersity as likewise observed for ZIF-8 synthesised in the ultrasound-assisted two-phase flow reactor.

This ultrasound-assisted two-phase flow reaction platform was created to explore the generalisation of this design for the scale-up synthesis of the Ca-NDS (water), ZIF-8, and UiO-66-NH_2 MOFs in aqueous solvent. In Chapter 2, silicone oil was used as the second phase, requiring significant separation and washing processes after synthesis. In Chapter 4, N_2 gas was used as the second phase to support long operation time and eliminate separation of a liquid carrier phase. The same flow rates were used for the N_2 gas and the precursor solution in order to create stable slug-flow patterns. Using this reaction platform, high-quality MOF crystals were fabricated in less than 1 min, and STYs and production rates reached 10^4 kg m^{-3} day^{-1} and 10 g h^{-1}, respectively. The reactor did not only offer higher STYs but also provided particle size control for smaller and more uniform MOF particles compared to batch and flow syntheses without ultrasound. I attribute these findings to the promotion of the nucleation rate by the ultrasound during crystal synthesis. Pellets and membranes prepared using ultrasound-assisted flow synthesized Ca-NDS (water) exhibited proton conductivities from EIS of 1.48 ± 0.05 and 0.94 ± 0.03 mS cm^{-1} at 80 °C in 95 % RH respectively, which were better than pellets and membranes made by batch synthesized samples that reported in Chapter 3. In Chapter 2, large crystals of Cu-SAT presented problems for homogenous membrane fabrication, requiring that they were ground into a smaller powder for better dispersion in the polymer. In contrast, in Chapter 4 the fabricated Ca-NDS (water) particles could be used to make membranes directly, offering an integrated solution for fabrication of optimal functional properties and form all while at a high production rate.

5.2 Future Research

This work establishes several paths for further development. One promising

direction is the enhancement of the continuous flow reactor described in Chapter 2 by integrating a bottle-style back-pressure regulator (BPR). This addition would enable more precise pressure control, mitigating air bubble formation and allowing higher synthesis temperatures by raising the solvent's boiling point. We have carried out some initial continuous synthesis of Cu-SQAT in the two-phase (oil and DMF/water) flow reactor using a bottle-style BPR, but further investigation is needed to establish the reliability and scalability of this method. The bottle-style BPR will limit the total collection volume, which can introduce additional complexity. Although a bottle-style BPR may introduce volume limitations, we can combine the bottle-style BPR with switching valves to facilitate dynamic concentration changes without interrupting the reaction process, providing additional flexibility for continuous synthesis.

From a scale-up perspective, this work lays the foundation for transitioning to larger reactors or parallel reactor configurations. Small lab scale flow reactors with less than 10 m PFA tubing and an inner diameter of 1.58 mm were used in this research. In the future designs, we could expand to tubing lengths exceeding 30 m with a broader diameter of ~3 mm, enabling higher flow rates and significantly boosting STYs. Such a design may lead to greater pressure build-up, requiring matched pumps suitable for such a scaled-up reactor system. For the same space time, higher flow rates can be achieved in the bigger flow reactor, promoting higher production rates and STYs under the similar temperatures and precursor concentrations. Alternatively, we could use parallel reactors, such as in the form of several small reactors working in parallel, for scaled-up synthesis by adding more channels or reactors, and it can be designed to fit a specific requirement for application with limited space area, though they require careful attention to operational complexity and equipment costs. [17]. Fouling of the flow reactor also deserves my future study, because it is a common challenge that can affect reaction efficiency, reproducibility, and scalability. Hydrophobic or hydrophilic coatings could be used to modify reactor surface to minimize adhesion of particles. Periodic cleaning of reactor by flushing with solvents or back-flushing and using antifouling additives are also good strategies that I can try to prevent the fouling of flow reactor.

The ultrasound-assisted synthesis in Chapter 4 presented much higher reaction rates than traditional hydrothermal or solvothermal batch reactions. In the future study, we would like to explore which specific reaction step (precursor coordination,

nucleation, or crystal growth) that most affected by ultrasonic input. Comparing the crystal induction time between batch and the ultrasound-assisted syntheses would advance this open question. The induction time is the period of time between reaching constant supersaturation and detecting the crystal [18]. Short induction times not only contribute to higher nucleation rates and smaller crystal size of MOFs, but also reduce the need for long heating times or additional energy inputs, making the synthesis process more energy efficient [19]. *In situ* XRD could be used to detect the induction time for MOF synthesis in the flow reactor. In the ultrasound-assisted continuous synthesis set-up, a section of tubing within the reactor could be connected with *in situ* XRD instrumentation for the real-time tracking crystalline phase formation. Some other characterization methods, such as dynamic light scattering, *in situ* UV-Vis or Raman spectroscopy can also be used to measure the induction time of MOFs. Induction time can provide information about nucleation kinetics, precursor behaviour, and reaction pathways in the MOF synthesis, key details for the reaction method optimization.

Three MOFs have been synthesized in the ultrasound-assisted reaction platform reported in the third experimental work. In the future, I could synthesize some further MOFs, such as HKUST-1 [20], and MIL MOFs [21] in this reaction platform to further demonstrate the general applicability of this approach for scalable MOF production. HKUST-1 and MIL MOFs have particularly high surface area with good gas adsorption and separation properties, offering further prospects of targeted functional properties and demand for scale-up in production. Beyond the sono-chemical approach, microwave-assisted reactions have also been reported for the fast synthesis of MOFs [22-24]. Microwave input can provide greater efficiency in heating than in conventional batch reaction, resulting in enhanced yield and reduced reaction times. Microwave-assisted synthesis may achieve higher nucleation rates than ultrasound-assisted synthesis without the requirement for an additional temperature controller set-up. Hence, the microwave-assisted continuous synthesis method would also represent a natural extension in the future for exploring scalable and green chemical synthesis of MOFs as well as across other particle syntheses.

In the Chapter 3, the experimental structure-function relationship between the tortuosity of the hydrogen bonding pathway and proton conductivities was established by analysing 7 different sulfonate CPs. To confirm the generality of this relationship,

we could synthesize and analyse some additional sulfonate CPs. Experiments to probe the proton conduction mechanisms or modelling would also extend and complement these lines of inquiry. Further sulfonate ligands such as N,N'-disulfonatenaphthalenediimide [25], 5-sulfoisophthalate [26, 27] and 4,4'-disulfo-2,2'-bipyridine-N,N'-dioxide [28] incorporating other functional groups and new metal ions i.e. Ba^{2+} could be used to create some new sulfonate CPs. The sulfonate CP synthesized by Ba^{2+} and NDS ligand with 3D structure has been reported by Cai *et al.* [13]. The materials investigated in Chapters 2-3 primarily focused on 2D sulfonate CPs, raising the question of whether proton conduction occurs strictly within the 2D sheets, a question that could be addressed by exploring 3D coordination geometries. Coordinating Ba^{2+} ions with different sulfonate ligands offers an opportunity to create new 3D-structured sulfonate crystals, opening a pathway to study a broader dimensionality of crystal structures and hydrogen bonding networks through systematically designed frameworks. This direction could help uncover sulfonate CPs with even higher proton conductivity. As some sulfonate MOFs [29, 30] exhibit proton conductivities of 10^{-1} to10^{-2} S cm^{-1} have been reported, the further improvement of the proton conductivity, advances in the stability of sulfonate MOFs, and the reduction in production costs may develop MOF-polymer membranes as suitable candidates to replace Nafion in the future.

5.3 References

[1] R. Moi, A. Ghorai, S. Banerjee, K. Biradha, Amino- and Sulfonate-Functionalized Metal–Organic Framework for Fabrication of Proton Exchange Membranes with Improved Proton Conductivity, Cryst. Growth Des. 20 (2020) 5557-5563.

[2] Jian, Meipeng, Wang, Huanting, Liu, Bao, Jiuhui, Zhang, Xiwang, Ruiping, Water-based synthesis of zeolitic imidazolate framework-8 with high morphology level at room temperature, RSC Adv. 5 (2015) 48433.

[3] Z. Hu, Y. Peng, Z. Kang, Y. Qian, D. Zhao, A Modulated Hydrothermal (MHT) Approach for the Facile Synthesis of UiO-66-Type MOFs, Inorg. Chem. 54 (2015) 4862-4868.

[4] E. Biemmi, S. Christian, N. Stock, T. Bein, High-throughput screening of synthesis parameters in the formation of the metal-organic frameworks MOF-5 and HKUST-1, Micropor. Mesopor. Mat. 117 (2009) 111-117.

[5] E. Stavitski, M. Goesten, J. Juan Alcaniz, A. Martinez-Joaristi, P. Serra Crespo, A.V. Petukhov, J. Gascon, F. Kapteijn, Kinetic control of metal-organic framework crystallization investigated by time-resolved in situ X-ray scattering, Angew. Chem. Int. Ed. 50 (2011) 9624-9628.

[6] E. Bagherzadeh, S.M. Zebarjad, H.R. Madaah Hosseini, P. Chagnon, Preparation, optimization and evolution of the kinetic mechanism of an Fe-MIL-88A metal–organic framework, CrystEngComm 21 (2019) 544-553.

[7] P. Ramaswamy, N.E. Wong, G.K. Shimizu, MOFs as proton conductors–challenges and opportunities, Chem. Soc. Rev. 43 (2014) 5913-5932.

[8] F. Zhang, T. Zhang, X. Zou, X. Liang, G. Zhu, F. Qu, Electrochemical synthesis of metal organic framework films with proton conductive property, Solid State Ionics 301 (2017) 125-132.

[9] H. Zhao, Z.H. Du, C.Y. Mu, G. Li, Proton conductive properties of a substituted imidazole dicarboxylate-based hydrogen-bonded organic framework and a related nickel-organic framework, J. Solid State Chem. 315 (2022) 123550.

[10] M. Casciola, G. Alberti, M. Sganappa, R. Narducci, On the decay of Nafion proton conductivity at high temperature and relative humidity, J. Power Sources 162 (2006) 141-145.

[11] N.A. Nazir, N. Kim, W.G. Iglesias, A. Jakli, T. Kyu, Conductive behavior in relation to domain morphology and phase diagram of Nafion/poly(vinylidene-co-trifluoroethylene) blends, Polymer 53 (2012) 196-204.

[12] M.A. Hickner, H. Ghassemi, Y.S. Kim, B.R. Einsla, J.E. McGrath, Alternative Polymer Systems for Proton Exchange Membranes (PEMs), Chem. Rev. 104 (2004) 4587-4612.

[13] J. Cai, C.H. Chen, C.Z. Liao, X.L. Feng, X.M. Chen, Solid-state structures of group 1 and group 2 metal 1,5-naphthalenedisulfonates: systematic investigation of lamellar three-dimensional networks constructed by metal arenedisulfonate, Acta Crystallogr. B 57 (2001) 520-530.

[14] S.C. Pal, M.C. Das, Superprotonic conductivity of MOFs and other crystalline platforms beyond 10^{-1} S cm^{-1}, Adv. Funct. Mater. 31 (2021) 2101584.

[15] V.V. Banakar, S.S. Sabnis, P.R. Gogate, A. Raha, Saurabh, Ultrasound assisted continuous processing in microreactors with focus on crystallization and chemical synthesis: A critical review, Chem. Eng. Res. Des. 182 (2022) 273-289.

[16] J. Cao, X. Peng, H. Li, L. Ren, T. Xu, K. Sun, Y. Zhang, D. Li, Ultrasound-assisted continuous-flow synthesis of PEGylated MIL-101(Cr) nanoparticles for hematopoietic radioprotection, Mater. Sci. Eng. C 129 (2021) 112369.

[17] R. Bareither, D. Pollard, A review of advanced small-scale parallel bioreactor technology for accelerated process development: Current state and future need, Biotechnol. Prog. 27 (2011) 2-14.
[18] S. Jiang, J.H. ter Horst, Crystal Nucleation Rates from Probability Distributions of Induction Times, Cryst. Growth Des. 11 (2010) 256-261.
[19] M.J. Van Vleet, T. Weng, X. Li, J. Schmidt, In situ, time-resolved, and mechanistic studies of metal–organic framework nucleation and growth, Chem. Rev. 118 (2018) 3681-3721.
[20] L.L. Jiang, X.z. Zeng, M.k. Li, M.Q. Wang, T.Y. Su, X.C. Tian, J. Tang, Rapid electrochemical synthesis of HKUST-1 on indium tin oxide, RSC Adv. 7 (2017) 9316-9320.
[21] F. Tan, M. Liu, K. Li, Y. Wang, J. Wang, X. Guo, G. Zhang, C. Song, Facile synthesis of size-controlled MIL-100 (Fe) with excellent adsorption capacity for methylene blue, Chem. Eng. J. 281 (2015) 360-367.
[22] C. Forsyth, T. Taras, A. Johnson, J. Zagari, C. Collado, M.M. Hoffmann, C.R. Reed, Microwave Assisted Surfactant-Thermal Synthesis of Metal-Organic Framework Materials, Appl. Sci. 10 (2020) 4563.
[23] A. Laybourn, J. Katrib, R.S. Ferrari-John, C.G. Morris, S. Yang, O. Udoudo, T.L. Easun, C. Dodds, N.R. Champness, S.W. Kingman, Metal–organic frameworks in seconds via selective microwave heating, J. Mater. Chem. A 5 (2017) 7333-7338.
[24] I. Thomas Hillman, L.A. Stevens, M. Lange, J. Mllmer, W. Lewis, C. Dodds, S.W. Kingman, A. Laybourn, Developing a sustainable route to environmentally relevant metal–organic frameworks: ultra-rapid synthesis of MFM-300(Al) using microwave heating, Green Chem. 21 (2019) 5039-5045.
[25] D.K. Panda, K. Maity, A. Palukoshka, F. Ibrahim, S. Saha, Li⁺ Ion-Conducting Sulfonate-Based Neutral Metal–Organic Framework, ACS Sustain. Chem. Eng. 7 (2019) 4619-4624.
[26] D.K. Maity, K. Otake, S. Ghosh, H. Kitagawa, D. Ghoshal, Sulfonic Group Functionalized Mixed Ligand Coordination Polymers: Synthesis, Characterization, Water Sorption, and Proton Conduction Studies, Inorg. Chem. 56 (2017) 1581-1590.
[27] B. Joarder, J.B. Lin, Z. Romero, G. Shimizu, Single Crystal Proton Conduction Study of a Metal Organic Framework of Modest Water Stability, J. Am. Chem. Soc. 139 (2017) 7176-7179.
[28] Brett, D., Chandler, Joanne, O., Yu, David, T., Cramb, George, Series of Lanthanide-Alkali Metal-Organic Frameworks Exhibiting Luminescence and Permanent Microporosity, Chem. Mater. 19 (2007) 4467–4473.
[29] M. Wahiduzzaman, S. Wang, J. Schnee, A. Vimont, V. Ortiz, P.G. Yot, R. Retoux, M. Daturi, J.S. Lee, J.S. Chang, A High Proton Conductive Hydrogen-Sulfate Decorated Titanium Carboxylate MOF, ACS Sustain. Chem. Eng. 7 (2019) 5776-5783.
[30] X.-M. Li, L.-Z. Dong, S.-L. Li, G. Xu, J. Liu, F.-M. Zhang, L.-S. Lu, Y.-Q. Lan, Synergistic Conductivity Effect in a Proton Sources-Coupled Metal–Organic Framework, ACS Energy Lett. 2 (2017) 2313-2318.